UNIVERSITÉ DE STRASBOURG

EDSC Ecole Doctorale des Sciences Chimiques

ÉCOLE DOCTORALE DES SCIENCES CHIMIQUES

[UMR 7177]

EN CO-TUTELLE AVEC

UNIVERSITÉ LIBRE DE BRUXELLES

ULB UNIVERSITÉ LIBRE DE BRUXELLES

FACULTÉ DES SCIENCES ULB

THÈSE

présentée par

[Anna ITKIN]

soutenue le : **14 Mai 2012**

pour obtenir le grade de

Docteur de l'université de Strasbourg

Discipline / Spécialité : Résonance magnétique et biophysique des membranes

Multidisciplinary study of Alzheimer's disease-related peptides: from Amyloid precursor protein (APP) to Amyloid β-oligomers and γ-secretase modulators

THÈSE dirigée par :

M. BECHINGER Burkhard	Prof., Université de Strasbourg
M. RAUSSENS Vincent	Prof., Université Libre de Bruxelles
M. RUYSSCHAERT Jean-Marie	Prof. Honoraire, Université Libre de Bruxelles

RAPPORTEURS :

M. HUSTER Daniel	Prof., University of Leipzig
M. WARSCHAWSKI Dror	H.d.R., CNRS-UMR 7099

MEMBRES DU JURY :

Mme. HELLWIG Petra	Prof., Université de Strasbourg
M. GOORMAGHTIGH Erik	Prof., Université Libre de Bruxelles
Mme. PRÉVOST Martine	Maître de Recherches F.R.S.-F.N.R.S., Université Libre de Bruxelles

RESUMÉ

INTRODUCTION

La maladie d'Alzheimer (AD) est une maladie neuro-dégénérative affectant presque 2% de la population des pays industrialisés. L'AD est la forme la plus commune de démence caractérisée par la destruction des cellules du cerveau, une perte de mémoire et une détérioration cognitive et des processus comportementaux suffisamment sérieuse pour affecter l'activité professionnelle, la vie sociale et les loisirs des personnes atteintes. Cette maladie mortelle s'aggrave au fil du temps. L'un des marqueurs histopathologiques caractéristiques de l'AD est la présence de dépôts protéiques et de plaques amyloïdes dans le cerveau. Ces plaques se composent de peptides bêta-amyloïdes (Aβ) de 40 et 42 résidus de longueur, et sont les produits du clivage par des protéases de la protéine précurseur de l'amyloïde (APP).

L'APP est une protéine membranaire intégrale avec un seul domaine transmembranaire (TM) exprimée dans de nombreux tissus et concentrée dans les synapses des neurones. L'APP est plus connue et plus communément étudiée en tant que molécule précurseur dont la protéolyse génère des peptides Aβ, des peptides de 38 à 42 acides aminés de longueur, et dont la forme fibrillaire est le principal composant des plaques amyloïdes retrouvées dans le cerveau des patients atteints de l'AD.

On a récemment découvert qu'un mécanisme de clivage protéolytique séquentiel de libération d'Aβ était à l'origine des multiples clivages par γ-sécrétase, générant des peptides Aβ de différentes longueurs. Il a été prouvé que la protéolyse intramembranaire par γ-sécrétase nécessitait un effilochage local de la structure hélicoïdale secondaire du domaine TM. En effet, certaines fonctions inhabituelles de la séquence APP_TM pourraient déstabiliser sa structure hélicoïdale dans la membrane. Premièrement, on constate une densité d'acides aminés bêta-branchés (Valine, Thréonine, Isoleucine) élevée autour des sites de clivage Aβ40- et Aβ42- susceptible de déstabiliser la structure secondaire des hélices TM.

Deuxièmement, plusieurs des glycines du domaine de l'APP_TM se produisent dans des motifs GxxxG, Gly625, Gly629, and Gly633, et on a constaté qu'elles jouaient un rôle de médiateur dans l'homodimérisation de l'hélice. On constate que l'hélice TM se déstabilise au point de transition proche du site de clivage-ε et les données de RMN solide indiquent que ces conformations hélicoïdales coexistent avec des conformations non hélicoïdales dans le domaine de l'APP_TM. Suggérant

que la variabilité conformationnelle du segment TM pourrait jouer un rôle dans le traitement de l'APP et donc dans la production d'Aβ.

La caractéristique pathologique de l'AD est attribuée à l'accumulation constante de fibrilles d'Aβ dans des plaques et à la formation de sites contenant une hyperphosphorylation de la protéine Tau, entraînant une perte neuronale. L'hypothèse de la cascade amyloïde (Hardy et Higgins, 1992) explique les effets toxiques des plaques amyloïdes sur les connexions synaptiques et les neurones. Cependant, les expériences menées pour établir une relation de cause à effet directe entre les dépôts d'Aβ et la neurodégénérescence à l'origine de l'AD n'ont pas été concluantes. Selon les récentes théories, de petits assemblages oligomériques solubles ou protofibrillaires d'Aβ sembleraient toxiques pour les neurones et leurs interconnexions vitales, ce qui expliquerait cette relation de cause à effet. Bien que les peptides Aβ puissent avoir différentes longueurs d'acides aminés comprises entre 38 et 43, les alloformes que l'on retrouve le plus dans le cerveau sont l'Aβ (1-40) et l'Aβ (1-42). On a retrouvé ces deux peptides dans des plaques amyloïdes et on a constaté qu'ils formaient des oligomères et des protofibrilles. Des analyses post-mortem prati-quées sur des sujets humains ont démontré que l'Aβ (1-40) plutôt que l'Aβ (1-42), que ce soit sous forme soluble ou insoluble, tendait à s'accumuler davantage chez les patients atteints de l'AD. En plus des cas sporadiques d'AD, on a découvert et étudié plusieurs mutations de la maladie d'Alzheimer familiale (FAD). La mutation Arctique dans la séquence Aβ (Aβ(1-40)E22G) crée des protofibrilles bien plus rapidement et en plus grande quantité que le type sauvage Aβ et induit une neurotoxicité rapidement. Les caractéristiques cliniques et anatomopathologiques de la FAD sont similaires aux cas sporadiques, sauf que la maladie se déclare bien plus tôt.

La recherche n'a, pour l'instant, pas permis d'établir le mécanisme primaire unique à l'origine de l'agrégation d'Aβ responsable de la dégénérescence neuronale et du décès des patients atteints de l'AD. Il semblerait, au contraire, que l'agrégation d'Aβ et le développement de la maladie découlent de nombreux processus. Tandis que la source d'ions Ca^{2+} est soit extracellulaire soit intracellulaire, l'activation neuronale est plus généralement associée à une augmentation de la concentration de Ca^{2+} intracellulaire ($[Ca^{2+}]_i$). Parmi les nombreuses hypothèses mises en avant pour expliquer l'étiologie de l'AD, on s'accorde à dire que le dérèglement de l'homéostase du Ca^{2+} joue un rôle très important dans le développement de la maladie. L'idée qu'une homéostase du Ca^{2+} altérée puisse servir de facteur déclenchant du développement de l'AD a été formulée pour la première fois en 1982 pour être plus tard revue par Khachaturian. Les nombreuses études sur l'AD ont déterminé une déficience du Ca^{2+} prouvant la relation entre le signal du Ca^{2+} et la voie amyloïdogénique.

Dans nos travaux, nous émettons l'hypothèse que lorsqu'un dérèglement du Ca^{2+} survient lors d'un vieillissement normal, il peut faciliter la formation d'oligomères Aβ pathogènes, qui à leur tour peuvent intensifier la dyshoméostasie du Ca^{2+}. Les espèces oligomériques pourraient dont être tenues pour responsable de la médiation de la blessure neuronale et de l'inhibition de LTP de l'AD chez les sujets d'âge avancé, similaire à la situation chez les patients FAD porteurs de la mutation Arctique.

Malgré les progrès incroyables faits dans la compréhension de l'AD, nous ne sommes toujours pas parvenus à développer de nouveaux médicaments suffisamment efficaces pour guérir, ou mieux encore, prévenir la maladie. Les études épidémiologiques ont démontré une association étroite entre la diminution du risque d'AD et l'usage prolongé de médicaments anti-inflammatoires non stéroïdiens (AINS). On a découvert que certains d'entre eux modulaient le clivage de la γ-sécrétase. Dont la molécule carprofène–un inhibiteur du COX-2–on l'a isolée des autres agents pharmacologiques disponibles dans le commerce et constaté que sa N-substitution créait des modulateurs puissants de γ-sécrétase. Le carprofène sulfonyle et le carprofène benzyle ont eut un effet minime voire nul sur le clivage de la γ-sécrétase du site-ε (Narlawar et al., 2006 ; Narlawar et al., 2007) mais ont une spécificité élevée dans la modulation de l'activité de la γ-sécrétase (Schmidt et al., 2006 ; Narlawar et al., 2006).

OBJECTIFS

L'objectif principal de cette thèse était de comprendre certains des processus clés à l'origine, du développement et du traitement de l'AD en suivant une approche multidisciplinaire.

Pour comprendre le mode d'action des protéines membranaires au niveau moléculaire, il est essentiel d'avoir des connaissances précises sur les propriétés structurelles de celles-ci, ainsi que sur la structure de base et les angles d'inclinaison des segments transmembranaires. Dans nos efforts de compréhension du rôle des variations structurelles de la séquence TM dans le traitement de l'APP, nous tentons de déterminer les détails structurels, les angles d'inclinaison d'hélice du peptide APP_TM dans son environnement naturel, la double couche lipidique de la membrane. La RMN solide s'est avérée être un outil biophysique très utile au sondage de la structure et des dynamiques parmi de nombreuses biomolécules inaccessibles par cristallographie ou par la RMN en phase liquide comme les protéines membranaires et les agrégats protéiniques liés à la maladie.

Dans le but de découvrir les mécanismes moléculaires responsables des risques de l'AD liés à l'âge, nous avons comparé l'agrégat d'Aβ (1-40) et d'Aβ (1-40)E22G dans le but d'étudier les similarités structurelles et morphologiques des espèces–oligomériques ou fibrillaires–

formées par les peptides avec ou sans Ca^{2+} ajouté. L'électrophorèse sur gel et le transfert de protéines, la fluorescence de la thioflavine T (ThT), la spectroscopie infrarouge à transformée de Fourier (FTIR) et la microscopie atomique (AFM) ont été utilisés.

Nous avons utilisé la RMN solide pour découvrir le mode d'action des deux puissants modulateurs de γ-sécrétase, le carprofène benzyle et le carprofène sulfonyle, dans les doubles couches lipidiques. La détermination de leur position et orientation dans les membranes lipidiques nous donnera un bon aperçu du mécanisme moléculaire du clivage protéolytique de la γ-sécrétase et donc de la production d'Aβ.

RÉSULTATS ET CONCLUSIONS

Le dérèglement de l'homéostase du Ca^{2+} dans le cerveau de sujets d'âge avancé et dans les maladies neurodégénératives joue un rôle essentiel dans de nombreux processus et contribue à la déficience des cellules et au décès. Nous avons émis l'hypothèse que le Ca^{2+} pourrait déclencher ou accélérer l'agrégation d'Aβ. Par conséquent, nous avons comparé les modèles d'agrégation de l'Aβ(1-40) et de l'Aβ(1-40)E22G avec ou sans Ca^{2+}.

Des échantillons d'Aβ(1-40) et d'Aβ(1-40)E22G ont été préparés et ont incubé pendant 96 heures avec ou sans 2 mM de Ca^{2+}. Après 0, 2, 4, 6, 24, 72, et 96 h, les échantillons ont été analysés par électrophorèse sur gel de polyacrylamide sans SDS (0,1% de SDS était présent dans le tampon de migration) et imagés par transfert de protéines. Le modèle d'agrégation de l'Aβ (1-40) a présenté des différences frappantes avec ou sans Ca^{2+} ajouté. À 72 h et à 96 h, l'Aβ (1-40) est constituée des monomères et des oligomères contenant du Ca^{2+} dont les masses moléculaires sont comprises entre celles des dimères (environ 8 kDa) et des hexamères et de celles des oligomères ayant une masse moléculaire plus élevée. Sans Ca^{2+}, principalement les oligomères, protofibrilles et fibrilles ayant une masse moléculaire élevée ont pu être détectés en raison de l'étendue de l'agrégation de l'Aβ(1-40). Contrairement à ceux d'Aβ(1-40), les échantillons d'Aβ(1-40)E22G n'ont présenté aucune différence dans leurs profils d'agrégation avec ou sans Ca^{2+} ajouté. Comparé aux résultats obtenus pour les deux peptides, nous avons clairement constaté qu'en présence de Ca^{2+}, l'Aβ(1-40), tout comme l'Aβ(1-40)E22G, s'agrégeait pour produire des oligomères et des protofibrilles, alors que sans Ca^{2+}, seul l'Aβ(1-40) formait des fibrilles.

La fluorescence de la ThT a été utilisée pour distinguer les oligomères et les fibrilles des peptides Aβ. Une étude a été menée, qui consistait en une incubation de 96 heures, avec ou sans Ca^{2+} ajouté pour les deux peptides. Après une incubation de 72 et de 96 heures de l'Aβ(1-40) sans Ca^{2+}, l'intensité de la fluorescence de la ThT a grandement augmenté, ce qui indique la formation de fibrilles. Après une incubation

de 96 heures de l'Aβ(1-40) avec du Ca^{2+}, l'intensité de la fluorescence de la ThT est relativement basse, ce qui indique la présence d'oligomères et l'absence de fibrilles. Avec de l'Aβ(1-40)E22G, avec ou sans Ca^{2+}, on a constaté une intensité de la fluorescence de la ThT stable voire même relativement basse pendant les 96 heures, ce qui signifie que le processus d'agrégation de l'Aβ(1-40) est bien plus lent que celui de l'Aβ(1-40)E22G, ou que ce dernier a une tendance relativement élevée à former des oligomères plutôt que des fibrilles.

Les structures secondaires des agrégats d'Aβ sont réputées comme possédant une haute teneur en feuillet bêta. Nous avons récemment découvert, au moyen de l'ATR-FTIR, qu'une signature caractéristique d'oligomères solubles d'Aβ indiquait une conformation de feuillet bêta antiparallèle, tandis qu'une présence de fibrilles d'Aβ indiquait une conformation de feuillet bêta parallèle. Dans le but d'évaluer la présence d'oligomères ou de fibrilles, nous avons étudié les modèles d'agrégation de l'Aβ(1-40) et de l'Aβ(1-40)E22G sur un temps d'incubation donné et avons suivi l'évolution des pics à 1630 cm^{-1} et 1695 cm^{-1}.

Au cours des premières 48 heures, nous avons observé deux caractéristiques particulières, et ce, pour toutes les conditions évaluées: deux pics, un à ~1695 cm^{-1} et un autre à ~1630 cm^{-1}. Les pics à ~1695 cm^{-1} et à ~1630 cm^{-1} dans le spectre infrarouge sont caractéristiques de la conformation du feuillet bêta antiparallèle, indiquant des espèces structurellement différentes des fibrilles. On a observé une réduction importante à ~1695 cm^{-1} puis un passage à des nombres d'ondes inférieurs et pour finir à une seconde diminution à ~1630 cm^{-1} au bout de 48 heures d'incubation d'Aβ(1-40) sans Ca^{2+} ajouté. Ceci illustre le processus de fibrillation dynamique du peptide Aβ(1-40) *in vitro*, ayant commencé avec des monomères et des dimères qui se sont transformés en fibrilles au fil du temps. On a remarqué, pour l'Aβ(1-40) avec du Ca^{2+}, les deux pics caractéristiques à ~1695 cm^{-1} et à ~1630 cm^{-1} à tous les points d'observation. Malgré la légère diminution d'intensité observée à ~1695 cm^{-1}, aucune réduction importante n'a été observée à ~1630 cm^{-1}. Il est également intéressant de noter que ce comportement spectral de l'Aβ(1-40) en présence de Ca^{2+} a les mêmes particularités que celui de l'Aβ(1-40)E22G avec ou sans Ca^{2+}. Dans les deux conditions et pendant 96 heures, les pics de l'Aβ(1-40)E22G à ~1695 cm^{-1} et à ~1630 cm^{-1} sont caractéristiques d'une conformation du feuillet bêta antiparallèle. Cette découverte confirme les résultats découlant de l'analyse PAGE et des expériences ThT, indiquant toutes–comme prévu, et conformément aux données publiées–la formation de nombreux oligomères et éventuellement de protofibrilles par l'Aβ(1-40)E22G.

L'imagerie AFM a révélé des similarités morphologiques entre les oligomères de l'Aβ(1-40) avec Ca^{2+} et de l'Aβ(1-40)E22G, qui étaient tous sphériques ou curvilignes. Nous ne savons toujours pas si la simi-

larité morphologique des oligomères de l'Aβ(1-40) formés en présence de Ca^{2+} aux oligomères de l'Aβ(1-40)E22G formés en l'absence de Ca^{2+} ajouté indique des effets toxiques similaires.

La similarité entre les modèles d'agrégation de l'Aβ(1-40) avec du Ca^{2+} et de l'Aβ(1-40)E22G avec ou sans Ca^{2+}, observée ici au moyen de trois techniques différentes, soulève une question fondamentale sur un changement éventuel dans le mécanisme de l'agrégation de l'Aβ(1-40) en présence de Ca^{2+}. Les ions Ca^{2+} semblent stimuler la formation préférentielle d'oligomères et de protofibrilles par l'Aβ, s'écartant ainsi de la voie de la fibrillogénèse préférable.

Les propriétés conformationnelles du segment TM de l'APP pourrait affecter son traitement protéolytique par la γ-sécrétase. Ces propriétés n'ont pas été définitivement établies. Afin de mieux comprendre le clivage protéolytique de l'APP à l'origine de la création de peptides Aβ, nous avons étudié les particularités structurelles de la séquence de l'APP TM qui pourrait s'avérer essentielles à son traitement par la γ-sécrétase. Nous avons réussi à synthétiser et à reconstituer chimiquement le domaine transmembranaire de l'APP en doubles couches POPC sous forme de dimère présentant en grande partie une conformation alpha hélicoïdale. Une étude détaillée de la RMN solide des peptides APP_TM4K marqués avec les isotopes ^{15}N et ^{2}H à divers points de la séquence TM, indique une importante hétérogénéité conformationnelle et orientationnelle aux positions Ala-630, Ala-642 et Val-646.

La valeur chimique ^{15}N du Gly-637 était de 191 ppm indiquant une orientation transmembranaire pour un peptide hélicoïdal. Il a été déjà publiéque le Gly-637 participait à la formation d'un dimère stable. Le Gly-637, faisant partie du dernier motif GxxxG, est le dernier acide aminé ancrant l'orientation transmembranaire et stabilisant le dimère. Cette stabilité pourrait s'avérer nécessaire à l'effilochage de la structure hélicoïdale aux points de clivage. La théorie du contrôle du traitement de l'APP par la force de la dimérisation a été avancée.

Le même peptide était également marqué avec du ^{2}H à la position Ala-642, et n'a pas présenté de division du quadrupole claire, mais plutôt de nombreuses divisions d'une largeur de ~ 27 kHz. L'explication la plus plausible quant à la forme du spectre de décalage chimique ^{15}N de l'Ala-642 est que ce site possède de nombreuses orientations différentes, mais pas toutes celles d'un échantillon de poudre. Une réorientation lente (plus lente que la gamme en kHz) de ce site est probablement responsable de l'apparition relativement importante du "pic principal " dans le spectre. Cela signifie que la structure pourrait ne pas être hélicoïdale à cet emplacement. Afin de bien comprendre les diverses orientations observées, on a simulé le spectre du décalage chimique ^{15}N. Le résultat indique que pour le spectre expérimental du ^{15}N Ala-642 une gamme restreinte d'orientations " autorisées " (ex. restreintes par les angles de liaison C_α–C_β) existe, dans laquelle

la plupart des liaisons NH sont orientées perpendiculairement à la membrane normale et une plus petite quantité de liaisons NH sont parallèles à la membrane normale. La liaison NH de l'Ala-642 adopte clairement de nombreuses orientations différentes. Cette découverte conforte l'idée qui veut que l'Ala-642 du site de clivage-γ se trouve dans une conformation non hélicoïdale.

Le troisième site marqué ^{15}N Val-646 était localisé à 209 $\pm$ 28 ppm présentant un large spectre de 26 kHz, indiquant une hélice transmembranaire possédant un nombre d'orientations correspondant au sens du champ magnétique. Nous avons découvert que pour une gamme complète d'angles d'attaque rotationnels (0° - 360°) éventuels, les angles d'inclinaison sont compris entre 0° à 50°.

Le Val-646 et l'Ala-642 se situent dans les sites de clivage ζ- et γ-, respectivement. Le première présente une orientation transmembranaire, tandis que le second présente une hétérogénéité conformationnelle ample et semble n'avoir aucune orientation définie. L'existence d'une conformation non hélicoïdale sur le site Ala-642 est proposée par Lu et al., 2011. Cependant, c'est la première fois qu'on observe une distribution orientationnelle avec une approche structurelle. Une preuve de la variabilité conformationnelle autour des sites de clivage γ- et ζ- peut avoir des implications importantes pour le mécanisme de clivage et donc pour la production d'Aβ.

Le peptide portant le marqueur ^{15}N Val-646 a également été marqué sur le site ^{2}H Ala-630. La largeur du spectre quadrupole ^{2}H sur le site Ala-630 était de 26 kHz indiquant une distribution hétérogène des alignements, qui ne sont pas un modèle de poudre (dans lequel toutes les orientations sont possibles). L'Ala-630 se trouve près de la limite de la membrane N-terminale et pourrait subir moins de contraintes près des interactions de van der Waals avec des molécules lipidiques et donc il est raisonnable de penser que cet acide aminé soit plus mobile. Cependant, des publications récentes prouvent qu'il implique l'existence de mouvements sur le site Ala-630 qui pourraient être associés à l'échange entre les conformations hélicoïdales et non hélicoïdales. Il est intéressant de noter que les spectres au deutérium des deux alanines, Ala-630 et Ala-642, ont une forme relativement semblable. Les deux sont relativement les larges ~26 kHz et ~27 kHz et ces deux valeurs maximales de clivage ont des orientations de la liaison C_α–C_β de 42° et 71°, pour les valeurs positives et négatives, respectivement. En gardant à l'esprit qu'il n'y a aucune structure du peptide APP_TM à aligner, le large spectre du décalage chimique du ^{15}N pour l'interaction quadrupole du Val-646 et du ^{2}H pour l'Ala-630 n'a pas été en mesure de donner des contraintes orientationnelles claires pour cette paire de marqueurs. Les spectres sont, par conséquent, en grande partie déterminés par la distribution orientationnelle des molécules par rapport à la direction du champ magnétique. Cette grande hétérogénéité conformationnelle démontrée est plus probable-

ment causée par la coexistence des conformations hélicoïdales et non hélicoïdales du peptide sur ces sites. En fonction des résultats de ces travaux, nous avons proposé un modèle des orientations et conformations possibles du peptide APP_TM4K dans les doubles couches POPC (voir le texte complet).

On a découvert que le carprofène benzyle et le carprofène sulfonyle étaient des modulateurs efficaces de la γ-sécrétase. Ils affectent le clivage sur les sites $\gamma 38$, $\gamma 40$, et $\gamma 42$ et bloquent, en particulier, la formation d'A$\beta 42$ pour améliorer la formation d'A$\beta 38$, présentant ainsi un profil similaire aux AINS efficaces. On en a trouvé sur la plupart des inhibiteurs puissants de l'A$\beta 42$ (Narlawar et al., 2006). Les connaissances sur l'interaction de ces molécules avec la double couche lipidique sont essentielles à la compréhension de leur mode d'action. Nous avons déterminé, dans ces travaux, l'orientation des dérivés du carprofène dans les doubles couches lipidiques au moyen de la RMN en phase solide.

Des fragments spécifiques de molécules de carprofène sulfonyle et de carprofène benzyle ont été marqués avec l'isotope ^{2}H. Les molécules ont été incorporées dans des doubles couches lipidiques composées d'un mélange lipidique tertiaire (POPC, cholestérol et sphyngomyéline) et on a préparé des échantillons pour les mesures à la RMN solide. L'analyse des données de la RMN solide a entraîné des contraintes orientationnelles pour les molécules de carprofène sulfonyle et de carprofène benzyle. Nous avons observé une liaison C–S du carprofène sulfonyle orientée à $\pm$ 27,4° par rapport à la direction du champ magnétique, ce qui correspondait aux deux orientations possibles (voir le texte complet). Quant au benzyle carprofène, l'orientation correspondant aux résultats expérimentaux est celle où l'angle d'attaque rotationnel (rotation autour de l'axe z) est de ~31° et où l'angle d'inclinaison rotationnel (rotation autour de l'axe y) est de ~137°. Les expériences de diffraction des neutrons (effectuées par nos collaborateurs) ont montrées que les molécules allaient se placer à l'interface de la membrane lipidique.

Le site d'interaction particulier de ces composants doit encore être identifié. Nous supposons qu'il pourrait interagir avec le PS1, l'unité catalytique de la γ-sécrétase ou directement avec l'APP. Les résultats de ces travaux soutiennent l'hypothèse d'une interaction directe avec l'APP. Sachant que le site catalytique du PS1 se situe dans la double couche lipidique et que les dérivés du carprofène se situent près des groupements chargés des lipides, il est difficile d'imaginer comment ils atteindraient le site actif. De plus, une interaction directe des dérivés du carprofène avec le PS1 semble arrêter, plutôt que modifier, l'activité de sa γ-sécrétase. Il semble plus probable que les dérivés du carprofène interfèrent avec la formation des dimères de l'APP, nécessaires au clivage séquentiel par la γ-sécrétase. Lorsque la stabilité d'un dimère TM est gravement affectée, le modèle de Munter et al., 2007 dit que

le clivage séquentiel se décale du clivage pour passer aux positions Aβ38/Aβ37 et Aβ35/Aβ34, diminuant ou réduisant fortement la production d'Aβ42.

Plus de 100 ans après sa découverte, l'AD est toujours un mystère. Malgré les nombreux efforts faits pour comprendre le processus d'agrégation de l'Aβ dans les plaques fibrillaires, qui était encore récemment considéré comme la cause de la maladie. Cependant, de nouvelles idées ont vu le jour, et les plaques amyloïdes ne sont peut être pas aussi néfastes qu'on le pensait. Il semblerait, au contraire, que les oligomères soient les espèces toxiques responsables de la plupart des dommages neuronaux. Toutefois, les questions sur le mécanisme de production de l'Aβ, la formation des oligomères Aβ et les traitements éventuels restent sans réponse. Nous pensons que les résultats de ces travaux permettront de mieux comprendre les processus de l'AD et nous éclaireront sur le mode d'action des médicaments potentiels.

...

ABSTRACT

Alzheimer's disease (AD) is a progressive neurodegenerative disorder and the most common form of dementia. There is no cure and the disease is fatal. One of the characteristic histopathological markers of AD is the presence of proteinaceous deposits, amyloid plaques, in the brain. These plaques are formed by the amyloid β-peptides (Aβ) 40- and 42-residue-long, which are protease cleavage products of the amyloid precursor protein (APP). Elucidation of some of the key processes in the cause and the development of AD is crucial for the development of new and efficient treatments.

Conformational properties of the transmembrane (TM) segment of APP may affect its proteolytic processing by γ-secretase. These properties have not been definitely established. In addressing the role of structural variations of the TM sequence in APP processing, structural details of the chemically synthesized APP_TM4K peptides within the membrane bilayers were studied using Attenuated total reflection Fourier transform spectroscopy (ATR-FTIR) and solid-state nuclear magnetic resonance (ssNMR) techniques. While the overall secondary structure of the APP_TM4K peptide is an α-helix, conformational and orientational heterogeneity was observed for the γ-cleavage site and, to a smaller extent, for the ζ-cleavage site. Evidence for the conformational variability around γ- and ζ-cleavage sites may have important implications for the cleavage mechanism and hence for the Aβ production. It was also found that the last glycine within the sequence of GxxxG motifs is in the transmembrane orientation, implying that dimerization via these motifs may act as an anchor, confining the TM dimer to the stable transmembrane orientation.

Amyloid β-peptide is directly linked to AD. Starting from its monomeric form, Aβ aggregates into fibrils and / or oligomers, the latter being the most neurotoxic. Dysregulation of Ca^{2+} homeostasis in aging brains and in neurodegenerative disorders plays a crucial role in numerous processes and contributes to cell dysfunction and death. Here we postulated that calcium may enable or accelerate the aggregation of Aβ. The aggregation pattern of Aβ(1-40) and of Aβ(1-40)E22G, an amyloid peptide carrying the Arctic mutation that causes early onset of the disease, were compared. We found that in the presence of Ca^{2+}, Aβ(1-40) preferentially formed oligomers similar to those formed by Aβ(1-40)E22G with or without added Ca^{2+}, whereas in the absence of added Ca^{2+} the Aβ(1-40) aggregated to form fibrils. Morphological similarities of the oligomers were confirmed by contact mode atomic force microscopy (AFM) imaging. The distribution of oligomeric and fibrillar species in different samples was detected

by gel electrophoresis and Western blot analysis, the results which were further supported by thioflavin T fluorescence experiments. In the samples without Ca^{2+}, Fourier transform infrared spectroscopy revealed conversion of oligomers from an anti-parallel β-sheet to the parallel β-sheet conformation characteristic of fibrils. Overall, these results led us to conclude that calcium ions stimulate the formation of oligomers of Aβ(1-40), that have been implicated in the pathogenesis of AD.

Despite the tremendous progress in understanding AD, there remains the challenge of the development of new and efficient drugs. In order to shed light onto the mechanism of action of two new potent γ-secretase modulators – benzyl-carprofen and sulfonyl-carprofen within lipid bilayers, ssNMR technique was employed. Using neutron scattering experiments it was previously found that sulfonyl-carprofen and benzyl-carprofen partition into the headgroup region of the lipid bilayer. The orientational constraints derived from the ssNMR experiments refined their position into precise orientation. Combined, these results indicate that carprofen-derivatives can directly interact with the region of APP that mediates dimerization. Such interaction, would interfere with proper APP-dimer formation, which is necessary for the sequential cleavage by γ-secretase, diminishing or greatly reducing Aβ42 production.

Results obtained during this work shed new light onto some of the key processes in AD: Aβ production from APP, formation of Aβ oligomers and insights into the mechanism of action of potential therapeutics. We believe that these results will promote a better understanding of the disease and will help in future drug design.

...

PUBLICATIONS

Some ideas and figures have appeared previously in the following publications:

"Calcium ions promote formation of Amyloid β-peptide (1-40) oligomers causally implicated in neuronal toxicity of Alzheimer's disease." Anna Itkin, Vincent Dupres, Yves F. Dufrêne, Burkhard Bechinger, Jean-Marie Ruysschaert, Vincent Raussens. PLoS ONE 6(3): e18250. cf. Appendix.

POSTERS

"Effects of Ca^{2+} Ions on Aggregation of Synthetic Amyloid β-peptides Associated with Alzheimer's disease" (Anna Itkin), 22nd Symposium of the Protein Society "Machines of Life" in San-Diego, California, US, 2008

"Effects of Ca^{2+} Ions on Aggregation and Conformational Changes of Synthetic Amyloid β-peptides Associated with Alzheimer's disease" (Anna Itkin, Burkhard Bechinger, Jean-Marie Ruysschaert, Vincent Raussens), 52nd Annual Meeting of the Biophysical Society & 16th International Biophysics Congress, Long Beach, California, US, 2008

A casual stroll through the lunatic asylum shows that faith does not prove anything.

Friedrich Nietzsche

Dedicated to my beloved grandmother Frida, without whom I would not have the opportunity to begin my academic pursuits many years ago. I owe this doctoral degree to her.

All things are subject to interpretation. Whichever interpretation prevails at a given time is a function of power and not truth. —

Friedrich Nietzsche

ACKNOWLEDGMENTS

I would like to express my gratitude to my supervisors Prof. Jean-Marie Ruysschaert, Prof. Vincent Raussens, and Prof. Burkhard Bechinger for their guidance and support and for enabling me to develop an understanding of this fascinating topic and of the complex biophysical tools. I am truly thankful to Jean-Marie and Vincent for their continuous interest in my work, much needed support and encouragement, even when I was already at another University.

I would like to thank our collaborators without whom this work would not be complete: Dr. Vincent Dupres from the Université catholique de Louvain who performed Atomic Force Microscopy (AFM) experiments and Dr. Thomas Haußfrom the Helmholtz-Zentrum in Berlin who provided the carprofen derivatives.

This thesis would not have been possible had a number of great scientists not have agreed to share their knowledge and their vast experience to help me in my journey through the complex subject matter of the ssNMR field. I would like to express my gratitude to Dr. Christopher Aisenbrey for his tremendous help with the solid-phase peptide synthesis, the ssNMR experiments, his advice and many interesting and stimulating discussions. I am very sad that he will not be able to attend my thesis defense due to his health condition, but he will be in my thoughts. I owe my deepest gratitude to Dr. Evgeniy Salnikov, who selflessly helped me with the ssNMR experiments and data analysis along with many critical discussions and review of this manuscript. It is my pleasure to thank Dr. Jésus Raya for being a true and very gifted teacher who showed me with pens and pencils how magnetization is affected by radiofrequency pulses, what this has to do with a spectrometer and which experiments are used for which nuclei. I also received lessons in fixing probe heads, which is an inseparable part (as I learned) in engaging in ssNMR experiments. I would also like to thank Dr. Philippe Bertani and Dr. Jérôme Hirshinger for their help as ssNMR specialists who contributed to my knowledge and understanding in this field.

I am indebted to many of my colleagues for supporting me, providing valuable insights and offerring their help in the laboratory. My special and warm thanks to Elise Glattard (who is also a Dr., but since she is my friend it is a bit strange to refer to her in this way) for being there to help and advise and support me at all times. To Barbara, who

began this long journey with me and defended her thesis some months ago. Barbara's spirit never failed, hiking and laughing together was our way to combat the difficulty of being PhD students. And at the end, her help with the word-processing software LyX was a life-saver. I will miss you!

I would like to thank my colleagues from Université Libre de Bruxelles, especially Rabia Sarroukh for introducing me to FTIR experiments.

It is my fortune to thank Danny, my amazing husband, life partner and my friend for his love and support, his patience and his humor, his courage to engage with me in this overseas affair and to stand by me at all times. I want to mention our daughter, who challenged me from the moment she was born and I owe it to her, more than to anybody else, to finish my dissertation and finally fulfill my long-standing promise to her – to spend more time together. Her unconditional love is my Northern star.

I would like to express my love and eternal gratitude to my grandmother. For her hard work and many sacrifices, which made it possible to start on this long academic journey in the first place. Few possess strength and humbleness like hers these days. And, of course, I am thankful to my parents for their love, support, advice, for listening to my complaints and for being themselves (I can always count on this). Many thanks to my wonderful parents-in-law for their belief in me, in us, and their support of all our adventures.

My special acknowledgments go to all my wonderful friends, who are with me for many years. You all were there to stand beside me and I deeply love you for that.

Accomplishment of this PhD thesis was made possible with the financial support from the European Community's Sixth Framework Program through a Marie Curie Research Training Network (—Biocontrol MRTN-CT-2006-033439). I would also like to thank "la Fondation David et Alice Van Buuren" for the prize they awarded me.

CONTENTS

NOMENCLATURE

$[Ca^{2+}]_i$ intracellular Ca2+ concentration

$\alpha - CTF$ alpha C-terminal fragments

$\beta - CTF$ beta C-terminal fragment

$A\beta$ amyloid beta-peptide

ACN Acetonitril

AD Alzheimer's disease

ADHH adiabatic passage through Hartman-Hahn condition

AFM Atomic force microscopy

AICD APP intracellular domain

$Aph-1$ anterior pharynx-defective 1

APP Amyloid precursor protein

APS Ammonium persulfate

BSA Bovine serum albumin

CaBPs calcium-binding proteins

cmc critical micelle concentration

CODEX Center-band Only Detection of Exchange

COX cyclooxygenase

CP Cross polarization

DCM dichloromethane

DMF dimethylformamide

EDT Ethanedithiol

EDTA Ethylenediaminetetraacetic acid

ER Endoplasmic reticulum

FAD Familial Alzheimer's disease

FID free induction decay

Fmoc Fluorenylmethyloxycarbonyl

FTIR Fourier transform infrared

GdnCl guanidine hydrochloride

HBTU Benzotriazole tetramethyl uronium hexafluoro phosphate

HH Hartman-Hahn

HPLC high performance liquid chromatography

IP3 Inositol trisphosphate

JM juxtamembrane

LMPG lyso-myristoylphosphatidylglycerol

LTP Long-term potentiation

MALDI matrix assisted laser desorption or ionization

MALDI matrix assisted laser desorption or ionization

MD molecular dynamics

MOPS 3-(N-morpholino)propanesulfonic acid

nAChR nicotinic acetylcholine receptor

Nct Nicastrin

NMDA N-methyl-D-aspartate

NMR nuclear magnetic resonance

NSAID nonsteroidal anti-inflammaroy drug

PAGE Polyacrylamide gel electrophoresis

Pen − 2 presenilin enhancer gene 2

POPC 1-palmitoyl-2-oleoyl-sn-glycero-3-phosphocholine

PS1 Presenilin 1

PS2 Presenilin 2

REDOR Rotational Echo DOble Resonance

RF radio frequency

Ry Ryanodine

SAP serum amyloid P

SDS Sodium dodecyl sulfate

SPPS solid phase peptide synthesis

ssNMR solid-state nuclear magnetic resonance

TEMED N, N, N′, N′-tetramethylethylenediamine

TFA Trifluoroacetic acid

ThT Thioflavine T

TIS Triisopropylsilan

TM transmembrane (domain)

TOF time of flight

Part I

INTRODUCTION AND METHODS

1 INTRODUCTION

1.1 AMYLOID PRECURSOR PROTEIN

Alzheimer's disease (AD) is a progressive neurodegenerative disorder that affects nearly 2% of the population in industrialized countries. AD is the most common form of dementia and is characterized by brain cell destruction, memory loss, and deterioration of cognitive and behavioral processes severe enough to affect work, lifelong hobbies, and social life. Symptoms worsen over time and the disease is fatal. One of the characteristic histopathological markers of AD is the presence of proteinaceous deposits, amyloid plaques, in the brain. These plaques are formed by amyloid β-peptides (Aβ) 40- and 42-residue-long, which are protease cleavage products of the amyloid precursor protein (APP).

APP is an integral membrane protein with a single transmembrane (TM) domain expressed in many tissues and concentrated in the synapses of neurons [Lambert et al., 1998]. Its primary function is not known, though it seems not to be required for the expression of a critical cell function but, may be involved in the modulation of neuronal functions at the cellular level. It has been shown that in brain a distinct percentage of APP is present on the cell surface as a membrane protein of type I (i.e. it has a single-pass transmembrane domain, with the portion of the polypeptide on the NH_2-terminal side of the TM domain exposed on the exterior side of the membrane and the COOH-terminal portion exposed on the cytoplasmic side). Involvement of APP in neuronal development, synaptogenesis, and synaptic plasticity indicated that some aspects of these processes are mediated by cell-associated APP [Nishimoto, 1998, Perez et al., 1997, Weidemann et al., 1989]. APP is best known and most commonly studied as the precursor molecule whose proteolysis generates Aβ peptides, a 38- to 42-amino acid-long peptides whose amyloid fibrillar form is the primary component of amyloid plaques found in the brains of AD patients (described in more details in the next section).

APP undergoes sequential cleavage (Figure 1 on page 4). First, the bulk ectodomain is removed by membrane-bound α- or β-secretases, leading to secreted forms of APP, sAPPα or sAPPβ respectively, and a membrane-bound α-C-terminal fragment (α-CTF) or β-C-terminal fragment (β-CTF), respectively [Annaert and De Strooper, 2002, Vassar et al., 1999]. Regulated transmembrane proteolysis of the β-CTF by γ-secretase occurs after ectodomain shedding and results in Aβ production [De Strooper and Annaert, 2000]. γ-Secretase cleavage also

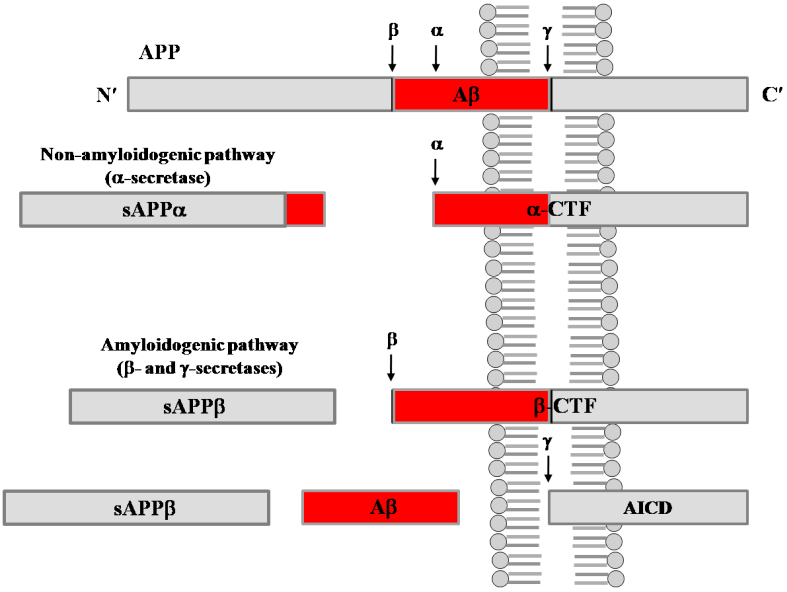

Figure 1: Schematic diagram illustrating proteolytic cleavage of the APP. α-secretase cleaves APP within the Aβ sequence (non-amyloidogenic pathway) to liberate two peptides, including the neuroprotective sAPPα. β- and γ-secretases act sequentially to cleave APP within the N- and C-terminal parts of the Aβ sequence, respectively producing Aβ peptide (amyloidogenic pathway) and AICD.

releases the APP intracellular domain (AICD), which could have a role in transcriptional regulation (Figure 1 on page 4). γ-Secretase is a multiprotein complex composed of presenilin 1 (PS1) or presenilin 2 (PS2); nicastrin (Nct), a type I transmembrane glycoprotein; anterior pharynx-defective 1 (Aph-1) and presenilin enhancer gene-2 (Pen-2), two multipass transmembrane proteins [Bergmans and De Strooper, 2010]. This complex is essential for the sequential intramembraneous proteolysis of a variety of transmembrane proteins. The functions of the various γ-secretase proteins and their interactions in the complex are not yet fully defined, but it has been suggested that the ectodomain of nicastrin recognizes and binds to the amino-terminal stubs of previously cleaved transmembrane proteins. Aph-1 aids the formation of a precomplex, which interacts with PS1 or PS2 while Pen-2 enters the complex [Edbauer et al., 2003, Go et al., 2004] to initiate the cleavage of PS1 or PS2 to form an N-terminal 28-kDa fragment and a C-terminal 18-kDa fragment, both of which are critical to the γ-secretase complex [Takasugi et al., 2003].

Recently, an explanation for the multiple cleavages by γ-secretase was provided, indicating a sequential proteolytic cleavage mechanism to release Aβ [Qi-Takahara et al., 2005, Zhao et al., 2004]. Accordingly, the first cut occurs at the cytoplasmic edge of the TM at the ε-site, that is, residue 49 or 48 of β-CTF (Figure 2 on page 5) [Sastre et al., 2001, Weidemann et al., 2002]. The products Aβ49/Aβ48 remain membrane bound and are further processed in a sequential mode into Aβ46/Aβ45,

Figure 2: Partial sequence of the APP where the TM domain is enclosed by dashed lines. The red rectangle marks the region synthesized for this study. Underlined are isotopically-labeled amino acids that were incorporated for solid-state nuclear magnetic resonance (ssNMR) studies. The β-branched amino acids are marked in blue. The positions of the glycines in the 3 consecutive GxxxG are presented in bold and labeled. The cleavage sites of α-, β-, γ-secretase are indicated with scissors.

that is, the ζ-site [Zhao et al., 2004]. Aβ46 is further processed into Aβ43 and finally Aβ40, whereas Aβ45 is the direct precursor of Aβ42 [Zhao et al., 2004, Qi-Takahara et al., 2005]. There is evidence that cellular APP exists as a homodimer, which promotes or attenuates the Aβ production in the β-secretory pathway [Scheuermann et al., 2001]. Therefore, further cleavage that generates Aβ38 and Aβ37 will occur only if not inhibited by strong dimerization between two TM helices of APP [Munter et al., 2007, Miyashita et al., 2009, Munter et al., 2010].

There are evidence that suggest that intramembraneous proteolysis by γ-secretase requires local unraveling of the helical secondary structure of the TM domain to expose backbone carbonyl carbons for nucleophilic attack by polarized water in the enzyme active site [Sato et al., 2009]. Indeed, there are some unusual features of the APP_TM sequence that might destabilize its helical structure in the membrane. First, there is a high density of β-branched amino acids (Valine, Threonine, Isoleucine) surrounding the Aβ40- and Aβ42-cleavage sites (Figure 2 on page 5). Sequential β-branched residues can have a destabilizing effect on the secondary structure of TM helices [Li and Deber, 1992].

Second, several of the glycines in the APP_TM domain occur in GxxxG motifs, which in TM sequences were shown to mediate helix dimerization [Russ and Engelman, 2000]. Mutational studies also show the importance of glycines in GxxxG motifs for APP processing [Munter et al., 2007, Kienlen-Campard et al., 2008]. Molecular dynamics and solid-state NMR (ssNMR) experiments point out that Gly_{625}, Gly_{629}, and Gly_{633} (Figure 2 on page 5) within GxxxG motifs mediate TM helix homodimerization, and that the TM helix breaks at the transition point near the ε-cut site [Sato et al., 2009, Miyashita et al., 2009]. There is ssNMR data that indicates that helical conformations coexist with non-helical conformations within the APP_TM domain [Lu et al., 2011]. These suggest that the conformational variability of the TM segment might play a role in APP processing and therefore in Aβ production [Antzutkin et al., 2003, Munter et al., 2007], for example

by facilitating the exposure of peptide bonds for hydrolysis at the γ-cleavage site [Lu et al., 2011] (isotopically-labeled amino acids are underlined in Figure 2 on page 5 and their ssNMR investigation is discussed in chapter 4).

1.2 AMYLOID β-PEPTIDES

The pathological hallmark of AD is attributed to the continuous accumulation of Aβ fibrils into plaques and formation of neurofibrillary tangles containing hyperphosphorylated Tau protein, causing neuronal loss. The toxic effects of amyloid plaques on synaptic connections and neurons were explained by the amyloid cascade hypothesis [Hardy and Higgins, 1992]. However, experiments aimed at establishing a direct causal relationship between Aβ deposition and the neurodegeneration that underlies AD dementia failed [Cummings and Cotman, 1995, Näslund et al., 2000]. This apparent discrepancy between plaque burden and neuronal dysfunction has been described in transgenic mouse models of AD [Irizarry et al., 1997, Chui et al., 1999]. Recent theories that apparently resolve this inconsistency refer to small soluble oligomeric or protofibrillar assemblies of Aβ [Klein et al., 2001, Hardy and Selkoe, 2002], shown to be toxic to neurons and their vital interconnections [Lue et al., 1999, Rowan et al., 2007, Mclean et al., 1999]. Results of studies that focused on the electrophysiological impact of Aβ oligomers suggested that the underlying memory loss is caused by rapid inhibition of long-term potentiation (LTP)—a classical model for synaptic plasticity and memory mechanisms [Bliss and Lomo, 1973]—by Aβ oligomers [Lambert et al., 1998, Walsh et al., 2002, Wang et al., 2002], which might explain, at least in part, the mild cognitive impairment observed in the early stages of AD [Rowan et al., 2007]. Although Aβ peptides may vary in length from 38 to 43 amino acids, as a result of multiple cleavages of the γ-secretase complex (see above section for details), the two main alloforms in the brain are Aβ(1-40) and Aβ(1-42). Both peptides have been found in amyloid plaques [Selkoe, 1991, 2001, Bossy-Wetzel et al., 2004] and shown to form oligomers and protofibrils [Stine et al., 2003]. Post-mortem analysis in human subjects disclosed that Aβ(1-40) rather than Aβ(1-42), whether in soluble or in insoluble form, discriminated more readily between AD patients and high pathology controls [Lue et al., 1999]. In addition to sporadic cases of AD, several familial Alzheimer's disease (FAD) mutations have been discovered and studied over the years. Most of these mutations cause an increase in Aβ by interfering with APP processing. A new mutation within the Aβ sequence, Aβ(E22G), found to cause AD in Swedish families, was reported in 2001 by Nilsberth et al., who named it the Arctic mutation (Figure 3 on page 7). Those authors observed that carriers of this mutation showed decreased amounts of Aβ(1-42) and Aβ(1-40) in the plasma,

Amyloid-β (1-40)

Asp-Ala-Glu-Phe-Arg-His-Asp-Ser-Gly-Tyr-Glu-Val-His-His-Gln-Lys-Leu-Val-Phe-Phe-Ala-**Glu**-Asp-Val-Gly-Ser-Asn-Lys-Gly-Ala-Ile-Ile-Gly-Leu-Met-Val-Gly-Gly-Val-Val

Amyloid-β E22G (1-40)

Asp-Ala-Glu-Phe-Arg-His-Asp-Ser-Gly-Tyr-Glu-Val-His-His-Gln-Lys-Leu-Val-Phe-Phe-Ala-**Gly**-Asp-Val-Gly-Ser-Asn-Lys-Gly-Ala-Ile-Ile-Gly-Leu-Met-Val-Gly-Gly-Val-Val

Figure 3: Amino acid sequence of Aβ(1-40) and of AβE22G(1-40) peptides. The Glutamic acid at position 22 of the Aβ(1-40) sequence is marked in bold, while the mutation to Glycine in AβE22G(1-40) sequence is marked in red.

and demonstrated that Aβ(1-40)E22G forms protofibrils much faster and more abundantly than the wild-type Aβ, whereas the rate of fibrillization remained the same [Nilsberth et al., 2001]. Later studies suggested that the clinical and pathological features of patients with the Arctic mutation are attributable to increased generation of Aβ intermediates formed early in fibrillogenesis, as well as their greater stability [Päiviö et al., 2004]. Moreover, Aβ(1-40)E22G was shown to rapidly induce neurotoxicity, and that this correlated with the formation of small pre-fibrillar assemblies, including protofibrils [Whalen et al., 2005]. Clinical and pathological features of FAD are indistinguishable from those of sporadic cases, but disease onset occurs at a much younger age in patients with the Arctic mutation [Nilsberth et al., 2001, Kamino et al., 1992].

Research has so far failed to establish any unique primary mechanism underlying the Aβ aggregation followed by neuronal degeneration and death in patients with AD. Rather, it seems likely that numerous processes participate both in Aβ aggregation and in the development of the disease. One of the many hypotheses put forward to account for the etiology of AD argues that a central role in AD pathology is played by dysregulation of calcium homeostasis [Mattson, 2004, Smith et al., 2005, Stutzmann, 2005]. The idea that altered calcium homeostasis might serve as a trigger in the development of AD was first formulated in 1982 and later revised by Khachaturian [Khachaturian, 1994]. The principal risk factor for AD is advanced age. In sporadic cases, the first manifestations of the disease symptoms occur towards the seventh decade of life.

Neuronal activation is usually associated with an increase in intracellular Ca^{2+} concentration ($[Ca^{2+}]_i$), while the source of the Ca^{2+} ions can be either extracellular or intracellular. Age-related alterations in Ca^{2+}-specific regulatory systems in neurons include increased amounts of intracellular Ca^{2+}, enhanced Ca^{2+} influx through voltage-dependent

Ca^{2+} channels, impaired mitochondrial ability to buffer or cycle Ca^{2+} [Xiong et al., 2002], and perturbed Ca^{2+} regulation in ryanodine (Ry)-sensitive and Ins(1,4,5)P3-sensitive (IP3) Ca^{2+} stores [Bezprozvanny and Mattson, 2008]. Numerous studies have implicated Ca^{2+} dysfunction in AD, demonstrating the bidirectional relationship between Ca^{2+} signaling and the amyloidogenic pathway [Bojarski et al., 2008, Green and LaFerla, 2008]. On the one hand, certain alterations in Ca^{2+} signaling are common to both sporadic and familial cases of AD [Etcheberrigaray et al., 1998, Ito et al., 1994]. Direct measurements of $[Ca^{2+}]_i$ show that cells exposed to Aβ exhibit disruption in calcium homeostasis [Mattson et al., 1992, Kawahara et al., 2000], which may in turn cause a variety of secondary effects such as activation of cellular enzymes, induction of apoptosis, and cytoskeletal modifications [Mattson et al., 1991, Mattson, 1994]. Aβ can reportedly trigger Ca^{2+} release from endoplasmic reticulum (ER) stores via interaction with IP3 and Ry receptors [Ferreiro et al., 2004, Paula-Lima et al., 2011], as well as an increase in calcium influx via the N-methyl-D-aspartate (NMDA) receptors [Stutzmann, 2007, De Felice et al., 2007]. Formation of cation-selective channels by Aβ in bilayer membranes and in living cells [Arispe et al., 1993a, Kagan et al., 2004] further enhances the ability of this peptide to alter cytosolic Ca^{2+} homeostasis. On the other hand, changes in the amounts and dynamics of Ca^{2+} alter the metabolism and production of Aβ [Green and LaFerla, 2008]. Influx of Ca^{2+} through calcium channels of the plasma membrane or through calcium release from ER stores increases Aβ generation [Querfurth and Selkoe, 1994]. An increase in cytosolic Ca^{2+} concentration, moreover, was shown to induce transient phosphorylation of APP and tau, leading to an increased production of intracellular Aβ [Pierrot et al., 2006]. Based on the above findings, we postulated that when calcium dysregulation takes place under conditions of normal aging, it may facilitate the formation of pathogenic Aβ oligomers, which in turn may intensify the Ca^{2+} dyshomeostasis. The oligomeric species may then be held accountable for mediating the neuronal injury and LTP inhibition characteristic of AD in elderly individuals, similar to the situation in FAD patients carrying the Arctic mutation.

1.3 CARPROFEN DERIVATIVES

Despite the tremendous progress in understanding AD, there remains the challenge of the development of new and efficient drugs to cure or better yet to prevent the disease. Approved drugs such as acetylcholinesterase inhibitors and memantine hydrochloride offer symptomatic treatment, but they address neither the mechanism(s), nor the pathology of the disease. The metabolism of APP, which is cleaved by β-secretase followed by γ-secretase, results in generation of two main alloforms 40 and 42 amino acid-long peptides Aβ40 and Aβ42,

the main components of oligomers and amyloid fibrils. It has been shown that γ-secretase activity can be controlled by inhibition of the active site of PS1, a catalytic subunit of the γ-secretase complex, or by interference with complex assembly or substrate recognition, the latter resulting in allosteric modulation or inhibition. The allosteric mechanisms are particularly attractive targets for drug development as they may control the ratio of the Aβ fragments: Aβ38, Aβ40, and Aβ42, while retaining the cleavage of other substrates [Weggen et al., 2001, Lleó et al., 2004].

Epidemiological studies have indicated a close association between prolonged use of non-steroidal anti-inflammatory drugs (NSAIDs), and reduced risk for AD. Some of them were found to modulate the γ-secretase cleavage, either to produce longer or shorter forms of Aβ, when added to a cell culture system or in mice models. For example, naproxen and aspirin were found to raise Aβ42 and to lower Aβ38 levels [Kukar et al., 2005], whereas ibuprofen had the inverse effect [Weggen et al., 2001] and Aβ40 remained unaffected. They seem to interfere with substrate recognition/cleavage and shift the precision of γ-secretase cleavage from the γ42 to the γ38 site (Figure 2 on page 5) to generate more Aβ38 and less Aβ42 [Lleó et al., 2004, Weggen et al., 2001], but the underlying mechanism is uncertain. Therefore, cyclooxygenase (COX) inhibitors such as flurbiprofen, sulindac sulfoxide and meclofenamic acid were converted into amides and esters and anticipated that the modification of acid functionality would reduce the COX inhibitory activity while increasing the γ-secretase modulatory activity. However, the conversion of the acid moiety of COX inhibitors into their amides or esters resulted either in inverse modulation or inhibition. Further efforts were then focused on carprofen, a COX-2 inhibitor which is approved for the use in dogs, cows and horses for the treatment of arthritis. Carprofen molecule was isolated from commercially available tablets and further N-substitution of carprofen resulted in potent modulators of γ-secretase, and the compounds displayed little or no effect on γ-secretase cleavage at the ε-site [Narlawar et al., 2006, 2007]. The compounds are therefore expected to have little or no impact on γ-secretase-mediated signaling via the AICD or via intracellular domains of other γ-secretase substrates [Narlawar et al., 2006]. Several carprofen derivatives were shown to have high specificity in modulating the γ-secretase activity: sulfonyl-carprofen and benzyl-carprofen (Figure 4 on page 10) [Schmidt et al., 2006, Narlawar et al., 2006].

1.4 GOALS

The main goal of this thesis was to elucidate some of the key processes in the cause, development and treatment of AD, using multidisciplinary approach.

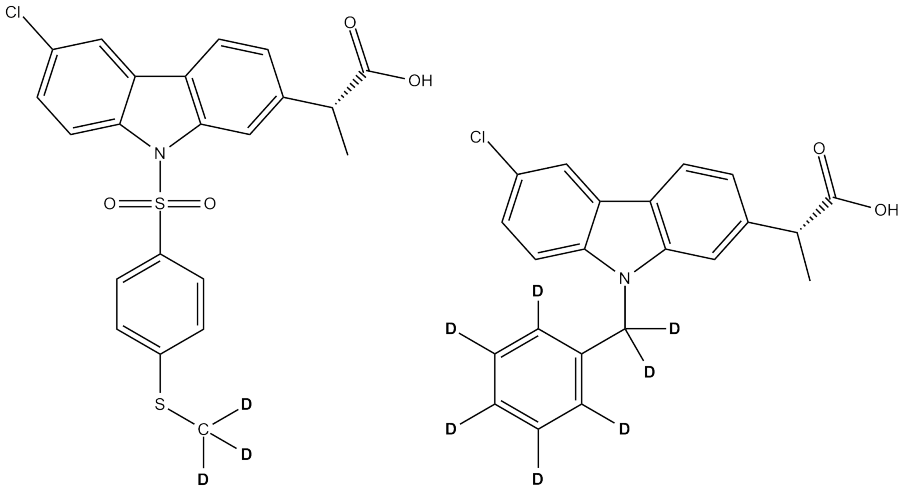

Figure 4: Graphical representation of deuterated sulfonyl-carprofen (left) and deuterated benzyl-carprofen (right).

To understand the mode of action of membrane proteins on a molecular level it is essential to have a detailed knowledge of the structural properties of these proteins, including precise backbone structure and tilt angles of the transmembrane segments. In addressing the role of structural variations of the TM sequence in APP processing it was the goal of this work to determine structural details, the tilt and the pitch angles of the APP_TM peptide within its natural environment, the membrane bilayer. Solid-state nuclear magnetic resonance (ssNMR) has proved to be a valuable biophysical tool for probing structure and dynamics in a wide range of bio-molecules that are inaccessible to crystallography or solution nuclear magnetic resonance (NMR), such as membrane proteins and disease-related protein aggregates.

With the goal of addressing the molecular mechanisms responsible for the age-related risks of AD, we compared the aggregation of Aβ(1-40) and Aβ(1-40)E22G to study the structural and morphological similarities of the species—oligomeric or fibrillar—formed by both peptides in the presence and in the absence of added Ca^{2+}. Gel electrophoresis and Western blot analysis, thioflavine T (ThT) fluorescence, Fourier transform infrared spectroscopy (FTIR), and atomic force microscopy imaging (AFM) were used.

In order to shed light onto the mechanism of action of two potent γ-secretase modulators – benzyl-carprofen and sulfonyl-carprofen (Figure 4 on page 10) within lipid bilayers [Narlawar et al., 2007], solid-state deuterium magnetic resonance technique was employed. Revealing their position and orientation in the lipid membranes will also provide a valuable insight into the molecular mechanism of the proteolytic cleavage of γ-secretase and therefore Aβ production.

In order to achieve these goals, the following techniques were used.

1.5 TECHNIQUES

1.5.1 *Model lipid membranes*

Everybody knows - biological membranes consist of phospholipids. However, they also include proteins (e.g. receptors, transporters, ion pumps, enzymes, etc.), cholesterol and sugars (i.e. glycolipids and glycoproteins). It makes it a complicated system to work with. In order to study membrane proteins or membrane-associated peptides and to focus on their structure and / or lipid-polypeptide interactions it is a common practice to use a simple model system. Such a system may be micelles, liposomes or oriented bi- or multi-layers consistent of one or a combination of phospholipids, which are varied depending on the desired parameters of the model.

Phospholipids are amphipathic, meaning that they consist of a polar head group (commonly phosphorylated alcohol) attached via a linker (commonly a glycerol) to a hydrophobic tail consistent of fatty acyl chains. Phospholipids are derived from either glycerol or sphingosine (a complex alcohol). The hydrocarbon chains vary in length and in degree of saturation (i.e. refers to the number of double bonds). The length and the degree of unsaturation of fatty acid chains have a profound effect on membrane fluidity as unsaturated lipids create a kink, preventing the fatty acids from packing together as tightly, thus decreasing the melting temperature (increasing the fluidity) of the membrane.

The following were used in this thesis to model lipid membranes (Figure 5 on page 12):

1) 1-palmitoyl-2-oleoyl-*sn*-glycero-3-phosphocholine (POPC) (16:0-18:1) - this lipid consists of a phosphocholine headgroup connected via glycerol to two acyl chains—16 and 18 carbons-long—while the 18 carbons-long chain has one double bond at position 9.

2) N-octadecanoyl-D-erythro-sphingosylphosphorylcholine (Sphingomyelin) - is a major constituent of cell membranes and is found at particularly high concentrations in the membranes of nerve cells. It was previously thought to have a purely structural role however, it is now appreciated that sphingomyelin has a high affinity for cholesterol and that these two lipids pack tightly into liquid-ordered domains among a liquid-disordered phase to form lipid rafts [Milhas et al., 2010]. These membrane microdomains are thought to function as signaling platforms that regulate the localization and interactions of proteins.

3) Cholesterol - is also amphipathic. It comprises a single polar hydroxyl group (R-OH), which interacts with water and the heads of other membrane lipids. The hydrophobic tail of cholesterol is embedded in the hydrophobic interior of the membrane. Cholesterol fits between the phospholipid molecules and interacts via van der

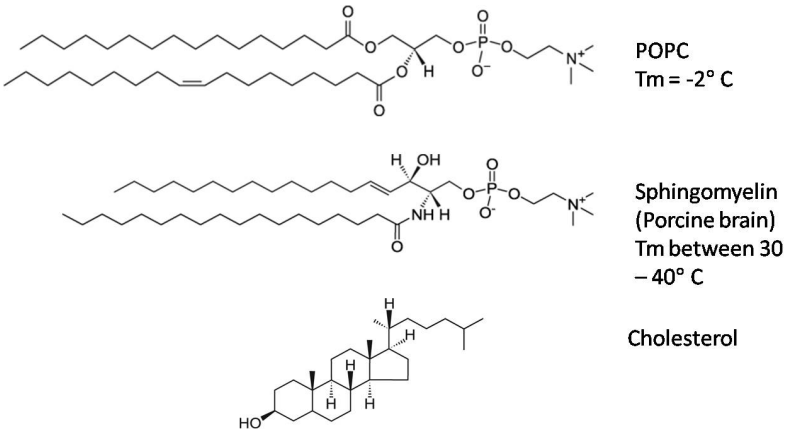

Figure 5: Schematic representation of the model membrane components used in this thesis. Images were taken from Avanti website. Transition temperature range of Sphingomyelin (Brain, Porcine) is taken from Shipley et al. [1974].

Waals forces with the lipid tails. Due to this characteristic behavior, at low temperatures cholesterol increases fluidity by preventing the phospholipids from packing too close together and therefore prevents "freezing". At high temperatures, the addition of van der Waals forces due to cholesterol binding decreases fluidity of the membrane. Thus the amount of cholesterol in the model membrane plays an important role in membrane characteristic behavior.

1.5.2 *Theory of NMR spectroscopy*

NMR THEORY Nuclei which contain an odd number of protons or neutrons exhibit in their ground state a magnetic moment, i.e. nuclear spin. Magnetic resonance occurs as a result of the quantum mechanical property of this spin. In general, the spin is connected with its angular momentum. This gives a nucleus a specific magnetic moment which will orient itself at discrete energy levels in an applied magnetic field.

A nucleus of spin I will have $2I + 1$ possible orientations (e.g. a nucleus with spin $1/2$ will have 2 possible orientations). In the absence of an external magnetic field, these orientations are of equal energy. If a magnetic field is applied, then the energy levels split.

The initial populations of the energy levels are determined by thermodynamics, as described by the Boltzmann distribution:

$$\exp^{(-\Delta E \backslash kT)} = \exp^{(\gamma \hbar m B_0 \backslash kT)}, \tag{1.1}$$

where ΔE is the energy difference between two energy states, T is the temperature, and k is Boltzmann's constant. It means that the lower energy level will contain slightly more nuclei than the higher level. It is possible to excite these nuclei into the higher level with electromagnetic radiation. The frequency of radiation is determined

by the difference in energy between the energy levels, which in turn depend on the strength of the external magnetic field B_o and on the gyromagnetic ratio γ, which is an intrinsic property of the nucleus. This frequency is called the Larmor frequency $\nu = \gamma B$.

A sample containing a large number of elementary spin-moments exhibits a net macroscopic magnetization when placed in a magnetic field. Applying a RF pulse tilts the magnetization away from its equilibrium position into the xy-plane by a specific angle which depends on the applied magnetic field and on the length of the pulse. The out-of-equilibrium magnetization vector precesses about the external magnetic field vector at the Larmor frequency of the spins. This oscillating magnetization vector induces a current in a nearby pickup coil, creating an electrical signal of the Larmor frequency. This signal is known as the free induction decay (FID), and it contains the vector sum of the NMR responses from all the excited spins. In order to obtain the frequency-domain NMR spectrum (NMR absorption intensity vs. NMR frequency) this time-domain signal (intensity vs. time) is Fourier transformed.

A more detailed explanation can be found in numerous textbooks, e.g. [Levitt, 2001] and [Keeler, 2002].

SOLID-STATE NMR In solution state the spin interactions are undergoing fast motional averaging and thus their resonances are characterized by sharp isotropic frequencies. The nuclear spin interactions which affect ssNMR spectra, chemical shielding, dipole-dipole coupling and quadrupolar coupling, are all dependent on the molecular orientations and therefore anisotropic. As a result of this, the NMR spectrum of a static powder sample contains broad lines, or powder patterns, as all the different molecular orientations that are present in the sample give rise to different spectral frequencies. However, these line-broadening effects encode valuable structural information, such as orientation relative to the magnetic field and are sensitive to internal molecular dynamics. In high-resolution ssNMR, RF irradiation, mechanical alignment and mechanical sample spinning replace molecular motions as line narrowing mechanisms.

The ssNMR approaches that are most successful for studying molecular dynamics rely on the concept of dilute spins to provide a natural isolation of the nuclear spin of interest. Nuclei with spin $S = 1/2$, such as ^{15}N, ^{31}P, and ^{13}C interact strongly with the abundant ^{1}H spins, but not among themselves. Their dominant spin interactions are heteronuclear dipolar coupling and chemical shift anisotropy. Deuterium with spin $S = 1$ has its NMR properties dominated by the effect of the nuclear quadrupole interaction [Opella, 1986].

1.5.2.1 *Chemical shielding (shift)*

The electrons in the molecular orbitals that surround a nucleus produce electrical current that induces local magnetic field at the nucleus. This field contributes to the total field felt at the nucleus and has a potential to change the resonance frequency of the nucleus. The interaction of the field produced by the electrons with the nucleus is called the shielding interaction. The frequency shift that this interaction causes in an NMR spectrum is called the *chemical shift*, and can be written as:

$$\omega = \gamma B = \gamma B_0 (1 - \sigma),$$

where B_0 is the static magnetic field and σ is the shielding parameter. The term σ is a second-rank Cartesian tensor, called the chemical shielding tensor.

1.5.2.2 *Chemical shift anisotropy (CSA)*

The chemical shielding introduced in the previous section is not the same in all directions, but rather orientation dependent. This means that a nucleus would resonate at different frequencies if the molecule changes its orientation with respect to the magnetic field, this is called a *chemical shift anisotropy*. If the molecule changes its orientation on a timescale faster than the inverse of the chemical shift anisotropy the chemical shift will be seen as a single narrow averaged resonance line, an isotropic resonance line, in the NMR spectrum. This behavior is observed in liquid-state NMR. In solid-state NMR in liquid crystals or in static powders (i.e. in the absence of fast isotropic averaging) broad line-shapes are observed due to insufficient averaging that arise from greatly reduced molecular reorientation.

A second-rank Cartesian tensor describes the orientation dependence of nuclear spin interactions, i.e. chemical shift (σ), dipolar (D) and quadrupolar (Q) interactions. For chemical shielding tensor σ as an example, it is represented by 3×3 matrix:

$$\boldsymbol{\sigma} = \begin{pmatrix} \sigma_{xx} & \sigma_{xy} & \sigma_{xz} \\ \sigma_{yx} & \sigma_{yy} & \sigma_{yz} \\ \sigma_{zx} & \sigma_{zy} & \sigma_{zz} \end{pmatrix}, \tag{1.2}$$

where x, y, z is some axis frame. It is possible to choose the axis frame such that the interaction tensor σ defined with respect to it will be diagonal. This axis frame is the principal axis frame (PAF) and the values on the diagonal of σ^{PAF} are the principal values of the shielding tensor (eq. (1.3).

$$\boldsymbol{\sigma}^{\mathbf{PAF}} = \begin{pmatrix} \sigma_{xx}^{PAF} & 0 & 0 \\ 0 & \sigma_{yy}^{PAF} & 0 \\ 0 & 0 & \sigma_{zz}^{PAF} \end{pmatrix}, \tag{1.3}$$

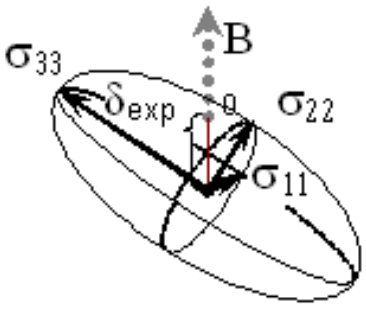

Figure 6: Graphical representation of the chemical shift anisotropy (CSA) tensor (cf. text). The length of the principal axes of the tensor is represented by $1/\sigma_{ii}$, with σ_{ii} being the main tensor elements σ_{11}, σ_{22}, σ_{33} [Bechinger and Sizun, 2003].

The orientation of the principal axis frame is determined by the local environment of the nucleus to which the interaction relates. The interaction tensor can be represented as an ellipsoid fixed within the molecule and centered on the nucleus it applies to (Figure 6 on page 15). The principal axes of the ellipsoid coincide with the principal axis frame of the shielding tensor, and the length of each principal axis of the ellipsoid is proportional to the magnitude of the principal value of the interaction tensor associated with that principal axis. If the molecular orientation in the laboratory frame changes, then so does the orientation of the interaction tensor. The interaction tensor also reflects the symmetry of the nucleus, if there is such. For example, for a nucleus at a site of axial symmetry, the z^{PAF} coincides with the symmetry axis and the principal values become $\sigma_{xx}^{PAF} = \sigma_{yy}^{PAF} \neq \sigma_{zz}^{PAF}$.

The three principal values can be also expressed in terms of isotropic value σ_{iso}, the anisotropy Δ_σ, and the asymmetry η_σ of the interaction. They are defined as follows:

$$\sigma_{iso} = \frac{1}{3}\left(\sigma_{xx}^{PAF} + \sigma_{yy}^{PAF} + \sigma_{zz}^{PAF}\right) \tag{1.4}$$

$$\Delta_\sigma = \sigma_{zz}^{PAF} - \sigma_{iso} \tag{1.5}$$

$$\eta_\sigma = \frac{\sigma_{xx}^{PAF} - \sigma_{yy}^{PAF}}{\Delta_\sigma} \tag{1.6}$$

The anisotropy is related to the length of the ellipsoid of the tensor; the asymmetry is a measure of how far a cross-section through the ellipsoid (parallel to the $x^{PAF} - y^{PAF}$ plane) deviates from circular; and the σ_{iso}value arises in the case of fast isotropic motion when the tensor is averaged to one single isotropic value.

The angular dependence of the observed signal can be described by:

$$\sigma_{zz} = \sigma_{11}\sin^2\Theta\cos^2\Phi + \sigma_{22}\sin^2\Theta\sin^2\Phi + \cos^2\Theta, \tag{1.7}$$

where σ_{zz} is the chemical shift, σ_{11}, σ_{22}, and σ_{33} are the main tensor elements, and the Euler angles Θ and Φ position the chemical shift tensor relative to the magnetic field direction of the NMR spectrometer (B_o) [Bechinger and Sizun, 2003]. Thus, the observed signal can be seen as the length from the center of the ellipsoid to the surface, in the direction of the external magnetic field B_0 (Figure 6 on page 15).

1.5.2.3 *Dipolar coupling*

The dipolar interaction is a direct through space interaction between two nuclear dipoles. If the interacting spins ($I = \frac{1}{2}$) are from different species, then one is marked I for the abundant spin while the other marked S for the rare spin and the interaction is heteronuclear. If two spins are from the same species, then the interaction is homonuclear i.e. $I - I$ or $S - S$. The second rank tensor of a dipolar interaction is usually symmetric around the internuclear vector. The interaction Hamiltonian is:

$$D_{zz} = \left(\frac{\mu_0}{4\Pi}\right) \frac{\gamma_1 \gamma_2 \hbar}{r^3} \left(3\cos^2\Theta - 1\right), \tag{1.8}$$

where $\left(3\cos^2\Theta - 1\right)$ describes the angular dependence of the dipolar interaction and the magnitude of the interaction depends on the gyromagnetic ratios γ_1 and γ_2 of the spins and relates to the internuclear distance as $\frac{1}{r^3}$. Within an amide bond the dipolar coupling between ^{15}N and ^{1}H spins can span several tens of kHz resulting in broad lines. In the solid state, the limited motions are not sufficient to average the dipolar coupling. This is usually solved by adding a decoupling pulse to the pulse sequence.

1.5.2.4 *Quadrupole coupling*

A nucleus that has a spin number $I > \frac{1}{2}$ has a non-spherical charge distribution, creating electrical quadrupolar moment (generally given as eQ). An asymmetric charge distribution around the nucleus causes an asymmetric electric field at the nucleus, characterized by a tensor quantity called the Electric Field Gradient (EFG) and written as ∇E. The strength of the interaction depends upon the magnitude of the nuclear quadrupole moment and the strength of the electric field gradient. The electric quadrupole interaction between those two quantities gives rise to a splitting in the nuclear energy levels (Figure 7 on page 17). The size of the quadrupolar interaction does not depend on the external magnetic field therefore, the quadrupolar splitting is given in (k)Hz units.

The Hamiltonian for a quadrupolar nuclei can be written as [Abragam, 1961]:

$$\mathcal{H} = -\gamma\hbar B_0 I_z + \left[e^2 qQ/4I\,(2I - I)\right]\left[3I_z^2 - I\,(I+1) + 1/2\eta\left(I_+^2 + I_-^2\right)\right], \tag{1.9}$$

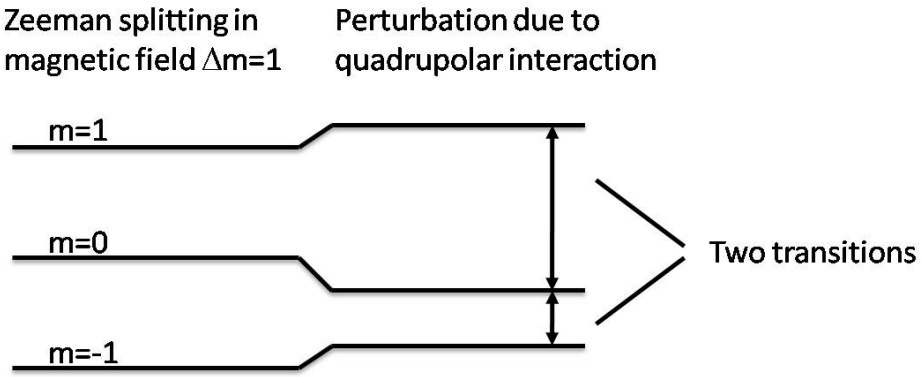

Figure 7: The spin 1 deuterium nucleus is characterized by three energy levels and thereby exhibits two Zeeman transitions with $\Delta m = 1$. The transitions are modulated by the quadrupolar interaction, therefore the two transitions exhibit different resonance frequencies that are separated by the deuterium quadrupole splitting ($\triangle \nu_Q$).

where B_0 is the applied magnetic field in the z-axis and I_z is the z-component of the spin angular momentum of the nucleus. Expressed in a principal axis frame V_{xx}^{PAF}, V_{yy}^{PAF} and V_{zz}^{PAF} (where the EFG tensor is diagonal) the following parameters are defined:

$$\eta_Q = \left(\frac{V_{xx}^{PAF} - V_{yy}^{PAF}}{V_{zz}^{PAF}} \right) \tag{1.10}$$

$$eq = V_{zz}^{PAF}, \tag{1.11}$$

where η_Q is the quadrupolar asymmetry parameter and e is the magnitude of the electron charge. With the additional stipulation that the z direction is always associated with the largest field gradient and y with the smallest $V_{zz} \geqslant V_{xx} \geqslant V_{yy}$ it follows that $0 \leqslant \eta \leqslant 1$. The trace of the electric field gradient tensor V is zero, so it has no isotropic component. Thus $eq = V_{zz}^{PAF}$ is the anisotropy of the electric field gradient tensor and it is the largest value of the electric field gradient. The orientation of the PAF is determined by the chemical structure around the nucleus and so is fixed relative to the molecule.

Taking the z-axis along the applied field B_0, the energy level is [Saitô et al., 2006]:

$$\begin{aligned} E_m^{(1)} &= -\gamma\hbar B_0 m + \left[3e^2 qQ/8I\,(2I-1)\right] \\ &\quad \left[3\cos^2\theta - 1 + \eta\sin^2\theta\cos 2\phi\right] \times \left[m^2 - I\,(I+1)\,/3\right] \end{aligned} \tag{1.12}$$

where θ and ϕ are the polar and azimuthal angles in the principal axes of the electric field gradient tensor (the C–^{2}H bond vector), and m is the quantum number for the z-component of the angular momentum I. The expected resonance frequency $\nu\,(m-1 \to m)$ is written as:

$$\begin{aligned}\nu(m-1\rightarrow m) &= \left(E^{(1)}_{m-1} - E^{(1)}_{m}\right)/h \\ &= \gamma B_0/2\pi - \left[3e^2qQ/4I(2I-1)\right] \\ &\quad \left[\left(3\cos^2\theta - 1 + \eta\sin^2\theta\cos 2\phi\right)(m-1/2)\right] \quad (1.13)\end{aligned}$$

For nucleus of spin number I=1, two transitions $\nu(1\rightarrow 0)$ and $\nu(-1\rightarrow 0)$ of equal intensity are expected. Therefore, the difference between the two transitions is:

$$\Delta\nu_Q = \left[3e^2qQ/4I(2I-1)h\right]\left(3\cos^2\theta - 1 + \eta\sin^2\theta\cos 2\phi\right) \quad (1.14)$$

For EFG tensor with axial symmetry, the asymmetry parameter cancels out and Eq. (1.14) reduces to:

$$\Delta\nu_Q = \left[3e^2qQ/4I(2I-1)h\right]\left(3\cos^2\theta - 1\right) \quad (1.15)$$

1.5.2.5 *Relaxation*

After a perturbation of a nuclear spin system in an NMR experiment with a RF pulse, the magnetization will return ti its initial state, or equilibrium, via relaxation. The relevant relaxation times are dependent on the time scale of existing molecular motions. If the interactions cause fluctuations at the Larmor frequency, the relaxation to the ground state will be most efficient. As a consequence, relaxation processes are dynamics dependent and manifest themselves in the linewidth of spectral discontinuities in the NMR spectrum. The relaxation process along z-axis is referred to as spin-lattice relaxation (T_1) while the relaxation in the *xy*-plane is a spin-spin relaxation (T_2). The time scales of these relaxation processes are often different since the relaxation in the z-direction and in the *xy*-plane are sensitive to fluctuations occurring on different time scales.

1.5.3 *Attenuated total reflection Fourier transform infrared spectroscopy*

Attenuated total reflection Fourier transform spectroscopy (ATR-FTIR) is one of the most powerful methods to study biological samples, in particular biological membranes. It allows to evaluate various parts on the molecules in an oriented sample, while yielding strong signal in a short time. Of great advantage is the possibility to study simultaneously lipids and proteins, which is what was done in this thesis. It is a powerful tool for protein secondary structure evaluation. With an attenuated total reflection (ATR), rather than measuring the absorption of the incident light (as in transmission mode), one measures the absorption of the evanescent wave that penetrates the sample when the incident light is reflected at the crystal/sample interface.

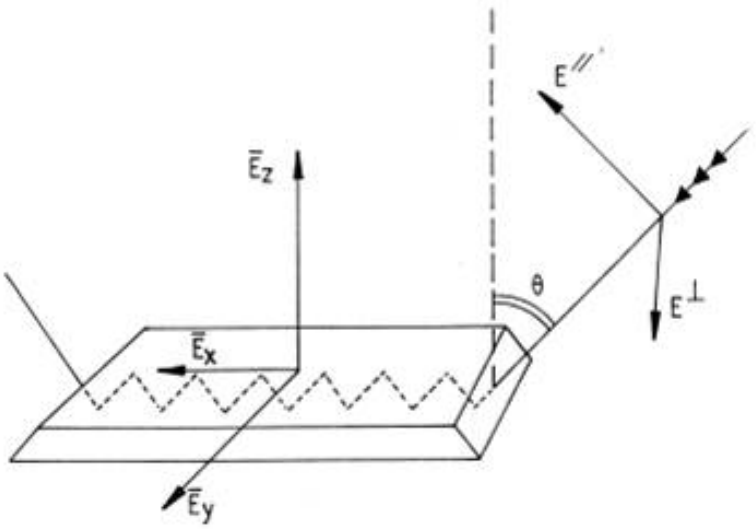

Figure 8: Schematic representation of the internal reflection element (IRE) and of the light pathway. The Cartesian components of the electric field are shown along the x, y and z axes. Two possible planes of polarization of the incident light are indicated by $E_{\parallel}$ (polarization parallel to the incidence plane) and $E_{\perp}$ (polarization perpendicular to the incidence plane). The incident beam makes an angle θ with respect to the normal to the IRE surface. The edges of the IRE are beveled so that the incident beam penetrates the IRE through the surface that is perpendicular to its propagation. Adapted from [Goormaghtigh et al., 1999].

Two ATR setups were used in this work: the most usual design – the trapezoidal plate of germanium crystal (Figure 8 on page 19) which allows molecular orientation of membranes and peptides to be determined via linear dichroism. In another setup the internal reflection element (IRE) was a diamond crystal of 2×2 mm with an aperture angle of 45° that yields a single internal reflection. Such a setup allowed to use only *nanograms* of peptide.

The principle of ATR-FTIR is that the infrared (IR) beam is directed into the IRE of high refractive index (transparent for the IR radiation). Refractive indices of the IRE and of the medium define a critical angle θ_c

$$\theta_c = \sin^{-1} n_{21} \tag{1.16}$$

where $n_{21} = n_2/n_1$ (n_2 being refractive index of the medium, and n_1 being refractive index of the IRE). If the angle of incidence is above the critical angle, the light is completely reflected by the IRE. However, due to the interference of the incident and of the reflected beams, standing waves are formed. A standing wave creates an electromagnetic disturbance in the medium called evanescent wave. Evanescent wave decreases exponentially with the distance from the interface (Figure 9 on page 20). The penetration depth of the evanescent wave is given by

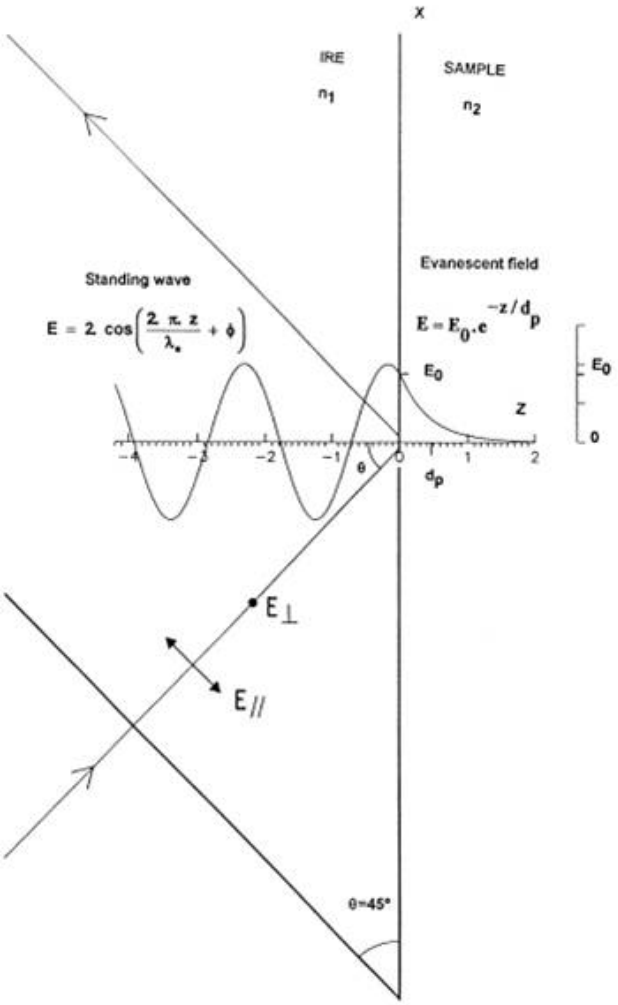

Figure 9: Side view of the IRE with details of the electric field of the electromagnetic radiation at one point of reflection. A standing wave exists within the IRE while the evanescent field decays exponentially outside the IRE. Z in μm. Adapted from [Goormaghtigh et al., 1999]

$$dp = \frac{\lambda_1}{2\Pi \left(\sin^2 \theta - n_{21}^2\right)^{\frac{1}{2}}}, \tag{1.17}$$

where $\lambda_1 = \lambda/n_1$. The larger λ or the smaller θ, the larger the penetration depth. Essentially, this is what allows the interaction between the IR radiation and the sample. Due to the nature of the evanescent field, the sample of lipids and proteins needs to be in close contact with the IRE and therefore it is spread in a form of a thin film.

A typical FTIR spectrum of a peptide in lipid bilayers covers a spectral range from 900 $cm^{-1}$to 4000 cm^{-1}, but often the region between 1000 cm^{-1} and 1800 cm^{-1} is sufficient (Figure 10 on page 22) for the analysis. In this work, we concentrated on the region between 1400 $cm^{-1}$and 1800 cm^{-1} as it contains absorption bands from the peptide amide regions, which are of special interest for determination of the secondary structure. The carboxyl stretching of the peptide backbone shows absorption band usually at 1650 cm^{-1} for α-helical peptides or at 1630 $cm^{-1}$and 1695 cm^{-1} for a β-sheet structure. These bands are located in the amide I region (1600 cm^{-1}– 1700 cm^{-1}). N–H bending of the peptide backbone amide shows absorption band usually at 1540 cm^{-1} and is located in amide II region (1500 cm^{-1}- 1600 cm^{-1}). Samples containing lipids have absorption bands from CH_2 asymmetric and symmetric stretching at 2920 cm^{-1} and 2850 cm^{-1}, respectively; from CH_3 asymmetric and symmetric stretching at 2956 cm^{-1} and 2872 cm^{-1}, respectively; from C–O stretching at 1100 cm^{-1} and 1400 cm^{-1}; from P=O stretching of the lipid headgroups at 1235 cm^{-1}; C=O stretching (in the lipid headgroup) exhibits two absorption bands near 1740 cm^{-1} and allows to assess the averaged orientation of the lipid bilayers.

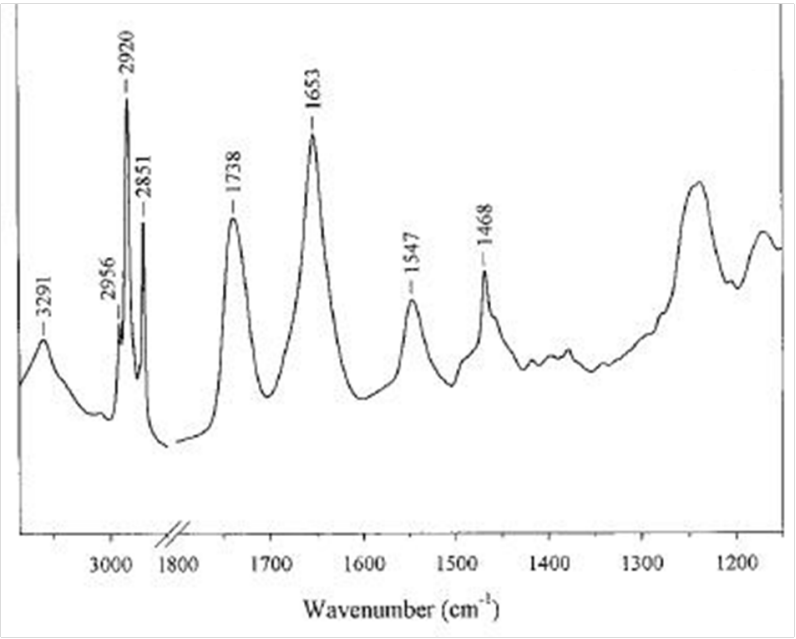

Figure 10: An example of FTIR spectrum of a membrane protein in lipids. The following peaks are observed: amide A at 3291 cm^{-1}; asymmetric stretch of CH_3 at 2956 cm^{-1}; asymmetric stretch of CH_2 at 2929 cm^{-1}; symmetric stretch of CH_3 at 2872 cm^{-1}; symmetric stretch of CH_2 at 2851 cm^{-1}; C=O stretch at 1738 cm^{-1}; amide I region - α-helix at 1653 cm^{-1}; amide II region - α-helix at 1549 cm^{-1}; $\gamma_w(CH_2)$ progression from 1200 cm^{-1} - 1350 cm^{-1}; CH bend and COO^- symmetric stretch 1350 cm^{-1} - 1500 cm^{-1}; C-C, C-O stretch, PO_2 symmetric stretch 1130 cm^{-1}- 1180 cm^{-1}.

2

METHODS

2.1 SOLID-STATE NMR EXPERIMENTS

Solid-state nuclear magnetic resonance spectroscopy is a powerful and proven method for biophysical characterization of peptides including their structure, dynamics and interactions in the presence of membranes. In static samples of oriented model membranes with incorporated polypeptides, the orientation dependence of chemical shift, dipolar or quadrupolar interactions provide angular constraints necessary for the calculation of the structure and orientaion of the polypeptide. Furthermore, ssNMR spectroscopy of aligned samples offers distinct advantages in allowing access to dynamic processes such as topological equilibrium or rotational diffusion in membrane environment [Bechinger et al., 2008].

2.1.1 *Solid-state NMR spectroscopy techniques: ^2H, ^{15}N, ^{31}P.*

2.1.1.1 *^2H solid-state NMR spectroscopy*

Deuterium with spin $S = 1$ has a relatively large quadrupole coupling constant and a relatively small gyromagnetic ratio. Therefore, line shapes and relaxation properties of ^2H resonances are determined almost exclusively by the nuclear quadrupole interaction [Opella, 1986, Muhandiram et al., 1995]. Because of the large quadrupole coupling constant, the frequency breadth of experimental spectra is large, consequently the acquired signal in the time domain is short therefore, the quadrupole echo pulse sequence is used in ^2H NMR experiments [Davis et al., 1976].

The quadrupole spin interaction arises from the electrostatic interaction of the nuclear quadrupole moment with the electric field gradient of the C–^2H bond. The electric field gradient is characterized by a symmetric second rank tensor, as a consequence, the resonance frequencies depend on the orientation of the C–^2H bond with respect to the applied magnetic field. Therefore, ^2H NMR is a useful way to study alignment and dynamics of various molecules as the ^2H NMR spectra reflect directly the residual quadrupole spin interaction.

Because of its large quadrupolar energy, in the high magnetic field the quadrupole interaction can be treated as a small perturbation of the magnetic energy. Under these conditions equation (1.15) reduces to:

$$\triangle\nu_Q = \frac{3}{2}\left(\frac{e^2qQ}{h}\right)\left(\frac{3\cos^2\theta - 1}{2}\right). \tag{2.1}$$

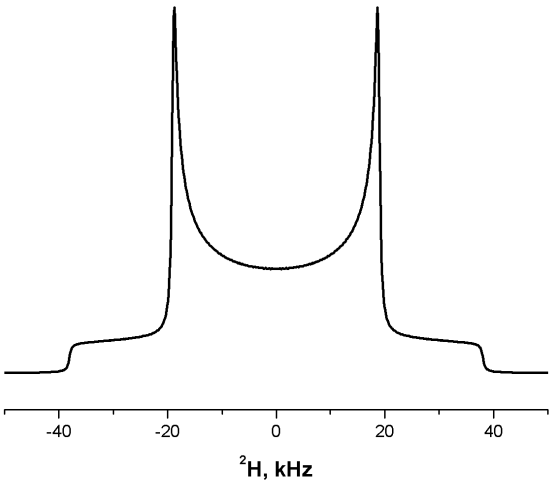

Figure 11: ²H powder pattern spectrum arising from two transitions, eq. 2.4.

This orientation-dependent splitting of peaks yields a clue on how a C–²H vector of a molecule under consideration is oriented relative to the applied magnetic field in single crystalline, or oriented samples.

In powder samples (where the molecules are randomly distributed), the observed ²H NMR frequency for $-1 \leftrightarrow 0$ and $0 \leftrightarrow 1$ transitions can be written as:

$$\nu_{zz} = \frac{1}{2}\delta\left(\cos^2\theta - 1\right) \quad \text{for} \quad -1 \leftrightarrow 0 \text{ transition} \tag{2.2}$$

$$\nu_{zz} = -\frac{1}{2}\delta\left(\cos^2\theta - 1\right) \quad \text{for} \quad 0 \leftrightarrow 1 \text{ transition,} \tag{2.3}$$

where $\delta = (3/4)\left(e^2qQ/h\right)$. The "powder pattern" of two homogeneously broadened peaks forms a so-called "Pake doublet" (Figure 11 on page 24). The separation of the "horns" in the powder pattern spectrum is:

$$\Delta\nu_{powder} = (3/4)\, e^2qQ/h, \tag{2.4}$$

where the deuterium quadrupole coupling constant, e^2qQ/h for C–²H fragments ranges from 160 to 210 kHz, depending upon the type of hybridization.

Detailed treatment of ²H NMR of bio-molecules can be found in [Seelig, 1977].

The local and global dynamics of the peptide influences the total intensity of the ²H NMR signal. In order to follow local dynamics of the peptide in this work, methyl groups of the alanine residues were labeled with ²H. This has a special advantage, as at room temperature the methyl group of alanine exhibits fast rotational motions around the

C_α - C_β bond. As a result, the three methyl deuterons are equivalent and exhibit overlapping resonances. This results in axially symmetric ^2H tensor with respect to the C_α - C_β bond vector. The measured splitting $\Delta\nu$ is then directly related to the angle θ between C_α - C_β bond and B_0 (2.1). As C_α is an integral part of the polypeptide backbone, the orientation of the C_α - C_β bond also reflects the alignment of the polypeptide.

2.1.1.2 *^{15}N solid-state NMR spectroscopy*

^{15}N ssNMR spectroscopy is a very attractive tool because there are nitrogen atoms located in amide bonds of the polypeptide backbone, which makes them a great probe for dynamical and structural studies. Most nitrogen sites exhibit chemical shift anisotropy and heteronuclear (^{15}N–^1H) dipole interactions.

Using model compounds and a wide variety of peptides the principal elements of the ^{15}N chemical shift tensor of an amide bond in Glycine, Alanine and Valine residues was determined [Lee et al., 1998, Hiyama et al., 1988, Naito et al., 1998, Oas et al., 1987, Roberts et al., 1987, Harbison et al., 1984, Shoji et al., 1998, Chekmenev et al., 2004, Lee et al., 1999, Glaser et al., 2005, Hartzell et al., 1987, Shoji et al., 1990, Lee et al., 2001], as reviewed and standardized in [Salnikov et al., 2009]. The accuracy of the analysis and the calculation of the orientational restrains of the data from oriented samples depends on the knowledge of the size of the principal values of the ^{15}N chemical shift tensor and their alignment within the molecular frame. A detailed analysis of the published data on ^{15}N chemical shift tensor shows that σ_{33} , σ_{22}, and σ_{11} are on average 226 ± 7, 81 ± 7 and 58 ± 7 ppm, respectively [Salnikov et al., 2009]. In α-helical peptides the NH vector and the σ_{33} component cover an angle of about 15°–25° and both are oriented within a few degrees of the helix long axis.

In a system with defined reference orientation (e.g. the lipid bilayer), the orientation of the protein can be determined with respect to this reference frame. Conveniently, due to the unique size of σ_{33} and its orientation almost parallel to the helix axis, we can correlate the alignment of the helix within oriented phospholipid bilayers with the ^{15}N chemical shift interaction [Bechinger and Sizun, 2003]. For samples with the membrane normal oriented parallel to the magnetic field, transmembrane α-helical peptides exhibit ^{15}N resonances > 200 ppm, whereas they resonate at < 100 ppm when aligned parallel to the membrane surface (Figure 12 on page 26).

2.1.1.3 *^{31}P solid-state NMR spectroscopy - orientation of the lipid bilayers*

ssNMR studies of ^{31}P are almost exclusively concerned with the large chemical shift anisotropy. There are few phosphorous atoms in proteins, but since biological membranes are predominantly composed of

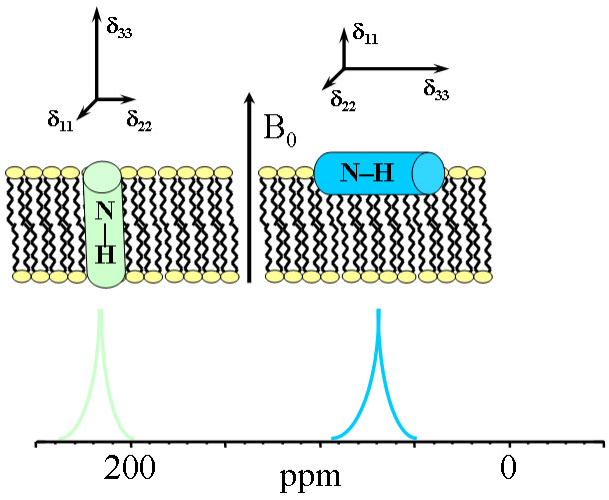

Figure 12: ^{15}N NMR of oriented α-helical peptides, showing the alignment of the ^{15}N–^{2}H vector. The figure is a courtesy of E. Salnikov.

phospholipids ^{31}P NMR is often used to study motions and average orientation of the lipid headgroups [Seelig, 1977]. The ^{31}P has a natural abundance of 100 % therefore, there is no need in isotopic labeling. The high gyromagnetic ratio makes the nucleus a very sensitive probe and a spectrum can be measured within minutes. In hydrated samples at room temperature, entire lipid molecule undergoes a fast rotational diffusion and the CSA is averaged to a residual axially symmetrical tensor.

^{31}P NMR was used to asses the lipid membranes alignment as a function of mechanical orientation between glass plates. The fast axial rotation of the phospholipids around their long axis averages the ^{31}P chemical shift to a symmetrical tensor where the tensor singular axis ($\sigma_{\parallel}$) coincides with the rotational axis. The ^{31}P NMR spectra of liquid crystalline phosphatidylcholine bilayers therefore, provide a classic example for averaging around the membrane normal [Seelig, 1978]. The signal at 30 ppm is thus indicative of phosphatidylcholine molecules with their long axis oriented parallel to the magnetic field direction, whereas a −15 ppm ^{31}P chemical shift is obtained for perpendicular alignments (Figure 13 on page 27). In perfectly aligned samples the phospholipid bilayer spectra consist of a single line. Intensities to the right of the main peak can arise if there are phospholipid molecules deviating from parallel orientation respective to the magnetic field direction. In addition, signals in this region (< 30 ppm) can be due to local conformational changes of the phospholipid head group for example, due to electrostatic interactions of the (-HPO_4^--CH_2-CH_2-$N^+(CH_3)_3$) dipoles of the phosphocholine head group, hydrogen bonding, and/or electric dipole–dipole interactions [Seelig et al., 1987, Bechinger and Seelig, 1991b,a].

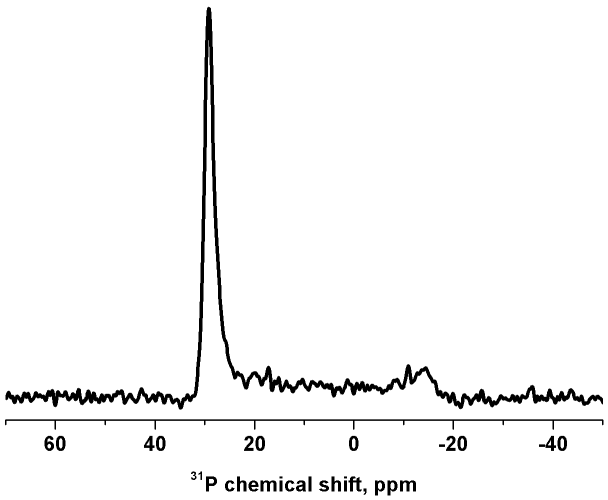

Figure 13: ^{31}P chemical shift spectrum of pure POPC lipids in oriented sample at RT. The chemical shift around 30 ppm corresponds to lipids oriented parallel to the external magnetic field, while a very small spectral discontinuity around -18 ppm corresponds to lipids oriented perpendicular to the external magnetic field.

2.1.2 *Hahn (spin) echo*

In magnetic resonance, a spin echo is the refocusing of spin magnetization by a pulse of resonant electromagnetic radiation [Hahn, 1950].

Broad lines arising from chemical shift anisotropy, dipolar coupling, etc., have rapidly decaying FIDs. Due to coil imperfection "ringing" of the receiver / transmitter coil after a pulse prevents measurement of the signal until immediately after a pulse (i.e. the dead time). This delay prevents a significant part of the rapidly decaying FID to be recorded, which leads to a loss of intensity and a spectral distortion.

Following an initial excitation pulse, the FID decays with time due to both spin relaxation and any inhomogeneous effects which cause different spins in the sample to precess at different rates. Relaxation leads to an irreversible loss of magnetization. The spin echo pulse sequence for lines broadened by chemical shift anisotropy or heteronuclear dipole-dipole coupling : A 90° pulse application onto a sample in the static magnetic field results in a flip of the net magnetization into the horizontal *xy*-plane. Due to local magnetic field inhomogeneities (variations in the magnetic field at different parts of the sample that are constant in time), as the net moment precesses, the signal decays. Then, a 180° pulse is applied (for spin 1/2) so that complete refocusing has occurred and at this time, an accurate T_2 echo can be measured with all the dephasing effects removed (Figure 14 on page 28).

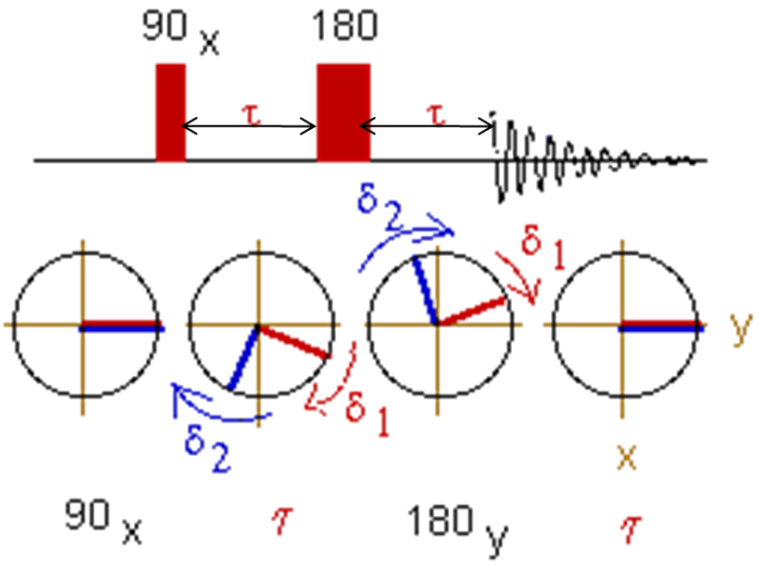

Figure 14: The spin-echo pulse sequence. The behaviour of the transverse magnetization component is shown. Magnetization components dephase under the effects of chemical shift anisotropy or heteronuclear dipolar coupling during the first τ period. The subsequent 180° pulse rotates the magnetization components 180° about the pulse axis (*y* in this case) so that the components refocus after a further τ period. The τ delay is chosen to be long enough to include the dead time of the probe. Then the FID can be completely recorded from the true echo maximum.

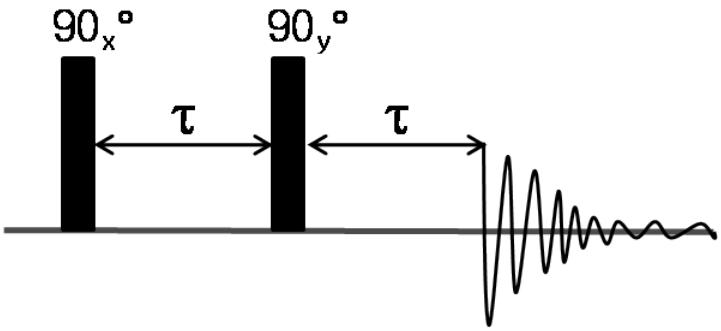

Figure 15: The quadrupole echo pulse sequence.

2.1.3 *Quadrupole (solid) echo*

The powder patterns for ^{2}H nuclei are very broad (100 -200 kHz), implying that much of the information is contained in the very early part of the FID. Since the dead-time of most spectrometers operating in this frequency range can be several tens of microseconds, much of the information about these broad components is lost and can not be reproduced correctly. In order to overcome this problem, a pulse sequence was proposed by [Davis et al., 1976]. A first 90^o pulse is applied then, after time τ, a second 90^o pulse is applied phase shifted by $\pi/2$ relative to the first pulse (Figure 15 on page 29). A quadrupole echo is formed at $t = 2\tau$ due to refocusing of the nuclear magnetization. Starting the Fourier transform at the echo maximum gives an undistorted spectrum.

2.1.4 *Cross-polarization*

Cross Polarization (CP) is one of the most widely used techniques in ssNMR, the other being magic-angle spinning. CP is used to enhance NMR signals of isotopically dilute nuclear spins S (e.g. ^{13}C and ^{15}N) in solids by repeatedly transferring polarization from a species I of high abundance (usually protons) to which they are coupled [Abragam, 1961]. The transfer of polarization is mediated by dipolar heteronuclear coupling and the effect is a sensitivity gain that goes as γ_I/γ_S. In addition, the relaxation times of the low abundance nuclei tend to be very long and with this technique the experiment time can be shortened due to the fast relaxation of protons (i.e. using short recycling delays).

The principle can be explained by two Zeeman energy reservoirs: one for the S-spins and another for the I-spins. The I-spins are brought into contact with S-spins and the energy flows via spin-flips. When the Hartman-Hahn (HH) [**?**] condition is satisfied

$$\gamma_I H_{1I} = \gamma_S H_{1S}, \tag{2.5}$$

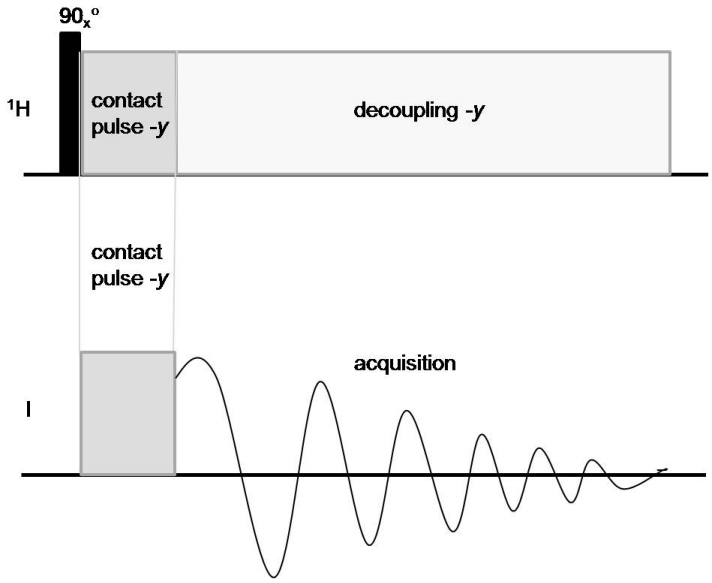

Figure 16: The cross polarization pulse sequence. The sequence is designed to transfer magnetization from the abundant ^1H spins in the sample to the I spins via dipolar coupling between ^1H and I spins. Reproduced from [Duer, 2004].

dipolar contact is established and the flips become energy-conserving, driving the system to equilibrium. Then the S-spins gain magnetization in the direction of the external magnetic field and can be directly detected. Decoupling of heteronuclear dipolar interactions can inclrease the resolution [Abragam, 1961].

In practice, typically an initial 90°_x pulse is applied to the ^1H spins creating magnetization along $-y$ in the ^1H rotating frame. An on-resonance, $-y$ ^1H contact pulse is then applied and this constitutes a spin-lock field ($B_1(^1H)$). Another contact pulse applied simultaneously to the S-spin type (spin-lock field $B_1(S)$ in a rotating frame. Then the amplitude of the two contact pulses must be carefully set in order to achieve the HH matching condition as in equation 2.5 (this procedure sets the energy gaps between the respective rotating frame spins to be equal). Then the $B_1(S)$ field is removed and the decay of the magnetization of S-spins can be observed. The S-spins return to their unpolarized state (Figure 16 on page 30). The contact is established again for n number of steps and the resulting signals are added and subjected to Fourier transformation to obtain the S-spin spectrum [Abragam, 1961].

2.2 SOLID-PHASE PEPTIDE SYNTHESIS USING FMOC CHEMISTRY

Invented by R.B. Merrifield [Merrifield, 1963] solid-phase peptide synthesis (SPPS) is a widely accepted method for peptide production in a laboratory. It utilizes a resin consistent of small insoluble, but porous

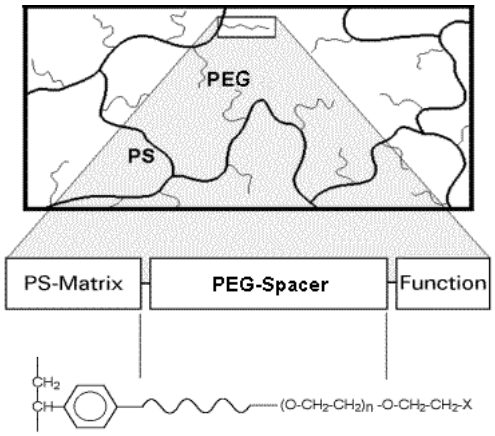

Figure 17: Chemical structure of TentaGel resin. The figure adopted from "Rapp Polymere" website.

beads with attached functional group (linker) on which a peptide can be built from C-terminus to the N-terminus by coupling one amino acid to another creating a peptide bond. Covalent bonding between the linker and a peptide keeps a peptide immobilized until cleaved from it under acidic conditions. Immobilizing the growing polypeptide chain allows to perform washes after each step in order to eliminate the excess reagents and facilitates cleavage. The general principle of SPPS is one of repeated cycles of coupling-wash-deprotection-wash.

There are two main types of SPPS – Fmoc and Boc – different protecting groups used for N-α- protection. In this work Fluorenylmethyloxycarbonyl (Fmoc) protecting group was used. The cleavage of the protecting group is achieved with piperidine (20-50%) in N,N-dimethylformamide (DMF), which exposes the α-amino site for reaction with an incoming activated amino acid [Steven A. Kates, 2000]. DMF is the primary solvent used for resin deprotection, coupling and washing. All the solvents were of highest purity (Sigma, HPLC grade).

We used Polyethylene Glycol Polystyrene-graft Copolymer support (Graft copolymers are a special type of branched copolymer in which the side chains are structurally distinct from the main chain), which consist of a low cross-linked polystyrene matrix on which polyethylene glycol is grafted (Figure 17 on page 31). Polystyrene particles provide a compact support, which contains the open channels for rapid diffusion of reactants throughout the gel matrix. The TentaGel R RAM resign was purchased from Rapp Polymere GmbH (Tübingen, Germany), substitution 0.190 meq/g.

The resin is first swollen to its maximum size with dichloromethane (DCM) followed by a solvent exchange to DMF.

The synthesis protocol is comprised of the following steps (Figure 18 on page 33):

1. Deprotection of the N-terminus by cleavage of the Fmoc group.

2. Activation of the incoming amino acid: the carboxyl group of the following amino acid is deprotonated and reacts with O-Benzotriazole-N,N,N′,N′-tetramethyl-uronium-hexafluoro-phosphate (HBTU), which creates an activated form of amino acid.

3. The activated amino acid is coupled to the N-terminus of the amino acid already attached to the resin. This cycle is repeated as many times as necessary to obtain a full length peptide.

4. The side-chains of amino acids are protected by different protecting groups (e.g. Thr(tBu), Lys(Boc)). All these groups can be cleaved under acidic condition (usually TFA) and at the same time as the polypeptide is cleaved from the resin.

2.2.0.1 *Synthesis of the APP_TM4K peptides*

The 30 amino acids-long polypeptide (amino acids 628 – 655), which corresponds to the transmembrane part of the full length APP (KGAIIGLMGGVVIATVIVITLVMLKKK) was synthesized using standard solid-phase Fmoc chemistry on the MilliGen 9050 PetSynthesizer (Millipore). The syntehsis was carried out at ~ 40°C (the column was wrapped with the rubber tube of a water bath heated to 40°C). Two additional steps were introduced to the synthesis protocol in order to improve the coupling of specific amino acid and to reduce the amount of non-full-length peptides. In the first synthesis large amount of truncated sequence was obtained. The problem arisen between amino acids Val_{644} and Ile_{645}. In order to solve it, double coupling was performed. Amino acid Ile was added again without deprotecting the N-α-site of the previous amino acid, to insure that only the sites that did not react in the first time will react in the second. In order to increase the yield of the full-length peptide and to avoid the formation of deletion sequences uncoupled amino acids were capped, in this case, before the activation step. In general capping is performed after the coupling however, because of the double coupling at one single site, capping would have prevented it. Therefore capping was done before deprotecting, to act on the amino acid prior to the last one coupled. The idea was that the capping would yield a truncated sequence(s) (shortened peptide) but the truncated sequences usually differ considerably from the final peptide and could be readily separated. Capping was realized through a short treatment of the peptide resin with a large excess of a highly reactive acetic anhydride and pyridine. At the end of the capping step the reagents were removed and the resin was carefully washed before proceeding to the next deprotection step.

2.2.0.2 *Simultaneous Cleavage from the Resin / Side-Chain Deprotection*

Concentrated TFA (94% aqueous TFA) is the reagent to perform the final cleavage of the peptide from the resin together with the removal of the side chain protecting groups.

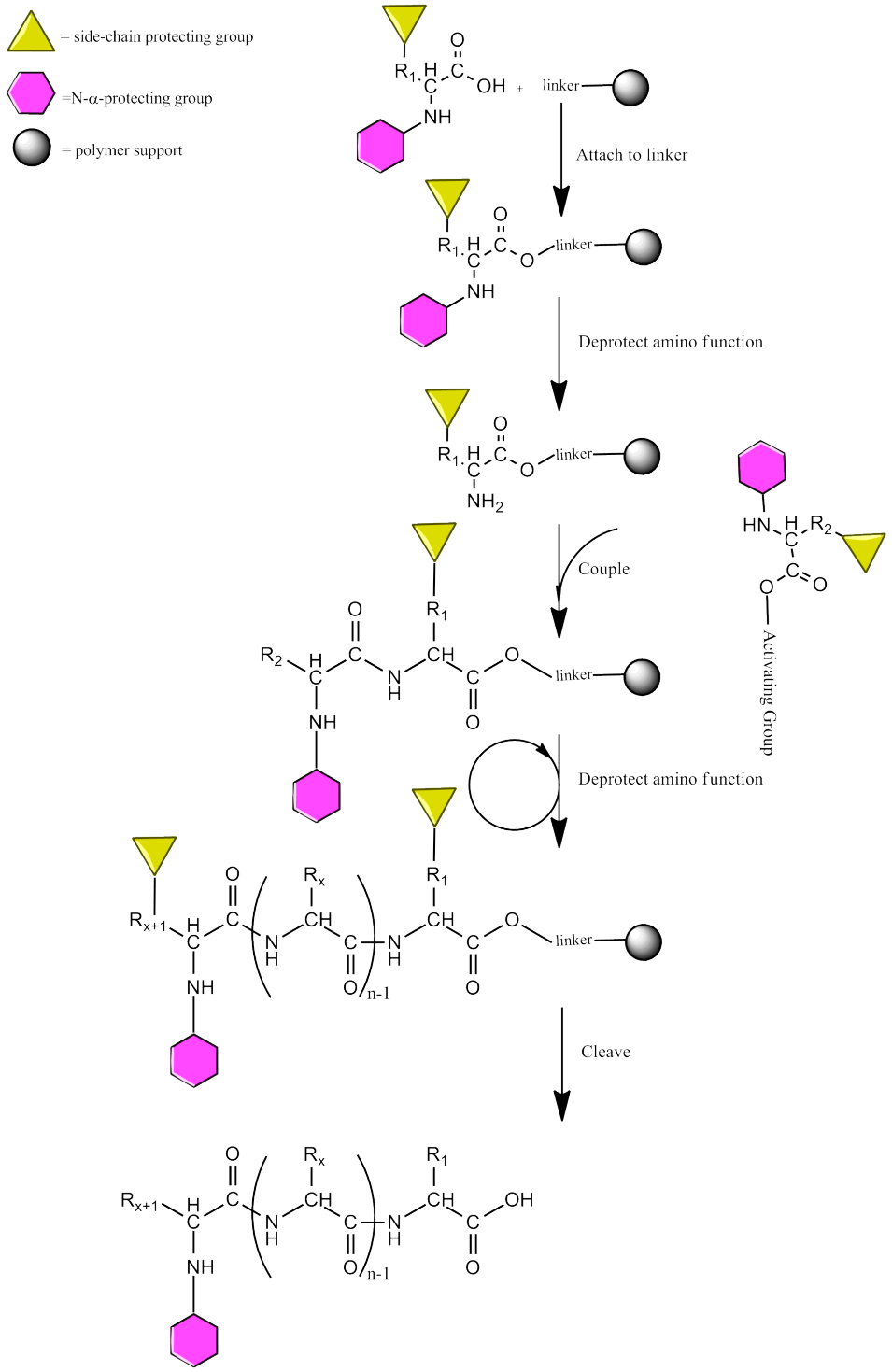

Figure 18: General scheme of SPPS. Reproduced from Novabiochem catalog (Merck Millipore).

During the reaction highly reactive carbocations are generated and it is necessary to trap them to avoid undesired reactions with sensitive amino acids such as Cys, Met, Set, Thr, Trp, Tyr (in our case Met, Thr). This effect is obtained by the addition of scavengers to the cleavage solution. The scavengers cocktail used included 2.5% of water, which is a moderately efficient scavenger (can be used as single scavenger for the cleavage of peptides devoid of Cys, Met and Trp) with 2.5% Ethanedithiol EDT, which is one of the most common and efficient scavengers for peptides containing sensitive amino acids. Also 1% of the silane derivative Triisopropylsilan (TIS) was added to the cocktail, as it shows good efficacy in quenching carbocations in sequences containing Arg and Trp residues. The cleavage reaction proceeded at room temperature for 4 hours.

2.2.0.3 *Peptide purification*

The cleaved peptide was separated from the resin with vacuum. The solvents were evaporated using rotary evaporator (B\"{U}CHI Labortechnik AG). The peptide was precipitated from the remaining solvent with cold diethyl ether. Centrifugation (Eppendorf 5804R, fixed-angle rotor F-34-6-38) for 20 min at 4° at rcf 15,550×g resulted in a white strong pellet, which was further washed under similar conditions until a relatively soft pellet formed (2-3 times). The pellet was dried in the air and then resuspended in a small volume of 4% acetic acid. The suspension was frozen in a liquid nitrogen and lyophilized (Finn Aqua, model LyoVac GT 2 E). The yield of the crude peptide varied between 60 % - 90 %.

Appropriate conditions for purification by high-performance liquid chromatography (HPLC) were found. Briefly, Isopropanol and 0.1 % Trifluoroacetic acid (TFA) were used as a mobile phase (buffer B) mixed with water and 0.1 % TFA (buffer A) using gradient of buffer B from 10 % to 60 % for 23 min at a flow-rate of 10 ml/min. All the solvents were of highest purity (HPLC grade, Sigma). Quality was assessed by matrix-assisted laser desorption/ionization (MALDI) with time-of-flight (TOF) mass spectrometer (Autoflex from Brücker Daltonics). The yield of the pure peptide varied between 10 % - 30 %.

2.3 LINEAR DICHROISM USING ATR-FTIR SPECTROSCOPY

Linear Dichroism (LD) is a spectroscopic technique that can be used with systems that are either intrinsically oriented, or can be oriented during an experiment by external forces. It gives information about conformation and orientation of structures within molecules. Recording LD spectra permits detection of several components underlying a broad amide band, in agreement with the results obtained by Fourier self-deconvolution. To measure LD the sample is oriented, then the difference in absorption of light linearly polarized parallel and per-

pendicular to the orientation axis is measured: $LD = A_{||} - A_{\perp}$ and it is that difference that indicates the degree of orientation.

Secondary structure determination and its orientation were evaluated as described in results and discussion chapter under experimental section of ssNMR study of amyloid precursor protein.

Part II

RESULTS AND DISCUSSION

3

RESULTS: CALCIUM IONS PROMOTE FORMATION OF AB(1-40) OLIGOMERS

Dysregulation of Ca^{2+} homeostasis in aging brains and in neurodegenerative disorders plays a crucial role in numerous processes and contributes to cell dysfunction and death. We postulated that calcium may enable or accelerate the aggregation of Aβ. Therefore, the aggregation pattern of Aβ(1-40) and of Aβ(1-40)E22G, an amyloid peptide carrying the Arctic mutation that causes early onset of the disease, were compared in the presence or the absence of Ca^{2+}.

3.1 PREFERENTIAL FORMATION OF OLIGOMERS OF Aβ(1-40) IN THE PRESENCE OF CA^{2+}.

3.1.1 *Experimental*

3.1.1.1 *Peptide preparation*

The amyloid β-peptides Aβ(1-40) and Aβ(1-40)E22G were purchased from American Peptide Company in the form of lyophilized powder. Prior to use, 1 mg aliquots were dissolved in double-distilled water, sonicated in a water bath for 1 min, and then held on ice for 1 min. This cycle was repeated five times. The peptide solution was then divided into 50-μg aliquots and dried under vacuum in a ThermoSavant SpeedVac (UVS400A Universal Vacuum System). Aβ films were stored at –20°C until use.

3.1.1.2 *Sample preparation*

The 50-μg aliquots of lyophilized Aβ peptide were hydrated at room temperature in either 50 mM phosphate buffer pH 7.4 and 100 mM NaCl ("$–Ca^{2+}$ condition") or 75 mM MOPS buffer (3-(N-morpholino) propanesulfonic acid) pH 7.4 and 2 mM $CaCl_2$ ("$+Ca^{2+}$ condition"). MOPS is an excellent buffer for many biological systems at near-neutral pH and was used here, because upon addition of $CaCl_2$ to phosphate buffer, an insoluble precipitant calcium phosphate is formed. There was no difference between the buffers on the properties and the aggregation profiles of Aβ peptides. The "$–Ca^{2+}$ condition" refers to the condition where no calcium was added to the buffer. However, residual calcium concentration (from doubly distilled MilliQ water) was 21 ± 1.3 μM, as was determined with inductively coupled plasma optical emission spectroscopy (ICP-OES). The final concentration of the peptide for all samples was 100 μM unless otherwise stated.

Samples were sonicated for 2 min in a water bath and incubated at 37°C without agitation.

3.1.1.3 *Western Blot analysis*

Polyacrylamide gel electrophoresis (PAGE) was used to separate different oligomeric species by size. Polyacrylamide gel consists of uniform pores, the size of which is controlled by varying the concentrations of acrylamide and bis-acrylamide used for gel preparation. First polyacrylamide gels were introduced in 1959 by Ornstein and Davis.

Aβ peptides samples were diluted in a PAGE sample buffer and separated on a 12% bis-Tris gel at 4°C for 2 h at 100 V. There was no SDS in the acrylamide gel, but the sample buffer contained 4% SDS. Unboiled samples were loaded on the gel. The separated bands of protein were transferred onto a nitrocellulose membrane, which was then blocked for 1 h in 5% nonfat dry milk in Tris-buffered saline (TBS)/Tween-20 buffer. The membrane was incubated with a mixture of two mouse monoclonal Aβ antibodies, 6E10 (1:3000) and 4G8 (1:2000) (Sigma-Aldrich). Detection was carried out by enhanced chemiluminescence using horseradish peroxidase-conjugated goat anti-mouse antibody (1:2000) (Boehringer Mannheim). Images were recorded and analyzed using the ImageQuant 400 gel imager and ImageQuant TL software (GE Healthcare).

3.1.2 *Results and discussion*

Samples of Aβ(1-40) and Aβ(1-40)E22G were prepared and incubated for 96 h in either the presence or the absence of 2 mM Ca^{2+}. At time points corresponding to t = 0, 2, 4, 6, 24, 72, and 96 h, samples were analyzed by electrophoresis in SDS-free polyacrylamide gel (0.1% SDS was present in the migration buffer) and imaged by Western blotting (Figure 19 on page 42). Over time, the aggregation pattern of Aβ(1-40) showed striking differences in the presence and in the absence of added Ca^{2+} (Figure 19 on page 42, panels A, C). Whereas after 24 h the range of oligomeric species in the samples with and without added Ca^{2+} was almost indistinguishable, at 72 h we observed a wide range of species in the presence of Ca^{2+}, but not in its absence. At 72 h and 96 h, Aβ(1-40) in the presence of Ca^{2+} contained monomers and oligomers whose molecular weights ranged from those consistent with dimers (around 8 kDa) to hexamers (Figure 19 on page 42, panel C, two last lanes). Additional streaks in the same lanes suggested the presence of oligomers of even higher molecular weight, though they were not clearly identified. In the same samples, protofibrils and apparently some fibrils were also detectable at the top portion of the gel. It was difficult to differentiate between these aggregates because of the low resolution in this part of the gel and their low electrophoretic mobility. Fibrils, because of their extremely high molecular weight,

do not penetrate into the separating part of the polyacrylamide gel; thus, when present, they appear as smears in the stacking portion of the gel. Though it is possible that fibrils are also present in this sample, the results of the following experiments (i.e. ThT fluorescence, AFM) do not support this possibility (see the relevant sections). In the absence of added Ca^{2+}, Aβ(1-40) molecules had aggregated to such an extent that we were able to detect only bands with low electrophoretic mobility corresponding mainly to high-molecular-weight oligomers, protofibrils and fibrils, located in or near the stacking part of the polyacrylamide gel (Figure 19 on page 42, panel A, two last lanes).

In contrast to Aβ(1-40), samples of Aβ(1-40)E22G showed no differences in their aggregation profiles in the presence or absence of added Ca^{2+} (Figure 19 on page 42, panels B, D), although incubated under the same conditions. Moreover, already at t = 0 h oligomers ranging from monomers to tetramers that were not present in Aβ(1-40) samples at the same time point were detected. From t = 24 h, an increase in the population of oligomers of low molecular weight as well as the appearance of high-molecular-weight oligomers in Aβ(1-40)E22G samples, in both conditions were observed. By t = 72 h and t = 96 h a wide range of oligomers, including protofibrils, could be seen. These findings clearly indicated that Ca^{2+} had no influence on the ability of Aβ(1-40)E22G to aggregate as expected, with the generation mainly of oligomers and protofibrils. A comparison of the results obtained for the two peptides thus clearly showed that in the presence of Ca^{2+} Aβ(1-40), like Aβ(1-40)E22G, aggregated to produce oligomers and protofibrils, whereas in the "–Ca^{2+}" condition fibrils were readily formed. The profile of oligomeric and protofibrillar species formed by Aβ(1-40) in the presence of Ca^{2+}, as detected by Western blot analysis, was essentially the same as that of Aβ(1-40)E22G in either condition.

3.2 Ca^{2+} inhibits formation of ThT-positive Aβ(1-40) species, but does not affect Aβ(1-40)E22G.

3.2.1 *Experimental*

3.2.1.1 *Thioflavin T fluorescence measurements*

The thioflavin T (ThT) (Sigma-Aldrich) fluorescence assay [Naiki et al., 1989] was used to follow the aggregation profile of Aβ peptides for 96 h using LS55 fluorimeter (Perkin Elmer Instruments). ThT is a benzothiazole dye that exhibits enhanced fluorescence upon binding to amyloid fibrils and is commonly used to diagnose amyloid fibrils, both *ex vivo* and *in vitro*. Upon binding of fibrils, ThT displays a dramatic shift of the excitation maximum (from 385 nm to 450 nm) and the emission maximum (from 445 nm to 482 nm) [Naiki et al., 1989]. Despite its widespread use in clinical and basic science applications, the molecular mechanism for the ability of ThT to recognize diverse

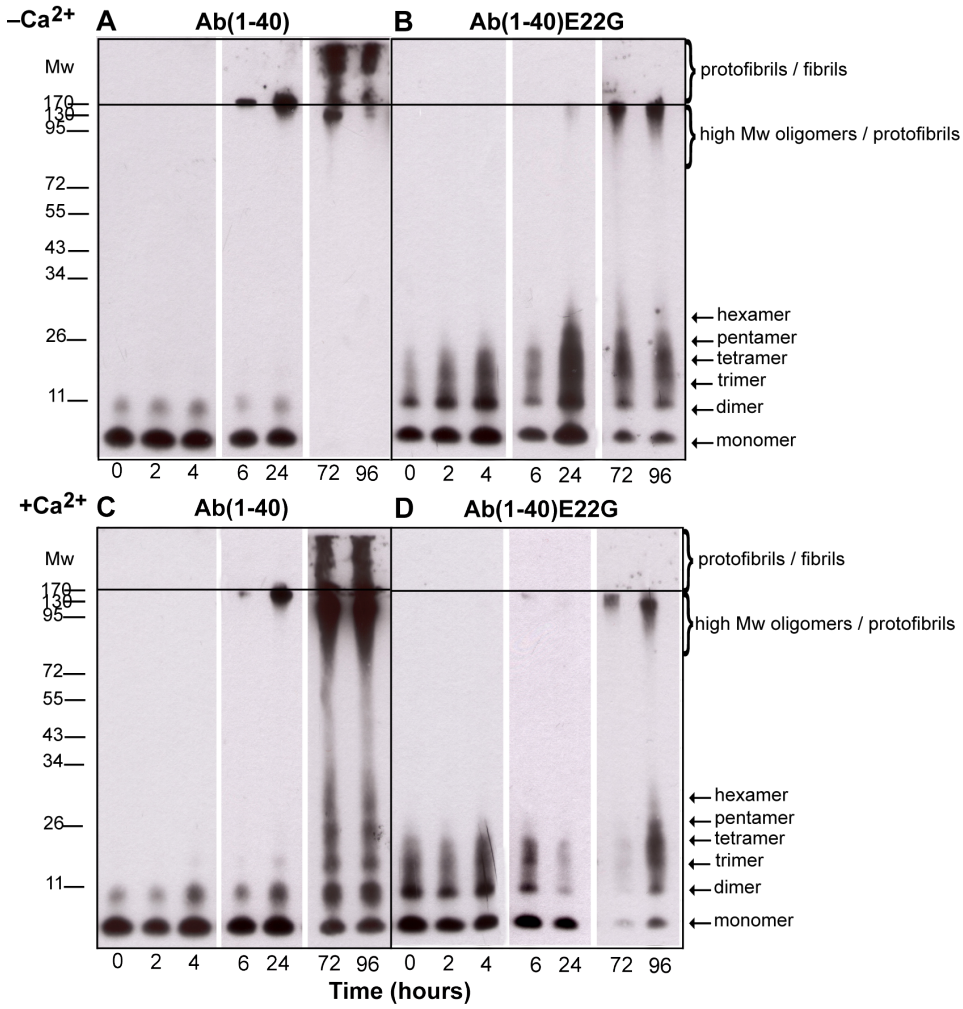

Figure 19: Aggregation profiles of Aβ(1-40) and Aβ(1-40)E22G during 96 h of incubation in the presence or absence of added Ca^{2+} were followed using Western blot analysis. Samples were separated using gel electrophoresis on a 12% bis-Tris gel. For each condition, samples were taken at t = 0, 2, 4, 6, 24, 72, and 96 h. Following the loading of 1 µg of protein sample into each lane, the membrane was probed with a mixture of monoclonal antibodies 6E10 and 4G8 that recognize residues 1-17 and 17-24, respectively. Panels A and B are representative Western blots of Aβ(1-40) and Aβ(1-40)E22G in phosphate buffer ("$–Ca^{2+}$ condition"), respectively. Panels C and D are representative Western blots of Aβ(1-40) and Aβ(1-40)E22G in 2 mM Ca^{2+} ("$+Ca^{2+}$ condition"), respectively. At least four separate experiments were carried out to confirm these results. All images were taken from a single 96-h experimental procedure.

types of amyloid fibrils and for the dye's characteristic fluorescence has only begun to be elucidated. The studies by Naiki et al. and LeVine [LeVine, 1993] showed that dye binding is linked to the presence of the cross-β structure of fibrils. Recent confocal microscopy studies of ThT aligned in stretched poly-vinyl alcohol films showed that the dye dipole excitation axis lies parallel to the long molecular axis. Therefore, ThT binds to amyloid fibrils such, that their long axes are parallel. It has been proposed that the binding occurs in 'channels' that run along the length of the β-sheet. Steric interactions between dye molecules and side chains indicate why ThT fluoresces more intensely when bound to amyloid fibrils and can explain why this interaction with amyloid fibrils is specific, but with varying efficiency [Krebs et al., 2005].

The experimental procedure was as follows: aliquots of 10 μl (~4 μg) of the incubated peptide solution were added to 1 ml of 50 mM glycine-NaOH buffer pH 8.5 and 5 μM ThT. The sample was maintained at 25°C in a circulating water bath. Excitation and emission wavelengths were 450 nm and 482 nm, respectively. The emission spectra were collected for 500 s. The intensity of each spectrum was then averaged over approximately 400 s, following subtraction of the averaged (100 s) background fluorescence.

3.2.2 *Results and discussion*

The increase in ThT fluorescence over time was used to follow fibrillogenesis of amyloid peptides Aβ(1-40) and Aβ(1-40)E22G in solution in the presence and absence of added Ca^{2+}. We found that Ca^{2+} inhibited the formation of ThT-positive species of Aβ(1-40), but had no effect on Aβ(1-40)E22G (Figure 20 on page 44).

A time-course study was performed during 96 h of incubation with or without Ca^{2+} for both peptides. In the case of Aβ(1-40), ThT fluorescence intensity did not change in either the presence or the absence of added Ca^{2+} and remained low for the first 6 h, demonstrating that after 6 h of incubation the predominant species are oligomers. This result is in agreement with the reported finding that ThT fluorescence clearly discriminates between oligomers and fibrils of Aβ [Benseny-Cases et al., 2007]. After 24 h of incubation, ThT fluorescence intensity was found to be increased significantly (about three fold) in the absence of added Ca^{2+} but only slightly in its presence. After 72 and 96 h of incubation the ThT fluorescence intensity in the absence of added Ca^{2+} increased dramatically, reaching values close to 500 arbitrary units. Control samples with known fibrillar content yielded similar fluorescence values (data not shown), leading to conclusion that fibrils were the main species in the sample. This conclusion is supported by a number of studies in which the characteristic fluorescence exhibited by ThT was attributed to the binding of ThT molecules within

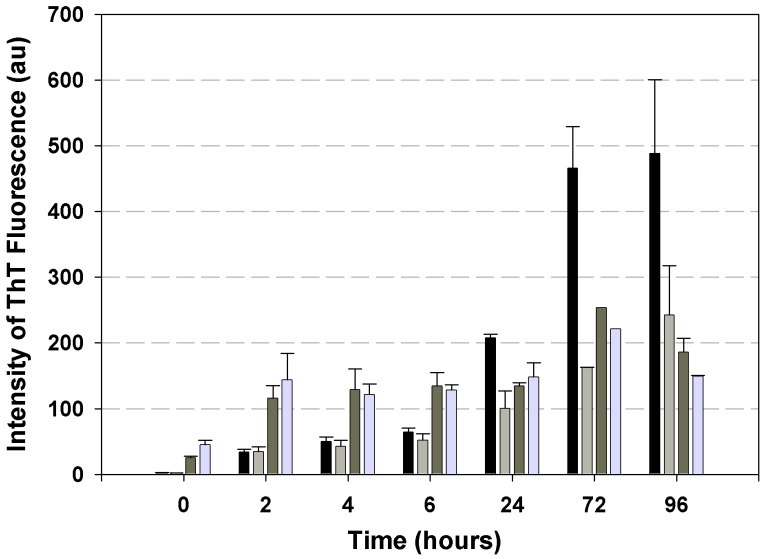

Figure 20: Oligomers and fibrils formation differentiated by ThT fluorescence. ThT fluorescence intensity was monitored to follow fibrillogenesis of Aβ(1-40) and Aβ(1-40)E22G in the presence and in the absence of 2 mM Ca^{2+}. Black bars, Aβ(1-40) in phosphate buffer ("–Ca^{2+} condition"); light grey bars, Aβ(1-40) in 2 mM $CaCl_2$; dark grey bars, Aβ(1-40)E22G in phosphate buffer; light blue bars, Aβ(1-40)E22G in $CaCl_2$. Shown are averages of values obtained in four independent experiments; error bars indicating the standard error of the average.

a cavity that was present in some proteins and amyloid fibrils, but not in others [Groenning et al., 2007, Krebs et al., 2005]. After 96 h of incubation of Aβ(1-40) in the presence of Ca^{2+}, fluorescence intensity values remained low and were attributed to the existence of only a small population of ThT-positive species.

By contrast Aβ(1-40)E22G, both with and without Ca^{2+}, exhibited stable and relatively low ThT fluorescence intensity over the course of 96 h (Figure 20 on page 44), implying either that the aggregation process is significantly slower than for Aβ(1-40) or that Aβ(1-40)E22G has a relatively high propensity to form oligomers rather than fibrils. A high tendency of Aβ(1-40)E22G to form oligomers and protofibrils has already been demonstrated in several studies [Lashuel et al., 2003, Nilsberth et al., 2001, Päiviö et al., 2004]. Moreover, it was suggested that this characteristic behavior may be responsible for the marked toxicity of Aβ(1-40)E22G [Whalen et al., 2005]. Individuals carrying the Arctic mutation are known to be prone to development of AD early in life [Nilsberth et al., 2001], possibly because of the formation of oligomers and protofibrils, considered to be more toxic aggregates of Aβ peptide than fibrils.

3.3 SIMILAR SECONDARY STRUCTURES FOR Aβ(1-40) AND Aβ(1-40)E22G OLIGOMERS IN THE PRESENCE OF CA^{2+}.

3.3.1 *Experimental*

3.3.1.1 *Fourier transform infrared (FTIR) spectroscopy measurements*

Infrared spectra were recorded on an Equinox 55 infrared spectrophotometer (Bruker Optics). The internal reflection element was a diamond crystal (2 × 2 mm) with an aperture angle of 45°, yielding a single internal reflection. The spectrometer was purged continuously with dried air. Spectra were obtained from 4000 cm^{-1} to 800 cm^{-1} at a resolution of 2 cm^{-1}. In order to achieve a good signal-to-noise ratio, 128 scans were acquired. All measurements were conducted at 24°C. Samples were prepared by spreading 2 µl of peptide solution on a diamond crystal surface and removing the excess fluid under nitrogen flow. The film was washed three times with milliQ water, which was then removed under nitrogen flow.

3.3.1.2 *Spectral analysis*

Data were processed using "Kinetics", a program developed in the laboratory of Prof. E. Goormaghtigh and running under MatLab. Briefly, spectra were subjected to water-vapor subtraction using a reference water vapor spectrum, and to a smoothing procedure to 4 cm^{-1}. Spectra were deconvoluted using the Lorentzian deconvolution function and the Gaussian apodization function. A linear baseline was subtracted from all spectra at 1708, 1602, and 1482 cm^{-1}.

3.3.2 *Results and discussion*

Secondary structures of Aβ aggregates are known to possess high β-sheet content. Using ATR-FTIR spectroscopy, our group recently showed that a characteristic signature of soluble oligomers of Aβ is an anti-parallel β-sheet conformation, whereas parallel β-sheet conformation is indicative of the presence of Aβ fibrils [Cerf et al., 2009, Chirgadze and Nevskaya, 1976]. Working with Aβ(1-42) and Aβ(1- 40), they demonstrated that in anti-parallel β-sheet structures the amide I region displays two typical components: the major component has an average spectral wavenumber at ~1630 cm^{-1} while the minor component, about five fold weaker than the major one, is characterized by an average wavenumber at ~1695 cm^{-1}. For parallel β-sheet structures the amide I region displays only the major component of ~1630 cm^{-1}. The intensity ratio of 1695/1630 was suggested to be proportional to the percentage of anti-parallel β-strands arranged in a β-sheet [Goormaghtigh et al., 1994].

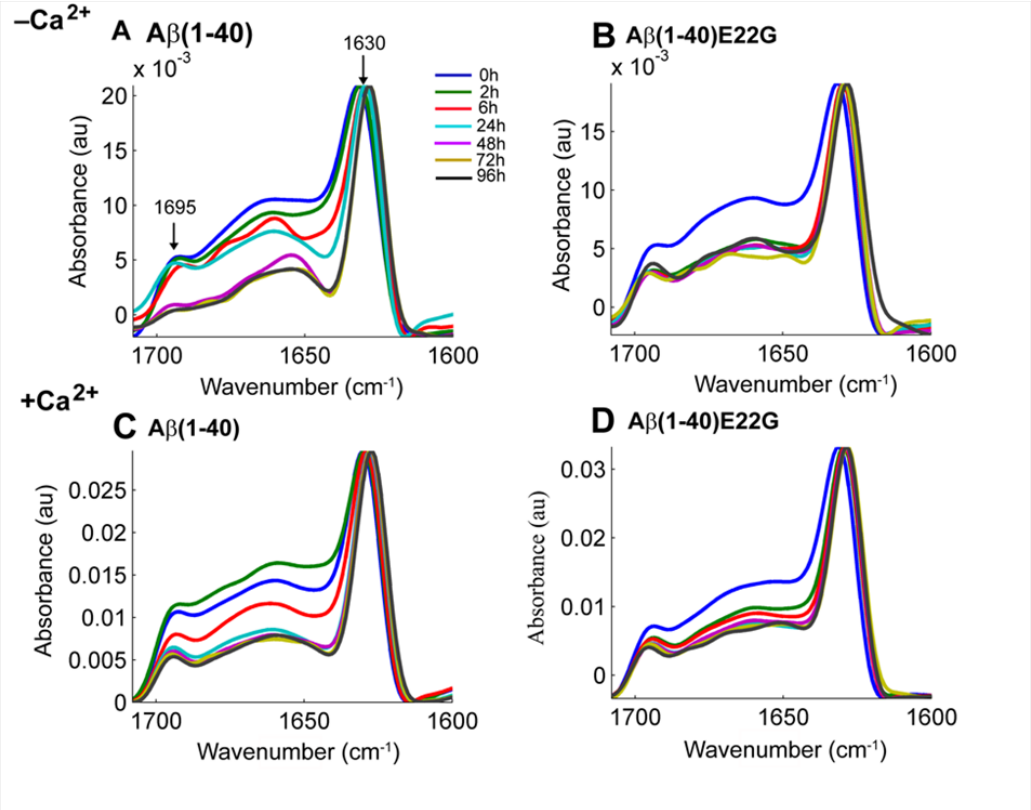

Figure 21: ATR-FTIR spectra of Aβ(1-40) and Aβ(1-40)E22G. FTIR spectra of Aβ(1-40) and Aβ(1-40)E22G were taken in the presence and in the absence of added Ca^{2+}, showing the amide I region of the spectra (1600–1700 cm^{-1}). Aliquots of 2 µl were taken from each sample at t = 0, 2, 6, 24, 48, 72, and 96 h (shown in blue, green, red, cyan, purple, mustard, and dark blue, respectively). The data shown here were collected in one continuous experiment and are representative of three independent trials.

Using ATR-FTIR, the aggregation patterns of Aβ(1-40) and Aβ(1-40)E22G were studied and the evolution of 1630-cm^{-1} and 1695-cm^{-1} peaks was followed to assess the presence of oligomers or fibrils as a function of incubation time, based on discrimination of a β-sheet conformation. Figure 21 on page 46 summarizes the results observed for each of these amyloid peptides in the presence and in the absence of added Ca^{2+}.

For all conditions evaluated, during the first 48 h two characteristic features were observed: one peak at ~1695 cm^{-1} and another at ~1630 cm^{-1} (Figure 21 on page 46, panels A–D). The presence of a peak at ~1695 cm^{-1} in the infrared spectrum, in addition to a peak at ~1630 cm^{-1}, is characteristic of an anti-parallel β-sheet conformation, indicative of species structurally different from fibrils [Cerf et al., 2009, Chirgadze and Nevskaya, 1976]. However, for Aβ(1-40) in the absence of added Ca^{2+} a significant decrease in the ~1695 cm^{-1} peak at t = 48 h (Figure 21 on page 46, panel A) and a shift towards lower wavenum-

bers and narrowing of the ~1630 cm^{-1} peak were observed. This shift (from 1633 cm^{-1} to 1629 cm^{-1}) and narrowing were also detectable to some extent at earlier time points. This specific feature indicated formation of stable and/or long β-strands and strong hydrogen bonds, as would be expected for a stable fibrillar structure [Dahlgren et al., 2002]. Given that the ratio of 1695/1630 is proportional to the percentage of anti-parallel arrangement of β-strands [Goormaghtigh et al., 1994], it was used to estimate the degree of structural change in the samples. For Aβ(1-40) in the "–Ca^{2+} condition" the 1695/1630 ratio decreased dramatically from 0.32 at t = 0 h to 0.08 at t = 96 h, meaning that there was four times less anti-parallel β-sheet structure after 96 h of incubation in the absence of added Ca^{2+}. This pattern of decrease in the amount of anti-parallel β-strands in a β-sheet points to the formation of fibrillar assemblies from oligomers initially present in the sample. This result complements the outcome of the PAGE analysis and the ThT fluorescence experiments, where after the first 24 h mainly oligomers whose binding affinity for ThT was low were detected, whereas at t = 96 h the species observed by PAGE were mainly of high molecular weight (including fibrils), which were highly ThT positive. This result for Aβ(1-40) in phosphate buffer portrayed a dynamic process of fibrillization of the Aβ(1-40) peptide *in vitro*, starting with monomers and dimers, which over time were converted into fibrils. It was interesting to note that at t = 72 h and t = 96 h, no monomers, dimers, or other low-molecular-weight oligomers were visible on Western blots (Figure 19 on page 42), indicating complete conversion to fibrils. The behavior of Aβ(1-40) samples in the presence of Ca^{2+} differed from their behavior in the absence of added Ca^{2+}. Throughout the duration of the experiment with Aβ(1-40) in the presence of Ca^{2+} we always observed the two characteristic peaks at ~1695 cm^{-1} and ~1630 cm^{-1} (Figure 21 on page 46, panel C). Despite the slight decrease observed over time in the intensity of the ~1695 cm^{-1} peak, no significant narrowing of the peak width at ~1630 cm^{-1} was detected. An interesting observation was that this spectral behavior of Aβ(1-40) in the presence of Ca^{2+} had the same features as that of Aβ(1-40)E22G in either the presence or the absence of Ca^{2+}. Under both conditions, the peaks exhibited by Aβ(1-40)E22G at ~1695 cm^{-1} and at ~1630 cm^{-1} throughout the 96-h time period were characteristic of an anti-parallel β-sheet conformation (Figure 21 on page 46, panels C, B, D), and the ratio between the peaks changed only slightly, mainly after the first 2 h. In addition, no narrowing of the peak at ~1630 cm^{-1} was detected. This finding, obtained by ATR-FTIR, showed good correlation with the results obtained by PAGE analysis and by ThT fluorescence experiments, all of which pointed—as expected, and in line with the published data [Päiviö et al., 2004, Whalen et al., 2005]—to the formation of a wide range of oligomers and possibly also protofibrils by Aβ(1-40)E22G. The similarity in aggregation patterns of Aβ(1-40) in the "+Ca^{2+} condition"

and of Aβ(1-40)E22G under both conditions, as observed here by three independent techniques, raises a fundamental question concerning a possible change in the mechanism of Aβ(1-40) aggregation when Ca^{2+} is present. It seems that calcium ions promote the preferential formation of oligomers and protofibrils, diverting the otherwise favored fibrillogenesis pathway.

3.4 MORPHOLOGICAL SIMILARITY BETWEEN Aβ(1-40) AND Aβ(1-40)E22G SPECIES FORMED IN THE PRESENCE OF CA^{2+}.

3.4.1 *Experimental*

3.4.1.1 *Atomic force microscopy (AFM)*

AFM experiments were conducted by Dr. Vincent Dupres as a part of collaboration with the laboratory of Prof. Yves F. Dufrêne (Université catholique de Leuvain, Unité de Chimie des Interfaces, Belgium). AFM contact mode images were obtained at room temperature with a Nanoscope IV Multimode AFM (Veeco). Fresh mica surfaces (36 mm^2) were glued onto steel sample discs (Veeco) with Epotek 377 (Gentec Benelux). Atomically smooth surfaces were generated by cleaving layers with adhesive tape. Peptide solution (100 µl; 0.1 mg/ml) was adsorbed onto bare mica surfaces for 1 h. The mounted samples were immediately transferred into the AFM liquid cell, while avoiding dewetting. They were then imaged with oxide-sharpened microfabricated Si_3N_4 cantilevers (Microlevers, Veeco) with minimal applied force (<500 pN). The spring constants of the cantilevers measured by the thermal noise method (Picoforce, Veeco) were 0.011 N/m. Images (5 µm × 5 µm) were obtained from several areas on each sample.

3.4.2 *Results and discussion*

Here we examined whether the oligomers formed by Aβ(1-40) in the presence of Ca^{2+} and the oligomers formed by Aβ(1-40)E22G in the presence and in the absence of added Ca^{2+} share morphological similarities. Using contact mode AFM, oligomerization and fibrillogenesis of Aβ(1-40) and of Aβ(1-40)E22G were followed, in all cases in the presence and absence of added Ca^{2+}, at three time points: t = 0, 6, and 72 h (Figure 22 on page 49).

These times were chosen because most of the differences detected by Western blot analysis, ThT fluorescence, and ATR-FTIR spectroscopy were observed after 0, 6, and 72 h of incubation. At t = 0 h, samples of Aβ(1-40) and of Aβ(1-40)E22G, both in the presence and in the absence of added Ca^{2+}, contained homogeneously distributed globular particles (Figure 22 on page 49, panels A, D, G, J), in agreement with previously reported data [Haass and Selkoe, 2007]. The height of the

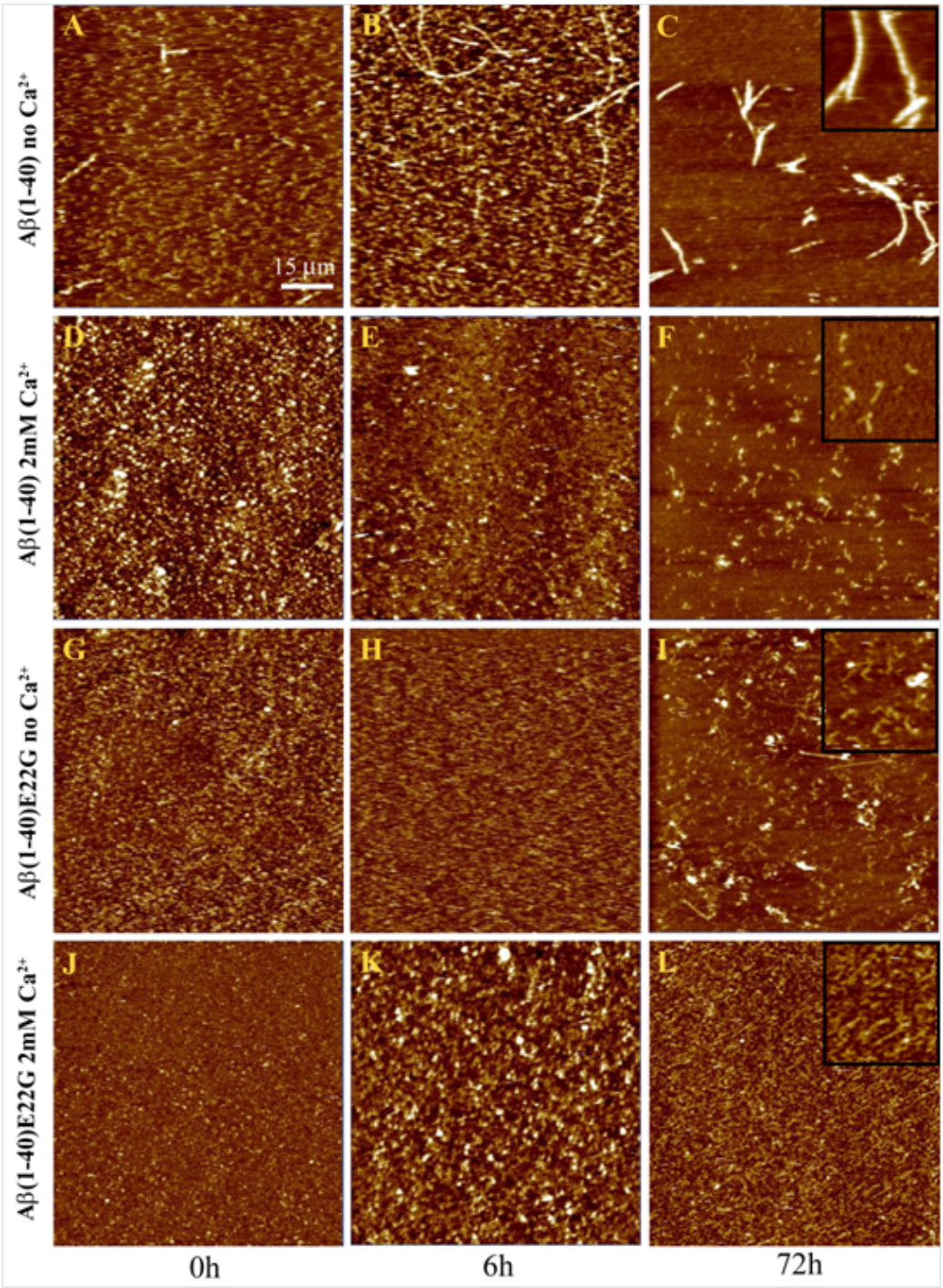

Figure 22: Morphological comparison of Aβ(1-40) and Aβ(1-40)E22G. Contact mode AFM images (5 µm × 5 µm, Z scale 15 nm) of Aβ(1-40) and Aβ(1-40)E22G peptides on mica, recorded either in phosphate buffer or in MOPS buffer with Ca^{2+}. Samples of Aβ(1-40) and Aβ(1-40)E22G in the presence and absence of added Ca^{2+} (marked as "+Ca^{2+}" or "–Ca^{2+}", respectively) at t = 0, 6, or 72 h. Closer views (1 µm × 1 µm, Z scale 15 nm) of oligomers, protofibrils and fibrils are shown as insets in the panel of t = 72 h (C, F, I, L). Images A, D, G, J were taken at t = 0; images B, E, H, K were taken at t = 6 h. Peptide concentration was the same in all samples.

spherical aggregates was 2.8 ± 0.3 nm (n = 51). Although some linear aggregates were detected in Aβ(1-40) samples in the absence of added Ca^{2+} (Figure 22 on page 49, panel A), most of the population consisted of globular particles. Since no contribution was seen from the linear aggregates when these samples were tested with other techniques, it seems reasonable to assume that only an insignificant percentage of the peptide was present in the linear aggregate form (perhaps structurally different from fibrils) at the initial stages of incubation. Notably, this population was observed only in the Aβ(1-40) samples lacking Ca^{2+}, even though all the samples received identical treatment. A second batch of samples was imaged at t = 6 h. As expected, no differences in aggregate morphology were noticed between the Aβ(1-40) samples in the presence of Ca^{2+} and the Aβ(1-40)E22G samples in the presence or absence of added Ca^{2+} (Figure 22 on page 49, panels E, H, K). All of the particles appeared to be globular, though somewhat larger than at t = 0 h (height 3.3 ± 0.5 nm, n = 20). Evolution of the species was observed only with Aβ(1-40) in the absence of added Ca^{2+}. In this case there was clear evidence of fibrillization, resulting in a large amount of string-like aggregates and a long, fibril-like species (Figure 22 on page 49, panel B). Although comparable in length (950 ± 460 nm, n = 20) to previously reported fibril lengths [Haass and Selkoe, 2007], they were too thin to be categorized as fibrils. The string-like structures had become more abundant, and the fraction of spherical particles that remained was small (Figure 22 on page 49, panel B). The most striking differences were those observed between samples imaged at t = 72 h. The Aβ(1-40) samples without Ca^{2+} exhibited well-organized fibrils (Figure 22 on page 49, panel C) whose dimensions (height 8.4 ± 0.5 nm, n = 13; width 124 ± 15 nm, n = 12; length 1 ± 0.6 μm, n = 67) mostly correlated with those previously published for Aβ(1-40) [Dahlgren et al., 2002]. When Aβ(1-40) was incubated in the presence of Ca^{2+} the resulting aggregates were not fibrillar, but rather spherical (height, 2.6 ± 0.4 nm; n = 24) and (mostly) curvilinear (Figure 22 on page 49, panel F) (height 3.0 ± 0.5 nm; n = 28; length 250 ± 73 nm; n = 40), which previous authors have referred to as oligomers and protofibrils, respectively [Lashuel et al., 2003]. Like the results described above and therefore in line with our expectations, Aβ(1-40) in the presence of Ca^{2+} and Aβ(1-40)E22G both in the presence and in the absence of added Ca^{2+} all formed the same oligomeric species: initially spherical particles, evolving to curvilinear structures after 72 h. These values are consistent with the data from [Mastrangelo et al., 2006], where the authors reported *z*-heights of 2-3 nm on average, for early (<1 h) oligomers and ~2 nm for monomers of Aβ(1-42) obtained by high resolution AFM under hydrated conditions. Detailed analysis of their results revealed that for low molecular weight oligomers as well as protofibrils the z-height ranged between 2 to 4 nm. Only for some of the high molecular weight oligomers Mastrangelo et

al. reported values of *z*-height 4 – 6 nm. It is likely that Aβ(1-40) and Aβ(1-42) do not form the same type of high molecular weight oligomers and the growth of Aβ(1-40) oligomers might be restricted to the lateral dimension, without causing height changes from monomers to oligomers. In the presence of Ca^{2+}, the aggregation pathway of Aβ(1-40) was clearly shifted towards formation of oligomers, and not of fibrils as occurred in the absence of added Ca^{2+}. Evidently, therefore, the presence of calcium ions has a significant impact on the aggregation process of Aβ(1-40).

Using four different techniques, it was shown that Aβ(1-40) forms oligomers and protofibrils in the presence of 2 mM Ca^{2+} similar to those produced by Aβ(1-40)E22G both in the presence and in the absence of added Ca^{2+} (21 μM of calcium ions were present in "–Ca^{2+} condition" buffer due to their traces in MilliQ water and in HPLC-grade buffer). In the "–Ca^{2+} condition" Aβ(1-40) readily formed fibrils, which were detectable by PAGE and by ThT fluorescence analysis as well as by FTIR, and differences in secondary structures were observed between oligomers and fibrils. Moreover, AFM imaging clearly revealed morphological similarities between oligomers of Aβ(1-40) and of Aβ(1-40)E22G, all of which were spherical or curvilinear in shape. Aβ(1-40)E22G has been shown to form oligomers and protofibrils *in vivo* and to cause early and severe signs of AD in mice [Isaacs et al., 2006]. It remains an open question whether the morphological similarity of oligomers of Aβ(1-40) formed in the presence of Ca^{2+} to oligomers of Aβ(1-40)E22G formed also in the absence of added Ca^{2+} implies that they have similar toxic effects. Previous studies of the role of Ca^{2+} in Aβ aggregation have revealed acceleration of Aβ(1-42) fibril formation in the presence of Ca^{2+} [Ahmad et al., 2009, Kuroda and Kawahara, 1994], but without acceleration in the kinetics of Aβ(1-40) fibrillization [Kuroda and Kawahara, 1994]. The focus of the present study however, was the role of Ca^{2+} in the formation of oligomers, rather than in fibril formation. It was shown that calcium can facilitate the formation of oligomers that might in turn be held responsible for neuronal toxicity.

There are numerous literature reports on the influence of a variety of divalent ions on Aβ aggregation. Aluminum and iron were reported to promote the aggregation of Aβ at physiological concentrations [Dyrks et al., 1992]. Kuroda et al. found that aluminum enhances the aggregation of Aβ(1-40) peptides, although no mechanism was proposed [Kuroda and Kawahara, 1994]. There exist conflicting statements about the role of Zn^{2+} and Cu^{2+} ions in Aβ aggregation. It was reported that Zn^{2+} induced the aggregation of Aβ [Bush et al., 1994, Brown et al., 1997, Esler et al., 1996], while Cu^{2+} dramatically induced Aβ aggregation under acidic conditions [Atwood et al., 1998]. In contrast, Yoshiike et al. showed that both Zn^{2+} and Cu^{2+} reduced cytotoxic-

ity by inhibiting Aβ aggregation. The authors found that Cu^{2+} both facilitates oxidative stress, through its interaction with soluble Aβ, and results in the formation of a precipitated complex that is less toxic than Aβ fibrils, while Zn^{2+} inhibits Aβ aggregation by inducing the formation of non-fibrillar, non-toxic aggregates [Yoshiike et al., 2001]. In contrast, in the presence of sodium dodecyl sulfate (SDS) Cu^{2+} promotes and stabilizes the formation of the non amyloidogenic soluble oligomeric β-sheet structures [Tew et al., 2008].

X-ray absorption spectroscopy studies suggest significant differences in the geometrical structure around the metals in Cu^{2+}-Aβ and Zn^{2+}-Aβ complexes. The observed differences suggest a different role played by the two ions. Stellato and coworkers [Stellato et al., 2006] have found that the coordination mode of the metal in the Cu^{2+}–Aβ40 complex, with three histidine residues and a tyrosine residue, is compatible with an intra-peptide coordination mode in agreement with the model suggested in [Suzuki et al., 2001]. In contrast, the coordination mode of the Zn^{2+} ion is such, that it prefers inter-peptide aggregation, although under specific conditions an open mode binding–where one zinc ion is bound to one histidine residue–is also possible [Stellato et al., 2006].

There is evidence that Cu^{2+} induces structural changes in Aβ(1-40) peptide with increases in β-sheet content. Presence of metal ions such as Cu^{2+} and Zn^{2+} appear to also modify the effect of Aβ on model lipid membranes [Lau et al., 2006].

Recent work by Danielsson et al. on the structural aspect of metal binding site or sites in Aβ shows that the high-affinity zinc-binding site is formed by three histidines and the N-terminus, whereas a second, low-affinity binding site, comprises residues 23–28 [Danielsson et al., 2007]. Their results show that Zn^{2+} and Cu^{2+} compete for the same high-affinity binding site and have a putative second weaker binding site. NMR and fluorescence experiments showed a selective zinc-binding site with His6, His13 and His14 and the N-terminal Asp1 as ligands, while Tyr10 is not directly involved in the binding, but is located close to the bound metal [Danielsson et al., 2007]. The authors propose a second binding site for Zn^{2+}, which involves residues 23, 24, 26 and 28. While for Cu^{2+} no precise binding site could be outlined apart from residue 21, which showed a loss of intensity in the NMR spectrum indicating that a central region might to be involved.

Neuronal calcium-binding proteins such as parvalbumin from cod muscles, alpha-lactalbumin from cow milk, calmodulin from bovine brain and neuronal calretinin were shown to bind Zn^{2+} and Cu^{2+} ions, which compete for the binding site distinct from that of Ca^{2+} and Mg^{2+} [Permiakov et al., 1988, Nair et al., 2010]. This indicates that for many proteins Ca^{2+} -binding site is distinct from that of Zn^{2+} and Cu^{2+}. Therefore, it is reasonable to assume that also for the Aβ(1-40)

peptide, Ca^{2+}-binding site differs from the binding site of Zn^{2+} and Cu^{2+}, which was shown to involve the three histidine residues.

Nair et al. found that glutamic acid and aspartic acid are relatively inefficient in metal ion binding when investigating Cu^{2+}, Zn^{2+} and Fe^{2+} binding efficiencies [Nair et al., 2010]. Yet, Ca^{2+}-binding sites in proteins are largely formed by ligand oxygen atoms from the side chains of charged carboxyl residues (i.e., Asp and Glu), main chain carbonyl, and solvent water molecules. For Ca^{2+}-binding proteins (CaBPs) there are significant variations in Ca^{2+} coordination properties, which correlate with the diversified biological functions of CaBPs with different binding affinities and Ca^{2+}-induced conformational change. It has been shown that glutamic acid residues are the main mediators of Ca^{2+} binding in human serum amyloid P (SAP) [Thompson et al., 2002]. Interestingly, SAP is a normal plasma protein, which exhibits universal association with amyloid fibrils in all types of amyloidosis [Pepys et al., 1997]. Isolated human SAP, in the presence of Ca^{2+}, auto-aggregated and precipitated in an interaction for which glutamic acid residue is critical and was inhibited by all of the known Ca^{2+}-dependent ligands recognized by SAP [Pepys et al., 1997, Thompson et al., 2002]. This clearly suggests that Ca^{2+}-binding site is involved in amyloid recognition and that Ca^{2+}-binding site in Aβ probably involves Glu and/or Asp residues. The results of our study showed that Glu22 plays a role in Ca^{2+} binding (mutation of Glu to Gly changes the aggregation profile of the peptide) and might comprise a Ca^{2+}-binding site. Further studies are needed in order to elucidate the Ca^{2+}-binding site of Aβ(1-40) peptide. Liquid NMR can be used to differentiate the residues involved in calcium binding. Molecular dynamics can also be helpful in establishing a proof of concept for Ca^{2+} involvement in oligomers formation.

4

RESULTS: SSNMR AND ATR-FTIR STUDY OF AMYLOID PRECURSOR PROTEIN

Three APP_TM4K (628-655) peptides were chemically synthesized using SPPS. Global secondary structure of the APP_TM4K peptide reconstituted into POPC lipid bilayers and the peptide orientation (i.e. transmembrane or in-plane) were studied by FTIR spectroscopy.

Different schemes of isotopic labels were introduced into the APP_TM4K peptides for ssNMR investigation: ^{15}N-Gly-637 / ^{2}H-Ala-642, ^{15}N-Ala-642 / ^{2}H-Ala-630, and ^{15}N-Val-646 / ^{2}H-Ala-630. Conformational details of the TM segment were studied by ^{15}N and ^{2}H ssNMR techniques. Proton-decoupled ^{15}N chemical shift is a good indicator of the helical tilt angle as it exhibits a direct functional relationship with the alignment of the main axis of α-helical polypeptides [Bechinger and Sizun, 2003]. Nevertheless, ^{15}N measurements remain rather insensitive to rotation of the peptide around the helix axis (rotational pitch angle) therefore, a complementary ^{2}H ssNMR spectroscopy was used. Alanine residues (630 and 642) were labeled with ^{2}H as its methyl group offers some distinct advantages over other amino acids (please refer to the Chapter 2, 2.1.1.1). ^{15}N measurements allow us to determine the orientation of α-helical peptides, while through ^{2}H measurements we can refine this information and follow the dynamics of the peptide. Orientational constrains from these experiments constitute the tilt and the pitch angles of the peptide helix with respect to the membrane normal.

4.1 ATR-FTIR MEASUREMENTS OF APP_TM4K

4.1.1 *Experimental*

4.1.1.1 *Sample preparation*

APP_TM4K peptide was dissolved in HFIP (Sigma) to a final concentration of 2 mg/ml. This solution was mixed with POPC lipids (Avanti Polar Lipids, Alabaster, AL) dissolved in chloroform (Sigma) to obtain the peptide to lipid ratio of 1:50. The solvents were evaporated and the sample was spread on the surface of germanium plate. At this point oriented thin multilayer films were formed.

4.1.1.2 *Recording of the spectra*

Attenuated total reflection infrared (ATR-FTIR) spectra were recorded on a Bruker IFS 55 infrared spectrophotometer equipped with a liquid-

nitrogen-cooled MCT detector. The internal reflection element was a germanium ATR plate (50 × 20 × 2 mm) with an aperture angle of 45°, yielding 25 internal reflections. A total of 128 scans were accumulated for each spectrum to improve the signal/noise ratio. Spectra were recorded at a nominal resolution of 2 cm^{-1}. The spectrophotometer was continuously purged with dried air. All the measurements were done at 24°C.

4.1.1.3 *Secondary Structure Determination*

Fourier self-deconvolution was applied to increase the resolution of the spectra in the amide I region, which is the most sensitive to the secondary structure of proteins. The self-deconvolution was carried out using a Lorenzian line shape for the deconvolution and a Gaussian line shape for the apodization. To quantify the area of different components of amide I revealed by the self-deconvolution, a least square iterative curve fitting was performed to fit Lorenzian line shapes to the spectrum between 1700 and 1600 cm^{-1}. Prior to curve fitting, a straight base line passing through the ordinates at 1700 and 1600 cm^{-1} was subtracted. To avoid introducing artifacts, the fitting was done on the non-deconvoluted spectrum. The proportion of a particular structural element is computed to be the sum of the area of all the fitted Lorenzian bands with their maximum in the frequency region concomitant with that particular structure divided by the area of all the Lorenzian bands having their maximum between 1689 and 1615 cm^{-1} [Goormaghtigh and Ruysschaert, 1990].

4.1.1.4 *Orientation of the secondary structure*

For the amount of material used in this experiment, the thickness of the deposited film was considered to be small compared to the IR wavelength. Therefore, the "thin film" approximation was used in establishing the equations describing the dichroic ratio as a function of the orientational order parameter [Goormaghtigh and Ruysschaert, 1990]. The potential energy distribution of amide I consists of about 80% ν(C=O), 10% ν(C–N), and 10% δ(N–H). In an α-helix, the main transition dipole moment lies approximately parallel to the helical axis, while in an anti-parallel β-sheet, the polarization is predominantly perpendicular to the long axis. It is therefore possible to determine the mean orientation of the α-helix and β-sheet structures from the orientation of the peptide bond C=O group [Goormaghtigh and Ruysschaert, 1990].

Spectra were recorded with incident light polarized parallel (0°) or perpendicular (90°) relative to the plane of the IRE (the Ge plate). The dichroic spectrum is the difference between the spectra recorded with parallel and perpendicular polarizations. A larger absorbance for the parallel polarization (upward deviation on the dichroism spectrum)

indicates a dipole oriented preferentially near the normal of the ATR plate. Conversely, a larger absorbance for the perpendicular polarization (downward deviation on the dichroism spectrum) indicates a dipole oriented approximately parallel to the ATR plate.

Polarization was expressed as the dichroic ratio $R_{atr} = A^{90°}/A^{0°}$ and the mean angle between the helix axes and a normal to the ATR plate surface was then calculated. In these calculations, an angle of 27° between the long axis of the α-helix and the C=O dipole moment was considered [Goormaghtigh and Ruysschaert, 1990, Goormaghtigh et al., 1994, Fringeli and Gühnthard, 1981].

The lipid (POPC) ester stretch ν(C=O) vibrations at 1738 cm^{-1} was used to characterize the lipids acyl chains orientation.

4.1.2 *Results*

To investigate the global secondary structure of the APP_TM4K peptide reconstituted into membrane bilayers, the alignment of the lipids and the peptide in the sample and to asses the overall peptide orientation in the lipid membrane (i.e. transmembrane or in-plane), FTIR spectroscopy experiments were performed. The amide I region of the spectrum (1700 - 1600 cm^{-1}) reveals a symmetric peak with a maximum at 1653 cm^{-1} characteristic of a helical structure (Figure 23 on page 58). Fourier self-deconvolution revealed several components within the amide I region, which were quantified by an iterative least square (i.e. non-linear) curve fitting procedure following [Goormaghtigh and Ruysschaert, 1990]. The calculated content of helical secondary structure is about 74 % and 18 % of random coil and turns, respectively.

The amide I region of the spectra was used to determine the orientation of the α-helix of APP_TM4K relative to the POPC hydrocarbon chains of the bilayer. A dichroic spectrum of the amide I band is strongly 90° polarized, as seen from the positive deviation located in the helix region of the amide I band (Figure 23 on page 58, black trace), indicating an orientation of the α-helix perpendicular to the germanium plate and therefore parallel to the acyl chains of the lipids. A quantitative estimation of the helix orientation was obtained computing the isotropic dichroic ratio (using the lipids ν(C=O) band at 1738 cm^{-1} as a reference band [Bechinger et al., 1999b]) was found to be 1.16 and for the amide I component 1.74, thus the estimated tilt angle relative to the normal of the germanium plate is 25°. When only the helical component was analyzed the tilt angle was found to be 20°. The orientation of lipids acyl chains was also assessed. The lipid dichroic ratio for the band at 2872 cm^{-1} ($\nu s(CH_3)$) was found to be 3.71 (data not shown), and accordingly the tilt angle between acyl chains and the normal of the germanium crystal is 20-25°. This indicates that the APP_TM4K peptide can be reconstituted into POPC bilayers in a non-aggregated mostly helical TM orientation.

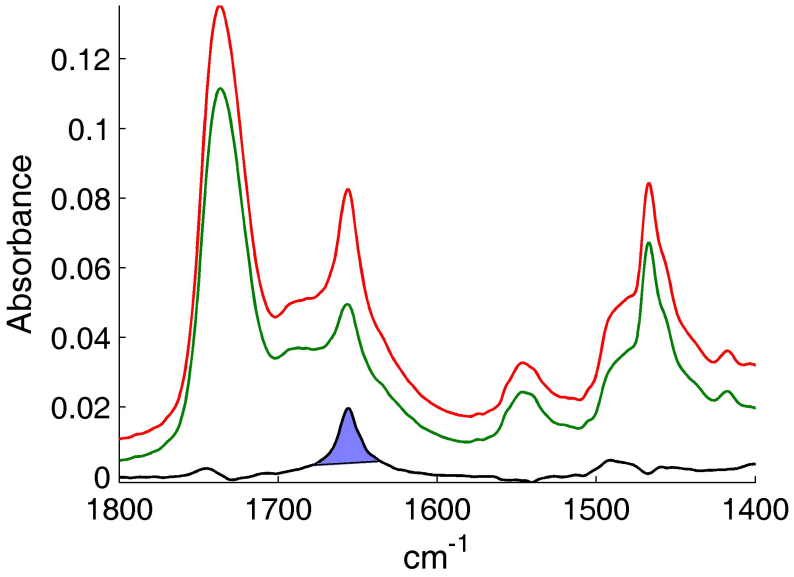

Figure 23: IR spectra of APP_TM4K in POPC bilayers. The spectrum in red was obtained with 90° polarized light. The spectrum in green was obtained with 0° polarized light. Spectrum in black is the difference between the red and the green spectra.

4.2 POLYACRYLAMIDE GEL ELECTROPHORESIS (PAGE) ANALYSIS

4.2.1 *Experimental*

Native bis-Tris gel was prepared using 1.25 M bis-Tris pH 6.5 (Bis-Tris ultra grade cat#391335, Calbiochem), acrylamide-bis-acrylamide 37.5:1 (A3699, Sigma), 10 % Ammonium persulfate (APS) (Roth, Germany) and Tetramethylethylenediamine (TEMED, Sigma). The gel had three layers: 4 % stacking gel, 10 % separating gel and 16 % running gel. Migration buffer consisted of 50 mM MOPS (M3183, Sigma), 50 mM Tris (Tris-base Sigma 7-9, #T1378, Sigma), 1 mM Ethylenediaminetetraacetic acid (EDTA) (purified grade 99 %, Sigma), 0.1.% sodium dodecyl sulfate (SDS) (ultra pure 4×, ⩾ 99 %, Euromedex), 0.001 M $Na_2S_2O_5$ (cat#31448, Sigma) added right before use. The buffer was cooled at 4°C O/N. Loading buffer consisted of 0.03 M Tris pH 6.5, 5 % glycerol (rotipuran ⩾ 99.5 % p.a., Roth, Germany), 1 % SDS, 0.005 % bromophenol blue (Roth, Germany), 2.5 % β-mercaptoethanol (Sigma) added right before use.

Gel migration was carried out at 4°C. For the migration duration, the voltage was kept constant. The first hour the migration was carried out at 30 V while the following 3.5 hours it was carried out at 85 V [Schägger and von Jagow, 1987].

Purified APP_TM was washed with 10 mM HCl 3 times in order to remove the ions of trifluoroacetic acid (TFA). Aβ peptides (1 mg)

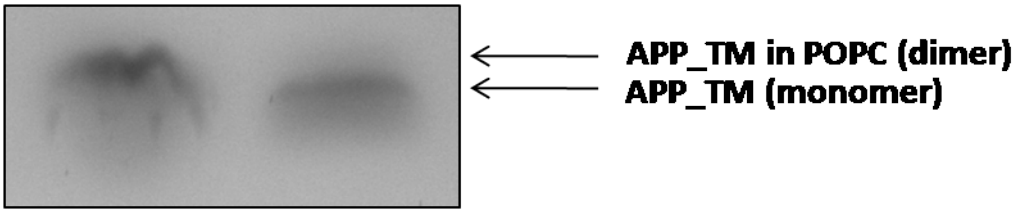

Figure 24: Bis-Tris acrylamide gel electrophoresis. APP_TM in the presence of POPC lipids migrated with an apparent molecular weight of a dimer (~5.6 kDa) and APP_TM without lipids migrated with an apparent molecular weight of a monomer (~2.8 kDa).

were dissolved in 1 ml of HFIP, while 20 mg of POPC were dissolved in chloroform. In order to obtain peptide to lipid ratio of 1:50, 15 µl of APP_TM stock and 10 µl of POPC stock were mixed. The solvents were evaporated with a stream of nitrogen gas and the film was lyophilized over night (O/N) to remove the traces of solvents. The film was rehydrated with 10 mM phosphate buffer pH 7.4 and vortexed to form multilamellar vesicles. Thereafter 5 µg of the sample were deposited on the gel.

The sample of APP_TM without lipids was prepared by dissolving a small amount of dry APP_TM in HFIP. The solvent was evaporated with the stream of nitrogen gas and the formed film was lyophilized O/N. The film was rehidrated with 10 mM phosphate buffer pH 7.4 and vortexed to maintain the same preparation conditions. Thereafter, 5 µl of the sample were deposited on the gel (the exact amount of the peptide is unknown).

4.2.2 *Results*

In order to verify that APP_TM peptides dimerize when reconstituted into POPC lipids, we used PAGE electrophoresis analysis to compare APP_TM oligomerization state in the presence and in the absence of POPC lipids. Native low-pH gel was used in order to detect the small difference between a dimer and a monomer of APP_TM (2.8 kDa for a monomer). Low-pH (pH 6.5) gel allows for increased resolution of the bands. A 10 % separating gel, usually used to separate small molecular weight proteins from SDS micelles, was used in order to achieve better size separation between monomers and dimers. It was crucial to omit SDS from the gel preparation as it was reported that APP forms dimers in the presence of SDS [Gorman et al., 2008]. As long as SDS was below its critical micelles concentration (cmc) APP_TM did not form dimers, unless lipids were present. In Figure 24 on page 59 the difference in the migration pattern between APP_TM in the presence of POPC and in its absence is clearly observed.

4.3 ^{15}N AND ^{2}H SSNMR INVESTIGATION OF APP_TM4K

4.3.1 *Experimental*

4.3.1.1 *Preparation of oriented samples for ssNMR*

The inherently low sensitivity of the NMR signal means that relatively large amounts of sample are required; therefore, an oriented bilayer sample for ssNMR purposes is actually composed of numerous stacked bilayers per pair of flat substrates that is, in reality, an oriented multilayer system. In keeping with the literature, however, an oriented multilayer sample will be referred to as an oriented bilayer sample.

For the purification of the APP_TM4K peptides the following equipment was used. Semipreparative HPLC with DAD 3L module for UV detection from Bischoff; McDAcq32 software; preparative column Grace Vydac (125 x 20 mm; P/N 1220 K040PS050) and the precolumn (30 x 20 mm P/N 0320 K040PS050) packed with Prontosyl 300-5-C4 (particles size of 5 μm with 300Å pores). Alternatively, preparative HPLC with the pump modules 331 and 332; the Liquid Handler module for automatic injection and fraction collection and the UV/Visible detector-156 from Gilson Software Trilution; preparative column Jupiter (150 x 30mm; 00F-4167-U0) and the precolumn (15 x 30 mm; AJ0-8314) with particles size of 5 μm with 300 Å pores, were used.

After the purification, TFA counter ions are associated with the peptide molecules. In order to remove these ions, dry peptide was solubilized in 2 mM HCl (Sigma) [Andrushchenko et al., 2007], frozen in liquid nitrogen and lyophilized (Finn Aqua Lyophilizer, model LyoVac GT 2 E). This procedure was repeated three times. APP_TM4K was reconstituted into POPC lipids with peptide to lipid ratio of 1:50.

3.5 mg of dry peptide were dissolved in a small volume of HFIP (Sigma) in a glass tube and 46.4 mg of POPC were dissolved in Chloroform in a separate glass tube. The solvent was evaporated with a gentle stream of nitrogen gas until the samples reached desired viscosity. The content of the tube was spread on ~ 20 ultra thin (100 μm) cover glasses (6 mm × 11 mm; Paul Marienfeld GmbH & Co. KG, Lauda-Königshofen, Germany). The films were dried first in air and thereafter under high vacuum over night to remove all traces of the organic solvent. The samples were hydrated for 24 hours at 93% relative humidity, achieved by a saturated salt solution of KNO_3 (see Note) at room temperature (~25°C) and left to equilibrate typically for about 3 days. Once the lipid films became translucent and soft the cover glasses were stacked on top of each other, with one empty cover glass used to cover the top surface. The stack was stabilized by wrapping with Teflon tape and then sealed in a plastic wrapping using an impulse sealer [Aisenbrey et al., 2010]. The solid-state NMR experiments were carried at 296 K (23°C).

Note: For ^{2}H experiments, the saturated solution was prepared with $^{2}H_2O$-depleted water.

4.3.1.2 *ssNMR experiments: ^{31}P, ^{15}N, ^{2}H*

The proton-decoupled ^{31}P solid-state NMR spectra were recorded at 202.41 MHz on a Bruker Avance wide-bore NMR spectrometer operating at 11.7 Tesla. A Hahn echo pulse sequence [Rance and Byrd, 1983] was used with the typical parameters: ^{1}H B_1 field 33 kHz, 90° pulse length 10 µs, echo delay 100 µs, spectral width 100 kHz, 2048 data points, typically 512 scans, and repetition time 3 s. The spectra were referenced relative to 85% phosphoric acid (0 ppm). An exponential apodization function corresponding to a line broadening of 100 Hz was applied before Fourier transformation.

The proton-decoupled ^{15}N cross polarization (CP) spectra of static aligned samples were acquired at 50.67 MHz on a Bruker Avance wide-bore NMR spectrometer operating at 11.7 Tesla. A commercial E-free triple-resonance solid-state NMR probe equipped with a flat coil was used. The adiabatic passage through Hartman-Hahn condition Hediger et al. [1995] CP (APHH-CP) pulse sequence was used with the typical parameters: spectral width 35.7 kHz, acquisition time 14.4 ms, CP contact time 600 µs. The ^{1}H B_1 field was swept from 40 -60 % following Tangent Amplitude-modulated slope and the average value corresponded to 47.6 kHz. About 30000 scans were accumulated with 1024 points. At the end of the acquisition the FIDs of two consecutive experiments were added to improve the S/N ratio. An exponential apodization function corresponding to a line broadening of 300 Hz was applied before Fourier transformation. Spectra were externally referenced to $^{15}NH_4Cl$ at 41 ppm.

Deuterium solid-state NMR spectra were recorded using a quadrupolar echo pulse sequence [Davis et al., 1976] with the typical parameters: ^{2}H B_1 field 40.3 kHz, echo delay 40 µs, spectral width 500 kHz, 16000 data points, about 62000 scans, and repetition time 1.5 s. The spectra were referenced relative to $^{2}H_2O$ (0 ppm). The FID was left-shifted by the correct number of points so that for each spectrum the part of the FID that was transformed began at the exact top of the echo. At the end of the acquisition the FIDs of two consecutive experiments were added to improve the S/N ratio. An exponential apodization function corresponding to a line broadening of 100 Hz was applied before Fourier transformation.

4.3.1.3 *Calculation of Orientational Constraints*

To evaluate the peptide orientations that agree with the experimental results, the static ^{15}N chemical shift tensor was oriented with respect to the molecular coordinate system of the polypeptide structure using an Euler algorithm. The chemical shift tensor describes the orientational dependence of interactions of the ^{15}N nuclei with the magnetic field of the NMR spectrometer. Static ^{15}N chemical shift tensors were

previously characterized [Oas et al., 1987, Hartzell et al., 1987, Teng and Cross, 1989]. Averaged values for glycine (40.4 ± 4.6, 66.8 ± 10.8, 217.4 ± 2.1), alanine and valine (55.8 ± 4.2, 81.4 ± 4.7, 223.2 ± 5.4) amino acids were taken from [Salnikov et al., 2009]. In the next step, a Cartesian coordinate system was defined in the laboratory frame in which the z-axis coincided with the magnetic field direction and the perpendicular axes were chosen arbitrary. The ^{15}N chemical shift tensor was rotated around the z- and y-axes in the molecular frame to obtain all possible orientations of the polypeptide with respect to the magnetic field direction. For every molecular orientation the resulting ^{15}N chemical shift values were calculated, assuming magnetic field direction being parallel to the original z-axes and visualized as a contour plot.

To evaluate the peptide orientations that agree with the experimental results of the ^{2}H quadrupole interactions of the alanine residue, the EFG tensor was oriented via C_α–C_β bond with respect to the molecular coordinate system. Quadrupole coupling constant of 186 kHz was used (i.e. for methyl group) [Lickfield et al., 1984]. A Cartesian coordinate system was defined in the laboratory frame in which the z-axis coincided with the magnetic field direction and the perpendicular axes were chosen arbitrary. The ^{2}H quadrupole tensor was rotated around the z- and y-axes in the molecular frame to obtain all possible orientations of the polypeptide with respect to the magnetic field direction. For every molecular orientation, the resulting ^{2}H quadrupole splittings were calculated assuming a magnetic field direction parallel to the original z-axes and visualized as a contour plot.

The simulation of the ^{15}N chemical shift of Ala-642 was based on the constraints from the ^{2}H-Ala-642 quadrupole spectrum. Within the range of constraints obtained from ^{2}H-Ala-642 spectrum, an arc covering the range of tilt angles from 25° to 120° was defined (covering about $3/4$ of a circle) (Figure 28 on page 67). For every pair of x- and y-values a corresponding ^{15}N chemical shift value was calculated. All the calculated functions were summarized and displayed as a plot. These assumptions are merely a model to account for the N–H bond orientations, that would agree with the experimental results.

4.3.2 *Results and discussion*

In order to investigate conformational details of the APP_TM4K TM helix, ssNMR spectroscopy was used. The ^{15}N spectra of static oriented samples of membrane-reconstituted APP_TM4K (628-655) containing ^{15}N-Gly-637, ^{15}N-Ala-642, and ^{15}N-Val-646 are shown in figure Figure 25 on page 63. All three peptides were also labeled with ^{2}H on one of the two alanine residues (Figure 2 on page 5). The spectra of ^{2}H-Ala-642 and ^{2}H-Ala-630 are shown in Figure 26 on page 64. Panel A in Figure 25 on page 63 shows the spectrum of APP_TM4K labeled

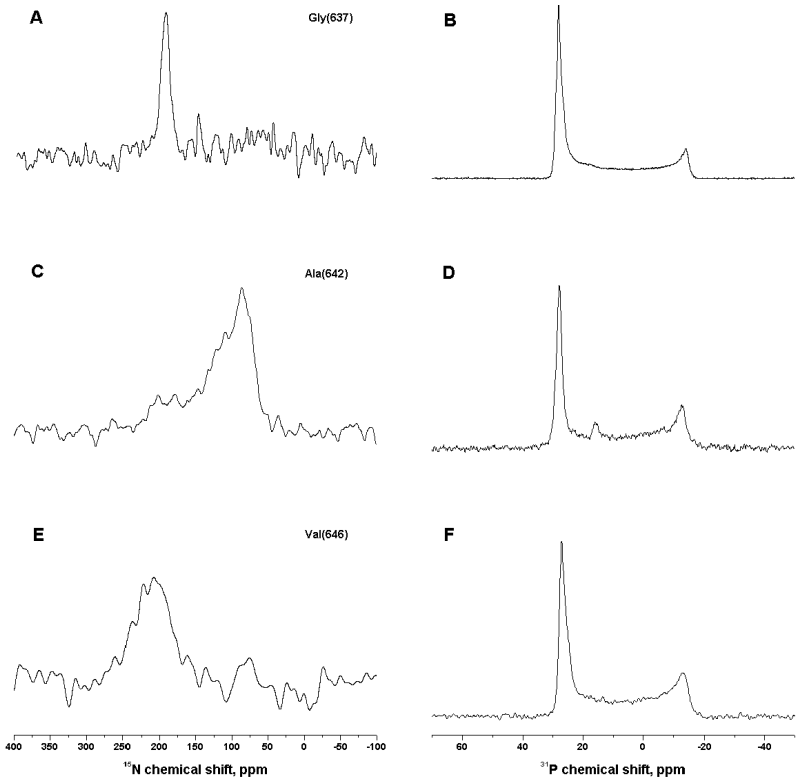

Figure 25: Proton-decoupled ^{15}N and ^{31}P spectra of APP_TM4K labeled with ^{15}N at positions Gly_{637} (A, B), Ala_{642} (C, D), Val_{646} (E, F) and reconstituted into oriented POPC lipid membranes. Samples were measured with the membrane normal parallel to the magnetic field direction.

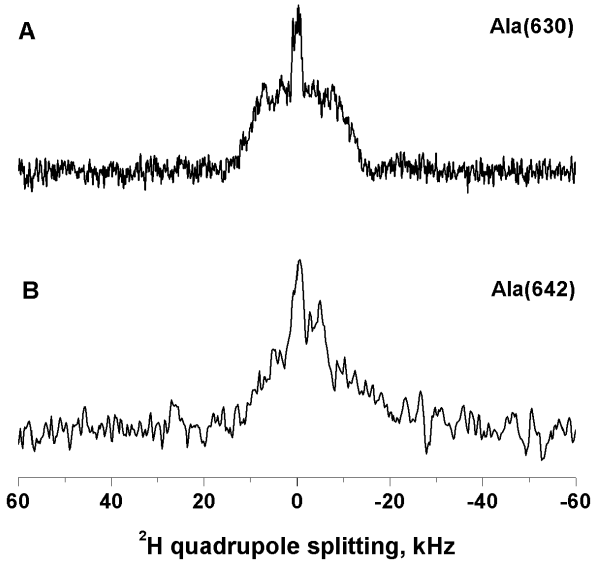

Figure 26: ²H NMR spectra of APP_TM4K peptides reconstituted into oriented POPC lipid membranes and labeled at positions ²H-Ala-630 (A) and ²H-Ala-642 (B). Samples were measured with the membrane normal parallel to the magnetic field direction. Spectrum in panel A is a representative spectrum of two peptides, APP_TM4K ¹⁵N-Ala-642 / ²H-Ala-630 and APP_TM4K ¹⁵N-Val-646 / ²H-Ala-630.

at position ¹⁵N-Gly-637 (Figure 2 on page 5) where its ¹⁵N chemical shift value is at 191 ppm and indicates transmembrane orientation for a helical peptide [Bechinger and Sizun, 2003]. The line-width at half-height is <600 Hz, indicating that the peptide is well-oriented with respect to the magnetic field direction. Corresponding proton-decoupled ³¹P spectrum of the sample was recorded to evaluate the quality of the alignment of the lipid bilayers (Figure 25 on page 63, panel B). The lipids predominantly resonate at 30 ppm ³¹P chemical shift, typical of phosphatidylcholine molecules in liquid crystalline lipid bilayers that are oriented with their normal parallel (~ 50 %) to the magnetic field direction. Small contributions between 30 and -15 ppm are also observed and can be attributed to differently aligned lipids and/or conformational changes of the phospholipid headgroups due to the presence of the peptide (~ 40 %). Small contribution around -15 ppm corresponds to lipids oriented perpendicular to the external magnetic field (~ 10 %).

In addition to the ¹⁵N-Gly-637 label, ²H-Ala-642 label (Figure 2 on page 5) was introduced into the same peptide. ¹⁵N chemical shift and ²H quadrupole interaction experiments were performed on the same sample. The deuterium spectrum of Ala-642 does not exhibit one clear quadrupole splitting, but rather many splittings that create the observed shape (Figure 26 on page 64, panel B). The breadth of the

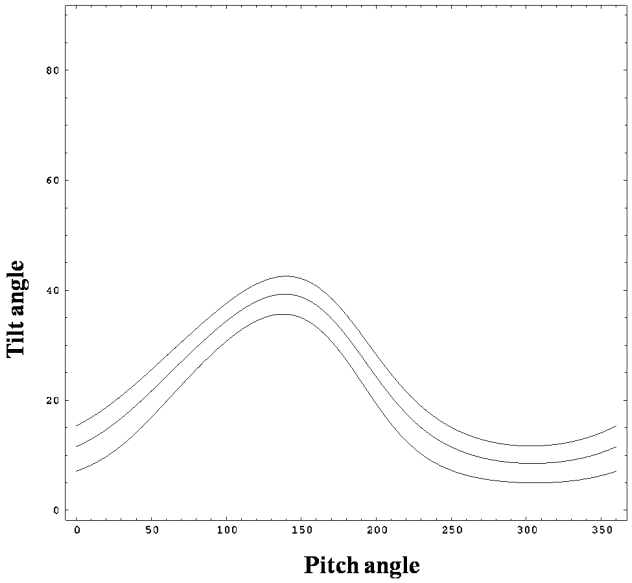

Figure 27: Contour plot that results from experimental measurements of the ^{15}N chemical shift (191 ± 7) ppm of Gly-637 in APP_TM4K peptide. x-Axis shows the rotational pitch angle around molecular z-axis (along the helix long axis), while y-axis shows the rotational tilt angle, relative to the membrane normal.

spectrum is around 27 kHz indicating structural and/or orientational heterogeneity of Ala-642 site in the peptide. This implies that in this site, the structure may not be helical. Therefore, we can not use the model of a perfect α-helix to orient the structure. Consequently, constructing a contour plot for ^{15}N-Gly-637/^{2}H-Ala-642 will not result in well defined angular pairs that agree with the experimental results. Nevertheless, plotting the contour plot for the ^{15}N chemical shift of Gly-637 alone reveals restrictions of the tilt angle of the peptide helix, but not of the rotational pitch angle (Figure 27 on page 65). While the complete range (0° - 360°) of rotational pitch angle values is allowed, the tilt angle is in the range of 7° - 42° .

Another sample with APP_TM4K labeled with ^{15}N at position Ala-642 (Figure 2 on page 5) was measured. This spectrum exhibits a more complicated spectral shape (Figure 25 on page 63, panel C): its ^{15}N chemical shift values are spread over 160 ppm and it appears as a powder pattern-like spectrum. One might conclude that the sample was destroyed during the experiment (perhaps due to dehydration or due to misalignment of the glass plates), creating unoriented sample. However, additional label of ^{2}H-Ala-630 within the same peptide measured on the same sample does not resemble a powder pattern (Figure 26 on page 64, panel A) as would have been expected for unoriented sample. In addition, corresponding proton-decoupled ^{31}P spectrum was measured and is shown in Figure 25 on page 63, panel D. The lipids predominantly resonate at 30 ppm^{31}P chemical shift, typical of phosphatidylcholine molecules in liquid crystalline lipid

bilayers that are oriented with their normal parallel to the magnetic field direction. Some contributions between 30 and -15 ppm are also observed and were attributed to a population of differently aligned lipids and/or conformational changes of the phospholipid headgroup due to the presence of the peptide, similar to the spectra obtained from the other samples. However, here additional contribution at 15 ppm is apparent and the origin of this contribution is not very clear, though there is evidence that it may indicate degradation of a small population of the lipid molecules (not published data). Nevertheless, from the ^{31}P spectrum it is clear that most of the lipids in the sample are aligned parallel to the magnetic field direction. Based on this reasoning the most likely explanation to the shape of the ^{15}N chemical shift spectrum of Ala-642 is that this site has a range of different orientations, but not all the orientations as in a powder sample. Slow motional reorientation (slower than kHz range) of this site is probably responsible for the wide appearance of the "main peak" in the spectrum.

The ^{2}H ssNMR spectrum for Ala-642 site (Figure 26 on page 64, panel B)–discussed previously–provides additional evidence that this site exhibits a range of orientations, but again, it is not a powder. The ^{2}H NMR spectrum has a breadth of ~27 kHz. Even though the spectrum does not show a well defined quadrupole splitting and is rather wide, there is limited range of possible orientations (e.g. C_α–C_β bond tilt angles are between 42° and 71° with respect to B_0 for the max. splitting of 27 kHz – were calculated using eq.2.1) as can be seen in the contour plot (Figure 28 on page 67). Since the ^{15}N chemical shift spectrum of Ala-642 can not provide any constrains, it was simulated (for details refer to the experimental section) considering the constrains imposed by the C_α–C_β bond orientations revealed by the contour plot for ^{2}H quadrupole interaction (Figure 28 on page 67).

It can be seen in Figure 29 on page 67 that the general shape of the simulated and the experimental spectra are in good agreement. Of course, the simulation took into account only the values of a few splittings from the ^{2}H spectrum (Figure 28 on page 67, dotted arc), not including many others that are concealed within the wide spectral shape. But clearly, even a few restrictions are sufficient to show that many orientations of the N–H bond are possible under the constraint of the C_α–C_β bond orientations. However, the majority of orientations correspond to the N–H bonds oriented perpendicularly to the membrane normal (~80 ppm). Notably, the simulated spectrum spans 50 - 200 ppm while the experimental spectrum extends until 230 ppm. These chemical shift values are missing from the simulated spectrum because angular constraints from 0° to 25° were not considered in the calculation. When a complete circle (rather than an arc) of restrictions were taken into account, the calculated spectrum resulted in additional large contribution between 200 - 230 ppm, corresponding to the transmembrane orientation of the segment. However, this does not

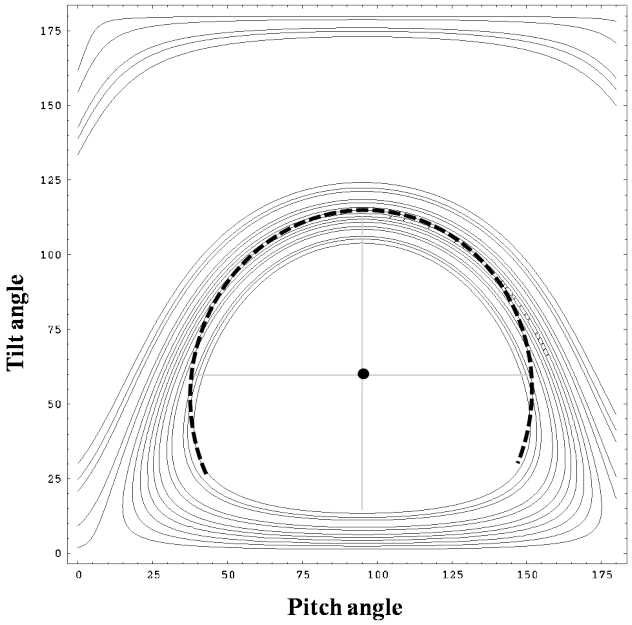

Figure 28: Contour plot that results from experimental measurements of the ^{2}H quadrupole interaction of ^{2}H-Ala-642 in APP_TM4K peptide. x-Axis shows the rotational pitch angle around molecular *z*-axis (along the helix long axis), while y-axis shows the rotational tilt angle, relative to the membrane normal. Dotted arc marks the angular pairs taken for the simulation of ^{15}N chemical shift values for Ala-642, cf. text for details.

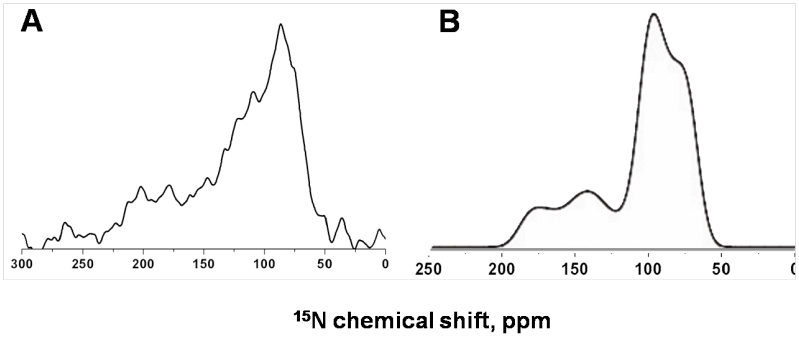

Figure 29: Comparison between the experimental (A) and the simulated (B) spectra of ^{15}N-Ala-642.

correlate with the experimental result. Probably, the ^{15}N chemical shift spectrum of Ala-642 could be better simulated taking into account the missing restrictions, but giving them a much lower weight than for the other orientations. These results indicate that for the experimental spectrum of ^{15}N chemical shift of Ala-642 a restricted range of "allowed" (i.e. restricted by the C_α–C_β bond angles) orientations exists, where majority of the N–H bonds are oriented perpendicular to the membrane normal and a smaller population of N–H bonds are oriented parallel to the membrane normal. Clearly, the N–H bond of Ala-642 adopts many different orientations. This finding correlates well with the idea that Ala-642 of the γ-cleavage site is in a non-helical conformation.

The third labeled site of APP_TM4K ^{15}N-Val-646 resonates at 209 $\pm$ 28 ppm (Figure 25 on page 63, panel E). The corresponding ^{31}P alignment (Figure 25 on page 63, panel F) shows a typical line shape with frequencies around 30 ppm and -15 ppm. Relative percentage of the lipids oriented parallel to the external magnetic field is 47 % (30 ppm), 19 % in perpendicular orientation (-15 ppm) and 34 % in all other orientations (from 30 ppm to -15 ppm). While the signal in panel E is wide with high noise level, the chemical shift values undoubtedly indicate transmembrane helix orientation. The breadth of the spectrum likely indicates a number of orientations that Val-646 adopts with respect to the magnetic field direction. From the restriction plot (Figure 30 on page 69) it is clear that for the complete range of rotational pitch angles (0° - 360°) possible tilt angles would range from 0° to 50°.

Peptide carrying the ^{15}N-Val-646 label, was also labeled at ^{2}H-Ala-630 site (Figure 26 on page 64, panel A). The breadth of the spectrum is 26 kHz and a small splitting of 1.5 kHz in the center is due to residual deuterium in the water molecules (0.015 % natural abundance) oriented on the membrane surface [Moraes and Bechinger, 2004]. The large breadth of the spectrum and its shape indicate that Ala-630 has a heterogeneous distribution of alignments, but it is not a powder (where all the orientations are possible). Ala-630 is located near the N-terminal membrane boundary (Figure 2 on page 5) and might experience less constrains from the van der Waals interactions with lipid molecules and therefore it is reasonable that this amino acid will be more mobile. Lu et. al. observed non-helical conformation for Ala-630 and through measurements of $^{1}H_\alpha$-$^{13}C_\alpha$ dipole-dipole couplings concluded the existence of rapid molecular motions that the authors associated with the exchange between helical and non-helical conformations [Lu et al., 2011]. Of course, the time scale for deuterium is very different and what is considered fast for $^{1}H_\alpha$-$^{13}C_\alpha$ dipole-dipole couplings may be in the slow or intermediate range on the ^{2}H time scale. If the motion was indeed rapid (> 200 kHz), we would expect to see averaged conformation and single orientation

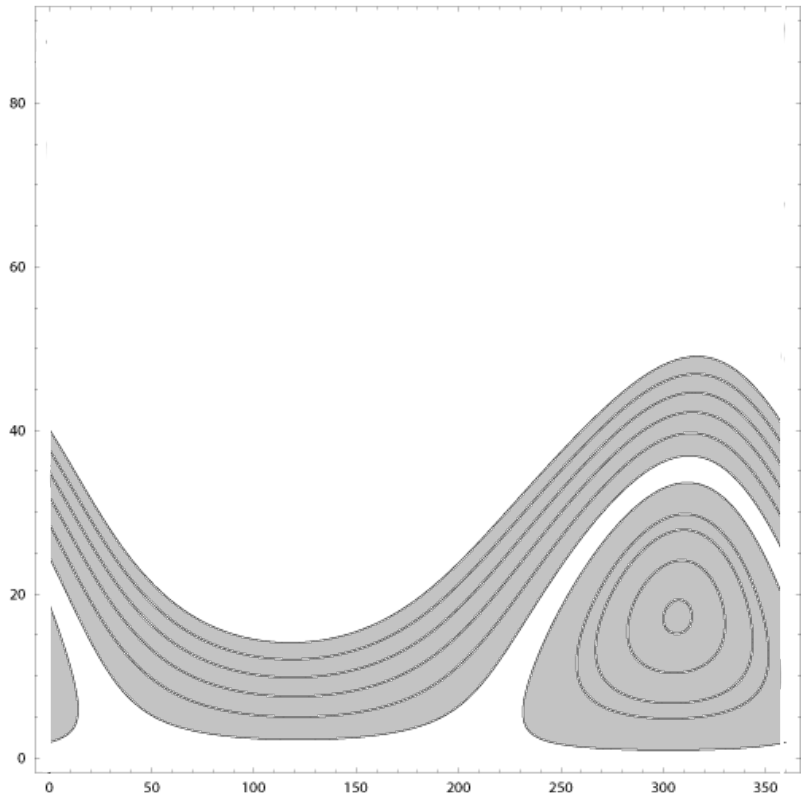

Figure 30: Contour plot that results from experimental measurements of the ^{15}N chemical shift (209 ± 28) ppm of Val-646 in APP_TM4K peptide. x-Axis shows the rotational pitch angle around molecular z-axis (along the helix long axis), while y-axis shows the rotational tilt angle, relative to the membrane normal. The grey area represents the space of possible pitch and tilt angles, while white areas are excluded from that space.

in the ^{2}H NMR spectra, which is not the case. Therefore, molecular motions of the Ala-630 are slow or intermediate on the time scale of ^{2}H NMR spectra. It is interesting to note that the deuterium spectra of both alanines – Ala-630 and Ala-642 (Figure 26 on page 64) – are somewhat similar in their shape. For both, the breadth is quite large ~26 kHz (A) and ~27 kHz (B) and for this maximal value of the splitting, C_α–C_β bond orientations are 42° and 71° for positive and negative values of the ^{2}H quadrupole splitting, respectively. Bearing in mind that there is no available structure of the APP_TM peptide to align, the wide spectra of ^{15}N chemical shift for Val-646 and of ^{2}H quadrupole interaction of Ala-630 can not provide clear orientational constrains for this pair of labels. The line shapes of these spectra are, therefore, determined to a large extent by the orientational distribution of molecules with respect to the magnetic field direction.

The ssNMR data described above indicate that APP_TM4K reconstituted into POPC bilayers experiences conformational and orientational heterogeneity. Ala-630 is located at the membrane boundary of APP_TM4K and previous studies have shown coexistence between helical and non-helical conformations for amino acids located at both termini of the APP_TM peptide [Lu et al., 2011]. Thus, slow mobility at the N′-terminal boundary that was evident from the ^{2}H ssNMR measurement can indicate also a conformational variability of Ala-630. However, in the full-length APP this behavior of Ala-630 may not be observed as the continuum of the amino acids sequence is not interrupted.

Gly-637 is located within the GxxxG sequence that was shown to mediate dimerization of the APP_TM helix [Munter et al., 2007, Miyashita et al., 2009, Sato et al., 2009] forming a stable structure in this region. Well defined transmembrane orientation of Gly-637 seen from ^{15}N chemical shift measurement correlates well with the notion of stable structure and therefore provides additional, though indirect, support for the dimer formation.

Ala-642 is the most ambiguous of all - it is located in the γ-secretase cleavage site and has drawn a lot of attention. Conflicting evidence exist for α-helical [Sato et al., 2009] and possible non-helical [Lu et al., 2011] conformations of this site. Analysis of the ^{15}N chemical shift and the ^{2}H quadrupole ssNMR spectra of Ala-642 showed a wide range of possible orientations and did not exhibit one well-defined alignment in the POPC bilayers. Either local unraveling of the helical structure or extensive conformational changes in this region could be responsible for the large spread of orientations observed here. These results strengthen the hypothesis that local structural fluctuations might be necessary for the γ-secretase cleavage.

Further in the sequence–within the ζ-cleavage site–Val-646 exhibits transmembrane orientation, but the width of the observed signal indicates existence of plural orientations for this site as well. Valine is

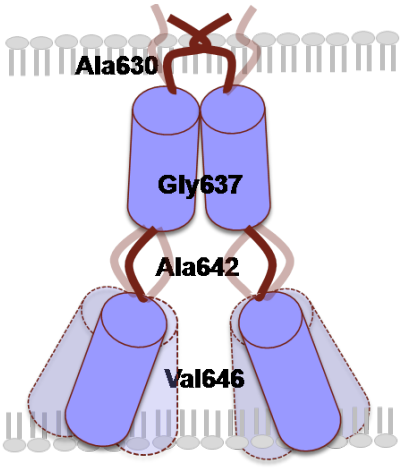

Figure 31: A possible model of the APP_TM4K peptide orientation and conformation in POPC bilayer, based on the results obtained in this work.

a β-branched amino acid that is known to contribute to destabilization of α-helical structures. The site of ζ-cleavage is rich in β-branched amino acids (Ile, Val and Thr), which probably contribute to the local unraveling of the structure. In the literature, there is evidence that Val-646 is located at a flexible site as paramagnetic relaxation was observed upon exposure of the APP TMD to Cu^{2+} [Lu et al., 2011]. Val-646 is located only two amino acids away from the ε-cleavage site, for which a transformation from helix-to-coil was shown in APP and in Notch1 peptides (the latter another γ-secretase substrate) [Sato et al., 2009]. It is, therefore, natural to conclude that this region is highly flexible. This would also favor the progressive cleavage theory from the ε- to the γ-cleavage sites, which proposes that γ-secretase sequentially cuts off one turn of the helix at a time [Beel et al., 2008, Munter et al., 2007, 2010].

Figure 31 on page 71 shows a model of possible orientations and conformations of the APP_TM4K peptide in POPC bilayers, proposed based on the results from this work. Ala-630 is shown to have a heterogeneous distribution of alignments. It is, however, likely that the heterogeneity of this site arises due to its location at the membrane boundary. In order to verify its orientation, additional experiments with longer variants of APP_TM peptide, that would include the juxtamembrane (JM) domain, should be considered. Gly-637 shows definitive transmembrane orientation. It is the last glycine in the sequence of GxxxG motifs and as such, could act as a transmembrane anchor of the TM domain. The question remains whether it is important for the dimerization of the peptide. Studies of mutated variants of APP_TM peptides could provide an answer to this question. The γ-cleavage site (Ala-642) is structurally heterogeneous. Also, in the ζ-cleavage site Val-646 is in a transmembrane orientation and is flexible.

This structural and/or orientational flexibility at both sites may be a part of the cleavage mechanism of γ-secretase, as was proposed by [Beel et al., 2008, Munter et al., 2007, 2010].

This structural peculiarity is not unique. For example, human voltage-gated potassium channel KCNE1 is a single transmembrane protein and largely α-helical. Recent careful NMR study from Sanders group showed for intact KCNE1 in lyso-myristoylphosphatidylglycerol (LMPG) micelles that its TM helix is interrupted by a nonhelical mobile segment located roughly between sites 59 and 61 [Tian et al., 2007]. The authors suggest that local loss of helicity for KCNE1 in its native complex with KCNQ1 would also be energetically feasible under native conditions if loss of classical helical backbone hydrogen bonds were offset by a rearrangement of hydrogen bonding partners within KCNE1 or through formation of favorable KCNQ1-KCNE1 interactions that satisfied KCNE1's hydrogen bonding potential around sites 59-61 [Tian et al., 2007]. From the structural point of view, the authors propose that the presence of a number of β-branched amino acids combined with two glycine residues in or near this segment may be a contributing factor. Because the nonhelical residues 59-61 of KCNE1 overlap with sites 57-59, which are involved in modulation of KCNQ1 channel function, the authors propose that the distinctive conformational and dynamic properties of this segment may be of the highest functional relevance [Tian et al., 2007]. Another example is nicotinic acetylcholine receptor (nAChR), a ligand-gated ion channel that is involved in neurotransmission [Karlin, 2002]. Its membrane-embedded αM1 segment forms an unstable α-helix near residue Leu18 in fully hydrated phospholipid bilayers (40–50% of the peptides) [**?**]. The authors propose that the presence of conserved proline residue at position 16 in the primary sequence imparts a conformational flexibility on the M1 segments that could enable membrane-mediated modulation of nAChR activity [**?**].

In this respect, TMD of APP might share similar reasoning for the presence of non-helical residues in the sequence. From the structural point of view, the presence of a number of β-branched amino acids combined with glycine residues were already mentioned as a contributing factor. From the functional point of view, non-helicity might serve as a recognition pattern necessary for the interaction with component or components of γ-secretase complex or alternatively, might be involved in signaling via protein-lipid interface to recruit γ-secretase complex. The latter will require extensive study of APP TMD interactions with adjacent lipid molecules. Are there structural or functional modulations of APP TMD by different lipids or a varying percentage of cholesterol? Answering this question might bring out a novel mechanism for γ-secretase cleavage site recognition.

Another extensive study from Sanders group focused on the C-terminal 99-residue domain of APP, C99, a single-span membrane

protein formed after β-secretase cleavage of APP. Subsequent cleavage of C99 at membrane-disposed sites by γ-secretase leads to release of both the amyloid-β (Aβ) peptides and the water-soluble APP intracellular domain (AICD). The authors offer some insights into motional and conformational dynamics of C99 as were derived from NMR studies of the peptide in LMPG micelles [Beel et al., 2008]. Under their experimental settings, C99 appears to be conformationally well ordered single unbroken α-helix. Most importantly, they argue that the residues comprising the γ-secretase cleavage sites are not involved in the dimer interface and are not recognized by γ-secretase on the basis of any unusual backbone conformational or dynamic features, because they reside in the most hydrophobic region of LMPG micelles [Beel et al., 2008]. However, the authors' choice to use LMPG micelles as membrane mimetics might lead to inaccurate extrapolation of their findings, because even though LMPG micelles have a diameter that approaches the hydrophobic span of a typical lipid bilayer, membrane fluidity/stiffness and its curvature affect orientation and structure of TDs. For example, the structure of membrane-bound α-synuclein was shown to be modulated in presence of curved vesicles and micelles or flat bicelles, confirming the importance of the environment upon protein folding into its final structure [Georgieva et al., 2008]. In addition, classical NMR is not sensitive to internal molecular dynamics and therefore it precludes detection of local structural fluctuations such as those observed in ssNMR experiments in this work.

To further investigate structural flexibility of the secondary structure of APP_TM4K peptide, FTIR can be used. Upon isotopic labeling with ^{15}N, there is a shift in the main spectral features of the amide I and amide II regions. Thus ^{15}N-labeled sites Gly-637, Ala-642 and Val-646 can be used for this purpose. This work is currently in progress.

5

RESULTS: SSNMR OF ^{2}H-LABELED CARPROFEN DERIVATIVES IN LIPID BILAYERS

Benzyl-carprofen and sulfonyl-carprofen were found to be effective modulators of γ-secretase. They affected the cleavage at the γ38, γ40, and γ42 sites to a different extent and particularly suppressed the formation of Aβ42 while enhancing the formation of Aβ38 and thus showed the typical profile of effective NSAIDs. They were found to be the most potent inhibitors of Aβ42 [Narlawar et al., 2006]. Deuterium ssNMR technique was used in order to elucidate the orientation of carprofen derivatives in lipid bilayers constituent of a ternary mixture of POPC/SM/Cholesterol. This ternary mixture of lipids was chosen because POPC, SM, and cholesterol are the main components of neurons. In addition, this combination of lipids is used to mimic lipid rafts in experimental settings. It has been shown that amyloidogenic processing of APP depends on cholesterol-rich lipid rafts [Ehehalt et al., 2003], while nonamyloidogenic processing prevails at the cell surface, in the cholesterol-poor bulk plusma membrane [Parvathy et al., 1999]. Therefore, knowledge about the interaction of carprofen derivatives with the lipid bilayer is essential for understanding the underlying mechanism of their action in modulating the γ-secretase activity.

5.1 EXPERIMENTAL

5.1.1 *Sample preparation*

Deuterated carprofen derivatives were synthesized by Binia Thomaszewski (laboratory of Prof. Boris Schmidt, Darmstadt Technical University, Institute for Organic Chemistry and Biochemistry, Darmstadt, Germany) and provided by Dr. Thomas Hauß(Helmholtz-Zentrum Berlin, Institute Soft Matter and Functional Materials, Germany) as well as the lipids and cholesterol.

All the experimental conditions were set to compare with neutron diffraction experiments, performed by Dr. Thomas Hauß. The solid-state NMR samples were prepared by dissolving cholesterol, sphingomyelin, and POPC separately in 1 ml of chloroform. These solutions were mixed such that the mass ratio of 5 : 5 : 1.75 (vol : vol) respectively, was satisfied. Carprofen derivatives were dissolved in 1 ml of 9:1 mixture of chloroform : methanol and a volume corresponding to 0.3 mg of carprofen was added to the freshly prepared lipid solution. The solvents were then evaporated with a stream of

nitrogen gas until the samples became viscous. The mixtures were spread on 15 ultra thin cover glasses (6 mm × 11 mm; Paul Marienfeld GmbH & Co. KG, Lauda-Königshofen, Germany) and dried first in air and thereafter under high vacuum over night to remove all traces of the organic solvent. The samples were hydrated for 24 hours at 93% relative humidity, achieved by a saturated salt solution of KNO_3 in ^{2}H-depleted water at room temperature (~25°C). After stacking the glass plates on top of each other the samples were physically stabilized by wrapping with a Teflon tape and sealed in a plastic bag of the suitable size. The solid-state NMR experiments were carried out at 288 K (15°C).

According to the literature, the ternary lipid mixture of POPC/SM/-Chol falls into the l_o/l_d coexistence region in the phase diagram at 310 K [de Almeida et al., 2003]. At temperatures $\leqslant$308 K, this mixture exhibit the typical domain structure, whilst with increased temperature lipids redistribute into the coexistence region [Bunge et al., 2008].The situation of the ternary mixture of POPC/PSM/Chol can be described as a heterogeneous liquid disordered phase at temperatures above the main phase transition of the two phospholipids (at 311 K for SM). Upon temperature decrease, there is a tendency for a redistribution of the cholesterol such that the l_d POPC phase is increasingly depleted of cholesterol and the l_o phase of PSM becomes enriched in the sterol [Bunge et al., 2008]. Therefore, we assumed that at 288 K, the ternary mixture is segregated into domains (cholesterol-rich and cholesterol-poor patches).

5.1.2 *ssNMR measurements*

ssNMR spectra were recorded on a Bruker Avance wide-bore NMR spectrometer operating at 11.7 Tesla. A commercial triple-resonance solid-state NMR probe equipped with a flat coil was used (BioPE). The spectra of samples oriented parallel and perpendicular (turned by 90°) relative to the magnetic field direction were acquired.

Proton-decoupled ^{31}P solid-state NMR spectra were recorded using a Hahn echo pulse sequence [Rance and Byrd, 1983] with the following parameters: ^{1}H B_1 field 33 kHz, 90° pulse length 7.5 µs, pre-scan delay 20 µs, spectral width 100 kHz, 1024 data points, typically 256 scans, and repetition time 2 s. The spectra were referenced relative to 85% phosphoric acid (0 ppm). An exponential apodization function corresponding to a line broadening of 100 Hz was applied before Fourier transformation.

Deuterium solid-state NMR spectra were recorded using a quadrupolar echo pulse sequence [Davis et al., 1976] with the typical parameters: ^{2}H B_1 field 47 kHz, inter-pulse delay 50 µs, spectral width 1 MHz, 4096 data points, 204800 scans, and repetition time 2 s. The spectra were referenced relative to ^2H_2O (0 ppm). The FID was left-shifted

by the correct number of points so that for each spectrum the part of the FID that was transformed began at the exact top of the echo. An exponential apodization function corresponding to a line broadening of 300 Hz was applied before Fourier transformation.

5.1.3 *Calculation of Orientational Constraints from Experimental Spectra*

5.1.3.1 *Sulfonyl-carprofen*

To evaluate the molecular orientations that agree with the experimental spectra, a Cartesian coordinate system was defined as follows. The motion of the methyl group is axially symmetric around the C–S bond (Figure 4 on page 10), similar to the rotation of the methyl group in a hydrocarbon chain [Seelig and Niederberger, 1974] making the analysis of the CD_3 group attached to the sulfonyl straightforward. Since the CD_3 group possess a threefold symmetry axis, the averaged ^2H tensor is axially symmetric with respect to the rotation axis (i.e. along the C-S bond vector). In the case of averaged quadrupolar splitting, $\Delta\nu_Q$ is given by $\Delta\bar{\nu}_Q = \Delta\nu_Q S$ with $S = \left(3\cos^2\Theta - 1\right)/2$ and Θ is the angle made by the C–D bond and the 3-fold axis. For tetrahedral geometry, $\Theta = 70.5^\circ$ and $S = -1/3$. In the absence of additional motions, the quadrupolar splitting $\Delta\nu_Q$ directly relates the orientation of the C–S bond with respect to the magnetic field direction via angle Θ, which was calculated from eq. 2.1. Static quadrupolar coupling constant for methyl group is $e^2qQ/h = 187\,\text{kHz}$ [Lickfield et al., 1984]. The calculations were made by using a librationally averaged quadrupolar coupling constant $e^2qQ/h = 164\,\text{kHz}$ ($S_{lib} = 0.88$) [Bechinger and Salnikov, 2012].

5.1.3.2 *Benzyl-carprofen*

The evaluation of this molecule is more complex and was done in several steps. Lets look at the benzyl ring, which has a C_2 symmetry and an internal motion about $C_\beta - C_\gamma$ bond axis (Figure 32 on page 78). Two parts of the benzyl were considered: the phenyl ring and the methylene group. While for the phenyl ring 180° flips about $C_\beta - C_\gamma$ bond axis occurring on the time scale faster compared with 0.2 MHz [Gall et al., 1981] were assumed (as was already shown for aromatic side chains [Kinsey et al., 1981]), the two C_β–D bonds of the methylene group were considered stationary on the NMR time scale (details are in the results section).

For well defined motional models, within the fast limit, we need to know the angles involved. For the flip averaged phenyl we will be concerned with the orientations of the $C_\epsilon D$ and $C_\delta D$ sites. When a molecule jumps between equally populated sites an averaged principal axes can be defined as illustrated in Figure 33 on page 78, where angle $\beta = 120^\circ$ is the angle between two interchangeable sites, then the

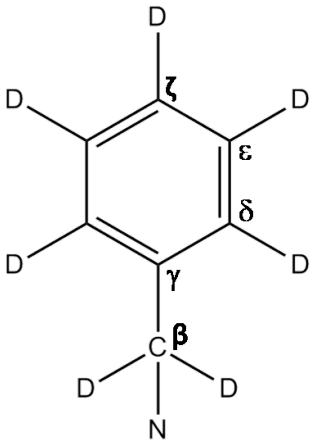

Figure 32: Schematic drawing of the [d_7] - benzyl.

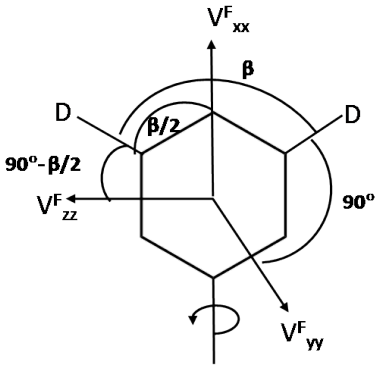

Figure 33: Illustration of the averaged ^{2}H quadrupolar tensor due to 180° flips about the $C_\beta - C_\gamma$ bond. Orientation of the averaged principal axes V^F_{xx}, V^F_{yy}, V^F_{zz} and the angles between them and either of the C–D bonds are shown. Reproduced with modifications from [Schmidt-Rohr and Spiess, 1994].

angles between the averaged principal axes V^F_{zz}, V^F_{xx}, V^F_{yy} and either of the C–D bonds are: $\theta_{xx} = \frac{1}{2}\beta$, $\theta_{yy} = 90°$, $\theta_{zz} = 90° - \frac{1}{2}\beta$.

The principal values for averaging by two-fold jumps are determined using

$$\omega_n = \omega(\theta_n) = \frac{1}{2}\left(3\cos^2\theta_n - 1\right), \tag{5.1}$$

where $n = xx, yy, zz$ and θ_n are defined in Figure 33 on page 78. We obtained $\omega_{xx} = -\frac{1}{2}$, $\omega_{yy} = -\frac{1}{8}$, $\omega_{zz} = \frac{5}{8}$ then the asymmetry parameter $\bar{\eta} = 0.6$. Detailed discussion and development of the equations can be found in "Multidimensional Solid-State NMR and Polymers" by [Schmidt-Rohr and Spiess, 1994]. Static quadrupolar coupling constant for aromatic C–D bond is 180 kHz as was determined by [Gall et al., 1981] for phenyl ring. However, at higher temperatures (300 K) due to small amplitude oscillations about the C_β–$C\gamma$ bond axis superimposed on the other ring motions, which affect the outer static

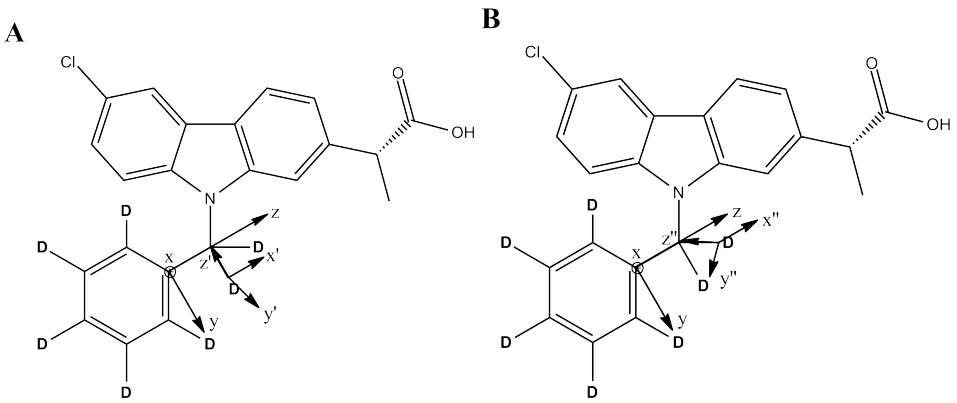

Figure 34: Benzyl-carprofen molecules showing quadrupole tensor elements attached to each of the methylene deuterons: (A) for D_1 atom the tensor elements are labeled as x', y', and z' (B) for D_2 atom the tensor elements are labeled as x'', y'', and z'' . The molecular coordinate system is shown where z-axis is along the C_γ-C_β bond, x axis is out of the page plane and y axis is orthogonal to them.

powder pattern reducing e^2qQ/h to 168 kHz [Gall et al., 1981]. In general, the angles Θ and ϕ (as were defined in the introduction) could be calculated using equation 1.14.

The C_ζ–D bond of the phenyl ring is not affected by motions about the $C_\beta - C_\gamma$ bond axis. Therefore, the largest field gradient parameter remains aligned with the C–D bond direction and is parallel to the axis of motion. Thus the tensor's principal values are $V_{zz} = 1$; $V_{xx} = -\frac{1}{2}$ and $V_{yy} = -\frac{1}{2}$, giving asymmetry parameter $\eta = 0$. Now the angles can be calculated using equation 2.1 with the same quadrupolar coupling constant of 168 kHz.

The segment left to analyze is the methylene group (Figure 32 on page 78). Its two C–D bonds were considered as static on the ^{2}H NMR time scale (this point is discussed in the next subsection). The tensors values were calculated and their position with respect to the molecular coordinate system was evaluated. The z-axis of the molecular coordinate system was chosen to be along the C_γ–C_β bond, it was a convenient choice as it is the axis of motion for benzyl ring (Figure 34 on page 79). The direction of the tensor elements for each of the deuterium atoms was defined by angles between each of the tensor elements and the molecular coordinate system. The main tensor element (V_{zz}) lies along the C–D bond, while the other two tensor elements (V_{yy}, V_{xx}) are equal and orthogonal to each other and to the main element. The quadrupolar coupling constant of 180 kHz [Lickfield et al., 1984] for methylene group was used and the rotation matrices were applied: first rotation around the z-axis and then rotation around the y-axis. The result was plotted as a contour plot, accounting for the experimental signal distribution.

To account for the constraints from different molecular segments and to deduce all possible molecular orientations a MATHEMATICA 3.0 software-based (Wolfram Research, Champaign, IL) script was used. Essentially, in a chosen origin the relevant tensor values in atomic coordinate system are multiplied by a quadrupolar coupling constant followed by application of rotation matrices to calculate the tensor values relative to the molecular coordinate system. The results are presented as a contour plot with the x-axis being a rotation around molecular z-axis (i.e. rotational pitch angle) and the y-axis being a rotation around molecular y-axis (i.e. rotational tilt angle). Each molecular segment with tensor's principal values calculated, was subjected to this analysis. Calculated orientational constraints are presented on the same contour plot and provide visual representation of all possible orientations that agree with the experimental results.

5.2 RESULTS AND DISCUSSION

5.2.1 *Sulfonyl-carprofen*

Sulfonyl-carprofen was reconstituted into oriented lipid membranes as described above, and investigated by ^{2}H ssNMR spectroscopy. Proton-decoupled ^{31}P spectrum of the sample was recorded to evaluate the alignment of the lipids (Figure 35 on page 81, panel C). The ^{31}P chemical shift value is dependent on the alignment of the lipid head group relative to the magnetic field direction (B_0), the latter being collinear with the glass plate normal (n). For pure POPC membranes in their fluid state at the sample orientation B_0 || n, values around 30 ppm are characteristic of lipids that align with their long axis parallel to B_0 and resonances at −15 ppm are indicative of perpendicular alignment. The latter probably corresponds to the maximum intensity typically observed for a powder pattern line shape (i.e. a random alignment of non-oriented sample) [Bechinger et al., 1999a]. Even though in this sample the membrane comprises of a mixture of POPC : sphingomyelin : cholesterol, the ^{31}P spectrum does not deviate from the expected values for pure POPC. Therefore, the ^{31}P NMR resonance around 30 ppm shows that the lipid membranes are well aligned with only a small contribution reaching into the −15 ppm region (Figure 35 on page 81, panel C).

^{2}H NMR spectra of sulfonyl-carprofen exhibit a single well-resolved quadrupolar splitting of 56 kHz when aligned parallel to the magnetic field direction (Figure 35 on page 81, panel A) and indicates fast rotational averaging of the CD_3 group around C-S bond, which ensures fast exchange of the positions of the methyl deuterons and results in a single quadrupolar splitting for all three labeled sites. In the center of the spectrum a small signal is apparent, which probably arises from the residual water deuterons (natural abundance 0.015 %). However,

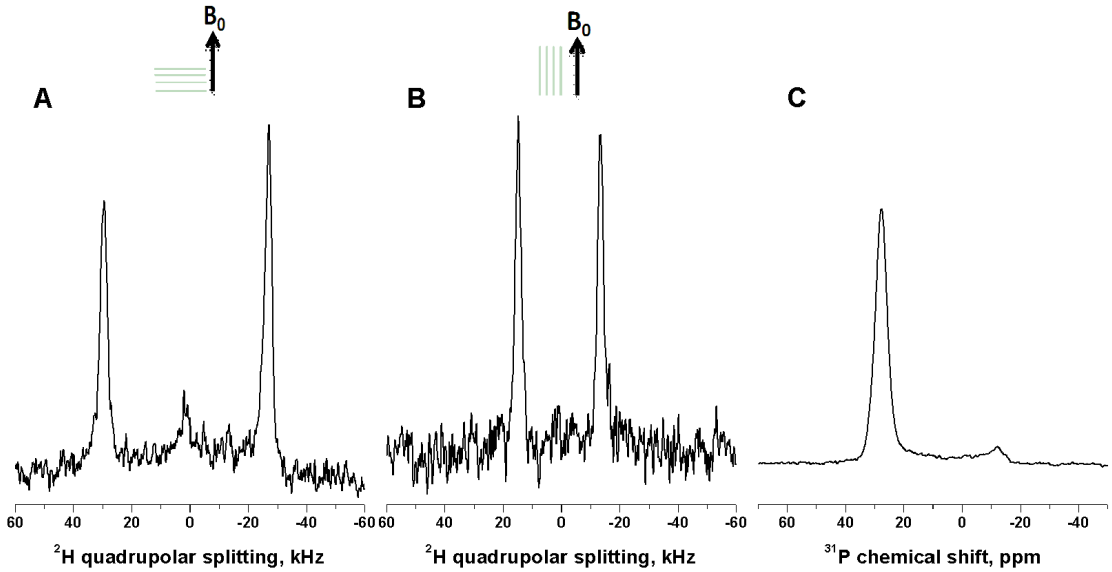

Figure 35: Deuterium solid-state NMR spectra of sulfonyl-carprofen reconstituted into model lipid membranes measured at 288 K (A and B). Spectrum in panel A is of the sample oriented parallel to the magnetic field direction; spectrum in panel B is of the sample oriented perpendicular to the magnetic field direction. Panel C shows the proton-decoupled ^{31}P chemical shift spectrum, indicating the orientation of the lipids membranes in the sample.

the signal to noise level does not permit to conclude whether there is a small splitting of this peak that would have indicated a small degree of ordering of the water molecules as a result of their interaction with the membrane (depending on hydration of the sample, the splittings should be about 1-2 kHz, but it is also a matter of resolution). The large breadth of the quadrupolar splitting (i.e. 56 kHz) is indicative of high order, which is not trivial for a small molecule. However, these molecules are quite rigid owing to the aromatic rings, which probably are the reason to the large ordering of the C–D bonds.

When the sample is measured in perpendicular alignment to the magnetic field direction (90°) the observed splitting is reduced to 28 kHz (Figure 35 on page 81, panel B). Within the experimental error, this is half of the value observed when oriented with the membrane normal parallel to the magnetic field direction. This indicates that at 288 K sulfonyl-carprofen exhibits fast rotational diffusion around the membrane normal concomitant with the ^{2}H NMR time scales.

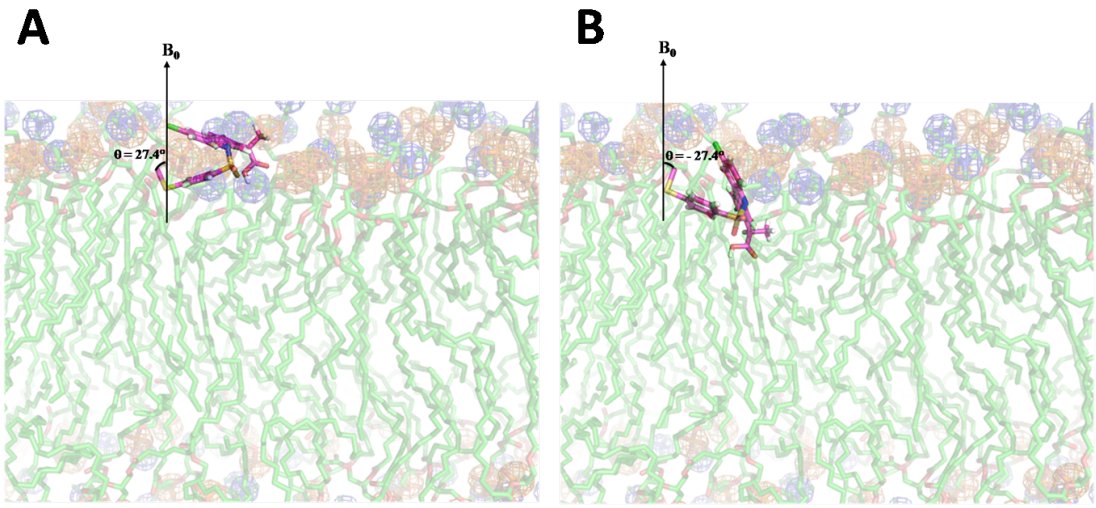

Figure 36: Alignments of sulfonyl-carprofen in oriented lipid membrane that agree with the experimental data. Only the orientations corresponding to $\theta = \pm 27.4°$ are shown. Orientations corresponding to $\theta = \pm 152.6°$ are not represented as these angles are complementary to 180°and are essentially the same. The structure of sulfonyl-carprofen was produced using ChemDraw3D software (CambridgeSoft, PerkinElmer Informatics) implementing MM2 energy minimization. It was then superimposed on the fluid phase POPC-only lipid bilayer generated by molecular dynamics simulation [Heller et al., 1993]. Panels A and B show the molecule oriented with different pitch angles.

Well-resolved peaks of the ^{2}H NMR spectra of sulfonyl-carprofen suggest that it exhibits a homogeneous orientation with respect to the magnetic field direction. The calculated angles are $\theta = \pm 27.4°$or $\theta = \pm 152.6°$ (complementary to 180°) indicate the orientation (i.e the tilt angle) of the C-S bond relative to the magnetic field direction. The uncertainty in the sign of the angles arises from the uncertainty in the sign of the quadrupole splitting. Angle $\pm 155.2°$ is complementary to 180°, because of the uncertainty in localization of the molecule on either side of a bilayer (top or bottom). In addition, neutron diffraction data showed that the CD_3 group of sulfonyl is located at ± 13 Å on the membrane profile, i.e. at the interface of the lipid head group (glycerol backbone) and the acyl chain (unpublished data from Dr. Hauß). This membrane region has an intermediate hydration level and spans ~ 3 Å. Taking all this into account, a model of sulfonyl-carprofen in lipid membrane was constructed (Figure 36 on page 82).

5.2.2 *Benzyl-carprofen*

Benzyl-carprofen was reconstituted into lipid membranes as described in methods, and investigated by ^{2}H ssNMR spectroscopy. Proton-

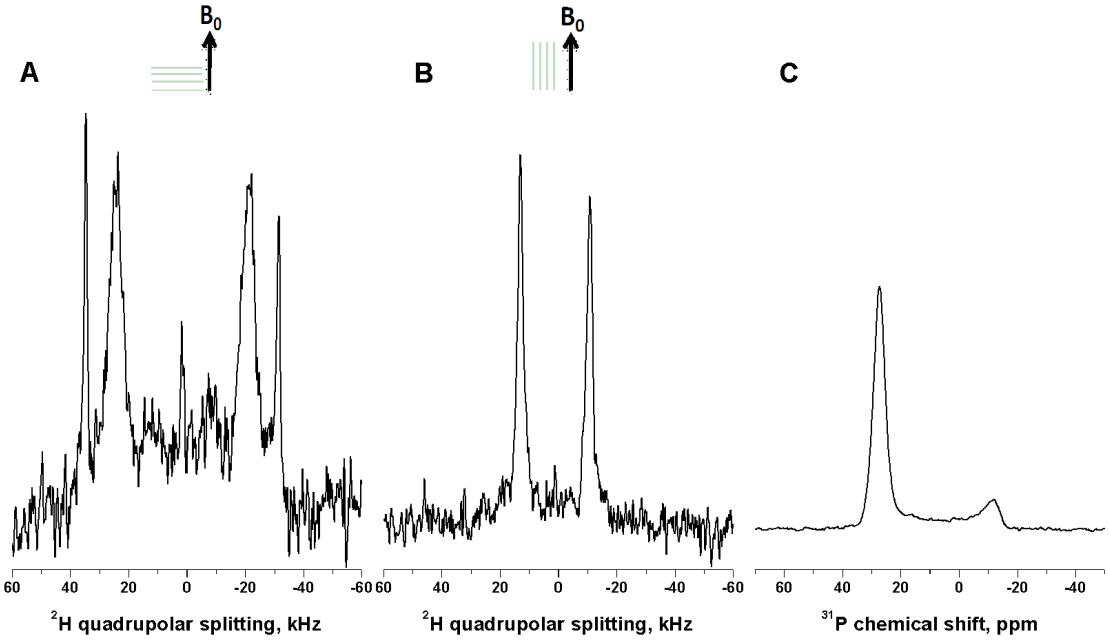

Figure 37: Deuterium solid-state NMR spectra of benzyl-carprofen reconstituted into model lipid membranes recorded at 288 K (panels A and B). Spectrum in panel A is of the sample oriented parallel to the magnetic field direction; spectrum in panel B is of the sample oriented perpendicular to the magnetic field direction. Panel C shows a proton-decoupled ^{31}P ssNMR spectrum, indicating the alignment of the lipid membranes in the sample.

decoupled ^{31}P spectrum of the sample was recorded to evaluate the quality of the orientation of the lipid bilayers (Figure 37 on page 83, panel C). Here as well, for the lipid normal oriented parallel to the magnetic field direction, the spectrum shows ^{31}P NMR resonance around 30 ppm and corresponds to well-oriented lipids, whereas a small contribution reaching into the –15 ppm region corresponds to unoriented part of the lipids in the measured sample. The unoriented contribution is somewhat higher than in the sample with sulfonyl-carprofen, but it is not significant in order to contribute to detectable misalignment of the benzyl-carprofen molecules. This conclusion is based on the previous evaluation of correlation between the amount of unoriented or poorly oriented lipids within bilayers with orientation of peptides embedded in those bilayers (Dr. Salnikov, not published data).

In Figure 37 on page 83 panel A, ^{2}H NMR spectrum of benzyl-carprofen exhibits two well resolved quadrupolar splittings, of 66

± 3 kHz and 46 ± 5 kHz and one that is not well resolved at 20 ± 10 kHz. The $\pm 3, \pm 5, \pm 10$ kHz represent the distribution width due to anisotropy of segmental orientations. As in this spectrum spectral lines are broad, it seemed appropriate to include the distribution values. Also here the large breadth of the quadrupolar splitting (i.e. 66 kHz) indicates a high order of the C–D bonds. Since benzyl-carprofen possesses several aromatic rings, the rigidity they impose onto molecular structure is a probable reason for high ordering of the bonds. They also might strongly interact and create a stable alignment with the membrane. Even though the splitting of 20 kHz is not very clear, longer experiment will not provide us with more information because of the low signal-to-noise ratio of the methylene deuterium signal.

Initial assignment of the quadrupolar splittings was done based on the integration of the area under the spectral lines, giving a ratio of 1:3.1:1.2 (beginning from the most outward). The expected ratio of 1:4:2, corresponding to the number of deuterons giving rise to the signal, is reduced owing to averaging motions occurring on the time scale of the quadrupolar interactions. The exchange of the 4 deuterons of the phenyl ring, imposed by 180° flips, caused an extra broadening of the lines at 46 ± 5 kHz. The analysis taking into account the dynamics of the labeled moieties provided a stronger basis for the assignment. The three quadrupolar splittings thus correspond to three deuterium populations: 66 ± 3 kHz to one deuteron bound to C_ζ, 46 ± 5 kHz to four deuterons of the phenyl ring (bound to C_ϵ and C_δ) and 20 ± 10 kHz to two deuterons of the $C_\beta D_2$.

Owing to the 180° flipping motion of the phenyl ring, the new averaged tensor of four deuterons (C_ϵ and C_δ) was calculated as explained in the experimental part above and the asymmetry parameter was found to be $\eta = 0.6$. In general, there are two possible aromatic ring reorientations: 1) 180° flips between two indistinguishable sites, where the atoms reside longer on the sites than time spend in transition; 2) continuous rotation, where the ring undergoes unhindered diffusion around C_β–C_γ bond. A number of deuterium solid-state NMR studies of powder pattern line shapes have concluded that phenyl side chains of the aromatic amino acids phenylalanine and tyrosine undergo 2-fold jumps about the C_β–C_γ bond axis in a variety of solid samples including the free amino acids, small natural and synthetic peptides, and proteins [Gall et al., 1981, Kinsey et al., 1981, Rice et al., 1981, Frey et al., 1985]. When trying to analyze the data considering continuous rotation, calculations did not agree with the experimental result. Therefore, also in benzyl-carprofen the likely motion of the phenyl ring is 180° flips between two indistinguishable sites.

The quadrupole splitting of 66 ± 3 kHz was assigned to the $C_\zeta D$ of the phenyl ring. The $C_\zeta D$ of the phenyl ring has an asymmetry parameter $\eta = 0$ and the associated angles were calculated as explained in methods.

The observed splitting of 20 ± 5 kHz was assigned to the methylene group CD_2. Let's consider the following arguments for this assignment. Because of the wide spectral line and low signal to noise ratio, it is difficult to conclude whether we observe one or perhaps two wide overlapping quadrupole splittings (Figure 37 on page 83, panel A). If the movements of the two C–D bonds are not identical and their tensors are not averaged, then two different quadrupole splittings have to be expected. If axially symmetric motion is considered, then one quadrupole splitting would be expected. For methylene groups of the fatty acyl chains *gauche-trans* isomerization is usually the prevailing motion. Considering the molecular structure of benzyl-carprofen, it is difficult to imagine any type of fast motion around the C–N bond. If this would happened, one could expect the entire benzyl group to flip 120° overcoming the steric hindrance of the carbazine with ease and this seems unlikely, if not impossible.

Orientational constraints from the phenyl deuterons were calculated and plotted in a contour plot to account for all spatial orientations (Figure 38 on page 86, red and dark blue lines for four and one deuterons, respectively). Orientational constraints from the methylene were calculated and plotted in the same contour plot and are shown in light blue and light green lines (Figure 38 on page 86). The internal lines in red and dark blue contours correspond to negative values, while external lines correspond to positive values. The internal lines in light blue and light green contours correspond to positive values, while external lines correspond to negative values. Positive and negative values arise due to uncertainty in the sign of the $\Delta\nu_Q$ (because we don't know which transitions produce the signal). The number of lines for either positive or negative values (3 lines for each) arise from the error bars of the observed spectral frequency–66 ± 3 kHz–resulted in the following frequencies: 63, 66, 69 kHz. Thus, for each quadrupole tensor there are 6 lines that delimit its orientational space.

Supplementary information can be obtained from the measurement of the sample with the membrane normal oriented perpendicularly to the external magnetic field direction. Such measurement usually can provide information on rotational diffusion of the molecules around the membrane normal [Aisenbrey and Bechinger, 2004]. Motional averaging is caused by rapid axial reorientation around the membrane normal, as common for small molecules in liquid crystalline bilayers. When the axis of motional averaging (i.e., the membrane normal) is aligned with the magnetic field, the observed splittings are not affected by this motion (Figure 37 on page 83, panel A). However, when the angle between the membrane normal and magnetic field is 90° (tilted orientation) this fast motion reduces the splittings of all affected signals by 50%, relative to their quadrupolar splitting in parallel orientation (Figure 37 on page 83, panel B). In the case of benzyl-carprofen sample tilted by 90°, the spectrum showed only

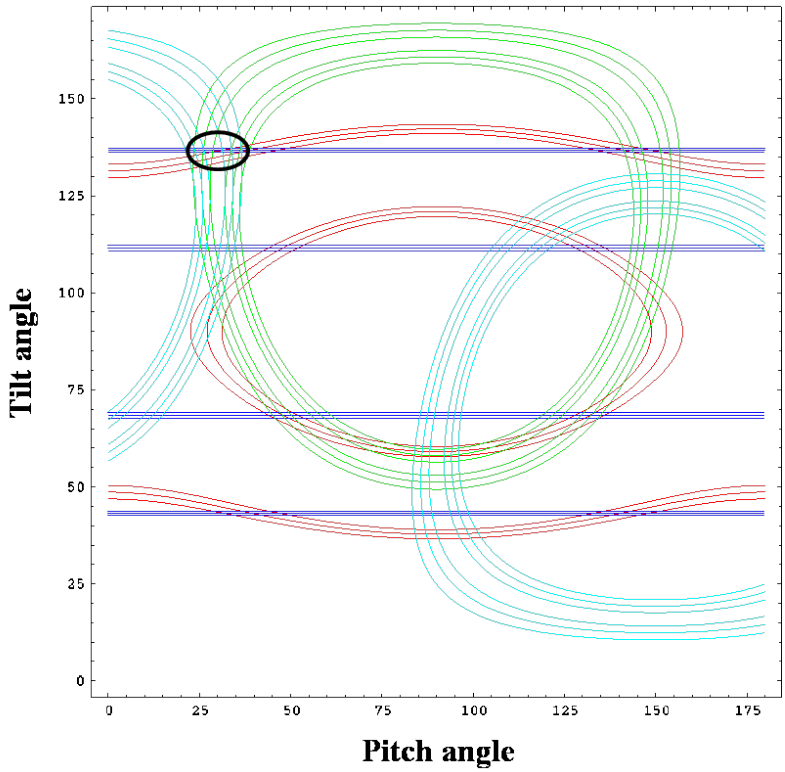

Figure 38: Contour plot depicting all spatial orientations of benzyl-carprofen, represented by the tilt and the pitch angles. The red lines trace angular pairs that agree with the experimental ^{2}H quadrupolar splitting of 46 $\pm$ 5 kHz, the dark blue lines are in agreement with the ^{2}H quadrupolar splitting of 66 $\pm$ 3 kHz, the green and the light blue lines are in agreement with the ^{2}H quadrupolar splitting of 20 $\pm$ 10 kHz. The circled cross section shows combinations of values that agree with the experimental results (where the constraints from all the segments meet in one point).

one splitting of 24 kHz (Figure 37 on page 83, panel B) and that was a very puzzling result as irrespective of the orientation of the sample, the number of splittings should not change if a fast motion occurs. However, motions on intermediate time scale could cause severe line broadening and have effects on relaxation, precluding the observation of all the signals. The single observed quadrupole splitting was assigned to the deuterons of the phenyl ring, which in parallel orientation gave rise to the quadrupolar splitting of 46 ± 5 kHz (Figure 37 on page 83, panel A). It is interesting to note that the broad spectral lines observed in the parallel orientation, appear narrow (scaled by -1/2) when the sample is in the tilted orientation. Clearly, rotational diffusion of the molecules around the membrane normal is fast enough to cause motional averaging of the anisotropy of the deuterium quadrupole interactions of the phenyl ring. Interestingly, quadrupole splitting from the methylene group was not observed in this orientation indicating that rotational diffusion of the molecule around the membrane normal is insufficient to average the anisotropy of quadrupole interactions of the methylene deuterons. Consequently, rotational correlation times should be faster than 10^{-5}sec (^{2}H NMR time scale). However, from the size of the molecule one could expect fast motional reorientation. For example, it was calculated that a single TM peptide should rotate fast enough around the membrane normal to average the interactions [Aisenbrey and Bechinger, 2004]. So why not this molecule? It is possible that benzyl-carprofen molecules stack together via the carbazine part to form oligomers, leaving the phenyl free to move. Lipid bilayers in these experiments were comprised of POPC, sphingomyelin and cholesterol leading to another possibility that benzyl-carprofen might interact with cholesterol molecules. This, in turn, would hinder the movement around the C–N bond resulting in nearly static methylene group. This could be studied using solid-state NMR techniques such as ^{13}C MAS NMR to follow the effects on chemical shifts of ^{13}C in carprofen, Rotational Echo DOuble Resonance (REDOR) or spin-diffusion or center-band-only detection of exchange (CODEX). Based on the above mentioned reasoning, the analysis of the methylene group was done referring to the methylene C–D bonds as static on the ^{2}H NMR time scale.

Most conventional approach to study molecular dynamics of solid state samples is static ^{2}H NMR. The width and appearance of the quadrupolar powder-pattern line shape can be significantly altered owing to partial averaging of the ^{2}H quadrupolar interaction and/or underlying linewidth changes that can result from molecular or atomic motion. Static line shape analysis can therefore give insight into the mechanism and timescale of the motional process. Unfortunately, it was not possible to perform static ^{2}H NMR experiments on the carprofen samples due to very small quantities of the material.

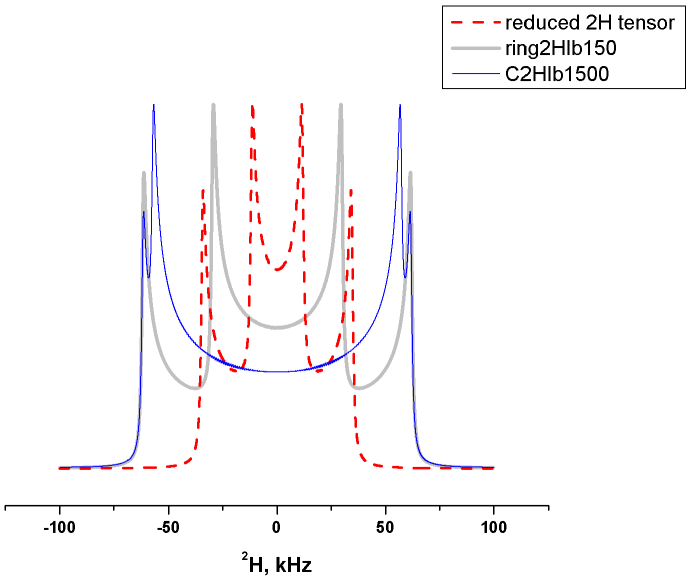

Figure 39: Simulated static ^{2}H NMR spectra of benzyl-carprofen deuterons in the tilted (90°) sample. The red line shape corresponds to reduced tensor of four benzyl ring deuterons; the grey line shape corresponds to single deuteron in position ζ of the benzyl ring; the blue line shape corresponds to methylene deuterons. Simulation was done by Dr. Salnikov E.

In order to explain the "disappearance" of the spectral frequency of the methylene deuterons from the spectrum of the tilted sample, we simulated static spectra (in the tilted orientation) for each group of deuterons in the benzyl-carprofen molecule. Figure 39 on page 88 shows calculated ^{2}H NMR spectra of three distinct groups of deuterons. The spectrum in red arises from four benzyl ring deuterons and exhibits full anisotropy of 45 kHz, which averages under fast rotational diffusion (~150 kHz), giving rise to one quadrupolar splitting of 24 kHz in the tilted orientation of the sample. The spectrum in grey arises from a single deuteron in position ζ of benzyl ring and exhibits full anisotropy of 90 kHz. Rotational diffusion needs to be at least three times faster than the quadrupolar interaction in order to average the latter. Here, rotational diffusion is not sufficiently fast to cause averaging and results in line broadening. The spectrum in blue arises from the methylene deuterons and exhibits full anisotropy of 120 kHz. Also here, the rotational diffusion is not sufficient to average the quadrupolar interaction and results in severe line broadening. Therefore, we believe that molecular motion is on the intermediate ^{2}H NMR time scale ($\leqslant 10^{-3}$ sec and $\geqslant 10^{-7}$sec) with respect to the quadrupolar interaction, which causes severe line broadening and results in "disappearance" of the spectral frequencies in the tilted sample.

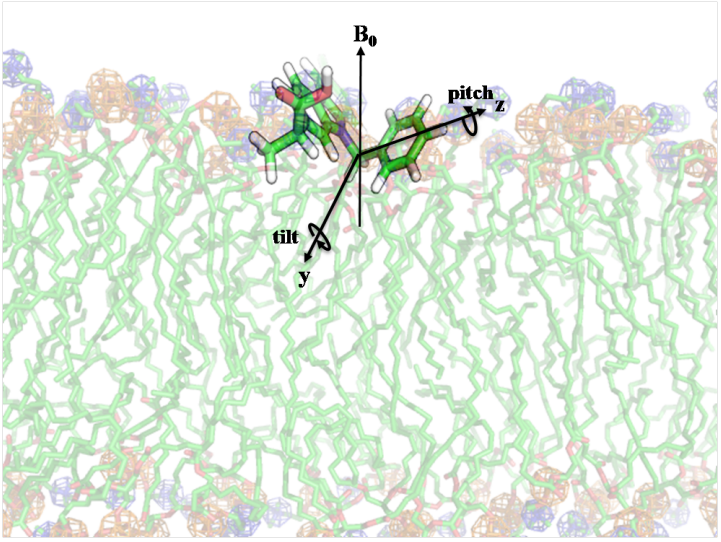

Figure 40: Alignment of benzyl-carprofen in oriented lipid membrane, corresponding to the spatial orientation shown in the contour plot. The structure of benzyl-carprofen was produced using ChemDraw3D software (CambridgeSoft, PerkinElmer Informatics) implementing MM2 energy minimization. It was then superimposed on the fluid phase POPC-only lipid bilayer generated by molecular dynamics simulation [Heller et al., 1993].

Neutron diffraction data showed that the deuterated benzyl (as the size of the benzyl segment comparable with the resolution of the neutron diffraction experiment, it is not possible to distinguish between phenyl and methylene) is located at ± 25 Å on the membrane profile, i.e. at the interface of the lipid headgroup and the water (unpublished data from Dr. Hauß). This region is fully hydrated and spans ~7-10 Å. Combining the knowledge from neutron scattering experiments and the analysis of the ssNMR data, a model of benzyl-carprofen in lipid membrane was constructed (Figure 40 on page 89).

It is interesting to note that carprofen derivatives being largely hydrophobic position themselves near the headgroups or at the interface of the lipids. It could have been expected that it would prefer a more hydrophobic part of the membrane (i.e. the middle of the membrane). This behavior might be due to entropic reasons. In the middle of the membrane in its fluid phase, the acyl chains are in high disorder. The presence of rigid molecules such as carprofen derivatives would force the acyl chains to arrange themselves around these molecules, which reduces the mobility of the chain ends. This in turn would decrease entropy. Hence, it is more favorable to accommodate carprofen derivatives molecules in the region closer to the headgroups, where the chain order is higher. It was shown for benzene for example, that it relocates from the bilayer core to the upper acyl chain region with increasing temperature [Bassolino-Klimas et al., 1993, 1995].

Remaining with benzene example, it has also been established that it has a large permanent quadrupole moment, leading to a negative partial charge within the ring and a positive partial charge on hydrogen atoms contributing to cation-π interactions. This concept was implemented for aromatic side chains of phenylalanine, tyrosine and tryptophane to explain their binding of cationic ligands or substrates [Dougherty, 1996]. In carprofen derivatives aromatic carbazine and benzene may thus favor interactions with partial positive charges such as those of choline headgroups of POPC and sphingomyelin (i.e. N^+H_3). The preference of carprofen derivatives for position of high molecular order near the lipid headgroups may thus be the result of a combination of all these effects.

In this work a mixture of POPC, SM and cholesterol was used to model lipid membranes. The behavior of such ternary mixture of SM, POPC, and cholesterol is complex. There is evidence that at low temperature (10°C) lateral domains are formed via segregation into phases: liquid-ordered phase comprised of SM and cholesterol and into liquid disordered phase comprised of predominantly POPC [Bunge et al., 2008]. The ssNMR experiments and neutron diffraction experiments of benzyl-carprofen were done at 15°C (neutron diffraction experiments at 37°C for benzyl-carprofen and experiments at 15°C for sulfonyl-carprofen are yet to be done; ssNMR measurements at 37°C were not performed), but from these experiments it is not evident whether carprofen derivatives localize in the domains formed by SM:cholesterol (rafts), or the liquid phase of POPC.

The lipid to cholesterol ratio used in these experiments is similar to the ratios that occur in neuronal membranes. The ratio of carprofen to lipids used here is the same as was found by [Narlawar et al., 2006] to be active under those conditions. From the numerous substitutions and activity experiments performed by [Narlawar et al., 2006], it seems that the activity of these carprofen derivatives consequent from their chemical structure and may be related to the interaction with cholesterol.

Benzyl-carprofen and sulfonyl-carprofen were found to be effective modulators of γ-secretase. They affected the cleavage at the γ38, γ40, and γ42 sites to a different extent and particularly suppressed the formation of Aβ42 while enhancing the formation of Aβ38 and thus showed the typical profile of effective NSAIDs. They were found to be the most potent inhibitors of Aβ42 [Narlawar et al., 2006]. The specific interaction site of these compounds has yet been identified. The speculation is that it might interact with PS1, the catalytic unit of γ-secretase, or that it can interact directly with APP. Considering the findings of this work, the possibility of direct interaction with APP seems more likely. The catalytic site of PS1 is located within the lipid bilayer and knowing that carprofen derivatives locate near the headgroups of the lipids, it is difficult to imagine how they would reach the

active site. In addition, direct interaction of carprofen-derivatives with PS1 is likely to abolish, rather than modify, its γ-secretase activity.

To further investigate the position and orientation of carprofen derivative molecules in lipid bilayer, molecular dynamics (MD) simulation study was launched. We believe that MD simulations will provide crucial complementary information at the atomistic level, including orientation, inter H-bonding and intermolecular electrostatic interactions.

Part III

CONCLUSIONS

6

CONCLUSIONS

Alzheimer's disease is a progressive neurological disease of the brain leading to the irreversible loss of neurons and the loss of intellectual abilities. To date there is no cure for AD and the disease is fatal. Its pathogenesis is complex, and involves marked molecular, cellular, and physiological changes.

The role of early preclinical processes that predate the pathology of AD and may enable or accelerate the aggregation of Aβ, thereby contributing to development of the disease, is still unknown. The Ca^{2+} hypothesis (refer to the Introduction for details), which introduced the concept of regulation by Ca^{2+} of neuronal death both in age-related and in pathogenic processes, attempts to explain how disruptions in Ca^{2+} homeostasis that continue over a prolonged period are a proximate cause of neurodegeneration in Alzheimer's disease. Numerous studies have linked Aβ to Ca^{2+} through demonstrating Ca^{2+} up-regulation by amyloid aggregates and relating Ca^{2+} dysregulation to AD-causing mutations. Accumulation of Aβ aggregates has been shown to initiate a complex pathological cascade, leading ultimately to memory alterations, cognitive impairments, and neuronal death [Lord et al., 2006]. Questions remain, however, concerning the possible contributory effect of normal physiological changes that take place in old age.

It was demonstrated in this work that 2 mM Ca^{2+} catalyze the formation of oligomers of Aβ(1-40), whereas in the absence of added Ca^{2+} mostly fibrils were formed. To the best of our knowledge, this is the first time that Ca^{2+} has been shown to induce Aβ(1-40) to form oligomers. The experiments were conducted with 2 mM added $CaCl_2$ and 100 µM Aβ. Ca^{2+} concentrations in the neuronal cytosol vary from hundreds of nanomolars to micromolars, which is consistent with the concentration of calcium traces in the "–Ca^{2+} buffer". Higher cytosolic calcium concentration may occur for prolonged periods during slow after-polarization current of ER after Ca^{2+} release from intracellular stores during LTP induction [Budd and Nicholls, 1999]. The cytosolic Ca^{2+} load is an important factor in regulating the size of mitochondrial Ca^{2+} stores [Budd and Nicholls, 1999], and during neuronal activity, which includes increases in cytosolic Ca^{2+}, mitochondria can take up significant loads of Ca^{2+} [LaFerla, 2002]. In addition, 2 mM Ca^{2+} is close to the concentration in the extracellular space, where formation of oligomers may be initiated and from where they might subsequently exert their toxic effect on the plasma membrane [Arispe et al., 1993b, Bucciantini et al., 2004]. Comparison of experiments carried out at 20

μm and 2 mM calcium suggests that extracellular calcium promotes oligomerization of Aβ(1-40). From additional information obtained by measuring residual calcium in the "–Ca^{2+}" buffer it is tempting to conclude that the intracellular concentration of calcium does not promote oligomerization. It remains however, that the intracellular Aβ peptides and calcium concentrations are difficult to evaluate and the existence of an intracellular effect can not be rejected at this stage. Studying these molecular processes in cell lines will be valuable in order to differentiate between the extracellular and intracellular Ca^{2+} effects. Based on the previously published data (as outlined in the Introduction) and the present findings, the potential effects of both extra- and intracellular calcium ions on Aβ and cells is schematically summarized in Figure 41 on page 97.

While the mechanism of Ca^{2+}-induced Aβ(1-40) aggregation is not known, the above finding might constitute the missing link that connects early dysregulation in Ca^{2+} signaling to subsequent onset of pathological and/or cognitive symptoms characteristic of AD. In their review focusing on intracellular Aβ production and its assembly states, LaFerla et al. [LaFerla et al., 2007] suggested that the buildup of intracellular Aβ might be an early event in the pathogenesis of AD as well as of Down syndrome. Taking that notion further, we contemplate that the early event in AD pathology might be the aggregation of intracellular Aβ in response to an increase in $[Ca^{2+}]_i$ as a result of natural aging processes. These early aggregates could in turn exert their toxic effect to alter Ca^{2+} signaling, which may account for the progressive decline in memory and the increase in neuronal cell apoptosis that occurs during AD. This may constitute a possible reason why in old age, when calcium imbalance is pronounced, the probability of developing AD is increased. It may also offer an alternative approach to prevention and treatment strategies for this disease, targeting mechanistic causes rather than late-stage symptoms.

In order to improve our understanding of the oligomerization mechanism, structural studies of the Ca^{+2}-binding site within Aβ(1-40) peptide should be considered. For example, formation of a salt bridge will induce chemical shift that will be observed in the HSQC spectrum.

An important followup of biological relevancy, could be cell toxicity experiments with Aβ(1-40) and Aβ(1-40)E22G oligomers and cell-cultural studies on the effect of increased intracellular Ca^{+2} on formation of Aβ(1-40) oligomers.

In a continuous effort to understand the proteolytic cleavage of APP, which leads to Aβ peptides production, this work focused on studying structural features within the APP TM sequence that may be essential for its processing by γ-secretase. The transmembrane domain of APP was chemically synthesized and successfully reconstituted into POPC bilayers exhibiting mostly α-helical conformation. Detailed ssNMR study of the APP_TM4K peptides isotopically labeled at several

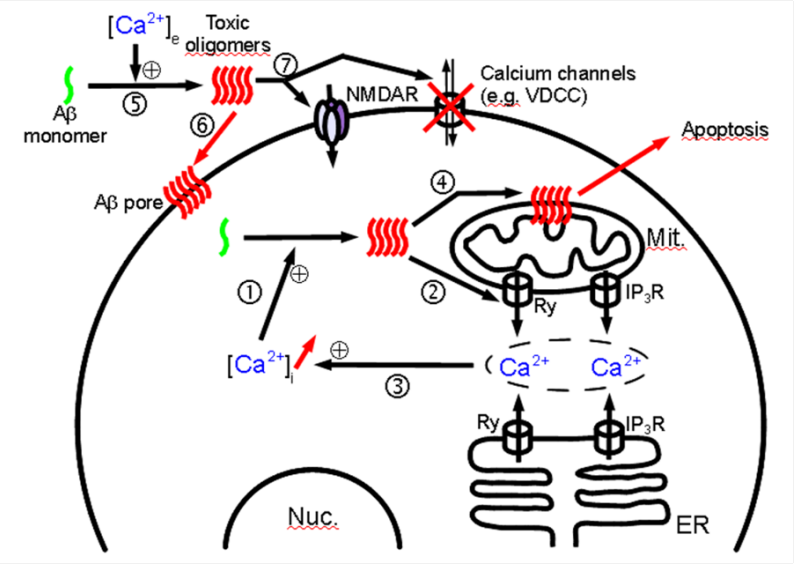

Figure 41: Potential interplay between Aβ oligomers, Ca^{2+}, and a target cell in the initial stages of Alzheimer's disease. (1) Age-related increase in $[Ca^{2+}]_i$ promotes oligomerization of intracellular Aβ. (2) Disruption of Ca^{2+} homeostasis by oligomers, by either binding to or modulating the activity of a number of receptors such as ryanodine (Ry) and inositol triphosphate (IP3R) [Stutzmann, 2005]. (3) Increase in $[Ca^{2+}]_i$. These three steps might form an inimical cycle leading to increases in both cytosolic calcium and Aβ oligomer concentrations. (4) Aβ oligomers disrupt intracellular membranes, leading to apoptosis [Kawahara et al., 2000, Arispe et al., 1993a,b]. (5) Extracellular calcium concentration ($[Ca^{2+}]_e$) promotes oligomerization of extracellular Aβ. (6) Oligomers form nonspecific pores in the plasma membrane, disturbing cellular integrity and leading to apoptosis [Bucciantini et al., 2004]. (7) Aβ oligomers can interact and impair calcium channels at the membrane surface, opening calcium importers and blocking calcium exporters such as the voltage-dependent calcium channel [Rovira et al., 2002]. Aβ oligomers can affect surface expression of N-methyl-D-aspartate receptors (NMDARs) [Dewachter et al., 2009], may increase [Molnár et al., 2004] or decrease the conductance [Shankar et al., 2007], and facilitate long-term synaptic depression by disrupting neuronal glutamate uptake [Li et al., 2009].

distinct sites dispersed throughout the TM sequence depicted large conformational and orientational heterogeneity at positions Ala-630, Ala-642 and Val-646. Clear transmembrane orientation was observed for Gly-637, which was previously shown to participate in the formation of stable dimer complexes [Munter et al., 2007, Miyashita et al., 2009, Sato et al., 2009]. Being a part of the last GxxxG motif, Gly-637 is the last amino acid that anchors the transmembrane orientation and stabilizes the dimer. This stability may be necessary in order to allow local unraveling of the helical structure at the cleavage sites. The strength of dimerization was proposed to control APP processing [Kienlen-Campard et al., 2008]. Residues near N′- and C′-terminal parts of the TM sequence, exhibit large conformational variability. Ala-630 and Val-646 show orientational distribution and likely experience conformational heterogeneity due to coexistence of helical and non-helical conformations [Lu et al., 2011]. Val-646 and Ala-642 are located within the ζ- and γ-cleavage sites, respectively, the former exhibits transmembrane orientation, while the latter shows extensive conformational heterogeneity and appears as having no defined orientation. The existence of non-helical conformation within the Ala-642 site was proposed by [Lu et al., 2011]. However, this is the first time that the orientational distribution was clearly observed by a structural approach. Evidence for conformational variability around γ- and ζ-cleavage sites may have important implications for the mechanism of cleavage and hence for Aβ production. Further detailed conformational studies of the adjacent residues within γ- and ζ-cleavage sites, as well as within the dimerization sequences, will provide a deeper understanding of the critical sites within the APP_TM domain. Precise structural characterization of these sites is necessary for further drug developments.

It will be beneficial to study longer sequences of APP such as TM+JM domains. Ala-630 for example, might behave differently as JM domain comes before Ala-630 in the sequence of APP.

APP_TM should be studied in different membrane compositions such as sphingomyelin, POPC and cholesterol, which will be more biologicaly relevant. Temperature variations should also be considered.

Benzyl-carprofen and sulfonyl-carprofen were found to be effective modulators of γ-secretase. They affected the cleavage at the γ38, γ40, and γ42 sites to a different extent and particularly suppressed the formation of Aβ42 while enhancing the formation of Aβ38 and thus showed the typical profile of effective NSAIDs. They were found to be the most potent inhibitors of Aβ42 [Narlawar et al., 2006]. Knowledge about the interaction of these molecules with lipid bilayer is essential for understanding of the underlying mechanism of their action. In this work we elucidated the orientation of carprofen derivatives in lipid bilayers using deuterium ssNMR.

Analysis of deuterium ssNMR data resulted in orientational constraints for sulfonyl-carprofen and for benzyl-carprofen molecules. The C–S bond of sulfonyl-carprofen was found to be oriented at $\pm 27.4°$ relative to the magnetic field direction, which corresponds to two possible orientations as shown in Figure 36 on page 82. For benzyl-carprofen the orientation that agrees with the experimental results is shown in Figure 40 on page 89, where rotational pitch angle (rotation about z-axis) is $\sim 31°$ and rotational tilt angle (rotation about y-axis) is $\sim 137°$. From neutron diffraction experiments (performed by our collaborators), it appears that both molecules prefer to position themselves near the headgroups or at the interface of the lipid membrane. This counter intuitive behavior might be due to entropic reasons – preference of the higher order of the lipid headgroups to avoid decrease in entropy within the acyl chain region, which are highly disordered in the fluid phase. Typically, interfacial partitioning should increase entropy due to increased chain disorder however, in this case a decrease in van der Waals interactions would counter-balance this effect [Jähnig, 1983]. Another possible contributing factor may be the cation-π interactions of the many aromatic rings in carprofen derivatives with partial positive charges, such as those of the choline headgroups of POPC and sphingomyelin (i.e. N^+H_3).

The specific interaction site of these compounds has yet been identified. The speculation is that it might interact with PS1, the catalytic unit of γ-secretase, or that it can interact directly with APP. Considering the findings of this work, the possibility of direct interaction with APP seems more likely. The catalytic site of PS1 is located within the lipid bilayer and knowing that carprofen derivatives locate near the headgroups of the lipids it is difficult to imagine how they would reach the active site. In addition, direct interaction of carprofen-derivatives with PS1 is likely to abolish, rather than modify, its γ-secretase activity. It seems more probable that carprofen-derivatives would interfere with proper APP-dimer formation, which is necessary for sequential cleavage by γ-secretase. In cases when the stability of a TM dimer is severely affected, a model from [Munter et al., 2007] proposes that the sequential cleavage is shifted from the ε-cut to positions Aβ38/Aβ37 and further to Aβ35/Aβ34 (Figure 2 on page 5), diminishing or greatly reducing Aβ42 production.

In order to refine the orientation of carprofen-derivatives in lipid bilayers, it would be interesting to obtain information on the carbazine part of these molecules, as neither of the derivatives studied here possessed deuterium labels on that part. This could provide additional constraints and would help to verify the constructed models. Segregated deuterium labeling of the benzyl part of benzyl-carprofen (i.e. phenyl ring and methylene group) could be beneficial to verify the chosen analysis approach in terms of assumed dynamics of the segments.

Partitioning of the carprofen-derivatives in complex lipid bilayers can be studied via ^{2}H-labeling of the lipids. Utilizing specific isotope labeling of lipids and / or of APP_TM peptide and of carprofen derivatives, the distances between labeled sites could be measured using REDOR or CODEX pulse sequences. These types of ssNMR experiments could provide insights into specific interactions of carprofen derivatives with lipids and / or with APP_TM peptide, which in turn could answer the following questions: are lipid rafts the target zone of carprofen-type molecules? How could this preference be correlated with the mechanism of action of carprofen derivatives? It would be of great interest to localize the specific peptide-drug interactions and to evaluate the location of carprofen derivatives within the ternary lipid mixture. The latter can be achieved by using deuterated lipids to detect phase separation [Mason et al., 2006] or by performing molecular dynamics simulations of this system, which can also provide an insight into the assumed orientations of these molecules, complementing the experimental results obtained and described in this work.

Studies with a single-type lipid membrane model will simplify the system and will allow to better asses the molecular orientation of the molecules in the membrane. Solid-state NMR spectra should be measured at different temperatures (e.g. 37° C), which will provide insight into dynamics of the carprofen molecules.

More than 100 years after its discovery AD is still, to a large extent, an unsolved mystery. Impressive progresses have been made in the field. However, most of the effort was concentrated on understanding the aggregation process of Aβ into fibrillar plaques, which until recently were considered the cause of the disease. But new ideas have emerged, and amyloid plaques may not be the evildoers everyone thought they were. More and more data suggest that oligomers are the toxic species that cause most of the neuronal damage. However, questions remain regarding the mechanism of Aβ production, Aβ oligomers formation and potential therapies. The results described here provide some answers to these questions. These inputs into the field of AD might be important and provide a better understanding of the disease processes and help in future potential drug design.

BIBLIOGRAPHY

A. Abragam. *The principles of nuclear magnetism*. Claredon Press, Oxford, 1961.

Atta Ahmad, Mahvish Muzaffar, and Vernon M. Ingram. Ca2+, within the physiological concentrations, selectively accelerates a[beta]42 fibril formation and not a[beta]40 in vitro. *BBA - Proteins Proteom*, 1794(10):1537–1548, October 2009. URL http://www.sciencedirect.com/science/article/B73DJ-4WR66HG-2/2/e25ddba9dfccc668b5b597664edef127.

Christopher Aisenbrey and Burkhard Bechinger. Investigations of polypeptide rotational diffusion in aligned membranes by 2h and 15n solid-state nmr spectroscopy. *Journal of the American Chemical Society*, 126(50):16676–16683, 2004. doi: 10.1021/ja0468675. URL http://pubs.acs.org/doi/abs/10.1021/ja0468675. PMID: 15600374.

Christopher Aisenbrey, Philippe Bertani, and Burkhard Bechinger. Solid-state nmr investigations of membrane-associated antimicrobial peptides. *Methods Mol Biol*, 618:209–233, 2010. doi: 10.1007/978-1-60761-594-1_14. URL http://dx.doi.org/10.1007/978-1-60761-594-1_14.

Valery V. Andrushchenko, Hans J. Vogel, and Elmar J. Prenner. Optimization of the hydrochloric acid concentration used for trifluoroacetate removal from synthetic peptides. *Journal of Peptide Science*, 13(1):37–43, 2007. ISSN 1099-1387. doi: 10.1002/psc.793. URL http://dx.doi.org/10.1002/psc.793.

Wim Annaert and Bart De Strooper. A cell biological perspective on alzheimer's disease. *Annu Rev Cell Dev Biol*, 18:25–51, 2002. doi: 10.1146/annurev.cellbio.18.020402.142302. URL http://dx.doi.org/10.1146/annurev.cellbio.18.020402.142302.

O.N. Antzutkin, J.J. Balbach, and R. Tycko. Site-specific identification of non-beta-strand conformations in alzheimer's beta-amyloid fibrils by solid-state nmr. *Biophysical Journal*, 84(5):3326–3335, 2003. URL ISI:000183123200050.

N. Arispe, H.B. Pollard, and E. Rojas. Giant multilevel cation channels formed by alzheimer disease amyloid beta-protein [a beta p-(1-40)] in bilayer membranes. *Proc Natl Acad Sci USA*, 90(22):10573–10577, November 1993a. URL http://www.pnas.org/content/90/22/10573.abstract.

N. Arispe, E. Rojas, and H.B. Pollard. Alzheimer disease amyloid beta protein forms calcium channels in bilayer membranes: blockade by tromethamine and aluminum. *Proceedings of the National Academy of Sciences of the United States of America*, 90(2):567–571, January 1993b. URL http://www.pnas.org/content/90/2/567.abstract.

C. S. Atwood, R. D. Moir, X. Huang, R. C. Scarpa, N. M. Bacarra, D. M. Romano, M. A. Hartshorn, R. E. Tanzi, and A. I. Bush. Dramatic aggregation of alzheimer abeta by cu(ii) is induced by conditions representing physiological acidosis. *J Biol Chem*, 273(21):12817–12826, May 1998.

D. Bassolino-Klimas, H. E. Alper, and T. R. Stouch. Solute diffusion in lipid bilayer membranes: an atomic level study by molecular dynamics simulation. *Biochemistry*, 32(47):12624–12637, Nov 1993.

Donna Bassolino-Klimas, Howard E. Alper, and Terry R. Stouch. Mechanism of solute diffusion through lipid bilayer membranes by molecular dynamics simulation. *Journal of the American Chemical Society*, 117(14):4118–4129, 1995. doi: 10.1021/ja00119a028. URL http://pubs.acs.org/doi/abs/10.1021/ja00119a028.

B. Bechinger and J. Seelig. Conformational changes of the phosphatidylcholine headgroup due to membrane dehydration. a 2h-nmr study. *Chem Phys Lipids*, 58(1-2):1–5, 1991a.

B. Bechinger and J. Seelig. Interaction of electric dipoles with phospholipid head groups. a 2h and 31p nmr study of phloretin and phloretin analogues in phosphatidylcholine membranes. *Biochemistry*, 30(16):3923–3929, Apr 1991b.

B. Bechinger, R. Kinder, M. Helmle, T. C. Vogt, U. Harzer, and S. Schinzel. Peptide structural analysis by solid-state nmr spectroscopy. *Biopolymers*, 51(3):174–190, 1999a. doi: 3.0.CO;2-7. URL http://dx.doi.org/3.0.CO;2-7.

B. Bechinger, J. M. Ruysschaert, and E. Goormaghtigh. Membrane helix orientation from linear dichroism of infrared attenuated total reflection spectra. *Biophys J*, 76(1 Pt 1):552–563, Jan 1999b. doi: 10.1016/S0006-3495(99)77223-1. URL http://dx.doi.org/10.1016/S0006-3495(99)77223-1.

B. Bechinger, P. Bertani, A. Marquette, A.J. Mason, S. Nedelkina, B. Perrone, M. Prudhon, E. Salnikov, V. Vidovic, S. Werten, and C. Aisenbrey. Coll 46-biophysical investigations of membrane-associated polypeptides by solid-state nmr: Applications to proteins and peptides involved in apoptosis, channel formation, antimicrobial action and transfection of nucleic acids. *Abstracts of Papers of the American Chemical Society*, 235:–, April 2008. URL ISI:000271775103488.

Burkhard Bechinger and Evgeniy S. Salnikov. The membrane interactions of antimicrobial peptides revealed by solid-state nmr spectroscopy. *Chemistry and Physics of Lipids*, 17 February 2012. doi: http://dx.doi.org/10.1016/j.chemphyslip.2012.01.009.

Burkhard Bechinger and Christina Sizun. Alignment and structural analysis of membrane polypeptides by 15n and 31p solid-state nmr spectroscopy. *Concepts Magn.Reson.*, 18A(2):130–145, 2003. URL http://dx.doi.org/10.1002/cmr.a.10070.

Andrew J. Beel, Charles K. Mobley, Hak Jun Kim, Fang Tian, Arina Hadziselimovic, Bing Jap, James H. Prestegard, and Charles R. Sanders. Structural studies of the transmembrane c-terminal domain of the amyloid precursor protein (app): does app function as a cholesterol sensor? *Biochemistry*, 47(36):9428–9446, Sep 2008. doi: 10.1021/bi800993c. URL http://dx.doi.org/10.1021/bi800993c.

Núria Benseny-Cases, Mercedes Cócera, and Josep Cladera. Conversion of non-fibrillar [beta]-sheet oligomers into amyloid fibrils in alzheimer's disease amyloid peptide aggregation. *Biochem Bioph Res Co*, 361(4):916–921, October 2007. URL http://www.sciencedirect.com/science/article/B6WBK-4P8984N-N/2/ea32ce77a56864b47e4c7d66588910ba.

Bruno A. Bergmans and Bart De Strooper. gamma-secretases: from cell biology to therapeutic strategies. *Lancet Neurol*, 9(2):215–226, Feb 2010. doi: 10.1016/S1474-4422(09)70332-1. URL http://dx.doi.org/10.1016/S1474-4422(09)70332-1.

Ilya Bezprozvanny and Mark P. Mattson. Neuronal calcium mishandling and the pathogenesis of alzheimer's disease. *Trends in Neurosci*, 31(9):454–463, September 2008. URL http://www.sciencedirect.com/science/article/B6T0V-4T4108G-1/2/f06be72ffa6e8931cdf23401364683a9.

T.V.P. Bliss and T. Lomo. Long-lasting potentiation of synaptic transmission in the dentate area of the anaesthetized rabbit following stimulation of the perforant path. *Journal Physiol*, 232(2):331–356, July 1973. URL http://jp.physoc.org/content/232/2/331.abstract.

L. Bojarski, J. Herms, and J. Kuznicki. Calcium dysregulation in alzheimer's disease. *Neurochemistry International*, 52(4-5):621–633, March 2008. URL ISI:000254968300013.

E. Bossy-Wetzel, R. Schwarzenbacher, and S.A. Lipton. Molecular pathways to neurodegeneration. *Nat Rev Neurosci*, 10:S2–S9, July 2004. URL ISI:000223202200002.

A. M. Brown, D. M. Tummolo, K. J. Rhodes, J. R. Hofmann, J. S. Jacobsen, and J. Sonnenberg-Reines. Selective aggregation of endogenous beta-amyloid peptide and soluble amyloid precursor protein in cerebrospinal fluid by zinc. *J Neurochem*, 69(3):1204–1212, Sep 1997.

Monica Bucciantini, Giulia Calloni, Fabrizio Chiti, Lucia Formigli, Daniele Nosi, Christopher M. Dobson, and Massimo Stefani. Prefibrillar amyloid protein aggregates share common features of cytotoxicity. *J.Biol.Chem.*, 279(30):31374–31382, July 2004. URL http://www.jbc.org/content/279/30/31374.abstract.

S.L. Budd and D.G. Nicholls. Mitochondria in the life and death of neurons. *Essays Biochem*, 33:43–52, 1999. URL ISI:000172821200004.

Andreas Bunge, Peter Müller, Martin Stöckl, Andreas Herrmann, and Daniel Huster. Characterization of the ternary mixture of sphingomyelin, popc, and cholesterol: support for an inhomogeneous lipid distribution at high temperatures. *Biophys J*, 94 (7):2680–2690, Apr 2008. doi: 10.1529/biophysj.107.112904. URL http://dx.doi.org/10.1529/biophysj.107.112904.

A. I. Bush, W. H. Pettingell, G. Multhaup, M. d Paradis, J. P. Vonsattel, J. F. Gusella, K. Beyreuther, C. L. Masters, and R. E. Tanzi. Rapid induction of alzheimer a beta amyloid formation by zinc. *Science*, 265(5177):1464–1467, Sep 1994.

E. Cerf, R. Sarroukh, S. Tamamizu-Kato, L. Breydo, S. Derclaye, Y.F. Dufrêne, V. Narayanaswami, E. Goormaghtigh, J.M. Ruysschaert, and V. Raussens. Antiparallel beta-sheet: a signature structure of the oligomeric amyloid beta-peptide. *Biochem J*, 421:415–423, August 2009. URL ISI:000268615900010.

Eduard Y. Chekmenev, Qianwen Zhang, Kevin W. Waddell, Mark S. Mashuta, and Richard J. Wittebort. 15n chemical shielding in glycyl tripeptides: measurement by solid-state nmr and correlation with x-ray structure. *J Am Chem Soc*, 126(1):379–384, Jan 2004. doi: 10.1021/ja0370342. URL http://dx.doi.org/10.1021/ja0370342.

Y.N. Chirgadze and N.A. Nevskaya. Infrared-spectra and resonance interaction of amide-one vibration of anti-parallel-chain pleated sheet. *Biopolymers*, 15(4):607–625, 1976. URL ISI:A1976BM81200001.

D.H. Chui, H. Tanahashi, K. Ozawa, S. Ikeda, F. Checler, O. Ueda, H. Suzuki, W. Araki, H. Inoue, K. Shirotani, K. Takahashi, F. Gallyas, and T. Tabira. Transgenic mice with alzheimer presenilin 1 mutations show accelerated neurodegeneration without amyloid plaque formation. *Nat Med*, 5(5):560–564, May 1999. URL ISI:000081497400038.

B.J. Cummings and C.W. Cotman. Image-analysis of beta-amyloid load in alzheimers-disease and relation to dementia severity. *Lancet*, 346(8989):1524–1528, December 1995. URL ISI:A1995TJ29100012.

Karie N. Dahlgren, Arlene M. Manelli, Jr. Stine, W.Blaine, Lorinda K. Baker, Grant A. Krafft, and Mary Jo LaDu. Oligomeric and fibrillar species of amyloid-beta peptides differentially affect neuronal viability. *J.Biol.Chem.*, 277(35):32046–32053, August 2002. URL http://www.jbc.org/cgi/content/abstract/277/35/32046.

Jens Danielsson, Roberta Pierattelli, Lucia Banci, and Astrid Gräslund. High-resolution nmr studies of the zinc-binding site of the alzheimer's amyloid beta-peptide. *FEBS J*, 274(1):46–59, Jan 2007. doi: 10.1111/j.1742-4658.2006.05563.x. URL http://dx.doi.org/10.1111/j.1742-4658.2006.05563.x.

J.H. Davis, K.R. Jeffrey, M. Bloom, M.I. Valic, and T.P. Higgs. Quadrupolar echo deuteron magnetic resonance spectroscopy in ordered hydrocarbon chains. *Chemical Physics Letters*, 42(2): 390 – 394, 1976. ISSN 0009-2614. doi: 10.1016/0009-2614(76)80392-2. URL http://www.sciencedirect.com/science/article/pii/0009261476803922.

Rodrigo F M. de Almeida, Aleksandre Fedorov, and Manuel Prieto. Sphingomyelin/phosphatidylcholine/cholesterol phase diagram: boundaries and composition of lipid rafts. *Biophys J*, 85(4):2406–2416, Oct 2003. doi: 10.1016/S0006-3495(03)74664-5. URL http://dx.doi.org/10.1016/S0006-3495(03)74664-5.

Fernanda G. De Felice, Pauline T. Velasco, Mary P. Lambert, Kirsten Viola, Sara J. Fernandez, Sergio T. Ferreira, and William L. Klein. Abeta oligomers induce neuronal oxidative stress through an n-methyl-d-aspartate receptor-dependent mechanism that is blocked by the alzheimer drug memantine. *J.Biol.Chem.*, 282(15):11590–11601, April 2007. URL http://www.jbc.org/content/282/15/11590.abstract.

B. De Strooper and W. Annaert. Proteolytic processing and cell biological functions of the amyloid precursor protein. *J Cell Sci*, 113 (Pt 11):1857–1870, Jun 2000.

I. Dewachter, R.K. Filipkowski, C. Priller, L. Ris, J. Neyton, S. Croes, D. Terwel, M. Gysemans, H. Devijver, P. Borghgraef, E. Godaux, L. Kaczmarek, J. Herms, and F. Van Leuven. Deregulation of nmda-receptor function and down-stream signaling in app[v717i] transgenic mice. *Neurobiol Aging*, 30(2):241–256, February 2009. URL http://www.sciencedirect.com/science/article/B6T09-4P90368-2/2/ba0c5abbc942f6dbb4f70adda4e1cc50.

D. A. Dougherty. Cation-pi interactions in chemistry and biology: a new view of benzene, phe, tyr, and trp. *Science*, 271(5246):163–168, Jan 1996.

Melinda J. Duer. *Introduction to solid-state NMR spectroscopy*. John Wiley & Sons, 2004.

T. Dyrks, E. Dyrks, T. Hartmann, C. Masters, and K. Beyreuther. Amyloidogenicity of beta a4 and beta a4-bearing amyloid protein precursor fragments by metal-catalyzed oxidation. *J Biol Chem*, 267(25): 18210–18217, Sep 1992.

Dieter Edbauer, Edith Winkler, Joerg T. Regula, Brigitte Pesold, Harald Steiner, and Christian Haass. Reconstitution of gamma-secretase activity. *Nat Cell Biol*, 5(5):486–488, May 2003. doi: 10.1038/ncb960. URL http://dx.doi.org/10.1038/ncb960.

Robert Ehehalt, Patrick Keller, Christian Haass, Christoph Thiele, and Kai Simons. Amyloidogenic processing of the alzheimer beta-amyloid precursor protein depends on lipid rafts. *The Journal of Cell Biology*, 160(1):113–123, January 2003. URL http://jcb.rupress.org/content/160/1/113.abstract.

W. P. Esler, E. R. Stimson, J. M. Jennings, J. R. Ghilardi, P. W. Mantyh, and J. E. Maggio. Zinc-induced aggregation of human and rat beta-amyloid peptides in vitro. *J Neurochem*, 66(2):723–732, Feb 1996.

R. Etcheberrigaray, N. Hirashima, L. Nee, J. Prince, S. Govoni, M. Racchi, R.E. Tanzi, and D.L. Alkon. Calcium responses in fibroblasts from asymptomatic members of alzheimer's disease families. *Neurobiol Dis*, 5(1):37–45, July 1998. URL ISI:000075183700004.

E. Ferreiro, C.R. Oliveira, and C. Pereira. Involvement of endoplasmic reticulum ca2+ release through ryanodine and inositol 1,4,5-triphosphate receptors in the neurotoxic effects induced by the amyloid-beta peptide. *J Neurosci Res*, 76(6):872–880, June 2004. URL ISI:000221836200012.

M. H. Frey, S. J. Opella, A. L. Rockwell, and L. M. Gierasch. Solid-state nmr of cyclic pentapeptides. *Journal of the American Chemical Society*, 107(7):1946–1951, 1985. doi: 10.1021/ja00293a025. URL http://pubs.acs.org/doi/abs/10.1021/ja00293a025.

U. P. Fringeli and Hs. H. Gühnthard. *Infrared membrane spectroscopy. In Molecular Biology, Biochemistry and Biophysics.*, volume 31. Springer Verlag, Berlin, 1981.

C. M. Gall, J. A. DiVerdi, and S. J. Opella. Phenylalanine ring dynamics by solid-state deuterium nmr. *Journal of the American Chemical Society*, 103(17):5039–5043, 1981. doi: 10.1021/ja00407a012. URL http://pubs.acs.org/doi/abs/10.1021/ja00407a012.

Elka R. Georgieva, Trudy F. Ramlall, Peter P. Borbat, Jack H. Freed, and David Eliezer. Membrane-bound alpha-synuclein forms an extended helix: Long-distance pulsed esr measurements using vesicles, bicelles, and rodlike micelles. *Journal of the American Chemical Society*, 130(39):12856–12857, 2008. doi: 10.1021/ja804517m.

URL http://pubs.acs.org/doi/abs/10.1021/ja804517m. PMID: 18774805.

Ralf W. Glaser, Carsten Sachse, Ulrich H N. Dürr, Parvesh Wadhwani, Sergii Afonin, Erik Strandberg, and Anne S. Ulrich. Concentration-dependent realignment of the antimicrobial peptide pgla in lipid membranes observed by solid-state 19f-nmr. *Biophys J*, 88(5):3392–3397, May 2005. doi: 10.1529/biophysj.104.056424. URL http://dx.doi.org/10.1529/biophysj.104.056424.

Young-Mi Go, Jerry J. Gipp, R Timothy Mulcahy, and Dean P. Jones. H202-dependent activation of gclc-are4 reporter occurs by mitogen-activated protein kinase pathways without oxidation of cellular glutathione or thioredoxin-1. *J Biol Chem*, 279(7):5837–5845, Feb 2004. doi: 10.1074/jbc.M307547200. URL http://dx.doi.org/10.1074/jbc.M307547200.

E. Goormaghtigh and J.-M. Ruysschaert. *Molecular Description of Biological Membrane Components by Computer Aided Conformational Analysis*, volume 1. CRC Press Inc., Boca Raton, FL, 1990.

E. Goormaghtigh, Cabiaux V., and J.M. Ruysschaert. Determination of soluble and membrane protein structure by fourier transform infrared spectroscopy. i. assignments and model compounds. *Subcell Biochem 23:*, (23):329–362, 1994.

Erik Goormaghtigh, Vincent Raussens, and Jean-Marie Ruysschaert. Attenuated total reflection infrared spectroscopy of proteins and lipids in biological membranes. *Biochimica et Biophysica Acta (BBA) - Reviews on Biomembranes*, 1422(2):105 – 185, 1999. ISSN 0304-4157. doi: 10.1016/S0304-4157(99)00004-0. URL http://www.sciencedirect.com/science/article/pii/S0304415799000040.

P.M. Gorman, S. Kim, M. Guo, R.A. Melnyk, J. McLaurin, P.E. Fraser, J.U. Bowie, and A. Chakrabartty. Dimerization of the transmembrane domain of amyloid precursor proteins and familial alzheimer's disease mutants. *Bmc Neuroscience*, 9:–, January 2008. URL ISI:000253965800001.

K.N. Green and F.M. LaFerla. Linking calcium to a beta and alzheimer's disease. *Neuron*, 59(2):190–194, July 2008. URL ISI:000258252700004.

M. Groenning, L. Olsen, M. van de Weert, J.M. Flink, S. Frokjaer, and F.S. Jorgensen. Study on the binding of thioflavin t to beta-sheet-rich and non-beta-sheet cavities. *J Struct Biol*, 158(3):358–369, June 2007. URL ISI:000246927800010.

C. Haass and D.J. Selkoe. Soluble protein oligomers in neurodegeneration: lessons from the alzheimer's amyloid beta-peptide.

Nat Rev Mol Cell Bio, 8(2):101–112, February 2007. URL ISI:000243730300012.

E. L. Hahn. Spin echoes. *Phys. Rev.*, 80:580–594, Nov 1950. doi: 10.1103/PhysRev.80.580. URL http://link.aps.org/doi/10.1103/PhysRev.80.580.

G.S Harbison, L.W Jelinski, R.E Stark, D.A Torchia, J Herzfeld, and R.G Griffin. 15n chemical shift and 15n-13c dipolar tensors for the peptide bond in [1-13c]glycyl[15n]glycine hydrochloride monohydrate. *Journal of Magnetic Resonance (1969)*, 60(1):79 – 82, 1984. ISSN 0022-2364. doi: 10.1016/0022-2364(84)90027-1. URL http://www.sciencedirect.com/science/article/pii/0022236484900271.

J. Hardy and D.J. Selkoe. Medicine - the amyloid hypothesis of alzheimer's disease: Progress and problems on the road to therapeutics. *Science*, 297(5580):353–356, July 2002. URL ISI:000176892600038.

J.A. Hardy and G.A. Higgins. Alzheimers-disease - the amyloid cascade hypothesis. *Science*, 256(5054):184–185, April 1992. URL ISI:A1992HM89600019.

C. J. Hartzell, M. Whitfield, T. Oas, and G. Drobny. Determination of the nitrogen-15 and carbon-13 chemical shift tensors of l-[13c]alanyl-l-[15n]alanine from the dipole-coupled powder patterns. *Journal of the American Chemical Society*, 109(20):5966–5969, 1987. doi: 10.1021/ja00254a012. URL http://pubs.acs.org/doi/abs/10.1021/ja00254a012.

S. Hediger, B.H. Meier, and R.R. Ernst. Adiabatic passage hartmann-hahn cross polarization in nmr under magic angle sample spinning. *Chemical Physics Letters*, 240(5, 6):449 – 456, 1995. ISSN 0009-2614. doi: 10.1016/0009-2614(95)00505-X. URL http://www.sciencedirect.com/science/article/pii/000926149500505X.

Helmut Heller, Michael Schaefer, and Klaus Schulten. Molecular dynamics simulation of a bilayer of 200 lipids in the gel and in the liquid crystal phase. *The Journal of Physical Chemistry*, 97(31):8343–8360, 1993. doi: 10.1021/j100133a034. URL http://pubs.acs.org/doi/abs/10.1021/j100133a034.

Yukio. Hiyama, Chien Hua. Niu, James V. Silverton, Alfonso. Bavoso, and Dennis A. Torchia. Determination of 15n chemical shift tensor via 15n-2h dipolar coupling in boc-glycylglycyl[15n glycine]benzyl ester. *Journal of the American Chemical Society*, 110(8):2378–2383, 1988. doi: 10.1021/ja00216a006. URL http://pubs.acs.org/doi/abs/10.1021/ja00216a006.

M.C. Irizarry, F. Soriano, M. McNamara, K.J. Page, D. Schenk, D. Games, and B.T. Hyman. A beta deposition is associated with neuropil changes, but not with overt neuronal loss in the human amyloid precursor protein v717f (pdapp) transgenic mouse. *J.Neurosci.*, 17(18):7053–7059, September 1997. URL ISI:A1997XY89600023.

Adrian M. Isaacs, David B. Senn, Menglan Yuan, James P. Shine, and Bruce A. Yankner. Acceleration of amyloid beta-peptide aggregation by physiological concentrations of calcium. *J.Biol.Chem.*, 281 (38):27916–27923, September 2006. URL http://www.jbc.org/cgi/content/abstract/281/38/27916.

E. Ito, K. Oka, R. Etcheberrigaray, T.J. Nelson, D.L. Mcphie, B. Tofelgrehl, G.E. Gibson, and D.L. Alkon. Internal ca2+ mobilization is altered in fibroblasts from patients with alzheimer-disease. *Proc Natl Acad Sci USA*, 91(2):534–538, January 1994. URL ISI:A1994MR98900023.

F Jähnig. Thermodynamics and kinetics of protein incorporation into membranes. *Proceedings of the National Academy of Sciences*, 80(12): 3691–3695, 1983. URL http://www.pnas.org/content/80/12/3691.abstract.

B.L. Kagan, R. Azimov, and R. Azimova. Amyloid peptide channels. *J Membrane Biol*, 202(1):1–10, November 2004. URL ISI:000225737000001.

K. Kamino, H.T. Orr, H. Payami, E.M. Wijsman, M.E. Alonso, S.M. Pulst, L. Anderson, S. O'dahl, E. Nemens, J.A. White, A.D. Sadovnick, M.J. Ball, J. Kaye, A. Warren, M. Mcinnis, S.E. Antonarakis, J.R. Korenberg, V. Sharma, W. Kukull, E Larson, L.L. Heston, G.M. Martin, T.D. Bird, and G.D. Schellenberg. Linkage and mutational analysis of familial alzheimer-disease kindreds for the app gene region. *Am J Hum Genet*, 51(5):998–1014, November 1992. URL ISI:A1992JU84000010.

Arthur Karlin. Emerging structure of the nicotinic acetylcholine receptors. *Nat Rev Neurosci*, 3(2):102–114, February 2002. ISSN 1471-003X. URL http://dx.doi.org/10.1038/nrn731.

Masahiro Kawahara, Yoichiro Kuroda, Nelson Arispe, and Eduardo Rojas. Alzheimer's beta-amyloid, human islet amylin, and prion protein fragment evoke intracellular free calcium elevations by a common mechanism in a hypothalamic gnrh neuronal cell line. *JBC*, 275(19):14077–14083, May 2000.

James Keeler. *Understanding NMR Spectroscopy*. John Wiley & Sons, Ltd., Department of Chemistry, University of Cambridge, UK, 1 edition, 2002.

Z.S. Khachaturian. Calcium hypothesis of alzheimer's disease and brain aging. *Ann NY Acad Sci*, 747(1):1–11, 1994. URL http://dx.doi.org/10.1111/j.1749-6632.1994.tb44398.x.

P. Kienlen-Campard, B. Tasiaux, J. Van Hees, M.L. Li, S. Huysseune, T. Sato, J.Z. Fei, S. Aimoto, P.J. Courtoy, S.O. Smith, S.N. Constantinescu, and J.N. Octave. Amyloidogenic processing but not amyloid precursor protein (app) intracellular c-terminal domain production requires a precisely oriented app dimer assembled by transmembrane gxxxg motifs. *Journal of Biological Chemistry*, 283(18):12680–12680, 2008. URL ISI:000255340000085.

R A Kinsey, A Kintanar, and E Oldfield. Dynamics of amino acid side chains in membrane proteins by high field solid state deuterium nuclear magnetic resonance spectroscopy. phenylalanine, tyrosine, and tryptophan. *Journal of Biological Chemistry*, 256(17):9028–9036, 1981. URL http://www.jbc.org/content/256/17/9028.abstract.

W.L. Klein, G.A. Krafft, and C.E. Finch. Targeting small abeta oligomers: the solution to an alzheimer's disease conundrum? *Trends in Neurosciences*, 24(4):219–224, April 2001. URL ISI:000168766000014.

M.R.H. Krebs, E.H.C. Bromley, and A.M. Donald. The binding of thioflavin-t to amyloid fibrils: localisation and implications. *J Struct Biol*, 149(1):30–37, January 2005. URL ISI:000226310900004.

Thomas Kukar, Michael Paul Murphy, Jason L. Eriksen, Sarah A. Sagi, Sascha Weggen, Tawnya E. Smith, Thomas Ladd, Murad A. Khan, Rajashaker Kache, Jenny Beard, Mark Dodson, Sami Merit, Victor V. Ozols, Panos Z. Anastasiadis, Pritam Das, Abdul Fauq, Edward H. Koo, and Todd E. Golde. Diverse compounds mimic alzheimer disease-causing mutations by augmenting abeta42 production. *Nat Med*, 11(5):545–550, May 2005. doi: 10.1038/nm1235. URL http://dx.doi.org/10.1038/nm1235.

Y. Kuroda and M. Kawahara. Aggregation of amyloid beta-protein and its neurotoxicity - enhancement by aluminum and other metals. *Tohoku J Exp Med*, 174(3):263–268, November 1994. URL ISI:A1994QE68400010.

F.M. LaFerla. Calcium dyshomeostasis and intracellular signalling in alzheimer's disease. *Nat Rev Neurosci*, 3(11):862–872, November 2002. URL ISI:000179041700017.

Frank M. LaFerla, Kim N. Green, and Salvatore Oddo. Intracellular amyloid-[beta] in alzheimer's disease. *Nat Rev Neurosci*, 8(7):499–509, July 2007. URL http://dx.doi.org/10.1038/nrn2168.

M.P. Lambert, A.K. Barlow, B.A. Chromy, C. Edwards, R. Freed, M. Liosatos, T.E. Morgan, I. Rozovsky, B. Trommer, K.L. Viola, P. Wals, C. Zhang, C.E. Finch, G.A. Krafft, and W.L. Klein. Diffusible, nonfibrillar ligands derived from a beta(1-42) are potent central nervous system neurotoxins. *Proc Natl Acad Sci USA*, 95(11): 6448–6453, May 1998. URL ISI:000073852600107.

Hilal A. Lashuel, Dean M. Hartley, Benjamin M. Petre, Joseph S. Wall, Martha N. Simon, Thomas Walz, and Peter T. Lansbury Jr. Mixtures of wild-type and a pathogenic (e22g) form of a[beta]40 in vitro accumulate protofibrils, including amyloid pores. *Journal of Molecular Biology*, 332(4):795–808, September 2003. URL http://www.sciencedirect.com/science/article/B6WK7-49G55G4-7/2/086615f62e58e6e6e2943b792b4869ff.

Tong Lay Lau, Ernesto E. Ambroggio, Deborah J. Tew, Roberto Cappai, Colin L. Masters, Gerardo D. Fidelio, Kevin J. Barnham, and Frances Separovic. Amyloid-[beta] peptide disruption of lipid membranes and the effect of metal ions. *Journal of Molecular Biology*, 356(3):759–770, February 2006. URL http://www.sciencedirect.com/science/article/B6WK7-4HVDS7T-5/2/9ccba002da9f017112bd211c96722bb1.

D. K. Lee, R. J. Wittebort, and A. Ramamoorthy. Characterization of 15n chemical shift and 1h 15n dipolar coupling interactions in a peptide bond of uniaxially oriented and polycrystalline samples by one-dimensional dipolar chemical shift solid-state nmr spectroscopy. *Journal of the American Chemical Society*, 120(34):8868–8874, 1998. doi: 10.1021/ja981599u. URL http://pubs.acs.org/doi/abs/10.1021/ja981599u.

D.K Lee, J.S Santos, and A Ramamoorthy. Nitrogen 15 chemical shift anisotropy and 1h 15n dipolar coupling tensors associated with the phenylalanine residue in the solid state. *Chemical Physics Letters*, 309 (3, 4):209 – 214, 1999. ISSN 0009-2614. doi: 10.1016/S0009-2614(99)00689-2. URL http://www.sciencedirect.com/science/article/pii/S0009261499006892.

Dong-Kuk Lee, Yufeng Wei, and A. Ramamoorthy. A two-dimensional magic-angle decoupling and magic-angle turning solid-state nmr method: An application to study chemical shift tensors from peptides that are nonselectively labeled with 15n isotope. *The Journal of Physical Chemistry B*, 105(20):4752–4762, 2001. doi: 10.1021/jp002902s. URL http://pubs.acs.org/doi/abs/10.1021/jp002902s.

H LeVine, 3rd. Thioflavine t interaction with synthetic alzheimer's disease beta-amyloid peptides: detection of amyloid aggregation

in solution. *Protein Sci*, 2(3):404–410, Mar 1993. doi: 10.1002/pro.5560020312. URL http://dx.doi.org/10.1002/pro.5560020312.

Malcolm H. Levitt. *Spin Dynamics: Basics of Nuclear Magnetic Resonance*. John Wiley & Sons, Ltd., Baffins Lane, Chichester, West Sussex PO19 1UD, England, 2001.

S.C. Li and C.M. Deber. Glycine and beta-branched residues support and modulate peptide helicity in membrane environments. *Febs Letters*, 311(3):217–220, October 1992. URL ISI:A1992JU87900009.

S.M. Li, S.Y. Hong, N.E. Shepardson, D.M. Walsh, G.M. Shankar, and D. Selkoe. Soluble oligomers of amyloid beta protein facilitate hippocampal long-term depression by disrupting neuronal glutamate uptake. *Neuron*, 62(6):788–801, June 2009. URL ISI:000267529300008.

G. C. Lickfield, A. L. Beyerlein, G. B. Savitsky, and L. E. Lewis. Deuteron quadrupole coupling constants of the methyl and methylene groups of ethanol from the direct carbon-13-deuterium and deuterium-deuterium couplings in deuterium nmr spectra. *The Journal of Physical Chemistry*, 88(16):3566–3570, 1984. doi: 10.1021/j150660a038. URL http://pubs.acs.org/doi/abs/10.1021/j150660a038.

Alberto Lleó, Oksana Berezovska, Lauren Herl, Susan Raju, Amy Deng, Brian J. Bacskai, Matthew P. Frosch, Michael Irizarry, and Bradley T. Hyman. Nonsteroidal anti-inflammatory drugs lower abeta42 and change presenilin 1 conformation. *Nat Med*, 10(10):1065–1066, Oct 2004. doi: 10.1038/nm1112. URL http://dx.doi.org/10.1038/nm1112.

A. Lord, H. Kalimo, C. Eckman, X.Q. Zhang, L. Lannfelt, and L.N.G. Nilsson. The arctic alzheimer mutation facilitates early intraneuronal a beta aggregation and senile plaque formation in transgenic mice. *Neurobiol Aging*, 27(1):67–77, January 2006. URL ISI:000234355800009.

J.X. Lu, W.M. Yau, and R. Tycko. Evidence from solid-state nmr for nonhelical conformations in the transmembrane domain of the amyloid precursor protein. *Biophys J*, 100(3):711–719, February 2011. URL ISI:000286957200022.

Lih Fen Lue, Yu Min Kuo, Alex E. Roher, Libuse Brachova, Yong Shen, Lucia Sue, Thomas Beach, Janice H. Kurth, Russel E. Rydel, and Joseph Rogers. Soluble amyloid beta peptide concentration as a predictor of synaptic change in alzheimer's disease. *Am J Pathol*, 155(3):853–862, September 1999. URL http://ajp.amjpathol.org/cgi/content/abstract/155/3/853.

Garland R. Marshall, Denise D. Beusen, Karol Kociolek, Adam S. Redlinski, Miroslaw T. Leplawy, Yong Pan, and Jacob Schaefer. Determination of a precise interatomic distance in a helical peptide by redor nmr. *Journal of the American Chemical Society*, 112(3):963–966, 1990. doi: 10.1021/ja00159a009. URL http://pubs.acs.org/doi/abs/10.1021/ja00159a009.

A James Mason, Amélie Martinez, Clemens Glaubitz, Olivier Danos, Antoine Kichler, and Burkhard Bechinger. The antibiotic and dna-transfecting peptide lah4 selectively associates with, and disorders, anionic lipids in mixed membranes. *FASEB J*, 20(2):320–322, Feb 2006. doi: 10.1096/fj.05-4293fje. URL http://dx.doi.org/10.1096/fj.05-4293fje.

I.A. Mastrangelo, M. Ahmed, T. Sato, W. Liu, C.P. Wang, P. Hough, and S.O. Smith. High-resolution atomic force microscopy of soluble a beta 42 oligomers. *Journal of Molecular Biology*, 358(1):106–119, April 2006. URL ISI:000236870700010.

Mark Mattson, M. Engle, and B. Rychlik. Effects of elevated intracellular calcium levels on the cytoskeleton and tau in cultured human cortical neurons. *Mol Chem Neuropathol*, 15(2):117–142, October 1991. URL http://dx.doi.org/10.1007/BF03159951.

M.P. Mattson. Calcium and neuronal injury in alzheimer's disease. *Ann NY Acad Sci*, 747(1):50–76, 1994. URL http://dx.doi.org/10.1111/j.1749-6632.1994.tb44401.x.

M.P. Mattson. Pathways towards and away from alzheimer's disease. *Nature*, 431(7004):107–107, September 2004. URL ISI:000223641500052.

M.P. Mattson, B. Cheng, D. Davis, K. Bryant, I. Lieberburg, and R.E. Rydel. Beta-amyloid peptides destabilize calcium homeostasis and render human cortical-neurons vulnerable to excitotoxicity. *J.Neurosci.*, 12(2):376–389, February 1992. URL ISI:A1992HE71000002.

C.A. Mclean, R.A. Cherny, F.W. Fraser, S.J. Fuller, M.J. Smith, K. Beyreuther, A.I. Bush, and C.L. Masters. Soluble pool of a beta amyloid as a determinant of severity of neurodegeneration in alzheimer's disease. *Ann Neurol*, 46(6):860–866, December 1999.

R. B. Merrifield. Solid phase peptide synthesis. i. the synthesis of a tetrapeptide. *Journal of the American Chemical Society*, 85(14):2149–2154, 1963. doi: 10.1021/ja00897a025. URL http://pubs.acs.org/doi/abs/10.1021/ja00897a025.

Delphine Milhas, Christopher J. Clarke, and Yusuf A. Hannun. Sphingomyelin metabolism at the plasma membrane: implications for bioactive sphingolipids. *FEBS Lett*, 584(9):1887–1894, May 2010. doi:

10.1016/j.febslet.2009.10.058. URL http://dx.doi.org/10.1016/j.febslet.2009.10.058.

Naoyuki Miyashita, John E. Straub, D. Thirumalai, and Yuji Sugita. Transmembrane structures of amyloid precursor protein dimer predicted by replica-exchange molecular dynamics simulations. *Journal of the American Chemical Society*, 131(10):3438–3439, 2009. doi: 10.1021/ja809227c. PMID: 19275251.

Zsolt Molnár, Katalin Soós, Imre Lengyel, Botond Penke, Viktor Szegedi, and Dénes Budai. Enhancement of nmda responses by [beta]-amyloid peptides in the hippocampus in vivo. *Neuroreport*, 15(10):1649–1652, July 2004.

Cléria Mendonça Moraes and Burkhard Bechinger. Peptide-related alterations of membrane-associated water: deuterium solid-state nmr investigations of phosphatidylcholine membranes at different hydration levels. *Magn Reson Chem*, 42(2):155–161, Feb 2004. doi: 10.1002/mrc.1321. URL http://dx.doi.org/10.1002/mrc.1321.

D. R. Muhandiram, Toshio Yamazaki, Brian D. Sykes, and Lewis E. Kay. Measurement of 2h t1 and t1.rho. relaxation times in uniformly 13c-labeled and fractionally 2h-labeled proteins in solution. *Journal of the American Chemical Society*, 117(46):11536–11544, 1995. doi: 10.1021/ja00151a018. URL http://pubs.acs.org/doi/abs/10.1021/ja00151a018.

Lisa-Marie Munter, Anne Botev, Luise Richter, Peter W. Hildebrand, Veit Althoff, Christoph Weise, Daniela Kaden, and Gerd Multhaup. Aberrant amyloid precursor protein (app) processing in hereditary forms of alzheimer disease caused by app familial alzheimer disease mutations can be rescued by mutations in the app gxxxg motif. *J Biol Chem*, 285(28):21636–21643, Jul 2010. doi: 10.1074/jbc.M109.088005. URL http://dx.doi.org/10.1074/jbc.M109.088005.

L.M. Munter, P. Voigt, A. Harmeier, D. Kaden, K.E. Gottschalk, C. Weise, R. Pipkorn, M. Schaefer, D. Langosch, and G. Multhaup. Gxxxg motifs within the amyloid precursor protein transmembrane sequence are critical for the etiology of a beta 42. *Embo Journal*, 26 (6):1702–1712, 2007. URL ISI:000245117500022.

Suman Nag, Jiji Chen, J. Irudayaraj, and S. Maiti. Measurement of the attachment and assembly of small amyloid-beta oligomers on live cell membranes at physiological concentrations using single-molecule tools. *Biophys J*, 99(6):1969–1975, Sep 2010. doi: 10.1016/j.bpj.2010.07.020. URL http://dx.doi.org/10.1016/j.bpj.2010.07.020.

H. Naiki, K. Higuchi, M. Hosokawa, and T. Takeda. Fluorometric-determination of amyloid fibrils invitro using the fluorescent dye,

thioflavine-t. *Anal Biochem*, 177(2):244–249, March 1989. URL ISI:A1989T773600003.

Nanditha G. Nair, George Perry, Mark A. Smith, and V Prakash Reddy. Nmr studies of zinc, copper, and iron binding to histidine, the principal metal ion complexing site of amyloid-beta peptide. *J Alzheimers Dis*, 20(1):57–66, 2010. doi: 10.3233/JAD-2010-1346. URL http://dx.doi.org/10.3233/JAD-2010-1346.

Akira Naito, Akira Fukutani, Michiel Uitdehaag, Satoru Tuzi, and Hazime Saitô. Backbone dynamics of polycrystalline peptides studied by measurements of 15n nmr lineshapes and 13c transverse relaxation times. *Journal of Molecular Structure*, 441(2, 3): 231 – 241, 1998. ISSN 0022-2860. doi: 10.1016/S0022-2860(97)00300-1. URL http://www.sciencedirect.com/science/article/pii/S0022286097003001. <ce:title>Solid-State NMR and Materials</ce:title>.

R. Narlawar, B.I.P. Revuelta, K. Baumann, R. Schubenel, C. Haass, H. Steiner, and B. Schmidt. N-substituted carbazolyloxyacetic acids modulate alzheimer associated gamma-secretase. *Bioorganic & Medicinal Chemistry Letters*, 17(1):176–182, January 2007. URL ISI:000243630500034.

Rajeshwar Narlawar, Blanca I. Pérez Revuelta, Christian Haass, Harald Steiner, Boris Schmidt, and Karlheinz Baumann. Scaffold of the cyclooxygenase-2 (cox-2) inhibitor carprofen provides alzheimer gamma-secretase modulators. *J Med Chem*, 49(26):7588–7591, Dec 2006. doi: 10.1021/jm0610200. URL http://dx.doi.org/10.1021/jm0610200.

J. Näslund, V. Haroutunian, R. Mohs, K.L. Davis, P. Davies, P. Greengard, and J.D. Buxbaum. Correlation between elevated levels of amyloid beta-peptide in the brain and cognitive decline. *Jama-J Am Med Assoc*, 283(12):1571–1577, March 2000. URL ISI:000085857300033.

Camilla Nilsberth, Anita Westlind-Danielsson, Christopher B. Eckman, Margaret M. Condron, Karin Axelman, Charlotte Forsell, Charlotte Stenh, Johan Luthman, David B. Teplow, Steven G. Younkin, Jan Naslund, and Lars Lannfelt. The 'arctic' app mutation (e693g) causes alzheimer's disease by enhanced a[beta] protofibril formation. *Nat Neurosci*, 4(9):887–893, September 2001. URL http://dx.doi.org/10.1038/nn0901-887.

I. Nishimoto. A new paradigm for neurotoxicity by fad mutants of beta app: A signaling abnormality. *Neurobiology of Aging*, 19(1):S33–S38, January 1998. doi: 10.1016/S0197-4580(98)00040-2.

Terrence G. Oas, Cynthia J. Hartzell, Frederick W. Dahlquist, and Gary P. Drobny. The amide nitrogen-15 chemical shift tensors of

four peptides determined from carbon-13 dipole-coupled chemical shift powder patterns. *Journal of the American Chemical Society*, 109 (20):5962–5966, 1987. doi: 10.1021/ja00254a011. URL http://pubs.acs.org/doi/abs/10.1021/ja00254a011.

S. J. Opella. Protein dynamics by solid state nuclear magnetic resonance. *Methods Enzymol*, 131:327–361, 1986.

A. Päiviö, J. Jarvet, A. Gräslund, L. Lannfelt, and A. Westlind-Danielsson. Unique physicochemical profile of [beta]-amyloid peptide variant a[beta]1-40e22g protofibrils: Conceivable neuropathogen in arctic mutant carriers. *JMB*, 339(1):145–159, May 2004. URL http://www.sciencedirect.com/science/article/B6WK7-4C47PRX-1/2/9e8c8e4f3b2cc90af2cc2516b5396776.

S. Parvathy, I. Hussain, E. H. Karran, A. J. Turner, and N. M. Hooper. Cleavage of alzheimer's amyloid precursor protein by alpha-secretase occurs at the surface of neuronal cells. *Biochemistry*, 38(30):9728–9734, Jul 1999. doi: 10.1021/bi9906827. URL http://dx.doi.org/10.1021/bi9906827.

A.C. Paula-Lima, T. Adasme, C. SanMartÃn, A. Sebollela, C. Hetz, M.A. Carrasco, S.T. Ferreira, and C. Hidalgo. Amyloid beta-peptide oligomers stimulate ryr-mediated ca2+ release inducing mitochondrial fragmentation in hippocampal neurons and prevent ryr-mediated dendritic spine remodeling produced by bdnf. *Antioxid Redox Signal*, 14(8):–, 2011.

M B. Pepys, D. R. Booth, W. L. Hutchinson, J. R. Gallimore, I. M. Collins, and E. Hohenester. Amyloid p component. a critical review. *Amyloid*, 4(4):274–295, 1997. doi: 10.3109/13506129709003838. URL http://informahealthcare.com/doi/abs/10.3109/13506129709003838.

R. G. Perez, H. Zheng, L. H. T. VanderPloeg, and E. H. Koo. The beta-amyloid precursor protein of alzheimer's disease enhances neuron viability and modulates neuronal polarity. *Journal of Neuroscience*, 17(24):9407–9414, December 1997.

EA Permiakov, LA Kalinichenko, LA Morozova, IuV Derezhkov, and J Bagelova. Interaction of copper nd zinc cations with calcium-binding proteins. *Mol Biol (Mosk)*, 22(4):984–991–, 1988. URL http://europepmc.org/abstract/MED/3185538.

N. Pierrot, S.F. Santos, C. Feyt, M. Morel, J.P. Brion, and J.N. Octave. Calcium-mediated transient phosphorylation of tau and amyloid precursor protein followed by intraneuronal amyloid-beta accumulation. *J.Biol.Chem.*, 281(52):39907–39914, December 2006. URL ISI:000243033900018.

Yue Qi-Takahara, Maho Morishima-Kawashima, Yu Tanimura, Georgia Dolios, Naoko Hirotani, Yuko Horikoshi, Fuyuki Kametani, Masahiro Maeda, Takaomi C. Saido, Rong Wang, and Yasuo Ihara. Longer forms of amyloid beta protein: implications for the mechanism of intramembrane cleavage by gamma-secretase. *J Neurosci*, 25 (2):436–445, Jan 2005. doi: 10.1523/JNEUROSCI.1575-04.2005. URL http://dx.doi.org/10.1523/JNEUROSCI.1575-04.2005.

H.W. Querfurth and D.J. Selkoe. Calcium ionophore increases amyloid-beta peptide production by cultured-cells. *Biochemistry*, 33(15):4550–4561, April 1994. URL ISI:A1994NH49300016.

Mark Rance and R.Andrew Byrd. Obtaining high-fidelity spin-12 powder spectra in anisotropic media: Phase-cycled hahn echo spectroscopy. *Journal of Magnetic Resonance (1969)*, 52(2): 221 – 240, 1983. ISSN 0022-2364. doi: 10.1016/0022-2364(83)90190-7. URL http://www.sciencedirect.com/science/article/pii/0022236483901907.

David M. Rice, Richard J. Wittebort, Robert G. Griffin, Eva Meirovitch, Evelyn R. Stimson, Yvonne C. Meinwald, Jack H. Freed, and Harold A. Scheraga. Rotational jumps of the tyrosine side chain in crystalline enkephalin. hydrogen-2 nmr line shapes for aromatic ring motions in solids. *Journal of the American Chemical Society*, 103(26):7707–7710, 1981. doi: 10.1021/ja00416a002. URL http://pubs.acs.org/doi/abs/10.1021/ja00416a002.

James E. Roberts, Gerard S. Harbison, Michael G. Munowitz, Judith Herzfeld, and Robert G. Griffin. Measurement of heteronuclear bond distances in polycrystalline solids by solid-state nmr techniques. *Journal of the American Chemical Society*, 109(14):4163–4169, 1987. doi: 10.1021/ja00248a006. URL http://pubs.acs.org/doi/abs/10.1021/ja00248a006.

Catherine Rovira, Nicolas Arbez, and Jean Mariani. A[beta](25-35) and a[beta](1-40) act on different calcium channels in ca1 hippocampal neurons. *Biochem Bioph Res Co*, 296(5):1317–1321, September 2002. URL http://www.sciencedirect.com/science/article/B6WBK-46MD2WB-1K/2/e4b9f61fdfa385998b7a1e8dfe8a0454.

M.J. Rowan, I. Klyubin, Q. Wang, N.W. Hu, and R. Anwyl. Synaptic memory mechanisms: Alzheimer's disease amyloid beta-peptide-induced dysfunction. *Biochem Soc T*, 35:1219–1223, November 2007. URL ISI:000251279800089.

W.P. Russ and D.M. Engelman. The gxxxg motif, a framework for transmembrane helix-helix association. *Journal of Molecular Biology*, 296(3):911–919, 2000. URL ISI:000085724500015.

Hazime Saitô, Isao Ando, and Akira Naito. *Solid State NMR Spectroscopy for Biopolymers. Principles and Applications*. Springer, the Netherlands, 2006.

Evgeniy Salnikov, Philippe Bertani, Jan Raap, and Burkhard Bechinger. Analysis of the amide (15)n chemical shift tensor of the c(alpha) tetrasubstituted constituent of membrane-active peptaibols, the alpha-aminoisobutyric acid residue, compared to those of di- and tri-substituted proteinogenic amino acid residues. *J Biomol NMR*, 45(4):373–387, Dec 2009. doi: 10.1007/s10858-009-9380-5. URL http://dx.doi.org/10.1007/s10858-009-9380-5.

M. Sastre, H. Steiner, K. Fuchs, A. Capell, G. Multhaup, M. M. Condron, D. B. Teplow, and C. Haass. Presenilin-dependent gamma-secretase processing of beta-amyloid precursor protein at a site corresponding to the s3 cleavage of notch. *EMBO Rep*, 2(9):835–841, Sep 2001. doi: 10.1093/embo-reports/kve180. URL http://dx.doi.org/10.1093/embo-reports/kve180.

T. Sato, T.C. Tang, G. Reubins, J.Z. Fei, T. Fujimoto, P. Kienlen-Campard, S.N. Constantinescu, J.N. Octave, S. Aimoto, and S.O. Smith. A helix-to-coil transition at the epsilon-cut site in the transmembrane dimer of the amyloid precursor protein is required for proteolysis. *Proceedings of the National Academy of Sciences of the United States of America*, 106(5):1421–1426, 2009. URL ISI:000263074600026.

H. Schägger and G. von Jagow. Tricine-sodium dodecyl sulfate-polyacrylamide gel electrophoresis for the separation of proteins in the range from 1 to 100 kda. *Anal Biochem*, 166(2):368–379, Nov 1987.

S. Scheuermann, B. Hambsch, L. Hesse, J. Stumm, C. Schmidt, D. Beher, T. A. Bayer, K. Beyreuther, and G. Multhaup. Homodimerization of amyloid precursor protein and its implication in the amyloidogenic pathway of alzheimer's disease. *Journal of Biological Chemistry*, 276 (36):33923–33929, September 2001. doi: 10.1074/jbc.M105410200.

Boris Schmidt, Stefanie Baumann, Rajeshwar Narlawar, Hannes A. Braun, and Gregor Larbig. Modulators and inhibitors of gamma- and beta-secretases. *Neurodegener Dis*, 3(4-5):290–297, 2006. doi: 10.1159/000095269. URL http://dx.doi.org/10.1159/000095269.

Klaus Schmidt-Rohr and Hans Wolfgang Spiess. *Multidimensional Solid-State NMR and Polymers*. Academic Press Inc. 24-28 Oval Road, London NW17DX and San Diego, CA 92101, 1 edition, 06 October 1994.

J. Seelig. Deuterium magnetic resonance: theory and application to lipid membranes. *Q Rev Biophys*, 10(3):353–418, Aug 1977.

J. Seelig. 31p nuclear magnetic resonance and the head group structure of phospholipids in membranes. *Biochim Biophys Acta*, 515(2):105–140, Jul 1978.

J. Seelig, P. M. Macdonald, and P. G. Scherer. Phospholipid head groups as sensors of electric charge in membranes. *Biochemistry*, 26 (24):7535–7541, Dec 1987.

Joachim Seelig and Werner Niederberger. Deuterium-labeled lipids as structural probes in liquid crystalline bilayers. deuterium magnetic resonance study. *Journal of the American Chemical Society*, 96(7):2069–2072, 1974. doi: 10.1021/ja00814a014. URL http://pubs.acs.org/doi/abs/10.1021/ja00814a014.

D.J. Selkoe. The molecular pathology of alzheimers-disease. *Neuron*, 6 (4):487–498, April 1991. URL ISI:A1991FH80200001.

D.J. Selkoe. Alzheimer's disease: Genes, proteins, and therapy. *Physiol Rev*, 81(2):741–766, April 2001. URL ISI:000167638300006.

Ganesh M. Shankar, Brenda L. Bloodgood, Matthew Townsend, Dominic M. Walsh, Dennis J. Selkoe, and Bernardo L. Sabatini. Natural oligomers of the alzheimer amyloid-beta protein induce reversible synapse loss by modulating an nmda-type glutamate receptor-dependent signaling pathway. *J.Neurosci.*, 27(11):2866–2875, March 2007. URL http://www.jneurosci.org/cgi/content/abstract/27/11/2866.

G. G. Shipley, L. S. Avecilla, and D. M. Small. Phase behavior and structure of aqueous dispersions of sphingomyelin. *J Lipid Res*, 15 (2):124–131, Mar 1974.

Akira Shoji, Takuo Ozaki, Teruaki Fujito, Kenzo Deguchi, Shinji Ando, and Isao Ando. Nitrogen-15 chemical shift tensors and conformation of solid polypeptides containing 15n-labeled l-alanine residue by 15n nmr. 2. secondary structure is reflected in .sigma.22. *Journal of the American Chemical Society*, 112(12):4693–4697, 1990. doi: 10.1021/ja00168a011. URL http://pubs.acs.org/doi/abs/10.1021/ja00168a011.

Akira Shoji, Takuo Ozaki, Teruaki Fujito, Kenzo Deguchi, Isao Ando, and Jun Magoshi. 15n chemical shift tensors and conformation of solid polypeptides containing 15n labeled glycine residue by 15n nmr. *Journal of Molecular Structure*, 441(2, 3): 251 – 266, 1998. ISSN 0022-2860. doi: 10.1016/S0022-2860(97)00258-5. URL http://www.sciencedirect.com/science/article/pii/S0022286097002585. <ce:title>Solid-State NMR and Materials</ce:title>.

I.F. Smith, K.N. Green, and F.M. LaFerla. Calcium dysregulation in alzheimer's disease: Recent advances gained from genetically modified animals. *Cell Calcium*, 38(3-4):427–437, September 2005. URL ISI:000232243700025.

Francesco Stellato, Gianfranco Menestrina, Mauro Dalla Serra, Cristina Potrich, Rossella Tomazzolli, Wolfram Meyer-Klaucke, and Silvia Morante. Metal binding in amyloid beta-peptides shows intra- and inter-peptide coordination modes. *Eur Biophys J*, 35(4):340–351, Apr 2006. doi: 10.1007/s00249-005-0041-7. URL http://dx.doi.org/10.1007/s00249-005-0041-7.

Fernando Albericio Steven A. Kates. *Solid-phase synthesis: a practical guide*. Boca Raton: CRC Press, 1st edition, 2000.

W.B. Stine, K.N. Dahlgren, G.A. Krafft, and M.J. Ladu. In vitro characterization of conditions for amyloid-beta peptide oligomerization and fibrillogenesis. *J.Biol.Chem.*, 278(13):11612–11622, March 2003. URL ISI:000181855400094.

G.E. Stutzmann. Calcium dyspegulation, ip3 signaling, and alzheimer's disease. *Neuroscientist*, 11(2):110–115, April 2005. URL ISI:000227704900009.

G.E. Stutzmann. The pathogenesis of alzheimers disease - is it a lifelong "calciumopathy"? *Neuroscientist*, 13(5):546–559, October 2007. URL ISI:000249763300020.

K. Suzuki, T. Miura, and H. Takeuchi. Inhibitory effect of copper(ii) on zinc(ii)-induced aggregation of amyloid beta-peptide. *Biochem Biophys Res Commun*, 285(4):991–996, Jul 2001. doi: 10.1006/bbrc.2001.5263. URL http://dx.doi.org/10.1006/bbrc.2001.5263.

Nobumasa Takasugi, Taisuke Tomita, Ikuo Hayashi, Makiko Tsuruoka, Manabu Niimura, Yasuko Takahashi, Gopal Thinakaran, and Takeshi Iwatsubo. The role of presenilin cofactors in the gamma-secretase complex. *Nature*, 422(6930):438–441, Mar 2003. doi: 10.1038/nature01506. URL http://dx.doi.org/10.1038/nature01506.

Q. Teng and T.A. Cross. The in situ determination of the 15n chemical shift tensor orientation in a polypeptide. *J. Magn. Reson*, 85:439–447, 1989.

Deborah J. Tew, Stephen P. Bottomley, David P. Smith, Giuseppe D. Ciccotosto, Jeffrey Babon, Mark G. Hinds, Colin L. Masters, Roberto Cappai, and Kevin J. Barnham. Stabilization of neurotoxic soluble beta-sheet-rich conformations of the alzheimer's disease amyloid-beta peptide. *Biophys J*, 94(7):2752–2766, Apr 2008. doi: 10.1529/biophysj.107.119909. URL http://dx.doi.org/10.1529/biophysj.107.119909.

D. Thompson, M. B. Pepys, I. Tickle, and S. Wood. The structures of crystalline complexes of human serum amyloid p component with its carbohydrate ligand, the cyclic pyruvate acetal of galactose. *J Mol Biol*, 320(5):1081–1086, Jul 2002.

Changlin Tian, Carlos G. Vanoye, Congbao Kang, Richard C. Welch, Hak Jun Kim, Alfred L. George, and Charles R. Sanders. Preparation, functional characterization, and nmr studies of human kcne1, a voltage-gated potassium channel accessory subunit associated with deafness and long qt syndrome. *Biochemistry*, 46(41):11459–11472, 2007. doi: 10.1021/bi700705j. URL http://pubs.acs.org/doi/abs/10.1021/bi700705j. PMID: 17892302.

R. Vassar, B. D. Bennett, S. Babu-Khan, S. Kahn, E. A. Mendiaz, P. Denis, D. B. Teplow, S. Ross, P. Amarante, R. Loeloff, Y. Luo, S. Fisher, J. Fuller, S. Edenson, J. Lile, M. A. Jarosinski, A. L. Biere, E. Curran, T. Burgess, J. C. Louis, F. Collins, J. Treanor, G. Rogers, and M. Citron. Beta-secretase cleavage of alzheimer's amyloid precursor protein by the transmembrane aspartic protease bace. *Science*, 286(5440): 735–741, Oct 1999.

D.M. Walsh, I. Klyubin, J.V. Fadeeva, W.K. Cullen, R. Anwyl, M.S. Wolfe, M.J. Rowan, and D.J. Selkoe. Naturally secreted oligomers of amyloid beta protein potently inhibit hippocampal long-term potentiation in vivo. *Nature*, 416(6880):535–539, April 2002. URL ISI:000174756500043.

H.W. Wang, J.F. Pasternak, H. Kuo, H. Ristic, M.P. Lambert, B. Chromy, K.L. Viola, W.L. Klein, W.B. Stine, G.A. Krafft, and B.L. Trommer. Soluble oligomers of beta amyloid (1-42) inhibit long-term potentiation but not long-term depression in rat dentate gyrus. *Brain Res*, 924(2):133–140, January 2002. URL ISI:000173275000001.

S. Weggen, J. L. Eriksen, P. Das, S. A. Sagi, R. Wang, C. U. Pietrzik, K. A. Findlay, T. E. Smith, M. P. Murphy, T. Bulter, D. E. Kang, N. Marquez-Sterling, T. E. Golde, and E. H. Koo. A subset of nsaids lower amyloidogenic abeta42 independently of cyclooxygenase activity. *Nature*, 414(6860):212–216, Nov 2001. doi: 10.1038/35102591. URL http://dx.doi.org/10.1038/35102591.

A. Weidemann, G. Konig, D. Bunke, P. Fischer, J. M. Salbaum, J. M. Baum, C. L. Masters, C., and K. Beyreuther. Identification, biogenesis, and localization of precursors of alzheimers-disease a4 amyloid protein. *Cell*, 57(1):115–126, April 1989. doi: 10.1016/0092-8674(89)90177-3.

Andreas Weidemann, Simone Eggert, Friedrich B M. Reinhard, Markus Vogel, Krzysztof Paliga, Gottfried Baier, Colin L. Masters, Konrad Beyreuther, and Geneviéve Evin. A novel epsilon-cleavage within the

transmembrane domain of the alzheimer amyloid precursor protein demonstrates homology with notch processing. *Biochemistry*, 41(8): 2825–2835, Feb 2002.

Brian M. Whalen, Dennis J. Selkoe, and Dean M. Hartley. Small non-fibrillar assemblies of amyloid [beta]-protein bearing the arctic mutation induce rapid neuritic degeneration. *Neurobiology of Disease*, 20(2):254–266, November 2005. URL http://www.sciencedirect.com/science/article/B6WNK-4G0494V-1/2/8d85248e4ced2b941a930c191bc6cde6.

Jie Xiong, Alex Verkhratsky, and Emil C. Toescu. Changes in mitochondrial status associated with altered ca2+ homeostasis in aged cerebellar granule neurons in brain slices. *J.Neurosci.*, 22(24): 10761–10771, December 2002. URL http://www.jneurosci.org/cgi/content/abstract/22/24/10761.

Yuji Yoshiike, Kentaro Tanemura, Ohoshi Murayama, Takumi Akagi, Miyuki Murayama, Shinji Sato, Xiaoyan Sun, Nobuo Tanaka, and Akihiko Takashima. New insights on how metals disrupt amyloid beta-aggregation and their effects on amyloid beta cytotoxicity. *J.Biol.Chem.*, 276(34):32293–32299, August 2001. URL http://www.jbc.org/content/276/34/32293.abstract.

Guojun Zhao, Guozhang Mao, Jianxin Tan, Yunzhou Dong, Mei-Zhen Cui, Seong-Hun Kim, and Xuemin Xu. Identification of a new presenilin-dependent zeta-cleavage site within the transmembrane domain of amyloid precursor protein. *J Biol Chem*, 279(49):50647–50650, Dec 2004. doi: 10.1074/jbc.C400473200. URL http://dx.doi.org/10.1074/jbc.C400473200.
1.

Part IV

APPENDIX

A

SUPPLEMENTARY EXPERIMENTS ON AMYLOID β-PEPTIDES

Our goal was to establish a reproducible protocol for preparation of Aβ oligomers to be used in ssNMR experiments. We intended to gain insights into molecular architecture of Aβ oligomers and ultimately solve their structure. Additional experiments were planned to investigate specific features that distinguish between oligomers and fibrils. We believe that formation of a salt bridge between amino acids Glu22 and Lys28 in Aβ(1-40) prevents fibrillization, as was discussed in Chapter 3. For this purpose, two specifically-labeled amino acids were designed: glutamic acid labeled at position $^{13}C^{\delta}$ with average chemical shift of 182.59 ppm and lysine labeled at $^{15}N^{\zeta}$with average chemical shift of 33.96 ppm and labeled backbone ^{15}N with average chemical shift of 121.06 ppm (Figure 42 on page 125). Signal from MOPS buffer would be around 46 and 66 ppm from the morpholino ring and ~36 ppm from the sulfonate carbon. Signals from the labeled amino acids were expected to be much stronger and well separated from the signal generated by MOPS molecules.

A.0.3 *Synthesis and purification*

Aβ(1-40) and Aβ(1-40)E22G peptides were chemically synthesized using solid-phase peptide synthesis utilizing Fmoc chemistry as described in the methods (Chapter 2). Quality of the synthesis was assessed by MALDI-TOF mass spectrometer (Autoflex from Brücker Daltonics) as seen in Figure 43 on page 127 and Figure 44 on page

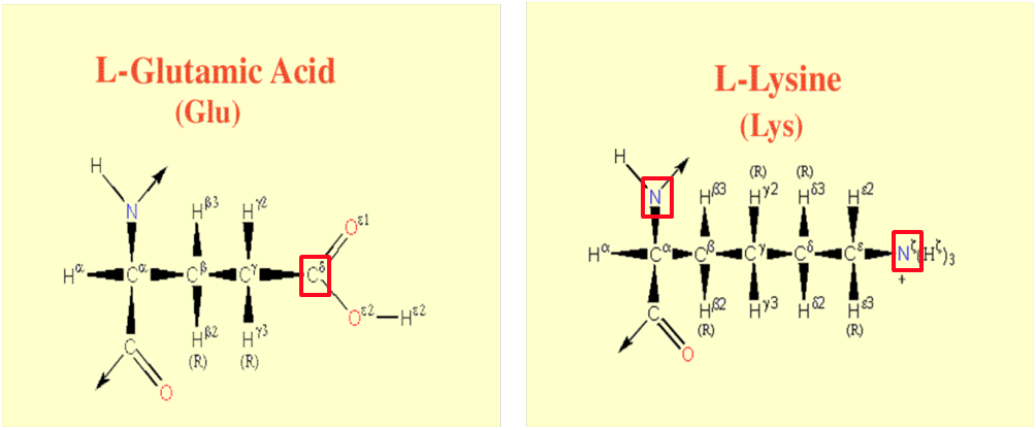

Figure 42: Specific isotopic labels on glutamic acid and lysine amino acids destined for peptide synthesis.

128. Unlabeled peptides were used to establish appropriate purification protocol and to find experimental conditions suitable for ssNMR experiments. Labeled Aβ(1-40) was prepared for REDOR experiments.

The best condition for purification by HPLC was found to be 100% Acetonitril (ACN) + 0.1 % TFA (buffer B) using a 17 % - 35 % gradient (Semi-preparative HPLC with the module DAD 3L for UV detection from Bischoff; McDAcq32 software; Preparative column Grace Vydac (125 x 20mm; P/N 1220 K040PS050) and a pre-column (30 x 20mm P/N 0320 K040PS050) packed with the phase Prontosyl 300-5-C4 (5µm with 300Å pores branched with C4 carbon chain)). It must be noted that each newly synthesized peptide batch required adjustments of the purification protocol. Extreme care was taken to prevent peptide aggregation during purification procedures. Peptides were solubilized in small quantities (typically up to 6 mg), sonicated to eliminate any pre-existing aggregates and kept on ice at all times before being injected into HPLC column.

Results can be seen in Figure 45 on page 128 and in Figure 46 on page 129. It is clear that labeled peptides had a different elution profile from that of unlabeled peptide. Due to splitted elution peaks of the labeled Aβ(1-40), it was difficult to establish which of them contains the peptide of interest and in which oligomeric state. Therefore, all 6 "sub-peaks" were collected and subjected to aggregation tests followed by PAGE and Western blot analyses (refer to the next subsection).

A.0.4 *Aggregation studies: PAGE and fluorescence analyses*

In order to characterize newly synthesized peptides and to evaluate their aggregation propensities, aggregation trials were conducted. Aggregation profiles of Aβ(1-40) and Aβ(1-40)E22G in PB and MOPS buffers were analyzed with PAGE and ThT fluorescence techniques (Chapter 2).

HPLC ELUTION PEAKS - CHECKING THE OLIGOMERS DISTRIBUTION

For Aβ(1-40) and Aβ(1-40)E22G peptides two elution peaks–as seen in Figure 45 on page 128–were checked and compared to an old Aβ sample (Figure 47 on page 129).

The results show that peak I of Aβ(1-40) has some pre-existing high molecular weight oligomers, while peak II of Aβ(1-40) shows an expected profile comprised of monomers, dimers and trimers at t = 0 h. Both peaks of Aβ(1-40) readily aggregated. Unfortunately, there was no difference between PB and MOPS conditions, which is inconsistent with the results described in chapter 3 (Chapter 3). Contrary, Aβ(1-40)E22G showed no high-molecular weight aggregates after 24h, consistent with the expectations.

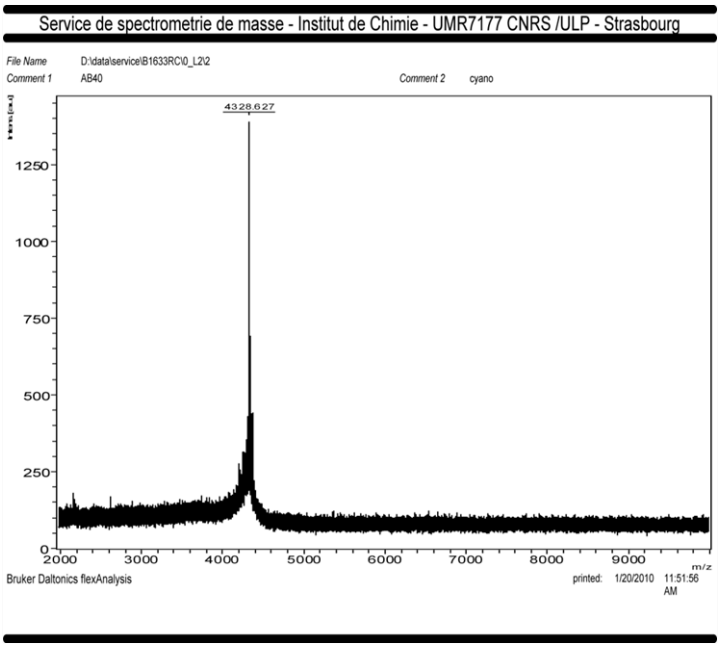

(a)

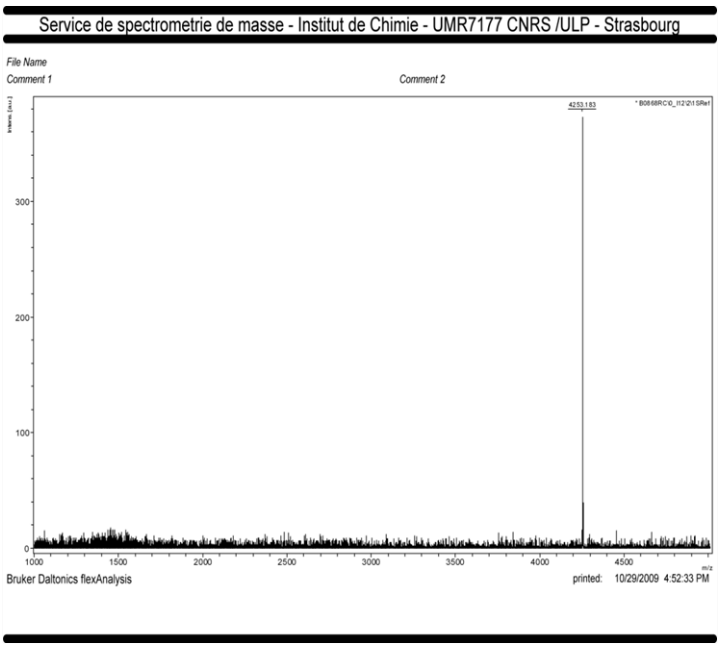

(b)

Figure 43: Mass spectrometric analysis of the crude synthetic unlabeled Aβ peptides. (a) Aβ(1-40) peptide with expected mass of 4329.8, (b) Aβ(1-40)E22G peptide with expected mass of 4257.8.

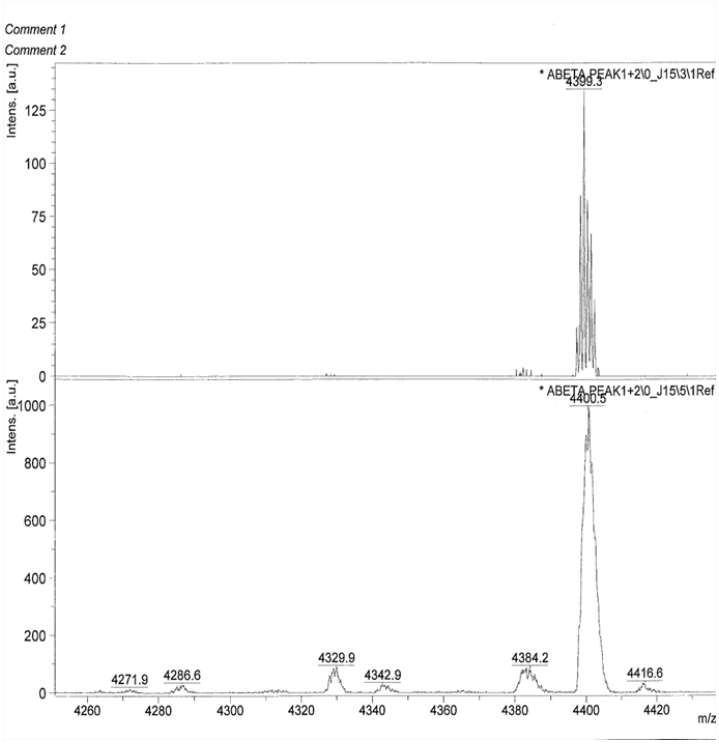

Figure 44: Mass spectrometric analysis of the crude labeled Aβ(1-40) peptides with expected mass of 4329.8. Here the apparent mass is 4399.3.

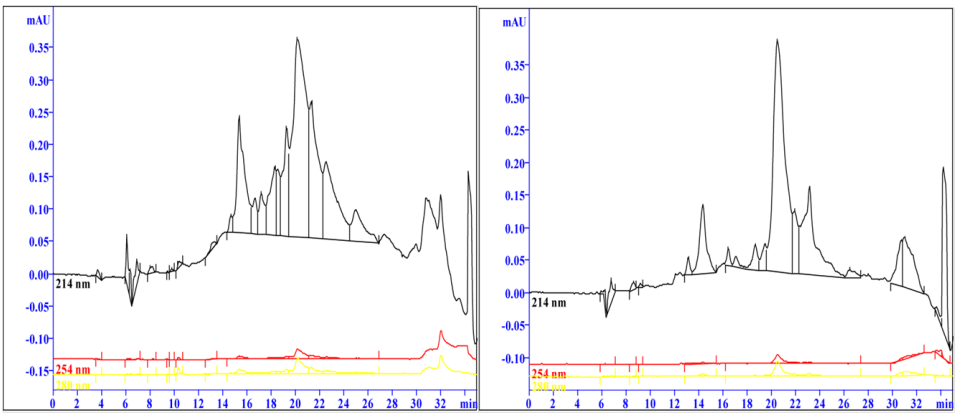

(a) (b)

Figure 45: HPLC purification of Aβ peptides - elution profiles: (a) Aβ(1-40) peptides eluted in two major peaks, (b) Aβ(1-40)E22G peptides eluted in one major peak and another smaller peak. For each peptide, two peaks were collected and analyzed.

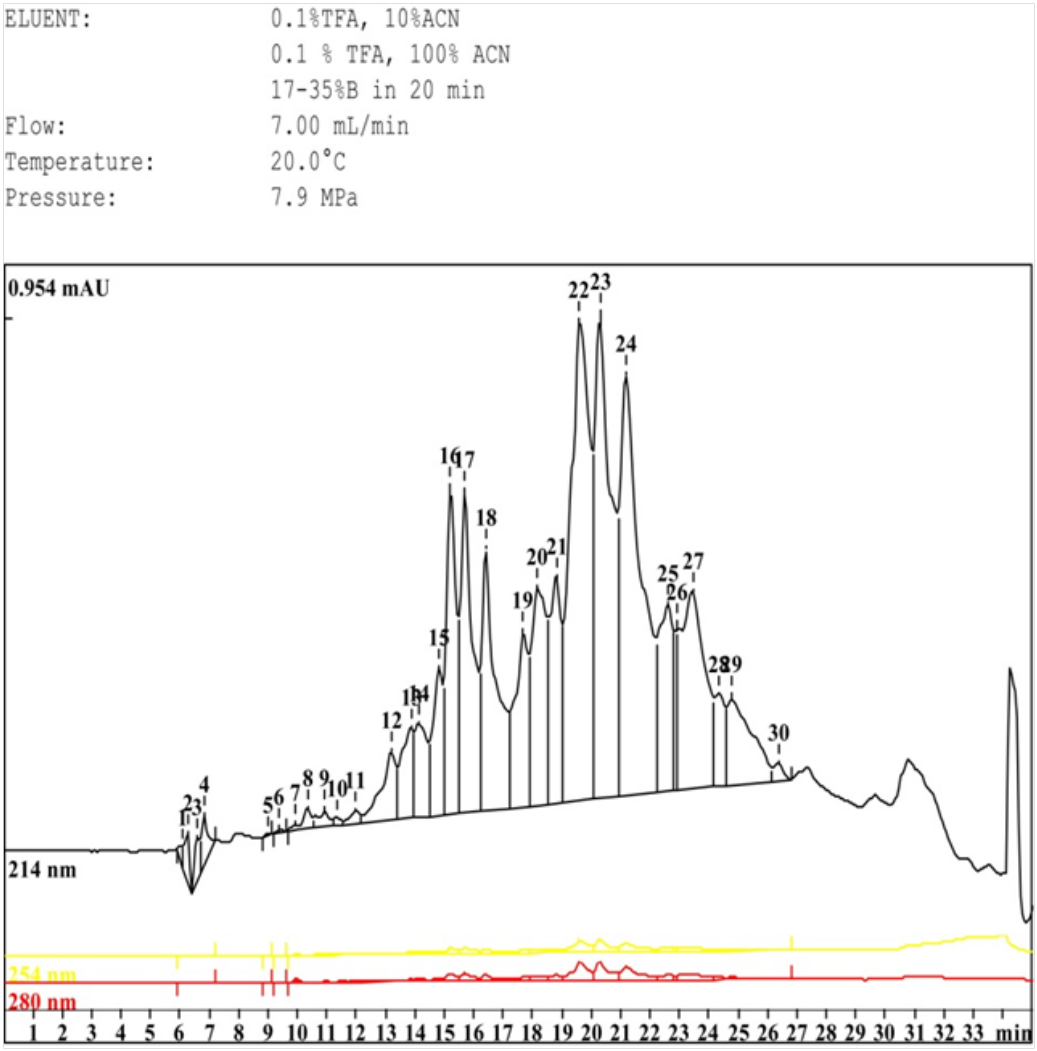

Figure 46: HPLC purification of labeled Aβ(1-40) peptides - elution profile. Two main peaks, each split into three smaller peaks.

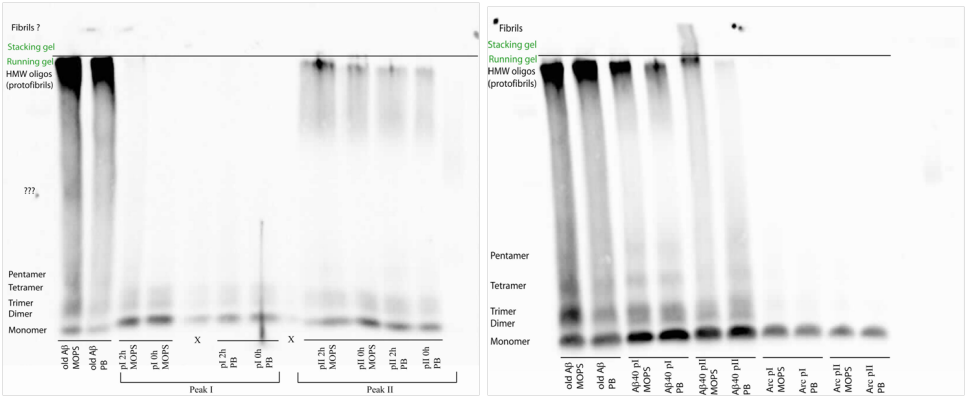

(a) (b)

Figure 47: Aggregation trial for Aβ(1-40) and Aβ(1-40)E22G in PB and MOPS buffers: oh, 2h and 24h samples: (a) Aβ(1-40) after oh and 2h of incubation, (b) Aβ(1-40) and Aβ(1-40)E22G after 24h of incubation.

TEMPERATURE EFFECT ON Aβ PEPTIDES AGGREGATION It has been previously shown that aggregation of Aβ peptides slows down significantly at 4°C. In Figure 48 on page 131 the aggregation profiles of both Aβ(1-40) and Aβ(1-40)E22G peptides were compared in order to examine the possibility to grow oligomers in a more amenable manner. The results, however, showed that at 4°C aggregation is extremely slow, which makes it impossible to use these conditions for oligomers growth.

COMPARING DIFFERENT BUFFER COMPOSITIONS Several buffer compositions were examined in order to find suitable buffer for following ssNMR measurements as MOPS exhibited strong NMR signal. Since we know that in the presence of calcium ions oligomers are stabilized, it was our interest to keep calcium in the buffer solution. It is well known that addition of $CaCl_2$ to PB results in rapid precipitation of insoluble solid calcium phosphate. Although several publications [Nag et al., 2010] reported that they prepared solutions composed of both calcium and phosphate without forming the precipitant. Buffer components included: 146 mM NaCl, 5.4 mM KCl, 1.8 mM $CaCl_2$, 0.8 mM $MgSO_4$, 0.4 mM KH_2PO_4, 5 mM d-glucose, 20 mM Na_2HPO_4. Upon mixing all the ingredients, calcium phosphate formed and precipitated (no replies to successive inquiries were received). Another common buffer used in experiments with mammalian cell lines is aCSF (148 mM NaCl, 2.7 mM KCl, 2.0 mM $CaCl_2$, 0.85 mM $MgCl_2$, 1.25 mM d-glucose). The salt concentrations were modified to a total of 15.55 mM and d-glucose was omitted to adapt the buffer for ssNMR measurements (10 mM NaCl, 2.7 mM KCl, 2.0 mM $CaCl_2$, 0.85 mM $MgCl_2$). Interestingly, Aβ(1-40)E22G peptides precipitated in NaKCaMg salt solution (it is not a true buffer), but not Aβ(1-40).

Sample preparation: 4 mg of Aβ(1-40) solubilized in 10 ml of NaKCaMg solution (pH 5.5) or alternatively, the peptides were resuspended in 10 mM MOPS, 5 mM NaCl, 2 mM $CaCl_2$ (pH 7.4). Both samples were sonicated for 2 min in a water bath, centrifuged in Amicon filter 50 kDa cutoff (Millipore) at 5,000 $\times$g at 4 °C for 20 min. The flow through was collected and incubated for 5 days at 37 °C. Samples were inverted from time to time to insure there was a homogeneous environment. During incubation small samples were taken for ThT measurements .

Figure 49 on page 132 clearly shows that in 10 mM MOPS, 5 mM Nacl and 2mM $CaCl_2$ Aβ(1-40) forms oligomers that exhibit only low ThT affinity and fluorescence. In contrast, in the salt solution we see an increase in fluorescence, possibly indicating formation of protofibrils as the solution is clear and no fibrils could be observed by eye. In addition, fluorescence of the salt solution oligomers is decreasing during the time of the measurement, indicating that these are fragile under mechanical stirring (a property observed before for

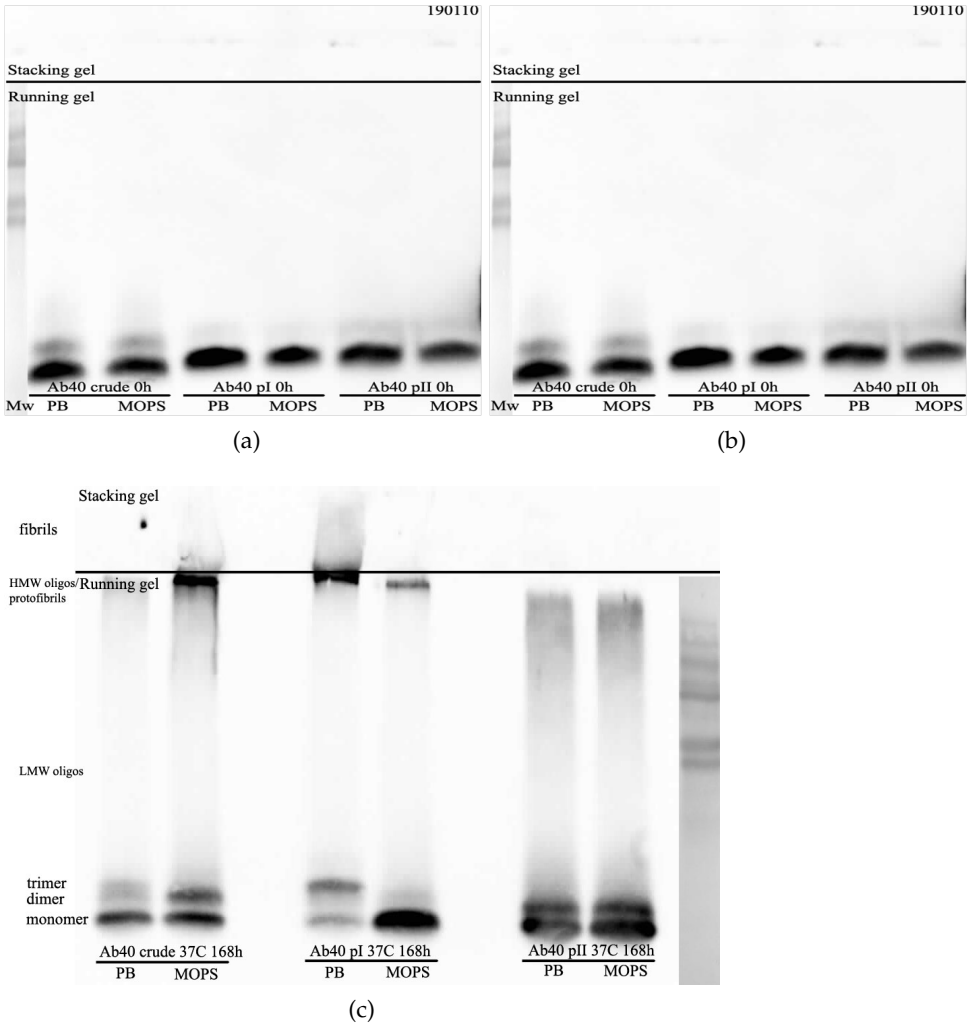

Figure 48: Aggregation trial for Aβ(1-40) crude preparation (peptide before purification), peak I and peak II at different temperatures in PB and MOPS buffers: representative oh and 168h samples. (a) Aβ(1-40) at time oh, crude peptide, peak I, peak II, (b) Aβ(1-40) crude peptide, peak I, peak II after incubation at 4°C for 168h, (c) Aβ(1-40) crude peptide, peak I, peak II after incubation at 37°C for 168h.

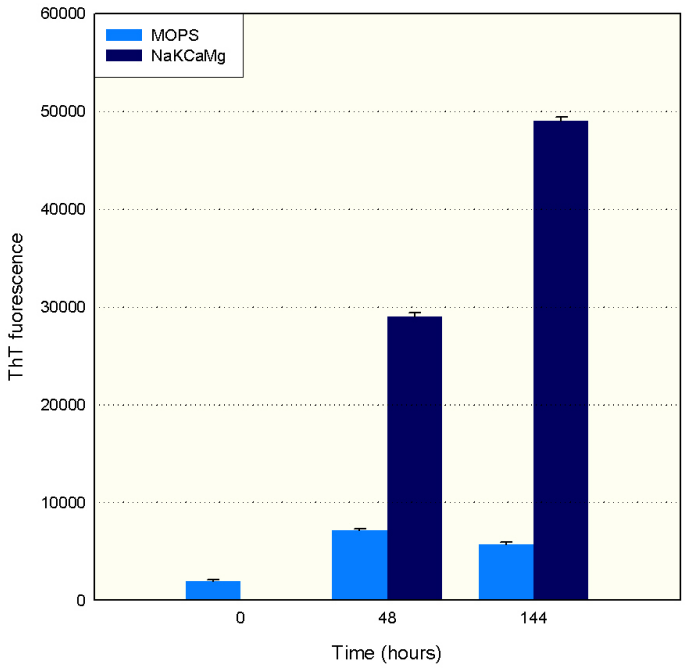

Figure 49: New buffer conditions for oligomers of Aβ(1-40) growth. The color coding is as follows: light blue is the MOPS buffer condition; dark blue is the salt condition - NaKCaMg.

oligomers, but not for fibrils). After 144 hours of incubation, samples were flash-frozen and lyophilized for ssNMR measurements.

In another experiment we used 50 mM MOPS + 100 mM NaCl + 2 mM $CaCl_2$ to grow Aβ(1-40) and Aβ(1-40)E22G oligomers for 96 h. Thereafter, they were filtered using Millipore centrifugal filter "Microcon 50 KDa" at 14,000 ×g for 5 min at RT. The flow-through was incubated again at 37 °C for 96 h. After 96 h, a second round of filtration was performed under the same conditions. All samples were analyzed using PAGE and Western blot analyses. For each peptide two HPLC elution peaks, as seen in Figure 45 on page 128, were analyzed. It must be mentioned that filtration ***before*** incubation resulted in abolishing of the oligomeric growth (probably due to removal of the seeds from which oligomers develop).

Figure 50 on page 133 shows Western blot images of the samples that were subjected to PAGE analysis. Two images are of the same blot, only the exposure time differs. Longer exposure time allows imaging of the less populated oligomeric states, such as in lanes 2 and 3, pII and pI after the 2^{nd} filtration, respectively (Figure 50b on page 133). Here, after longer exposure, trimers, tetramers and even pentamers can be seen. While in Figure 50a on page 133, same lanes show only monomers, dimers and very faint band for trimers. It also exposes the disadvantage of this technique for oligomers detection. Nevertheless, after two growth-filtration cycles, a nice distribution of low-molecular

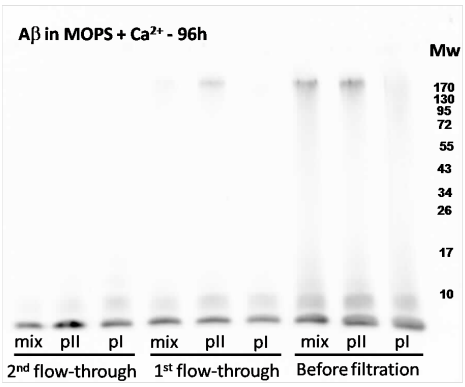

(a) Aβ(1-40) - correct exposure during blot imaging (no saturation of the bands)

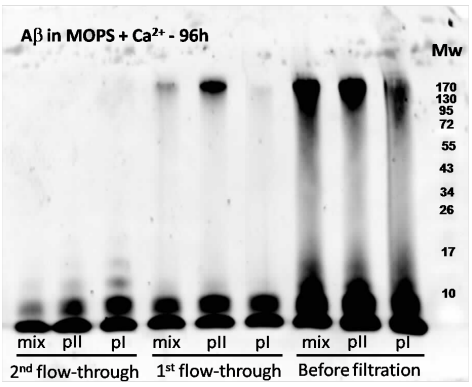

(b) Aβ(1-40) - longer exposure during blot imaging (some bands are saturated)

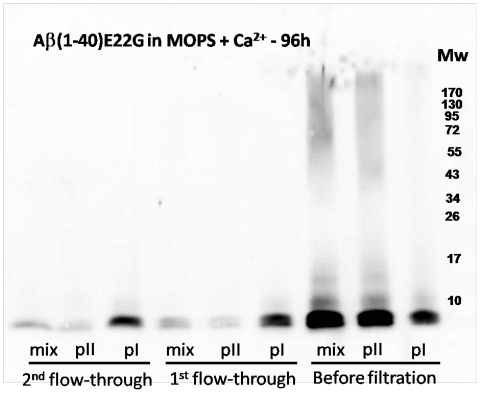

(c) Aβ(1-40)E22G - correct exposure during blot imaging (no saturation of the bands).

Figure 50: Spin-filter separation trials of Aβ(1-40) and Aβ(1-40)E22G oligomers grown in high-salt conditions.

weight oligomers of Aβ(1-40) was obtained. Potentially, they could be used for ssNMR experiments, if larger quantities of oligomers could be obtained. At this stage, however, the amount remaining after double filtration is insufficient for ssNMR study. Figure 50c on page 133 shows the same experiment with Aβ(1-40)E22G oligomers. Here, the untreated samples in high salt, produced high-molecular weight oligomers - not something we have observed before. However, already after the first filtration no oligomers grew even after 96 h. Over-saturated image did not show additional bands and therefore is not presented here. These conditions are definitely not suitable for Aβ(1-40)E22G oligomers preparation.

THE EFFECT OF SALTS ON AGGREGATION OF LABELED AND NON-LABELED Aβ(1-40) AND Aβ(1-40)E22G As in ssNMR experiments salt concentration presents an obstacle, it is advisable to use as little amount of salts as possible. For Aβ aggregation experiments 75 mM MOPS + 2 mM Ca^{2+} were used, as described in Chapter 3. Two problems have arisen from this condition (and conditions with higher salt concentration): 1) the amount of salts was high for ssNMR 2) MOPS buffer produced a very strong signal in the carbonyl region of ssNMR spectrum, which interfered with the expected signal from Aβ. We were looking into a possibility, where we could use the MOPS buffer, but to minimize its concentration. We also looked into the possibility of using deuterated MOPS for some of the experiments.

The following buffer compositions were compared:

1) 5 mM MOPS + 2 mM Ca^{2+}

2) 5 mM MOPS + 2 mM Ca^{2+} + 145 mM NaCl

3) 5 mM $MOPS_{deuterated}$ + 2 mM Ca^{2+}

4) 5 mM MOPS + 2 mM Ca^{2+} + 145 mM NaCl with isotopically labeled Aβ(1-40) peptide

PAGE and Western blot analyses were done at two time points: 0 h and 72 h for both Aβ(1-40) and Aβ(1-40)E22G peptides. Six eluted fractions of labeled Aβ(1-40) peptide were collected (the elution peaks appeared different than those of unlabeled peptides - a problem of inconsistent elution profiles). In fact, those were two major peaks, each exhibiting three "shoulders" that were collected separately in order to investigate the oligomerization state of the eluted species in each peak. The results are shown in Figure 51 on page 135.

The results show that there was no difference between the aggregation profiles of Aβ(1-40)E22G in all the conditions evaluated. Aβ(1-40) aggregation profiles are very similar in all conditions. Most surprisingly, there was no difference between low and high-salt conditions. Oligomers growth of Aβ(1-40) was not hindered by the presence of deuterated MOPS buffer, and therefore, it could be used in the future experiments (although it will be better to repeat this test for every new batch of synthetic Aβ(1-40)).

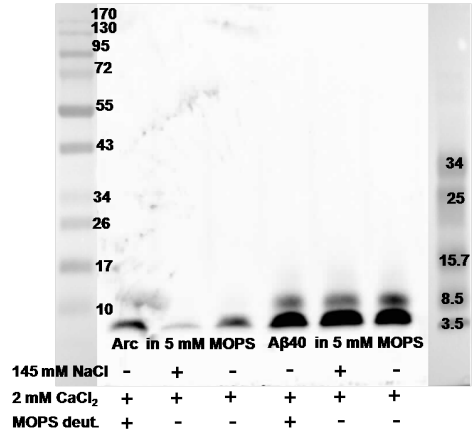

(a)

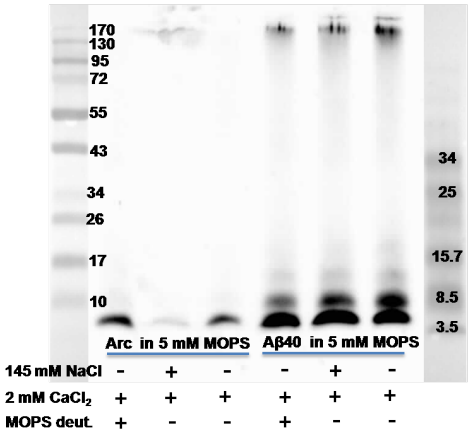

(b)

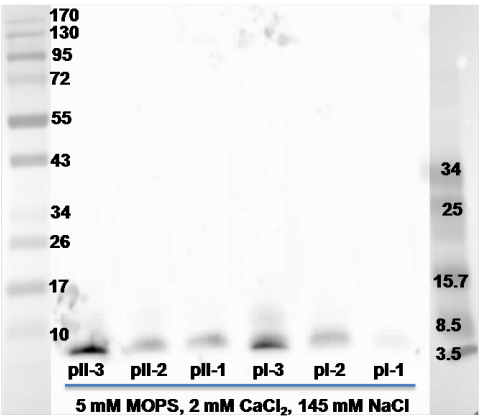

(c) Aggregation of labeled Aβ(1-40) in high-salt condition - 0 h

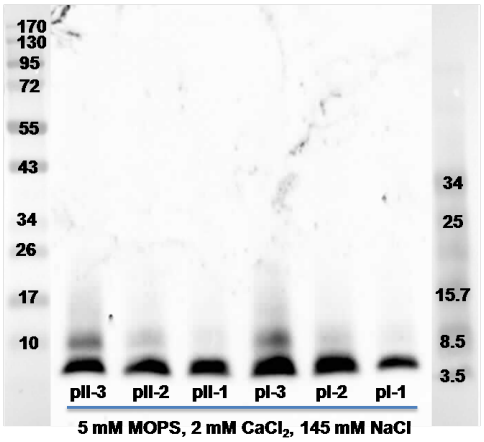

(d) Aggregation of labeled Aβ(1-40) in high-salt condition - 72 h

Figure 51: Effect of salts on aggregation of labeled and non-labeled Aβ(1-40) and Aβ(1-40)E22G peptides - in preparation for ssNMR experiments: (a) aggregation profiles of Aβ(1-40) and of Aβ(1-40)E22G at t = 0 h, (b) aggregation profiles of Aβ(1-40) and of Aβ(1-40)E22G at t = 72 h, (c) aggregation profiles of isotopically labeled Aβ(1-40) at t = 0 h, (d) aggregation profiles of isotopically labeled Aβ(1-40) at t = 72 h.

Labeled Aβ(1-40) in high-salt condition readily produced low-molecular weight oligomers (Figure 51c on page 135 and Figure 51d on page 135). Interestingly, the aggregation of the labeled peptide was slower than that of the non-labeled. Notably, after 72 h only oligomers from monomers to pentamers were observed. There was no significant difference between the three elution peaks tested. The small difference between them is probably related to the differing amount of oligomers of every size category initially present.

A.0.5 *Oligomers separation trials using FPLC*

Equipment: FPLC (Bio-Rad) composed of several units: Biologic (BioFrac), fraction collector, Biologic Quad-Teck, UV-Vis detector, Biologic DuoFlow, Biologic maximizer. A gel filtration column Sephacryl S-100 HiPrep 16/60 HR was used.

Standardizing sample: total volume of 1.2 ml, protein concentration 3 mg/ml: 2 mg of Bovine serum albumin (BSA), 1mg Aprotenin and 1 mg Lyzozyme were solubilized in 50 mM PB pH 7.4 and 50 mM NaCl.

The sample of standardizing protein mixture (Figure 52 on page 137) was eluted at the rate of 1.5 ml/min. Several additional elution trials were performed at different flow rates (1 ml/min and 0.5 ml/min). All showed very similar elution profiles (data not shown).

The idea of "on-column" oligomerization of Aβ(1-40) peptides was explored: 3 mg of Aβ(1-40) peptides were dissolved in guanidine hydrochloride (GdmCl) and injected into the gel filtration column. The elution buffer was 50 mM PB pH 7.4 and 50 mM NaCl at the rate of 1 ml/min. Results are shown in Figure 52a on page 137. After the elution, small amount of the sample was taken for PAGE analysis. Western blot image is shown in Figure 52b on page 137. It is difficult to see, but the oligomers profile observed in this image ranges from monomers to pentamers. This means that under those experimental conditions, it is possible to obtain a mixture of low-molecular weight oligomers formed from denatured Aβ(1-40) peptides. However, it was not possible to obtain fine separation of the low-molecular weight species.

A.0.6 *Oligomers separation using spin filters*

In the literature, there is a number of publications in which authors used spin filters or centrifugal concentrators to obtain a fraction of oligomers of a certain size distribution. Here we checked four commercially available spin filters to assess the possibility of using them for the preparation of Aβ(1-40) oligomers.

The following units were used:

1) Amicon ultra 30 KDa, Millipore

2) Amicon ultra (Centricon) 10 KDa, Millipore

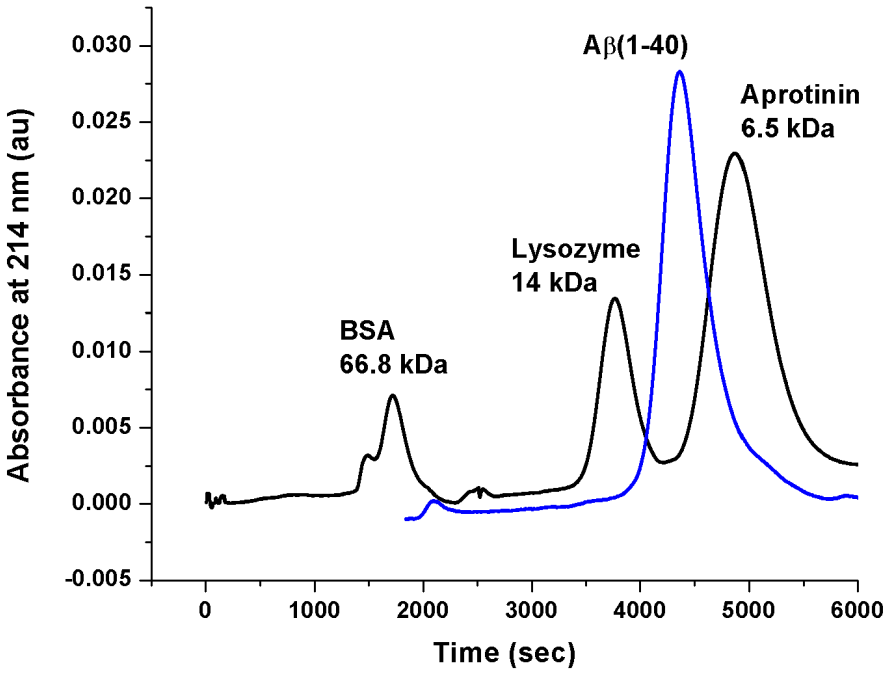

(a) Elution profiles of standard proteins and of Aβ(1-40): black trace - standardizing FPLC column with known size proteins: BSA (66.8 kDa), Lyzozyme (14.0 kDa), Aprotenin (6.5 kDa); blue trace - on-column oligomerization of GdmCl-denatured Aβ(1-40).

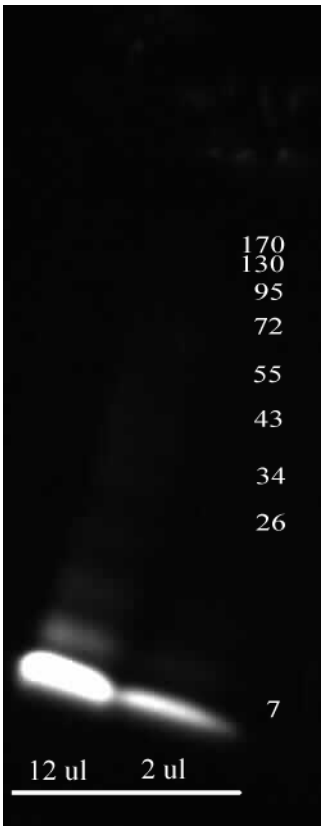

(b) PAGE analysis of Aβ(1-40) eluted from FPLC column.

Figure 52: On-column oligomerization of Aβ(1-40). FPLC elution profile and its consequent PAGE analysis.

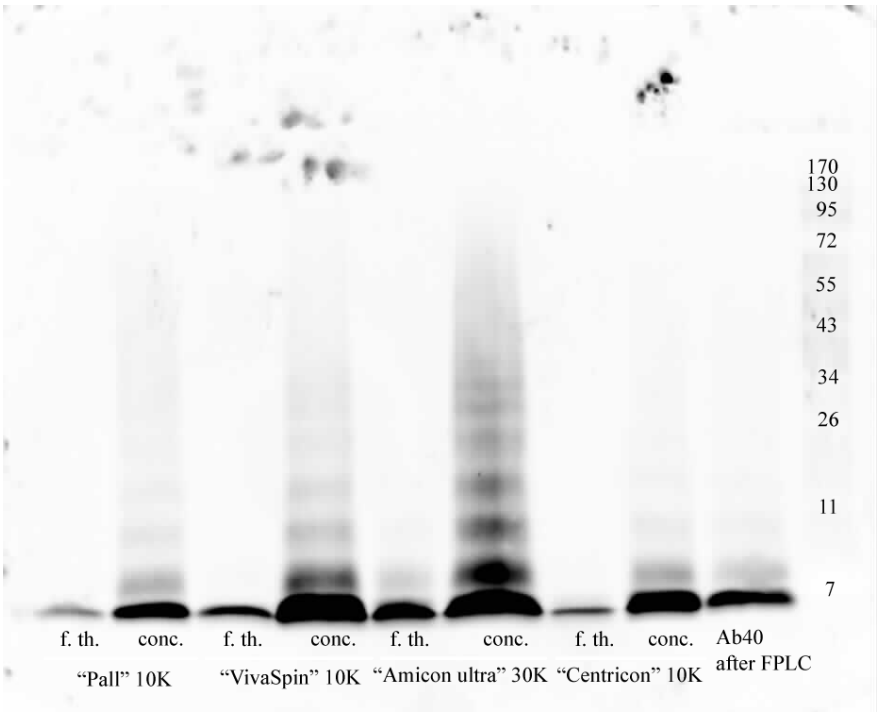

Figure 53: Oligomers separation using centrifugal concentration units, comparison of different brands. The order of the samples is as follows from right to left: Aβ(1-40) after elution from FPLC, concentrate and a flow-though from "Centricon", concentrate and flow-through from "Amicon ultra" 30 K, concentrate and flow-though from "Vivaspin", and concentrate and flow-through from "Macrosep".

3) Viva Spin 10 KDa, GE Healthcare
4) Macrosep Advance 10 KDa, Pall Corporation

All the centrifugal filter units were washed with MilliQ water at 5,000 ×g for 30 min at RT. Aβ(1-40) samples (old FPLC elution batch from Sephacryl S-100 HiPrep 16/60 HR) in 50 mM PB and 150 mM NaCl were added to each of the centrifugal units and spun at 5,000 ×g for 10 min at RT (Centricon and Macrosep units were spun for 20 min). Concentrates and flow-through were analyzed with PAGE and Western blot.

From the results shown in Figure 53 on page 138 it is clear that concentrating the sample, helps to visualize oligomers of higher molecular weight. Alternatively, centrifugal force may be a contributing factor in driving the aggregation of peptides in close physical proximity (due to the concentration process). The effect is stronger with "Amicon ultra" unit than with other units tested. Flow-through from all the samples seem to include mainly monomers, but in case of "Amicon ultra" unit, also some dimers and maybe trimers. This is also consistent with the fact that "Amicon ultra" has a cut off of 30 KDa, while all the other units have a cut off of 10 KDa.

A.0.7 *NMR experiments*

HRMAS (high resolution magic angle spinning) NMR experiments were performed to follow the behavior of the peptide in buffer solutions that were used to study Aβ(1-40) aggregation (i.e. Phosphate buffer and MOPS buffer). Each sample contained 2 mg of peptide in an NMR tube. Experiments were carried out at 310°K (37 °C) on a spectrometer operating at 11.7 Tesla. Samples were measured every 30 min, 32 experiments were conducted.

Already after the first experiment, 20 % of the intensity was lost and changes in peaks shape were observed (Figure 54 on page 140 and Figure 55 on page 141). We concluded that those changes are due to oligomerization process as they are short lived and no turbidity of the sample was noticed. Rapid formation of oligomers as a result of spinning precluded us from using HRMAS NMR for Aβ oligomers investigations.

We also attempted to perform DOSY (diffusion ordered spectroscopy) experiment, which provides a way to separate the different compounds in a mixture based on the differing translation diffusion coefficients (and therefore differences in size and shape of the molecule) of each chemical species in solution. In this case, the intention was to try to separate different oligomeric species in the sample. Sample consisted of 0.3 mg of Aβ(1-40) in 0.5 ml PB (90 % H_2O + 10 % D_2O). Unfortunately, this experiment did not work as there was radiation damping problem (Dr. Allouche from liquid NMR services of the UDS). Another trial to perform DOSY using micro-sample holder had also failed.

A.0.7.1 *^{13}C and ^{15}N CP experiments of Aβ oligomers and pure Aβ(1-40) powder in preparation for REDOR experiment (with Dr. Philippe Bertani).*

REDOR NMR - This technique for solids utilizes magic-angle spinning and measures directly the heteronuclear dipolar coupling between isolated pairs of labeled nuclei, which allows interatomic distances to be measured without the need to invoke simplifying assumptions. In a solid with ^{13}C-^{15}N dipolar coupling, the ^{13}C rotational spin echoes that form each rotor period following a ^{1}H-^{13}C cross-polarization transfer can be prevented from reaching full intensity by inserting two ^{15}N π-pulses per rotor period. One of the π-pulses is synchronized with the completion of the rotor period and the other with a time less than or equal to half the rotor period. The difference between a ^{13}C NMR spectrum obtained under these conditions and one obtained with no ^{15}N π-pulses measures the ^{13}C-^{15}N coupling [Marshall et al., 1990].

Sample 1: 2 mg of unlabeled Aβ(1-40) peptides were incubated in 4.6 ml of 5 mM MOPS buffer pH 7.4 + 2 mM $CaCl_2$. After 72 h and 96 h, the samples were filtered with a 50 kDa cut off filter, flash frozen

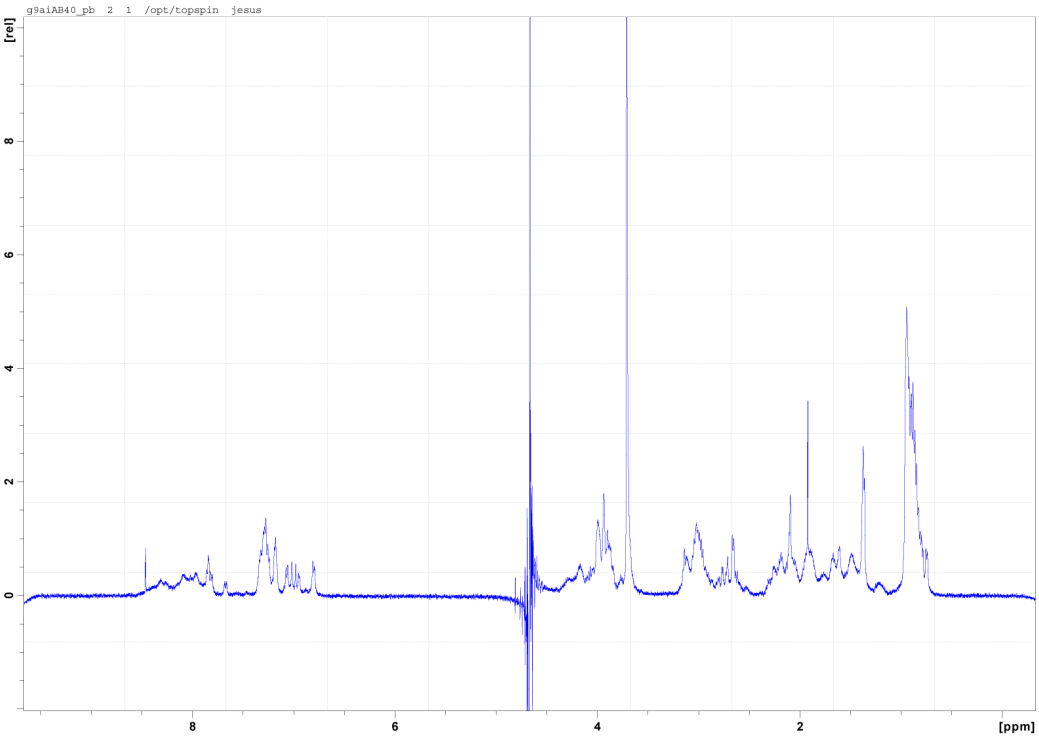

(a)

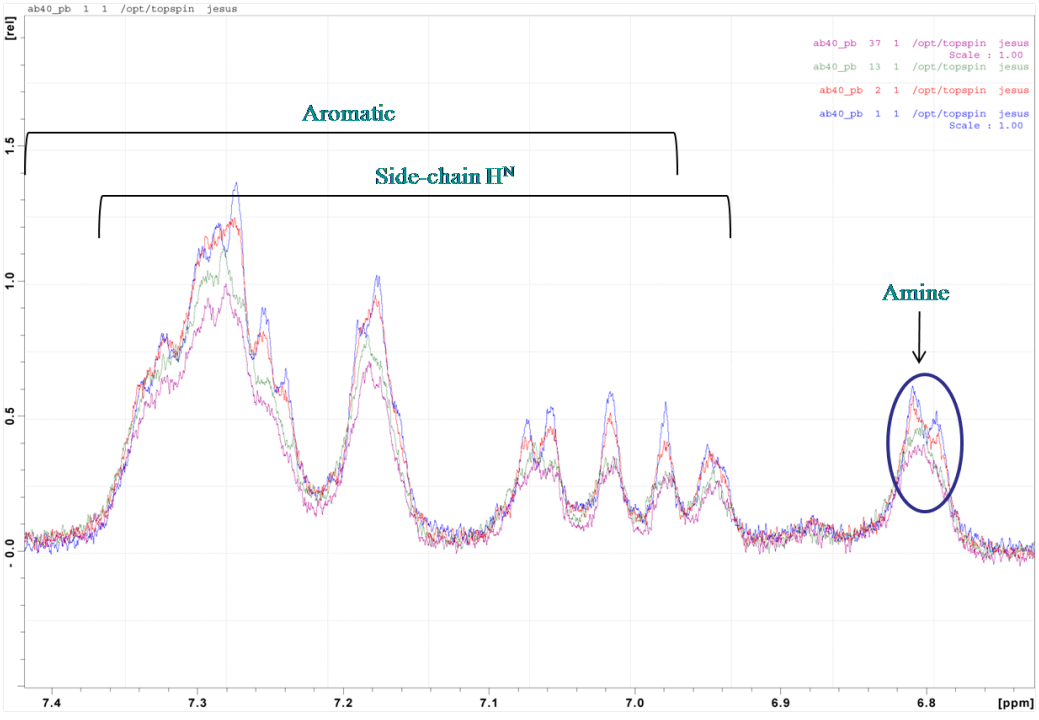

(b)

Figure 54: NMR spectrum of Aβ(1-40) in phosphate buffer. (a) full spectrum, (b) closeup into the aromatic and amine regions.

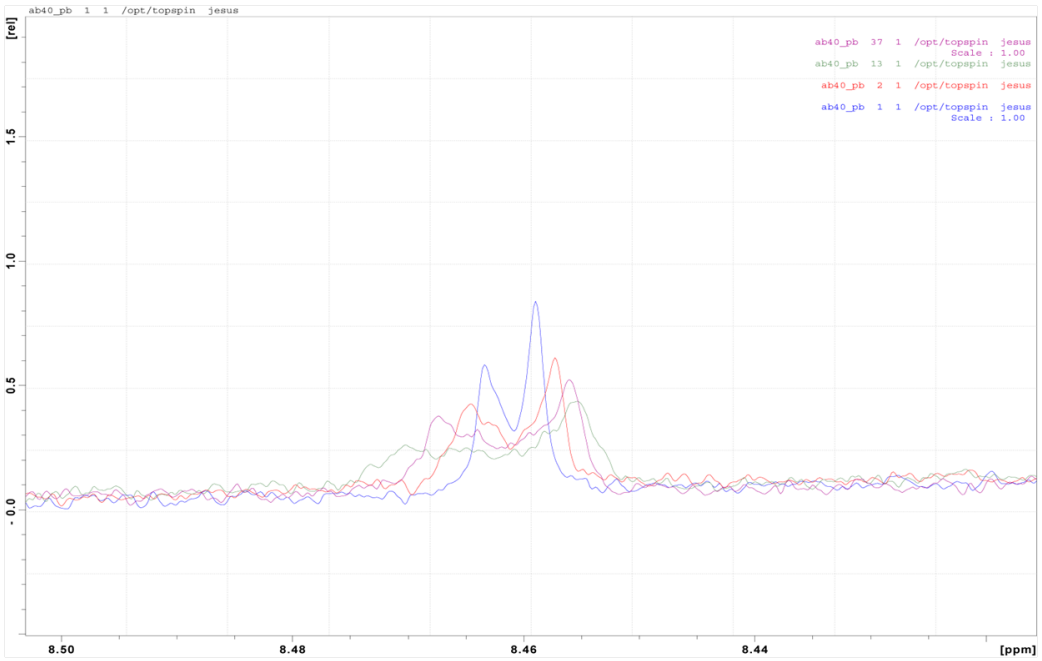

(a)

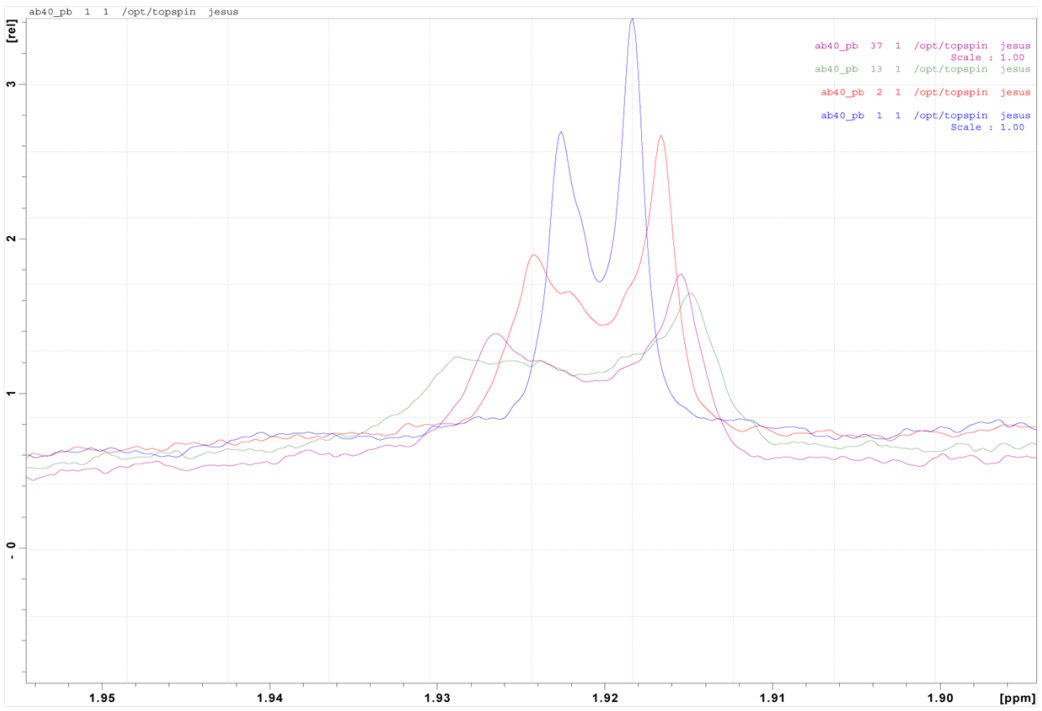

(b)

Figure 55: NMR spectrum of Aβ(1-40) in phosphate buffer. (c) closeup into the backbone amide region, (d) closeup into the aliphatic region.

and lyophilized. Approximately 0.4 mg (!) of the peptide was left after filtration. Do not filtrate after growth!

NMR EXPERIMENTAL DETAILS: cross-polarization, magic-angle spinning ^{13}C NMR spectra were obtained at room temperature on a Bruker Avance NMR spectrometer operating at 7.0 Tesla. A commercial double-resonance 3.2 mm MAS NMR probe was used with the spinning rate of 10 kHz (file name: ai_oligomermop). Radiofrequency (rf) field strength for carbon was 50 kHz with contact time of 1.6 msec for a basic CP experiment. A total of 102400 scans were collected to acquire the black-trace spectrum (Figure 56a on page 143). Radiofrequency (rf) field strength for carbons and protons was 83 kHz during acquisition on X with high-power proton decoupling. Red-trace spectrum with a total of 30720 scans collected (Figure 56a on page 143). No NMR signal from the peptides amide region was detected (Figure 56b on page 143).

MOPS exhibited very strong NMR signal (Figure 56a on page 143) that interfered with the protein signal, which was very weak in the first place (Figure 56b on page 143). Lowering MOPS concentration did not work - peptides precipitated, probably due to low electrostatics in the sample.

Sample 2: 8.8 mg of Aβ(1-40) peptides isotopically labeled at Glu22 and Lys28 were incubated in 20 ml buffer consistent of 10 mM MOPS + 5 mM NaCl + 2 mM $CaCl_2$ for 52 h. The sample was centrifuged at 13,200 $\times$g for 15 min. Only the top 70 % of the solution were collected, frozen and lyophilized.

NMR EXPERIMENTAL DETAILS: cross-polarization, magic-angle spinning ^{13}C and ^{15}N NMR spectra were obtained at room temperature on a Bruker Avance NMR spectrometer operating at 11.7 Tesla. A commercial double-resonance 3.2 mm MAS NMR probe was used with the spinning rate of 17 kHz. Radiofrequency (rf) field strength for carbon was 50 kHz, 8.3 kHz for nitrogen and for protons 83 kHz during cross-polarization. A total of 32768 scans were collected. CP was set up for O/N, because there was no signal after small number of scans (file name: ai_oligo_11_10). Even after O/N experiment, there was mainly signal from the MOPS molecules (Figure 57a on page 144) and a very small ^{13}C signal from the peptide. Also for ^{15}N CP no signal was detected above the noise level after 5 h (Figure 57b on page 144).

Sample 3: It was decided to look at the ^{13}C and ^{15}N chemical shifts of purified labeled Aβ(1-40) peptide powder (not oligomers), in order to verify that the isotopic labels are present.

NMR EXPERIMENTAL DETAILS: cross-polarization, magic-angle spinning ^{13}C and ^{15}N NMR spectra were obtained at room temperature on a Bruker Avance NMR spectrometer operating at 11.7 Tesla. A commercial double-resonance 3.2 mm MAS NMR probe was used with spinning rate of 17 kHz. Radiofrequency (rf) field strength for

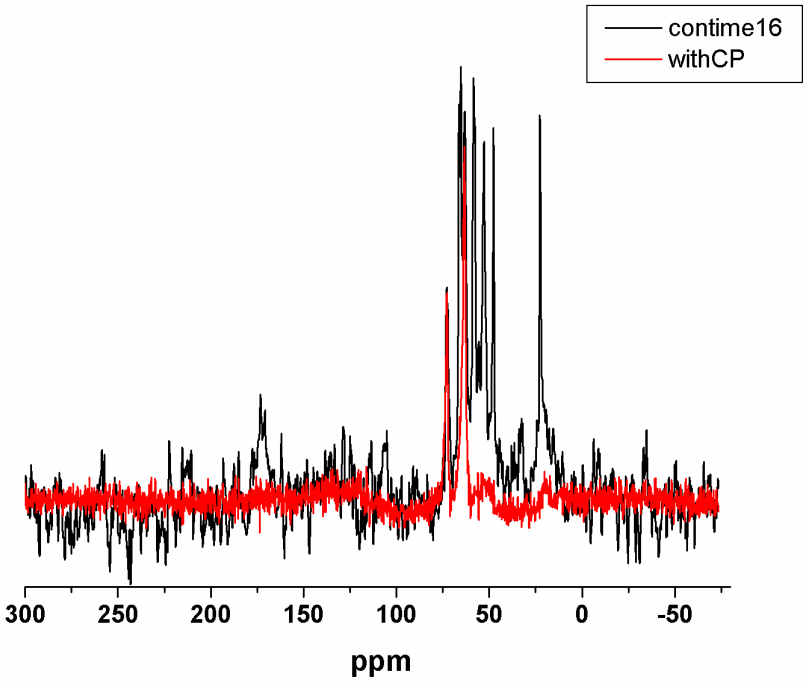

(a) ^{13}C natural abundance - full spectrum. Black trace with contact time 1.6 msec; red trace with proton decoupling.

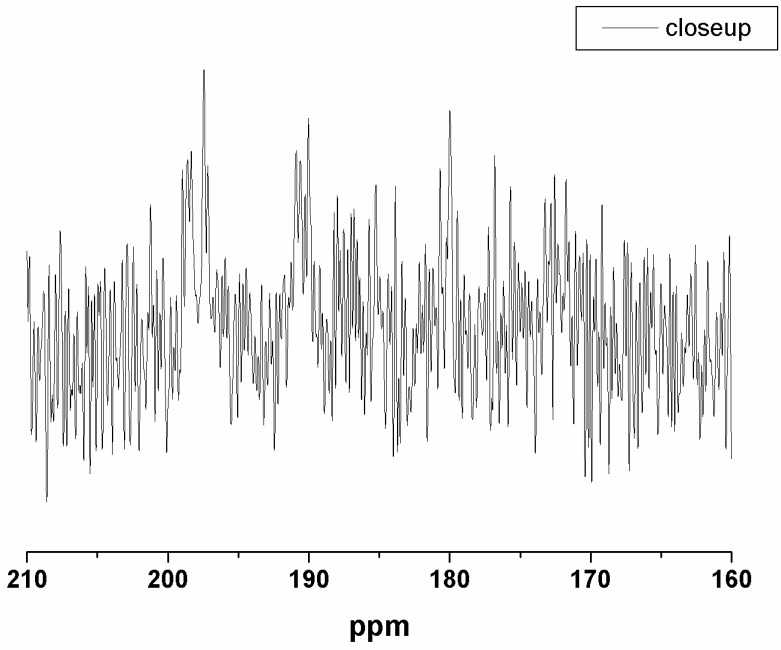

(b) ^{13}C natural abundance - closeup into the carbonyl region

Figure 56: Aβ(1-40) ^{13}C natural abundance, MAS NMR at RT.

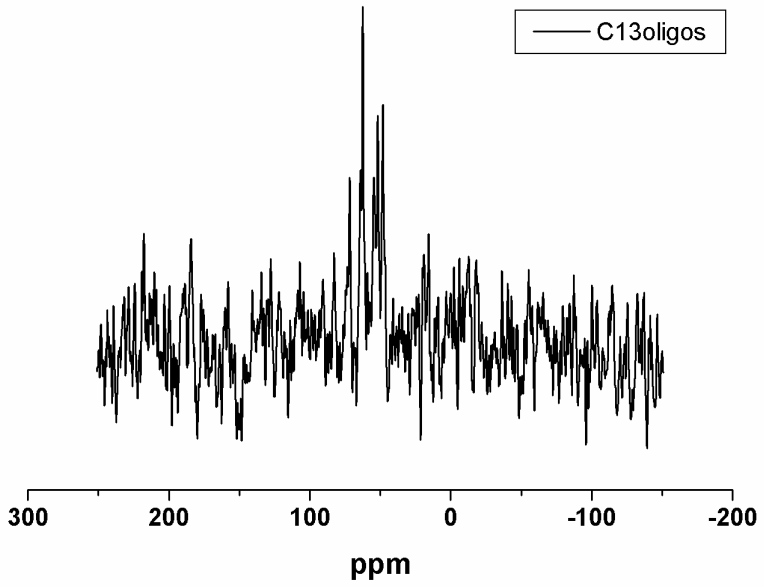

(a) ^{13}C-Glu22 chemical shifts of Aβ(1-40) oligomers grown in MOPS buffer

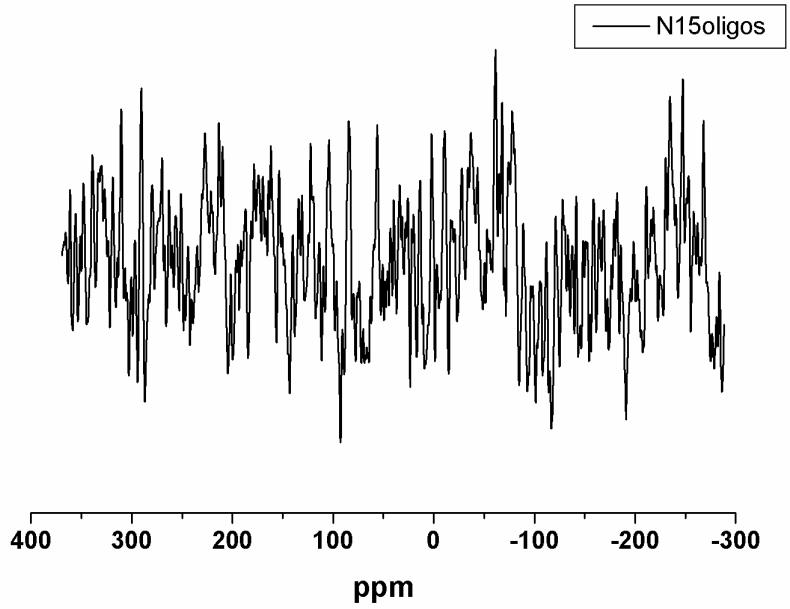

(b) ^{15}N-Lys28 chemical shifts of Aβ(1-40) oligomers grown in MOPS buffer

Figure 57: ^{13}C and ^{15}N chemical sifts from CP experiments of Aβ(1-40) oligomers grown in MOPS buffer.

carbon was 70 kHz, 43.7 kHz for nitrogen and for protons 83 kHz during cross-polarization. A total of 128 and 256 scans were collected for ^{13}C and ^{15}N, respectively (file name: ai_synthAb40_11_10).

CP on ^{13}C gave several strong signals: two corresponded to the MOPS molecules (large spectral discontinuity from ~ 11 ppm to 60 ppm) and one corresponded to 173.2 ppm that arose from ^{13}C-Glu22 (Figure 58a on page 146). This result means that the peptide is isotopically labeled with ^{13}C on the correct amino acid. In addition, CP on ^{15}N produced two peaks at 36 ppm and 124.7 ppm, roughly corresponding to the expected averaged values for backbone nitrogen (121.06 ppm) and to N^{ζ}(33.96 ppm) (Figure 58b on page 146). Therefore, the reason for the absence of the signal from oligomers samples is probably due to the low amount of the final material and further optimization of the protocol is required.

We explored the possibility of avoiding using MOPS as buffer and using PB. The following sample was prepared.

Sample 4: starting with 10 mg of Aβ(1-40) peptide labeled at Glu22 and Lys28, as previously described. Peptides were resuspended in 23 ml of 10 mM PB pH 7.4 + 5 mM NaCl, filtrated using centrifugal filter Amicon 50K at 12,000 ×g (centrifugation at 13,200 ×g caused one filter to collapse) at 4°C for 15 min. Thereafter, samples were incubated at 37°C for 96 h, flash frozen and lyophilized.

NMR EXPERIMENTAL DETAILS: cross-polarization, magic-angle spinning ^{13}C and NMR spectra were obtained at 244 K on a Bruker Avance NMR spectrometer operating at 11.7 Tesla. A commercial double-resonance 3.2 mm MAS NMR probe was used with spinning rate of 17 kHz. Radiofrequency (rf) field strength for carbon was 70 kHz and for protons 83 kHz during cross-polarization. A total of 9216 scans were collected (file name: ai_synthAb40_11_10 exp. # 10 and # 11 and ai_oligoPB_11_10 exp. # 10).

In Figure 59 on page 147, the black trace shows the signal that arose from ^{13}C of Aβ(1-40) oligomers, while the red trace shows the signal that arose from purified dry Aβ(1-40) peptides. No signal was obtained from ^{15}N CP experiment. Aβ(1-40) oligomers were grown in PB buffer and no MOPS molecules were present therefore, the observed signal comes from oligomers only. Clearly, the chemical shifts of oligomers are distinct from those of the dry peptide. It looks like it might be a characteristic signature of Aβ oligomers, but additional experiments are needed to verify it.

A.0.8 *SANS measurements (in collaboration with Dr. Preu Julia and Forschungszentrum Jülich)*

Large preliminary work was done in order to establish whether it will be possible to perform SANS experiment with Aβ peptides grown in the presence of 60 % D_2O. According to our collaborator Dr. Julia Preu,

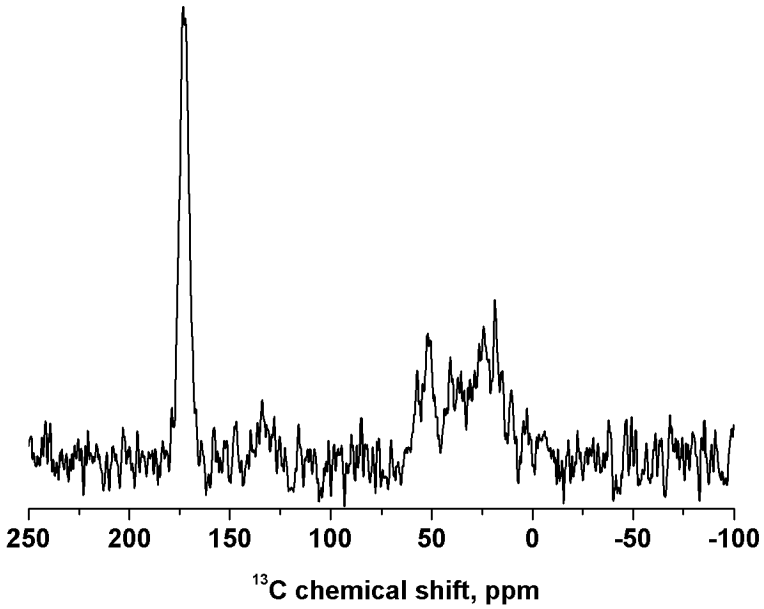

(a) ^{13}C chemical shifts from Glu22 of Aβ(1-40), natural abundance and MOPS molecules. Collected at 294 K.

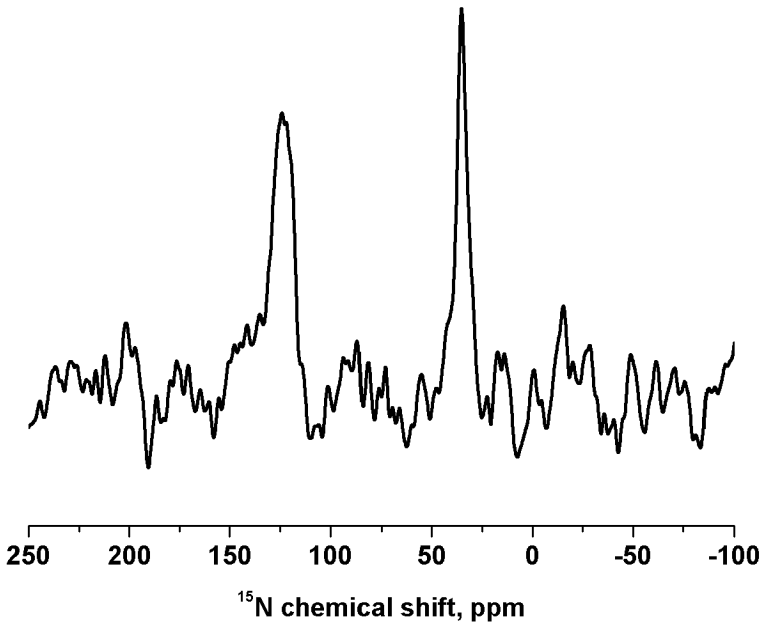

(b) ^{15}N chemical shifts from Lys28 of Aβ(1-40). Collected at 245 K.

Figure 58: ^{13}C and ^{15}N chemical shift CP spectra of pure synthetic Aβ(1-40) peptide labeled at Glu22 and Lys28.

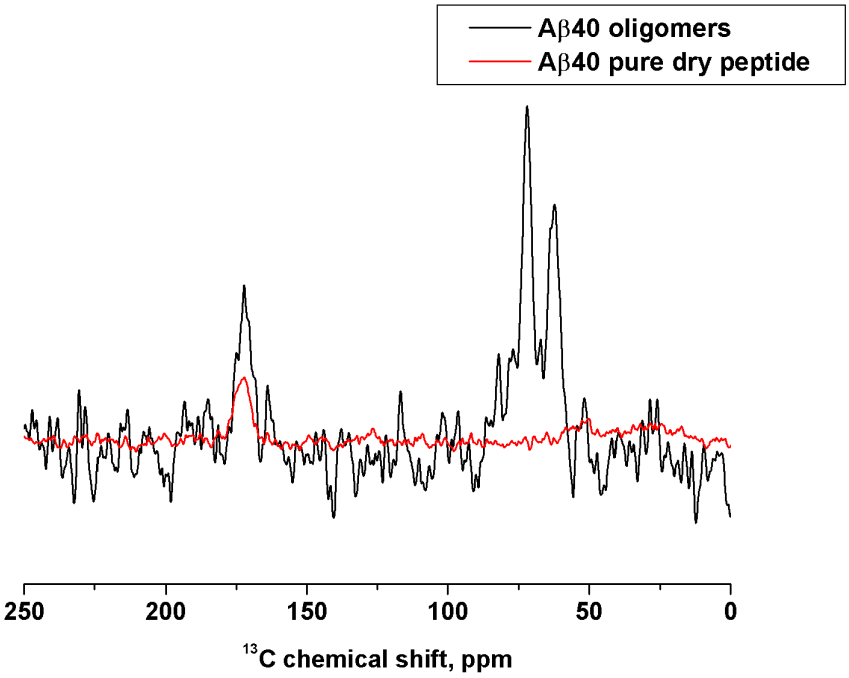

Figure 59: ^{13}C CP of Aβ(1-40) oligomers from PB (black trace) and purified dry powder of Aβ(1-40) (red trace), measured at 244°K.

having 60 % D_2O in the buffer should have given a good contrast in the SANS experiment.

Sample growth trials: 2 mg of Aβ peptides–Aβ(1-40) and Aβ(1-40)E22G–were dissolved in either 75 mM MOPS pH 7.4 alone or in 75 mM MOPS pH 7.4 + 2 mM Ca^{2+} in 60 % D_2O and were grown for 72 h. Throughout the growth, small volumes were taken from all the samples–Aβ(1-40) and Aβ(1-40)E22G in both conditions–and subjected to PAGE and Western blot analyses (Figure 60 on page 148).

The results in Figure 60 on page 148 show that under these experimental conditions both Aβ(1-40) and Aβ(1-40)E22G aggregate faster than in previously measured conditions. It seems that the oligomers can be harvested already after 24 h of growth. However, it does not seem that after 72 h there are many more high molecular weight aggregates or fibrils. Therefore, it was decided to harvest oligomers after 72 h as they were suppose to be filtered for the final sample preparation.

Preparation of oligomers for SANS experiments: 2 mg of Aβ peptides–Aβ(1-40) and Aβ(1-40)E22G–were dissolved in either 50 mM PB pH 7.4 or in 75 mM MOPS pH 7.4 + 2 mM Ca^{2+} and were grown for 72 h. Thereafter, 500 µl of each sample were filtered using centrifugal filter Amicon Ultra - 0.5 (Millipore) at 14,000 ×g for 10 min at 4°C. Flow-through was collected, flash-frozen with liquid nitrogen and lyophilized.

Sample names and their content were as follows:

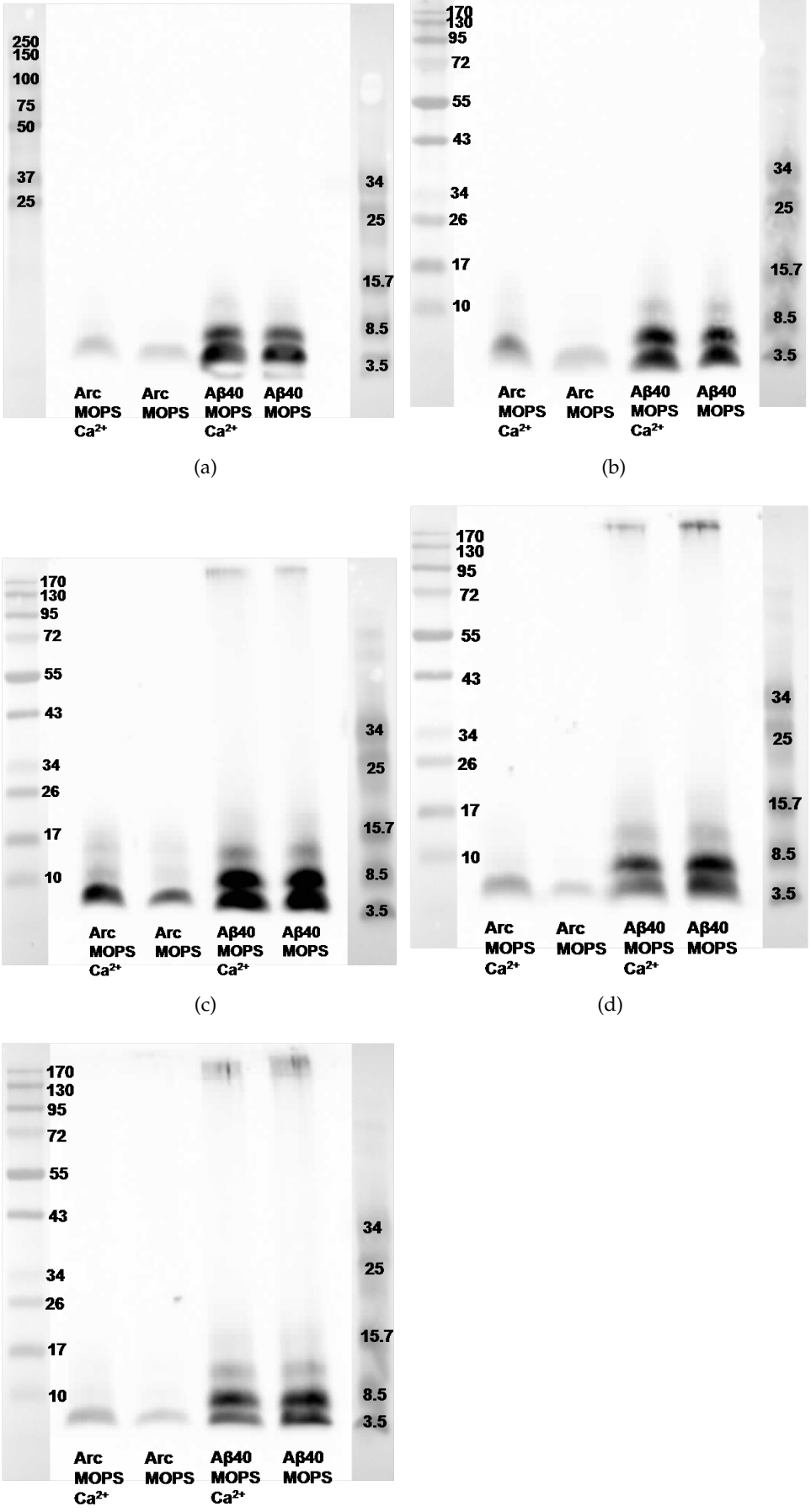

Figure 60: Effect of 60 % D_2O on aggregation profiles of 1mM Aβ40 and Aβ40E22G in MOPS or MOPS + 2mM Ca^{2+}(a) sample at 0 h, (b) sample at 4 h, (c) sample at 24 h, (d) sample at 48 h, (e) sample at 72 h.

1. AB-Oligos - stands for Aβ(1-40) pre-formed dry oligomers, were rehydrated with buffer on-site.

2. ARC-Oligos - stands for Aβ(1-40)E22G pre-formed dry oligomers, rehydrated on-site

3. AB-MOPS-oh - Aβ(1-40)crude sample in MOPS buffer. The start point for oligomer growth was on-site. These were "kinetics samples" - NO D2O.

4. ARC-MOPS-oh - Aβ(1-40)E22G crude sample in MOPS buffer. The start point for oligomer growth was on-site. Also "kinetics samples" - NO D2O.

5. AB-PB-oh and ARC-PB-oh - same as samples #3 and #4 only in phosphate (PB) buffer. "Kinetics samples" - NO D2O.

6. AB-MOPS-5-D2O and ARC-MOPS-5-D2O - Aβ(1-40) or Aβ(1-40)E22G, crude sample in MOPS buffer pH 5 and 55% D2O. Were already in solution when arrived to the site.

7. ARC-MOPS-D2O in MOPS buffer in 55% D2O (the sample with Aβ(1-40) was lost during preparation). Was already in solution when arrived on site.

8. AB-PB-D2O and ARC-PB-D2O - both peptides in phosphate buffer (PB) in 55% D2O. Were already in solution when arrived on site.

* The percentage of D2O needed to be reduced on-site in order to achieve better contrast (according to the SANS scientist on the site).

* Samples that "arrived in solution" were aggregated to some extent and gave large scattering.

* Samples in D2O had a very bad contrast (not much scattering was observed).

The data is shown in Figure 61 on page 150, Figure 62 on page 151, Figure 63 on page 152, Figure 64 on page 153.

At first, a pair distance distribution function was calculated, to get an idea about the particle dimensions. Unfortunately, it was quite difficult to obtain reasonable model from the collected data. Nevertheless, the results point towards a rod-like shape, rather than an elliptical shape.

A.0.9 ^{2}H *NMR of lipids and Aβ peptides*

The following experiments were performed as a preparation for the future study of specifically labeled Aβ(1-40) peptides with lipids. The objective was to find lipid combinations most suitable to investigate lipid-peptide interactions and structural studies of Aβ oligomers.

The simplest lipid combination consisted of POPC and POPE lipids. Then POPS, Cholesterol and sphingomyelin were added one at a time and in combination. Fot these initial studies, non-labeled peptides were used.

Sheet1_2

Sample	Runs	C	D	lambda	Beam	Sum	Duration	cps	Date	Time	Sample-Nr
[1]EC-01	34242	4	1.2	4.5	30x30|5x5	1.82E+006	300	6052.33	08/17/10	16:56:37.00	1
[2]EB-01	34243	4	1.2	4.5	30x30|5x5	1.51E+006	300	5038.5	08/17/10	17:01:53.00	2
[3]PlexiStandard-01	34244	4	1.2	4.5	30x30|5x5	1.94E+007	300	64548.7	08/17/10	17:07:08.00	3
[4]B4C-01	34245	4	1.2	4.5	30x30|5x5	570495	300	1901.65	08/17/10	17:12:24.00	4
[1]EC-01	34246	4	3.7	4.5	30x30|5x5	537703	600	896.17	08/17/10	17:19:39.00	1
[2]EB-01	34247	4	3.7	4.5	30x30|5x5	482214	600	803.69	08/17/10	17:29:52.00	2
[3]PlexiStandard-01	34248	4	3.7	4.5	30x30|5x5	4.39E+006	600	7312.87	08/17/10	17:40:06.00	3
[4]B4C-01	34249	4	3.7	4.5	30x30|5x5	173141	600	288.57	08/17/10	17:50:19.00	4
#1											
AB-Oligos-01	34266	4	1.2	4.5	30x30|5x5	3.09E+007	600	51460.2	08/17/10	19:29:54.00	11
ARC-Oligos-01	34267	4	1.2	4.5	30x30|5x5	3.07E+007	600	51099.8	08/17/10	19:40:11.00	12
Mops7.4-01	34268	4	1.2	4.5	30x30|5x5	1.54E+007	300	51245	08/17/10	19:50:28.00	13
AB-MOPS-0h-01	34269	4	1.2	4.5	30x30|5x5	1.53E+007	300	51124.7	08/17/10	19:55:45.00	14
ARC-MOPS-0h-01	34270	4	1.2	4.5	30x30|5x5	1.54E+007	300	51343.3	08/17/10	20:01:02.00	15
PB-7-4-01	34271	4	1.2	4.5	30x30|5x5	1.52E+007	300	50744.7	08/17/10	20:06:17.00	16
AB-PB-oh-01	34272	4	1.2	4.5	30x30|5x5	1.53E+007	300	50973.7	08/17/10	20:11:32.00	17
ARC-PB-oh-01	34273	4	1.2	4.5	30x30|5x5	1.53E+007	300	51019	08/17/10	20:16:47.00	18
MOPS-5-D2O-01	34274	4	1.2	4.5	30x30|5x5	1.05E+007	300	34913.3	08/17/10	20:22:36.00	21
ARC-MOPS-5-D2O-01	34275	4	1.2	4.5	30x30|5x5	1.04E+007	300	34721.7	08/17/10	20:27:51.00	22
AB-MOPS-5-D2O-01	34276	4	1.2	4.5	30x30|5x5	1.04E+007	300	34545.3	08/17/10	20:33:06.00	23
MOPS-7.4-D2O-01	34277	4	1.2	4.5	30x30|5x5	1.03E+007	300	34205.3	08/17/10	20:38:21.00	24
ARC-MOPS-D2O-01	34278	4	1.2	4.5	30x30|5x5	1.02E+007	300	34028	08/17/10	20:43:37.00	25
PB-7.4-D2O-01	34279	4	1.2	4.5	30x30|5x5	1.01E+007	300	33790.7	08/17/10	20:48:52.00	26
ARC-PB-D2O-01	34280	4	1.2	4.5	30x30|5x5	1.01E+007	300	33799.3	08/17/10	20:54:07.00	27
AB-PB-D2O-01	34281	4	1.2	4.5	30x30|5x5	1.02E+007	300	33988.7	08/17/10	20:59:22.00	28
AB-Oligos-01	34282	4	3.7	4.5	30x30|5x5	7.01E+006	1200	5844.03	08/17/10	21:06:38.00	11
ARC-Oligos-01	34283	4	3.7	4.5	30x30|5x5	6.93E+006	1200	5771.18	08/17/10	21:26:52.00	12
Mops7.4-01	34284	4	3.7	4.5	30x30|5x5	3.45E+006	600	5751.28	08/17/10	21:47:07.00	13
AB-MOPS-0h-01	34285	4	3.7	4.5	30x30|5x5	3.51E+006	600	5856.28	08/17/10	21:57:22.00	14
ARC-MOPS-0h-01	34286	4	3.7	4.5	30x30|5x5	3.60E+006	600	5994.2	08/17/10	22:07:38.00	15
PB-7-4-01	34287	4	3.7	4.5	30x30|5x5	3.44E+006	600	5732.1	08/17/10	22:17:53.00	16
AB-PB-oh-01	34288	4	3.7	4.5	30x30|5x5	3.57E+006	600	5944.77	08/17/10	22:28:08.00	17

Page 1

(a) page 1

Sheet1_2

ARC-PB-oh-01	34289	4	3.7	4.5	30x30|5x5	3.64E+006	600	6060.13	08/17/10	22:38:23.00	18
MOPS-5-D2O-01	34290	4	3.7	4.5	30x30|5x5	2.39E+006	600	3990.38	08/17/10	22:49:12.00	21
ARC-MOPS-5-D2O-01	34291	4	3.7	4.5	30x30|5x5	2.38E+006	600	3958.83	08/17/10	22:59:27.00	22
AB-MOPS-5-D2O-01	34292	4	3.7	4.5	30x30|5x5	2.37E+006	600	3945.28	08/17/10	23:09:42.00	23
MOPS-7.4-D2O-01	34293	4	3.7	4.5	30x30|5x5	2.32E+006	600	3868.23	08/17/10	23:19:57.00	24
ARC-MOPS-D2O-01	34294	4	3.7	4.5	30x30|5x5	2.32E+006	600	3863	08/17/10	23:30:12.00	25
PB-7.4-D2O-01	34295	4	3.7	4.5	30x30|5x5	2.30E+006	600	3837.8	08/17/10	23:40:27.00	26
ARC-PB-D2O-01	34296	4	3.7	4.5	30x30|5x5	2.30E+006	600	3836.17	08/17/10	23:50:42.00	27
AB-PB-D2O-01	34297	4	3.7	4.5	30x30|5x5	2.33E+006	600	3887.4	08/18/10	00:00:57.00	28
#2											
AB-Oligos-02	34298	4	1.2	4.5	30x30|5x5	4.65E+007	900	51620.6	08/18/10	00:13:12.00	11
ARC-Oligos-02	34299	4	1.2	4.5	30x30|5x5	4.61E+007	900	51268.2	08/18/10	00:28:27.00	12
AB-Oligos-02	34300	4	3.7	4.5	30x30|5x5	1.05E+007	1800	5849.06	08/18/10	00:45:42.00	11
ARC-Oligos-02	34301	4	3.7	4.5	30x30|5x5	1.04E+007	1800	5777.17	08/18/10	01:15:56.00	12
#3											
AB-Oligos-03	34302	4	1.2	4.5	30x30|5x5	4.64E+007	900	51594	08/18/10	01:48:12.00	11
ARC-Oligos-03	34303	4	1.2	4.5	30x30|5x5	4.61E+007	900	51195.1	08/18/10	02:03:27.00	12
AB-Oligos-03	34304	4	3.7	4.5	30x30|5x5	1.05E+007	1800	5847.61	08/18/10	02:20:41.00	11
ARC-Oligos-03	34305	4	3.7	4.5	30x30|5x5	1.04E+007	1800	5764.61	08/18/10	02:50:56.00	12
#4											
AB-Oligos-04	34306	4	1.2	4.5	30x30|5x5	4.63E+007	900	51409.2	08/18/10	03:23:11.00	11
ARC-Oligos-04	34307	4	1.2	4.5	30x30|5x5	4.60E+007	900	51135.9	08/18/10	03:38:26.00	12
Mops7.4-04	34308	4	1.2	4.5	30x30|5x5	1.53E+007	300	51129	08/18/10	03:53:41.00	13
AB-MOPS-0h-04	34309	4	1.2	4.5	30x30|5x5	1.53E+007	300	51082.7	08/18/10	03:58:56.00	14
ARC-MOPS-0h-04	34310	4	1.2	4.5	30x30|5x5	1.54E+007	300	51193.7	08/18/10	04:04:12.00	15
PB-7-4-04	34311	4	1.2	4.5	30x30|5x5	1.53E+007	300	50916.7	08/18/10	04:09:27.00	16
AB-PB-oh-04	34312	4	1.2	4.5	30x30|5x5	1.54E+007	300	51237.7	08/18/10	04:14:42.00	17
ARC-PB-oh-04	34313	4	1.2	4.5	30x30|5x5	1.53E+007	300	51143.3	08/18/10	04:19:56.00	18
MOPS-5-D2O-04	34314	4	1.2	4.5	30x30|5x5	1.05E+007	300	34873	08/18/10	04:25:47.00	21
ARC-MOPS-5-D2O-04	34315	4	1.2	4.5	30x30|5x5	1.04E+007	300	34722	08/18/10	04:31:02.00	22
AB-MOPS-5-D2O-04	34316	4	1.2	4.5	30x30|5x5	1.04E+007	300	34608.7	08/18/10	04:36:17.00	23

Page 2

(b) page 2

Figure 61: Results from SANS experiment arranged in a table.

Sheet1_2

MOPS-7.4-D2O-04	34317	4	1.2	4.5	30x30|5x5	1.02E+007	300	34108	08/18/10	04:41:32.00	24
ARC-MOPS-D2O-04	34318	4	1.2	4.5	30x30|5x5	1.02E+007	300	33889.7	08/18/10	04:46:48.00	25
PB-7.4-D2O-04	34319	4	1.2	4.5	30x30|5x5	1.01E+007	300	33723.3	08/18/10	04:52:03.00	26
ARC-PB-D2O-04	34320	4	1.2	4.5	30x30|5x5	1.01E+007	300	33748	08/18/10	04:57:18.00	27
AB-PB-D2O-04	34321	4	1.2	4.5	30x30|5x5	1.02E+007	300	34146.3	08/18/10	05:02:33.00	28
AB-Oligos-04	34322	4	3.7	4.5	30x30|5x5	1.05E+007	1800	5850.67	08/18/10	05:09:49.00	11
ARC-Oligos-04	34323	4	3.7	4.5	30x30|5x5	1.04E+007	1800	5787.61	08/18/10	05:40:03.00	12
Mops7.4-04	34324	4	3.7	4.5	30x30|5x5	3.46E+006	600	5774.45	08/18/10	06:10:18.00	13
AB-MOPS-0h-04	34325	4	3.7	4.5	30x30|5x5	3.54E+006	600	5897.4	08/18/10	06:20:33.00	14
ARC-MOPS-0h-04	34326	4	3.7	4.5	30x30|5x5	3.61E+006	600	6013.63	08/18/10	06:30:49.00	15
PB-7-4-04	34327	4	3.7	4.5	30x30|5x5	3.44E+006	600	5725.18	08/18/10	06:41:04.00	16
AB-PB-oh-04	34328	4	3.7	4.5	30x30|5x5	3.58E+006	600	5958.65	08/18/10	06:51:19.00	17
ARC-PB-oh-04	34329	4	3.7	4.5	30x30|5x5	3.65E+006	600	6083.92	08/18/10	07:01:34.00	18
MOPS-5-D2O-04	34330	4	3.7	4.5	30x30|5x5	2.39E+006	600	3979.93	08/18/10	07:12:23.00	21
ARC-MOPS-5-D2O-04	34331	4	3.7	4.5	30x30|5x5	2.38E+006	600	3959.63	08/18/10	07:22:37.00	22
AB-MOPS-5-D2O-04	34332	4	3.7	4.5	30x30|5x5	2.37E+006	600	3943	08/18/10	07:32:52.00	23
MOPS-7.4-D2O-04	34333	4	3.7	4.5	30x30|5x5	2.33E+006	600	3875.48	08/18/10	07:43:07.00	24
ARC-MOPS-D2O-04	34334	4	3.7	4.5	30x30|5x5	2.31E+006	600	3845.8	08/18/10	07:53:23.00	25
PB-7.4-D2O-04	34335	4	3.7	4.5	30x30|5x5	2.30E+006	600	3829.95	08/18/10	08:03:38.00	26
ARC-PB-D2O-04	34336	4	3.7	4.5	30x30|5x5	2.29E+006	600	3821.92	08/18/10	08:13:53.00	27
AB-PB-D2O-04	34337	4	3.7	4.5	30x30|5x5	2.33E+006	600	3887.53	08/18/10	08:24:08.00	28
#5											
AB-Oligos-05	34338	2	1.2	4.5	30x30|5x5	2.06E+008	900	228763	08/18/10	08:36:24.00	11
ARC-Oligos-05	34339	2	1.2	4.5	30x30|5x5	2.05E+008	900	228182	08/18/10	08:51:39.00	12
AB-Oligos-05	34340	2	3.7	4.5	30x30|5x5	3.38E+008	1800	187834	08/18/10	09:08:53.00	11
ARC-Oligos-05	34341	2	3.7	4.5	30x30|5x5	3.42E+008	1800	190007	08/18/10	09:39:07.00	12
#6											
AB-Oligos-06	34342	4	1.2	4.5	30x30|5x5	3.09E+007	600	51521.7	08/18/10	10:22:25.00	11
ARC-Oligos-06	34343	4	1.2	4.5	30x30|5x5	3.07E+007	600	51186.7	08/18/10	10:32:41.00	12
AB-Oligos-06	34344	4	3.7	4.5	30x30|5x5	7.02E+006	1200	5848.41	08/18/10	10:44:56.00	11
ARC-Oligos-06	34345	4	3.7	4.49	30x30|5x5	5.98E+006	1035	5780.59	08/18/10	11:05:13.00	12
[2]EB	34346	20	3.7	4.5	30x30|10x10	83126	600	138.54	08/18/10	11:32:38.00	2

Page 3

(a) page 3

Sheet1_2

[3]PlexiStandard	34347	20	3.7	4.5	30x30|10x10	1.04E+006	600	1740.83	08/18/10	11:42:55.00	3
[4]B4C	34348	20	3.7	4.5	30x30|10x10	22833	600	38.06	08/18/10	11:53:11.00	4
[1]EC	34349	20	19.7	4.5	30x30|10x10	745280	1200	621.07	08/18/10	12:16:35.00	1
[4]B4C	34350	20	19.7	4.5	30x30|10x10	16385	900	18.21	08/18/10	12:37:01.00	4
#4 (20m)											
AB-Oligos-04	34351	20	19.7	4.5	30x30|10x10	359205	900	399.12	08/18/10	12:52:49.00	11
ARC-Oligos-04	34352	20	19.7	4.5	30x30|10x10	353759	900	393.07	08/18/10	13:08:04.00	12
AB-MOPS-0h-04	34353	20	19.7	4.5	30x30|10x10	608222	900	675.8	08/18/10	13:23:22.00	14
ARC-MOPS-0h-04	34354	20	19.7	4.5	30x30|10x10	416741	900	463.05	08/18/10	13:38:38.00	15
AB-PB-oh-04	34355	20	19.7	4.5	30x30|10x10	373934	900	415.48	08/18/10	13:53:56.00	17
ARC-PB-oh-04	34356	20	19.7	4.5	30x30|10x10	408433	900	453.81	08/18/10	14:09:11.00	18
AB-PB-D2O-04	34357	20	19.7	4.5	30x30|10x10	427979	900	475.53	08/18/10	14:24:59.00	28
#7											
AB-Oligos-07	34358	4	1.2	4.5	30x30|5x5	4.65E+007	900	51632.4	08/18/10	16:46:27.00	11
ARC-Oligos-07	34359	4	1.2	4.5	30x30|5x5	4.61E+007	900	51220.6	08/18/10	17:01:45.00	12
AB-Oligos-07	34360	4	3.7	4.5	30x30|5x5	1.05E+007	1800	5848.5	08/18/10	17:19:02.00	11
ARC-Oligos-07	34361	4	3.7	4.5	30x30|5x5	1.04E+007	1800	5782.94	08/18/10	17:49:19.00	12
#8											
AB-Oligos-08	34362	4	1.2	4.5	30x30|5x5	3.09E+007	600	51551.3	08/18/10	18:21:36.00	11
ARC-Oligos-08	34363	4	1.2	4.5	30x30|5x5	3.08E+007	600	51277	08/18/10	18:31:51.00	12
Mops7.4-08	34364	4	1.2	4.5	30x30|5x5	1.54E+007	300	51235.7	08/18/10	18:42:06.00	13
AB-MOPS-0h-08	34365	4	1.2	4.5	30x30|5x5	1.53E+007	300	51103	08/18/10	18:47:21.00	14
ARC-MOPS-0h-08	34366	4	1.2	4.5	30x30|5x5	1.54E+007	300	51353.7	08/18/10	18:52:38.00	15
PB-7-4-08	34367	4	1.2	4.5	30x30|5x5	1.53E+007	300	50919.3	08/18/10	18:57:53.00	16
AB-PB-oh-08	34368	4	1.2	4.5	30x30|5x5	1.54E+007	300	51200	08/18/10	19:03:08.00	17
ARC-PB-oh-08	34369	4	1.2	4.5	30x30|5x5	1.54E+007	300	51355	08/18/10	19:08:23.00	18
MOPS-5-D2O-08	34370	4	1.2	4.5	30x30|5x5	1.69E+007	480	35124	08/18/10	19:14:13.00	21
ARC-MOPS-5-D2O-08	34371	4	1.2	4.5	30x30|5x5	1.68E+007	480	34902.1	08/18/10	19:22:28.00	22
AB-MOPS-5-D2O-08	34372	4	1.2	4.5	30x30|5x5	1.67E+007	480	34810.2	08/18/10	19:30:43.00	23
MOPS-7.4-D2O-08	34373	4	1.2	4.5	30x30|5x5	1.65E+007	480	34331.5	08/18/10	19:38:59.00	24
ARC-MOPS-D2O-08	34374	4	1.2	4.5	30x30|5x5	1.63E+007	480	33994.6	08/18/10	19:47:15.00	25

Page 4

(b) page 4

Figure 62: Results from SANS experiment arranged in a table. Continue.

Sheet1_2

PB-7.4-D2O-08	34375	4	1.2	4.5	30x30|5x5	1.62E+007	480	33821.7	08/18/10	19:55:30.00	26
ARC-PB-D2O-08	34376	4	1.2	4.5	30x30|5x5	1.63E+007	480	33897.5	08/18/10	20:03:45.00	27
AB-PB-D2O-08	34377	4	1.2	4.5	30x30|5x5	1.03E+007	300	34234	08/18/10	20:12:01.00	28
AB-Oligos-08	34378	4	3.7	4.5	30x30|5x5	5.12E+006	900	5691.13	08/19/10	09:08:19.00	11
ARC-Oligos-08	34379	4	3.7	4.5	30x30|5x5	5.22E+006	900	5797.26	08/19/10	09:23:34.00	12
Mops7.4-08	34380	4	3.7	4.5	30x30|5x5	3.47E+006	600	5786.08	08/19/10	09:38:49.00	13
AB-MOPS-0h-08	34381	4	3.7	4.5	30x30|5x5	3.56E+006	600	5925.47	08/19/10	09:49:04.00	14
ARC-MOPS-0h-08	34382	4	3.7	4.5	30x30|5x5	3.64E+006	600	6062.85	08/19/10	09:59:21.00	15
PB-7-4-08	34383	4	3.7	4.5	30x30|5x5	3.45E+006	600	5758	08/19/10	10:09:36.00	16
AB-PB-oh-08	34384	4	3.7	4.5	30x30|5x5	3.58E+006	600	5960.18	08/19/10	10:19:51.00	17
ARC-PB-oh-08	34385	4	3.7	4.5	30x30|5x5	3.70E+006	600	6163.68	08/19/10	10:30:06.00	18
MOPS-5-D2O-08	34386	4	3.7	4.5	30x30|5x5	2.89E+006	720	4007.85	08/19/10	10:40:56.00	21
ARC-MOPS-5-D2O-08	34387	4	3.7	4.5	30x30|5x5	2.86E+006	720	3971.01	08/19/10	10:53:11.00	22
AB-MOPS-5-D2O-08	34388	4	3.7	4.5	30x30|5x5	2.85E+006	720	3962.69	08/19/10	11:05:26.00	23
MOPS-7.4-D2O-08	34389	4	3.7	4.5	30x30|5x5	2.80E+006	720	3886.99	08/19/10	11:17:41.00	24
ARC-MOPS-D2O-08	34390	4	3.7	4.5	30x30|5x5	2.77E+006	720	3848.31	08/19/10	11:29:57.00	25
PB-7.4-D2O-08	34391	4	3.7	4.5	30x30|5x5	2.76E+006	720	3828.94	08/19/10	11:42:13.00	26
ARC-PB-D2O-08	34392	4	3.7	4.5	30x30|5x5	2.77E+006	720	3853.49	08/19/10	11:54:28.00	27
AB-PB-D2O-08	34393	4	3.7	4.5	30x30|5x5	2.81E+006	720	3896.32	08/19/10	12:06:43.00	28
AB-Oligos-08	34394	4	1.2	4.5	30x30|5x5	4.65E+007	900	51613.4	08/19/10	12:20:59.00	11
ARC-Oligos-08	34395	4	1.2	4.5	30x30|5x5	4.62E+007	900	51327.3	08/19/10	12:36:14.00	12
AB-Oligos-08	34396	4	3.7	4.5	30x30|5x5	1.05E+007	1800	5853.5	08/19/10	12:53:29.00	11
ARC-Oligos-08	34397	4	3.7	4.5	30x30|5x5	1.04E+007	1800	5767.39	08/19/10	13:23:44.00	12
AB-Oligos-08	34398	4	1.2	4.5	30x30|5x5	4.64E+007	900	51581.3	08/19/10	13:56:00.00	11
ARC-Oligos-08	34399	4	1.2	4.5	30x30|5x5	4.60E+007	900	51136.8	08/19/10	14:11:15.00	12
AB-Oligos-08	34400	4	3.7	4.5	30x30|5x5	1.05E+007	1800	5845.89	08/19/10	14:28:31.00	11
ARC-Oligos-08	34401	4	3.7	4.5	30x30|5x5	1.04E+007	1800	5779.72	08/19/10	14:58:45.00	12
AB-Oligos-08	34402	4	1.2	4.5	30x30|5x5	4.66E+007	900	51769.4	08/19/10	15:31:02.00	11
ARC-Oligos-08	34403	4	1.2	4.5	30x30|5x5	4.63E+007	900	51420.2	08/19/10	15:46:17.00	12
AB-Oligos-08	34404	4	3.7	4.5	30x30|5x5	1.06E+007	1800	5865.17	08/19/10	16:03:32.00	11
ARC-Oligos-08	34405	4	3.7	4.5	30x30|5x5	1.04E+007	1800	5789	08/19/10	16:33:47.00	12
#9											
AB-Oligos-09	34406	4	1.2	4.5	30x30|5x5	3.57E+007	900	39654.2	08/19/10	17:06:03.00	11
ARC-Oligos-09	34407	4	1.2	4.5	30x30|5x5	4.62E+007	900	51309.2	08/19/10	17:21:18.00	12

Page 5

(a) page 5

Sheet1_2

Mops7.4-09	34408	4	1.2	4.5	30x30|5x5	1.54E+007	300	51310	08/19/10	17:36:33.00	13
AB-MOPS-0h-09	34409	4	1.2	4.5	30x30|5x5	1.54E+007	300	51304.7	08/19/10	17:41:49.00	14
ARC-MOPS-0h-09	34410	4	1.2	4.5	30x30|5x5	1.55E+007	300	51507	08/19/10	17:47:05.00	15
PB-7-4-09	34411	4	1.2	4.5	30x30|5x5	1.53E+007	300	51096	08/19/10	17:52:20.00	16
AB-PB-oh-09	34412	4	1.2	4.5	30x30|5x5	1.54E+007	300	51309.3	08/19/10	17:57:35.00	17
ARC-PB-oh-09	34413	4	1.2	4.5	30x30|5x5	1.54E+007	300	51369.7	08/19/10	18:02:51.00	18
MOPS-5-D2O-09	34414	4	1.2	4.5	30x30|5x5	1.68E+007	480	34937.5	08/19/10	18:08:40.00	21
ARC-MOPS-5-D2O-09	34415	4	1.2	4.5	30x30|5x5	1.67E+007	480	34754.4	08/19/10	18:16:56.00	22
AB-MOPS-5-D2O-09	34416	4	1.2	4.5	30x30|5x5	1.67E+007	480	34712.1	08/19/10	18:25:11.00	23
MOPS-7.4-D2O-09	34417	4	1.2	4.5	30x30|5x5	1.64E+007	480	34207.5	08/19/10	18:33:26.00	24
ARC-MOPS-D2O-09	34418	4	1.2	4.5	30x30|5x5	1.63E+007	480	33884.4	08/19/10	18:41:42.00	25
PB-7.4-D2O-09	34419	4	1.2	4.5	30x30|5x5	1.62E+007	480	33745.4	08/19/10	18:49:58.00	26
ARC-PB-D2O-09	34420	4	1.2	4.5	30x30|5x5	1.63E+007	480	34017.1	08/19/10	18:58:13.00	27
AB-PB-D2O-09	34421	4	1.2	4.5	30x30|5x5	1.64E+007	480	34156.9	08/19/10	19:06:28.00	28
AB-Oligos-09	34422	4	3.7	4.5	30x30|5x5	1.06E+007	1800	5864.78	08/19/10	19:16:44.00	11
ARC-Oligos-09	34423	4	3.7	4.5	30x30|5x5	1.04E+007	1800	5796.06	08/19/10	19:46:59.00	12
Mops7.4-09	34424	4	3.7	4.5	30x30|5x5	3.46E+006	600	5760.28	08/19/10	20:17:14.00	13
AB-MOPS-0h-09	34425	4	3.7	4.5	30x30|5x5	3.55E+006	600	5911.4	08/19/10	20:27:30.00	14
ARC-MOPS-0h-09	34426	4	3.7	4.5	30x30|5x5	3.62E+006	600	6026.08	08/19/10	20:37:46.00	15
PB-7-4-09	34427	4	3.7	4.5	30x30|5x5	3.44E+006	600	5740.75	08/19/10	20:48:01.00	16
AB-PB-oh-09	34428	4	3.7	4.5	30x30|5x5	3.58E+006	600	5959.3	08/19/10	20:58:16.00	17
ARC-PB-oh-09	34429	4	3.7	4.5	30x30|5x5	3.70E+006	600	6172	08/19/10	21:08:31.00	18
MOPS-5-D2O-09	34430	4	3.7	4.5	30x30|5x5	2.88E+006	720	3999.42	08/19/10	21:19:21.00	21
ARC-MOPS-5-D2O-09	34431	4	3.7	4.5	30x30|5x5	2.85E+006	720	3965.26	08/19/10	21:31:36.00	22
AB-MOPS-5-D2O-09	34432	4	3.7	4.5	30x30|5x5	2.85E+006	720	3960.22	08/19/10	21:43:51.00	23
MOPS-7.4-D2O-09	34433	4	3.7	4.5	30x30|5x5	2.80E+006	720	3888.39	08/19/10	21:56:06.00	24
ARC-MOPS-D2O-09	34434	4	3.7	4.5	30x30|5x5	2.78E+006	720	3859.29	08/19/10	22:08:23.00	25
PB-7.4-D2O-09	34435	4	3.7	4.5	30x30|5x5	2.76E+006	720	3833.47	08/19/10	22:20:38.00	26
ARC-PB-D2O-09	34436	4	3.7	4.5	30x30|5x5	2.78E+006	720	3857.14	08/19/10	22:32:53.00	27
AB-PB-D2O-09	34437	4	3.7	4.5	30x30|5x5	2.81E+006	720	3902.14	08/19/10	22:45:08.00	28
#10											
AB-Oligos-10	34438	4	1.2	4.5	30x30|5x5	4.66E+007	900	51750.7	08/19/10	22:59:24.00	11
ARC-Oligos-10	34439	4	1.2	4.5	30x30|5x5	4.63E+007	900	51403.3	08/19/10	23:14:39.00	12
AB-Oligos-10	34440	4	3.7	4.5	30x30|5x5	1.06E+007	1800	5876.72	08/19/10	23:31:55.00	11
ARC-Oligos-10	34441	4	3.7	4.5	30x30|5x5	1.04E+007	1800	5793.83	08/20/10	00:02:10.00	12

Page 6

(b) page 6

Figure 63: Results from SANS experiment arranged in a table. Continue.

Sheet1_2

#11											
AB-Oligos-11	34442	4	1.2	4.5	30x30|5x5	4.66E+007	900	51722.6	08/20/10	00:34:26.00	11
ARC-Oligos-11	34443	4	1.2	4.5	30x30|5x5	4.63E+007	900	51401.3	08/20/10	00:49:41.00	12
AB-Oligos-11	34444	4	3.7	4.5	30x30|5x5	1.06E+007	1800	5869.44	08/20/10	01:06:56.00	11
ARC-Oligos-11	34445	4	3.7	4.5	30x30|5x5	1.04E+007	1800	5799.89	08/20/10	01:37:11.00	12
#12											
AB-Oligos-12	34446	4	1.2	4.5	30x30|5x5	4.64E+007	900	51602	08/20/10	02:14:44.00	11
ARC-Oligos-12	34447	4	1.2	4.5	30x30|5x5	4.61E+007	900	51218.7	08/20/10	02:30:02.00	12
AB-Oligos-12	34448	4	3.7	4.5	30x30|5x5	1.05E+007	1800	5852.67	08/20/10	02:47:19.00	11
ARC-Oligos-12	34449	4	3.7	4.5	30x30|5x5	1.04E+007	1800	5783.11	08/20/10	03:17:36.00	12
#13											
AB-Oligos-13	34450	4	1.2	4.5	30x30|5x5	3.09E+007	600	51486.7	08/20/10	03:49:53.00	11
ARC-Oligos-13	34451	4	1.2	4.5	30x30|5x5	3.07E+007	600	51235.8	08/20/10	04:00:08.00	12
Mops7.4-13	34452	4	1.2	4.5	30x30|5x5	1.54E+007	300	51195.3	08/20/10	04:10:24.00	13
AB-MOPS-0h-13	34453	4	1.2	4.5	30x30|5x5	1.53E+007	300	51099.3	08/20/10	04:15:39.00	14
ARC-MOPS-0h-13	34454	4	1.2	4.5	30x30|5x5	1.54E+007	300	51189.7	08/20/10	04:20:55.00	15
PB-7-4-13	34455	4	1.2	4.5	30x30|5x5	1.52E+007	300	50753.7	08/20/10	04:26:11.00	16
AB-PB-oh-13	34456	4	1.2	4.5	30x30|5x5	1.54E+007	300	51168.7	08/20/10	04:31:26.00	17
ARC-PB-oh-13	34457	4	1.2	4.5	30x30|5x5	1.54E+007	300	51301.3	08/20/10	04:36:41.00	18
MOPS-5-D2O-13	34458	4	1.2	4.5	30x30|5x5	1.69E+007	480	35169.4	08/20/10	04:42:31.00	21
ARC-MOPS-5-D2O-13	34459	4	1.2	4.5	30x30|5x5	1.68E+007	480	35015.6	08/20/10	04:50:46.00	22
AB-MOPS-5-D2O-13	34460	4	1.2	4.5	30x30|5x5	1.67E+007	480	34727.3	08/20/10	04:59:01.00	23
MOPS-7.4-D2O-13	34461	4	1.2	4.5	30x30|5x5	1.64E+007	480	34198.1	08/20/10	05:07:16.00	24
ARC-MOPS-D2O-13	34462	4	1.2	4.5	30x30|5x5	1.63E+007	480	33905.8	08/20/10	05:15:33.00	25
PB-7.4-D2O-13	34463	4	1.2	4.5	30x30|5x5	1.62E+007	480	33785.4	08/20/10	05:23:48.00	26
ARC-PB-D2O-13	34464	4	1.2	4.5	30x30|5x5	1.63E+007	480	34026.2	08/20/10	05:32:03.00	27
AB-PB-D2O-13	34465	4	1.2	4.5	30x30|5x5	1.03E+007	300	34296	08/20/10	05:40:18.00	28
AB-Oligos-13	34466	4	3.7	4.5	30x30|5x5	5.28E+006	900	5869.67	08/20/10	05:47:35.00	11
ARC-Oligos-13	34467	4	3.7	4.5	30x30|5x5	5.21E+006	900	5792.21	08/20/10	06:02:50.00	12
Mops7.4-13	34468	4	3.7	4.5	30x30|5x5	3.47E+006	600	5775.83	08/20/10	06:18:05.00	13
AB-MOPS-0h-13	34469	4	3.7	4.5	30x30|5x5	3.55E+006	600	5921.4	08/20/10	06:28:20.00	14

Page 7

(a) page 7

Sheet1_2

ARC-MOPS-0h-13	34470	4	3.7	4.5	30x30|5x5	3.62E+006	600	6029.18	08/20/10	06:38:36.00	15
PB-7-4-13	34471	4	3.7	4.5	30x30|5x5	3.43E+006	600	5715.78	08/20/10	06:48:52.00	16
AB-PB-oh-13	34472	4	3.7	4.5	30x30|5x5	3.58E+006	600	5958.47	08/20/10	06:59:07.00	17
ARC-PB-oh-13	34473	4	3.7	4.5	30x30|5x5	3.71E+006	600	6176.15	08/20/10	07:09:22.00	18
MOPS-5-D2O-13	34474	4	3.7	4.5	30x30|5x5	2.88E+006	720	4003.08	08/20/10	07:20:11.00	21
ARC-MOPS-5-D2O-13	34475	4	3.7	4.5	30x30|5x5	2.86E+006	720	3970.18	08/20/10	07:32:27.00	22
AB-MOPS-5-D2O-13	34476	4	3.7	4.5	30x30|5x5	2.85E+006	720	3957.42	08/20/10	07:44:42.00	23
MOPS-7.4-D2O-13	34477	4	3.7	4.5	30x30|5x5	2.80E+006	720	3886.39	08/20/10	07:56:57.00	24
ARC-MOPS-D2O-13	34478	4	3.7	4.5	30x30|5x5	2.76E+006	720	3827.03	08/20/10	08:09:13.00	25
PB-7.4-D2O-13	34479	4	3.7	4.5	30x30|5x5	2.75E+006	720	3819.75	08/20/10	08:21:29.00	26
ARC-PB-D2O-13	34480	4	3.7	4.5	30x30|5x5	2.77E+006	720	3844.71	08/20/10	08:33:44.00	27
AB-PB-D2O-13	34481	4	3.7	4.5	30x30|5x5	2.81E+006	720	3899.19	08/20/10	08:45:59.00	28
[3]PlexiStandard	34484	4	3.7	4.49	30x30|5x5	2.89E+006	398	7267.71	08/20/10	09:21:05.00	3
[13] Added :: 34268. 34308. 3	34268005	4	1.2	4.5	30x30|5x5	7.68E+007	1500	51223	08/17/10	19:50:28.00	13
[13] Added :: 34284. 34324. 3	34284005	4	3.7	4.5	30x30|5x5	1.73E+007	3000	5769.6	08/17/10	21:47:07.00	13

Page 8

(b) page 8

Figure 64: Results from SANS experiment arranged in a table. Continue.

A.0.9.1 *ssNMR experiments:*

Samples: 6.3 $\times 10^{-6}$ mole (total weight 5 mg) of lipids (one type of lipid or a combination) in 50 µl of 75 mM MOPS buffer pH 7 in deuterium-depleted H_2O. The lipid ratios used for vesicle preparations are: for two components system, the molar ratio was 70 (POPC) : 30 (POPE or POPS), for three components system, the molar ratio was 40 (POPC) : 30 (POPE or POPS) : 30 (cholesterol), for four components system, the molar ratio was 30 (POPC) : 30 (POPE or POPS) : 30 (cholesterol) : 10 (SM). For some samples 1 %, 3 % or 5 % of Aβ(1-40) were added. Purified non-labeled Aβ(1-40) peptides were solubilized in buffer and sonicated to eliminate any preformed aggregates. It is known from PAGE analysis that after this treatment the sample contains monomers and dimers, but no higher molecular weight oligomers.

PE lipids have a smaller headgroup than PC, which gives the lipid a cone shape and it can hydrogen bond to proteins through its ionizable amine group. On its own, PE does not for bilayers, but inverted hexagonal phases. With other lipids in a bilayer, it is believed to exert a lateral pressure that stabilizes membrane proteins in their optimum conformation. PE lipids are found in nervous tissue (white matter, nerves, neural tissue, spinal cord), it has a polar headgroup and creates a more viscous lipid membrane compared to PC lipids. In contrast to PC, PE is concentrated with PS in the inner leaflet of the plasma membrane.

Experimental settings: Deuterium solid-state NMR spectra were recorded on Bruker Avance Spectrometer operating at 7.0 Tesla using a quadrupolar echo sequence [Davis et al., 1976] with the typical parameters: ^2H B_1 field 46.3 kHz, echo delay 40 µs, spectral width 100 kHz, 8000 data points, 130000 scans, and repetition time 0.5 sec. Commercially available triple resonance probe was used.

Graph A in Figure 65 on page 155 clearly shows that addition of 3 % Aβ(1-40) exerts only mild effect on the POPE lipids. Even though the experiment was performed with lipid vesicles, the only deuterated lipids in the mixture were POPE lipids (deuterated on one of the acyl chains) and therefore the observed effect is the effect on POPE. The width of the spectrum in the presence of the peptide is slightly reduced indicating that peptide molecules insert into the vesicles where POPE lipids are present and disrupt, to a certain extent, their order.

In graph B of Figure 65 on page 155 the effect of cholesterol is depicted. Upon incorporation of cholesterol into the lipid vesicles, increase in the order was observed, as expected. When looking into the sample of the same composition via deuterated POPC acyl chains, larger quadrupolar splitting was observed Figure 65 on page 155, graph (c). These results indicate that Aβ peptides interact with both, POPE and POPC lipids, while the effect on the latter is more pronounced.

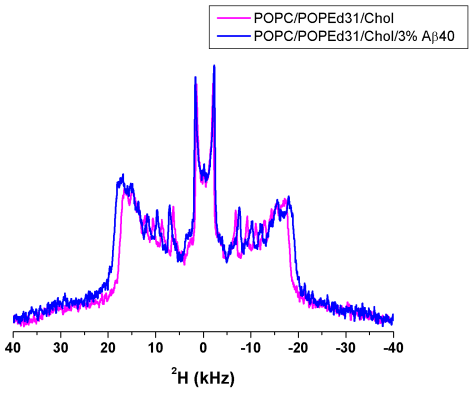

(a)

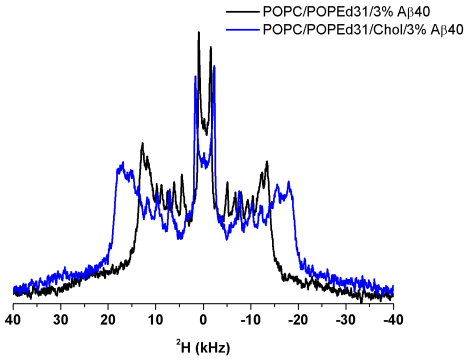

(b)

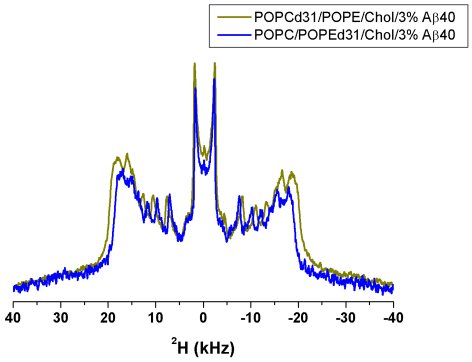

(c)

Figure 65: Effect of 3 % Aβ(1-40) or cholesterol addition to lipid vesicles mixture, which include ^{2}H-labeled POPE: (a) effect of Aβ(1-40) on POPE lipids as observed through quadrupolar splittings of ^{2}H POPE incorporated in lipid vesicles consistent of POPC, POPE, cholesterol; (b) effect of cholesterol on POPE lipids as observed through quadrupolar splittings of ^{2}H POPE incorporated in lipid vesicles consistent of POPC, POPE with 3 % Aβ(1-40); (c) effect of the Aβ(1-40) on lipids measured via d31POPC or via d31POPE.

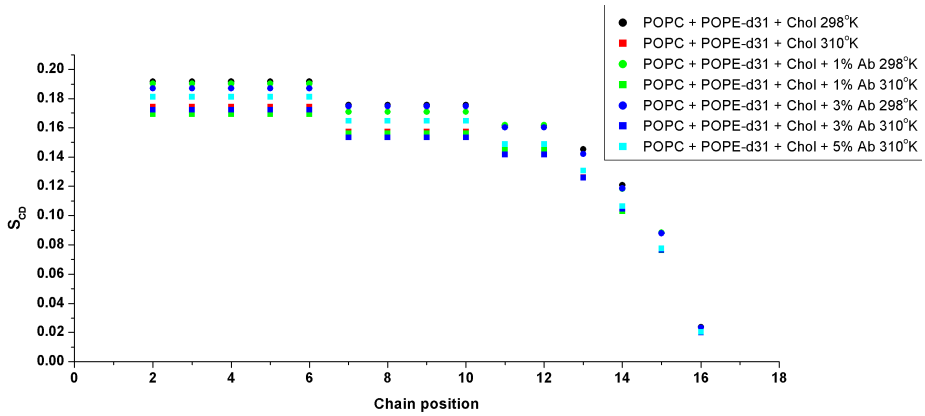

Figure 66: Temperature effect on the order parameter. POPC, deuterium labeled d31POPE and cholesterol vesicles with 1% or 3 % of Aβ(1-40) peptide or without were measured either at 298 °K or at 310 °K. The legend inside the figure specifies the color coding.

As expected, temperature has the largest effect on the order parameter Figure 66 on page 156. Interestingly, addition of 1 % of Aβ(1-40) (light green rectangles) reduces the order parameter, i.e. increasing the mobility of the POPE acyl chains. With 3 % of Aβ(1-40) (dark blue rectangles) there is a slight increase in the order parameter, while with 5 % there is a significant increase (light blue rectangles). These results indicate that Aβ(1-40) peptides interact with lipids acyl chains, i.e. incorporate into the lipid vesicles.

From comparison of the first four samples, it is clear that in the presence of POPE lipids, when monitored via POPC, the order parameter is higher even when compared to the same sample monitored via POPE (red circles) (Figure 67 on page 157). Comparison of the last four samples with cholesterol shows similar pattern as was observed for the first samples. As expected for cholesterol, the order parameter is significantly higher, but the tendency to observe the highest order parameter is by monitoring POPC in the presence of POPE and 3 % Aβ(1-40) remains.

Graph (a) in Figure 68 on page 158 clearly shows that there is no change in the order parameter of d31POPC in the presence of POPS upon addition of 3 % of Aβ (1-40) peptides. This result indicates that there is no indirect effect of Aβ (1-40) on POPS lipids.

Graph (b) in Figure 68 on page 158 shows changes in the order parameter of POPE in the vesicles comprising of POPC, d31POPE, cholesterol and SM as a function of temperature and percentage of added Aβ peptides. As expected, at lower temperatures, the order parameter is higher (black squares, red stars and green, magenta, light blue triangles). While at 310°K, the order parameter is lower (magenta, red, dark and light blue circles). At 310°K the order parameter does not change much upon addition of 1, 3 and 5 % of Aβ(1-40). The change is more pronounced at 298°K, where addition of larger amount of

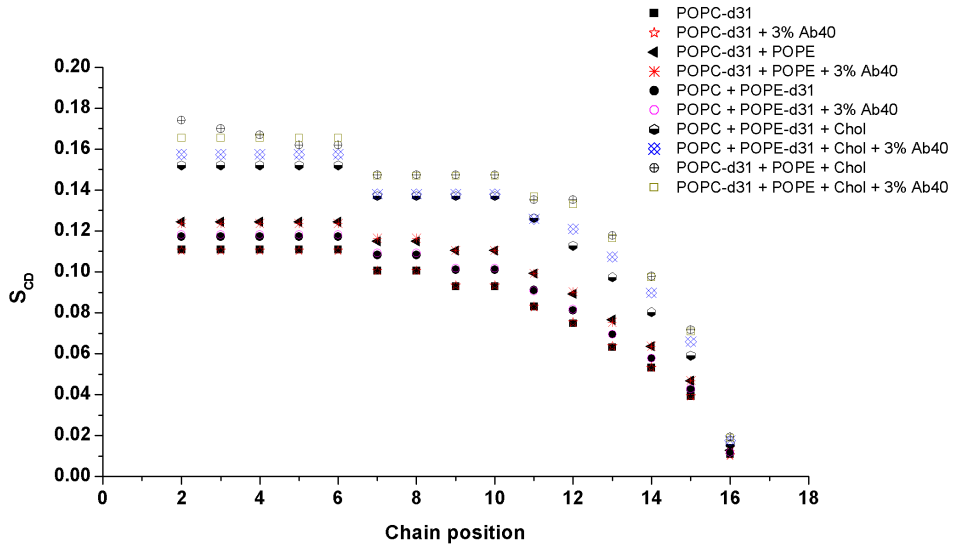

Figure 67: Comparison of the order parameter between different lipid vesicles compositions, monitoring quadrupolar splittings of either d31POPC or d31POPE. The color coding is as follows: black rectangles - d31POPC only; red stars - d31POPC with 3 % Aβ; black triangles - d31POPC, POPE; red snowflakes - d31POPC, POPE, 3 % Aβ(1-40); black circles - POPC, d31POPE; red circles - d31POPE, POPC, 3 % Aβ(1-40); black and white circles - POPC, d31POPE, cholesterol; blue 4-x symbols - POPC, d31POPE, cholesterol, 3 % Aβ(1-40); black plus-in-a-circle symbols - d31POPC, POPE, cholesterol; empty grey squares - d31POPC, POPE, cholesterol, 3 % Aβ(1-40).

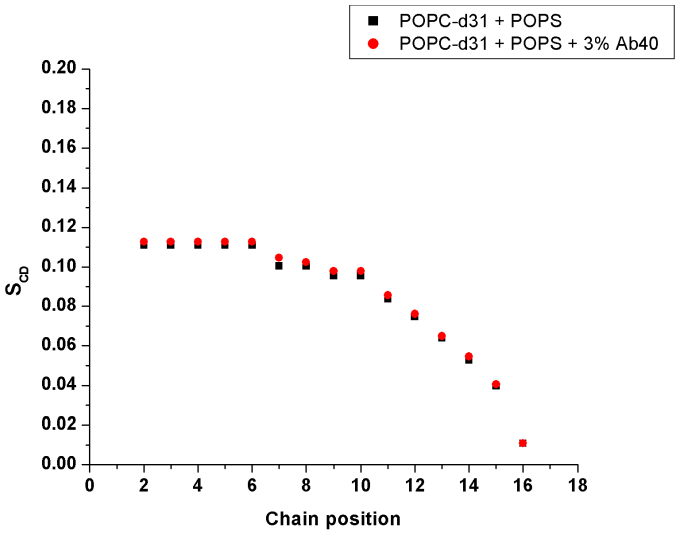

(a)

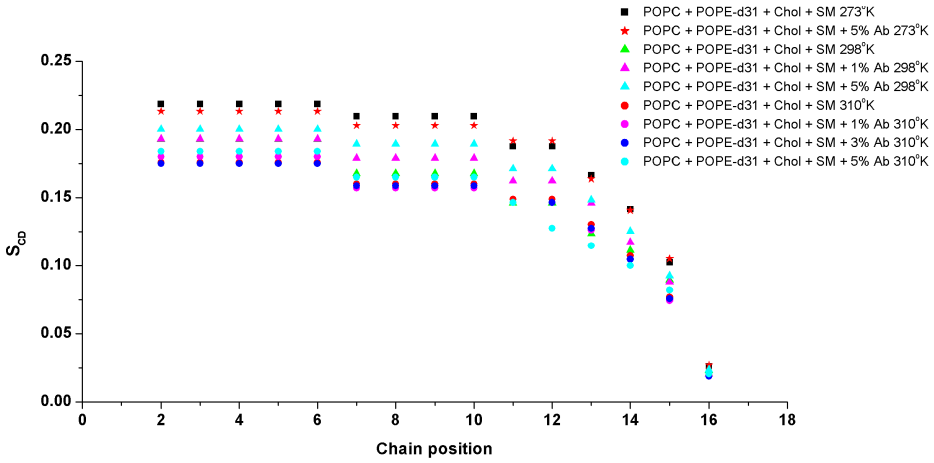

(b)

Figure 68: Effect of POPS and of Aβ (1-40) peptides in the presence of sphingomyelin and varying temperatures on the order parameter of POPE. (a) the order parameter of POPC lipids in the presence of POPS and Aβ(1-40); (b) the effect of the temperature and the amount of Aβ (1-40) peptides on the order parameter in the presence of SM (all vesicles have the same composition). The legend inside the figure specifies the color coding.

Aβ(1-40) increases the order parameter. At 273°K addition of 5 % Aβ(1-40) does not cause a significant increase in the order parameter. Comparing the order parameter with (blue circles in Figure 68 on page 158) and without SM (blue 4-x Figure 67 on page 157) shows that in the presence of SM, the order parameter is higher (0.17 vs. 0.15).

B

PUBLICATIONS

OPEN ACCESS Freely available online

PLoS one

Calcium Ions Promote Formation of Amyloid β-Peptide (1–40) Oligomers Causally Implicated in Neuronal Toxicity of Alzheimer's Disease

Anna Itkin[1,2], Vincent Dupres[3], Yves F. Dufrêne[3], Burkhard Bechinger[2], Jean-Marie Ruysschaert[1], Vincent Raussens[1]*

1 Laboratory of Structure and Function of Biological Membranes, Center for Structural Biology and Bioinformatics, Université Libre de Bruxelles, Brussels, Belgium, **2** International Center for Frontier Research in Chemistry, Chemistry Institute, Membrane Biophysics and NMR, Université de Strasbourg, Strasbourg, France, **3** Institute of Condensed Matter and Nanosciences, Université Catholique de Louvain, Louvain-la-Neuve, Belgium

Abstract

Amyloid β-peptide (Aβ) is directly linked to Alzheimer's disease (AD). In its monomeric form, Aβ aggregates to produce fibrils and a range of oligomers, the latter being the most neurotoxic. Dysregulation of Ca^{2+} homeostasis in aging brains and in neurodegenerative disorders plays a crucial role in numerous processes and contributes to cell dysfunction and death. Here we postulated that calcium may enable or accelerate the aggregation of Aβ. We compared the aggregation pattern of Aβ(1–40) and that of Aβ(1–40)E22G, an amyloid peptide carrying the Arctic mutation that causes early onset of the disease. We found that in the presence of Ca^{2+}, Aβ(1–40) preferentially formed oligomers similar to those formed by Aβ(1–40)E22G with or without added Ca^{2+}, whereas in the absence of added Ca^{2+} the Aβ(1–40) aggregated to form fibrils. Morphological similarities of the oligomers were confirmed by contact mode atomic force microscopy imaging. The distribution of oligomeric and fibrillar species in different samples was detected by gel electrophoresis and Western blot analysis, the results of which were further supported by thioflavin T fluorescence experiments. In the samples without Ca^{2+}, Fourier transform infrared spectroscopy revealed conversion of oligomers from an anti-parallel β-sheet to the parallel β-sheet conformation characteristic of fibrils. Overall, these results led us to conclude that calcium ions stimulate the formation of oligomers of Aβ(1–40), that have been implicated in the pathogenesis of AD.

Citation: Itkin A, Dupres V, Dufrêne YF, Bechinger B, Ruysschaert J-M, et al. (2011) Calcium Ions Promote Formation of Amyloid β-Peptide (1–40) Oligomers Causally Implicated in Neuronal Toxicity of Alzheimer's Disease. PLoS ONE 6(3): e18250. doi:10.1371/journal.pone.0018250

Editor: Sergio Ferreira, Federal University of Rio de Janeiro, Brazil

Received November 15, 2010; **Accepted** March 1, 2011; **Published** March 28, 2011

Funding: This work received funding from the European Community's Sixth Framework Programme through a Marie Curie Research Training Network ("Biocontrol" MRTN-CT-2006-033439, http://ibis.tau.ac.il/wiki/biocontrol/index.php/Main_Page). Work in the team of V.D. and Y.F.D. was supported by the National Foundation for Scientific Research (FNRS, www.frs-fnrs.be), the Foundation for Training in Industrial and Agricultural Research (FRIA, http://www1.frs-fnrs.be/fr/financer-les-chercheurs/carriere-chercheur/doctorants/86-bourse-du-fria.html), the Université Catholique de Louvain (Fonds Spéciaux de Recherche), the Federal Office for Scientific, Technical and Cultural Affairs (Interuniversity Attraction Poles Programme), and the Research Department of the Communauté Française de Belgique (Concerted Research Action). The funders had no role in study design, data collection and analysis, decision to publish, or preparation of the manuscript.

Competing Interests: The authors have declared that no competing interests exist.

* E-mail: vrauss@ulb.ac.be

Introduction

Alzheimer's disease (AD) is a progressive neurodegenerative disorder that affects nearly 2% of the population in industrialized countries. AD is the most common form of dementia and is characterized by brain cell destruction, memory loss, and deterioration of cognitive and behavioral processes severe enough to affect work, lifelong hobbies, and social life. Symptoms worsen over time and the disease is fatal.

For many years, the pathologic hallmark of AD was attributed to the continuous accumulation of amyloid β-peptide (Aβ) fibrils into plaques. Their toxic effects on synaptic connections and neurons were explained by the amyloid cascade hypothesis [1]. However, experiments aimed at establishing a direct causal relationship between Aβ deposition and the neurodegeneration that underlies AD dementia failed [2,3]. This apparent discrepancy between plaque burden and neuronal dysfunction has been described in transgenic mouse models of AD [4,5]. Recent theories that apparently resolve this inconsistency refer to small soluble oligomeric or protofibrillar assemblies of Aβ [6,7], shown to be toxic to neurons and their vital interconnections [8–10]. Results of studies that focused on the electrophysiological impact of Aβ oligomers suggested that the underlying memory loss is caused by rapid inhibition of long-term potentiation (LTP)—a classical model for synaptic plasticity and memory mechanisms [11]—by oligomers [12–14], which might explain, at least in part, the mild cognitive impairment observed in the early stages of AD [9].

Aβ peptide is a product of the proteolytic cleavage of the amyloid precursor protein (APP). Although Aβ peptides may vary in length from 38 to 43 amino acids, the two main alloforms in the brain are Aβ(1–40) and Aβ(1–42). Both peptides have been found in amyloid plaques [15–17] and shown to form oligomers and protofibrils [18]. Post-mortem analysis in human subjects disclosed that Aβ(1–40) rather than Aβ(1–42), whether in soluble or in insoluble form, discriminated more readily between AD patients and high pathology controls [8]. In addition to sporadic cases of AD, several familial Alzheimer's disease (FAD) mutations have been discovered and studied over the years. Most of these

mutations cause an increase in Aβ by interfering with APP processing. A new mutation within the APP sequence Aβ(E22G), found to cause AD in Swedish families, was reported in 2001 by Nilsberth et al., who named it the Arctic mutation. Those authors observed that carriers of this mutation showed decreased amounts of Aβ(1–42) and Aβ(1–40) in the plasma, and demonstrated that Aβ(1–40)E22G forms protofibrils much faster and more abundantly than the wild-type Aβ, whereas the rate of fibrillization remained the same [19]. Later studies suggested that the clinical and pathological features of patients with the Arctic mutation are attributable to increased generation of Aβ intermediates formed early in fibrillogenesis, as well as their greater stability [20]. Moreover, Aβ(1–40)E22G was shown to rapidly induce neurotoxicity, and that this correlated with the formation of small prefibrillar assemblies, including protofibrils [21]. Clinical and pathological features of FAD are indistinguishable from those of sporadic cases, but disease onset occurs at a much younger age in patients with the Arctic mutation [19,22].

Research has so far failed to establish any unique primary mechanism underlying the Aβ aggregation followed by neuronal degeneration and death in patients with AD. Rather, it seems likely that numerous processes participate both in Aβ aggregation and in the ultimate development of the disease. One of the many hypotheses put forward to account for the etiology of AD argues that a central role in AD pathology is played by dysregulation of calcium homeostasis [23–25]. The idea that altered calcium homeostasis might serve as a trigger in the development of AD was first formulated in 1982 and later revised by Khachaturian [26].

The principal risk factor for AD is advanced age. In sporadic cases, the first manifestations of the disease symptoms occur towards the seventh decade of life. Neuronal activation is usually associated with an increase in intracellular Ca^{2+} concentration ($[Ca^{2+}]_i$), while the source of the Ca^{2+} ions can be either extracellular or intracellular. Age-related alterations in Ca^{2+}-specific regulatory systems in neurons include increased amounts of intracellular Ca^{2+}, enhanced Ca^{2+} influx through voltage-dependent Ca^{2+} channels, impaired mitochondrial ability to buffer or cycle Ca^{2+} [27], and perturbed Ca^{2+} regulation in ryanodine (Ry)-sensitive and Ins(1,4,5)P_3-sensitive Ca^{2+} stores [28].

Numerous studies have implicated Ca^{2+} dysfunction in AD, demonstrating the bidirectional relationship between Ca^{2+} signaling and the amyloidogenic pathway [29,30]. On the one hand, certain alterations in Ca^{2+} signaling are common to both sporadic and familial cases of AD [31,32]. Direct measurements of $[Ca^{2+}]_i$ show that cells exposed to Aβ exhibit disruption in calcium homeostasis [33,34], which may in turn cause a variety of secondary effects such as activation of cellular enzymes, induction of apoptosis, and cytoskeletal modifications [35,36]. Aβ can reportedly trigger Ca^{2+} release from endoplasmic reticulum (ER) stores via interaction with IP_3 and Ry receptors [37,38], as well as an increase in calcium influx via the NMDA receptors [39,40]. Formation of cation-selective channels by Aβ in bilayer membranes and in living cells [41,42] further enhances the ability of this peptide to alter cytosolic Ca^{2+} homeostasis. On the other hand, changes in the amounts and dynamics of Ca^{2+} alter the metabolism and production of Aβ [30]. Influx of Ca^{2+} through calcium channels of the plasma membrane or through calcium release from ER stores increases Aβ generation [43]. An increase in cytosolic Ca^{2+} concentration, moreover, was shown to induce transient phosphorylation of APP and tau, leading to an increased production of intracellular Aβ [44].

In this study we used gel electrophoresis and Western blot analysis, thioflavine T (ThT) fluorescence, Fourier transform infrared spectroscopy (FTIR), and atomic force microscopy imaging (AFM) to compare the aggregation of Aβ(1–40) and Aβ(1–40)E22G, in order to study the structural and morphological similarities of the species—oligomeric or fibrillar—formed by both peptides in the presence and in the absence of added Ca^{2+}. We postulated that when calcium dysregulation takes place under conditions of normal aging, it may facilitate the formation of pathogenic Aβ oligomers, which in turn may intensify the Ca^{2+} dyshomeostasis. The oligomeric species may then be held accountable for mediating the neuronal injury and LTP inhibition characteristic of AD in elderly individuals, similar to the situation in FAD patients carrying the Arctic mutation. Detailed knowledge of the action of Ca^{2+} upstream of Aβ is a prerequisite for complete understanding of the molecular mechanism(s) responsible for the age-related risks of Alzheimer's disease. Because Aβ plays a fundamental part in the development and devastating progression of AD, we believe that understanding of the formation and properties of its toxic forms will provide a key to the comprehension of the disease mechanism, thereby enabling us to develop novel preventive and therapeutic approaches.

Methods

Chemicals

All chemicals were purchased from Sigma-Aldrich or Bio-Rad, unless stated otherwise.

Peptide preparation

The amyloid β-peptides Aβ(1–40) and Aβ(1–40)E22G were purchased from American Peptide Company in the form of lyophilized powder. Prior to use, 1 mg aliquots were dissolved in double-distilled water, sonicated in a water bath for 1 min, and then held in ice for 1 min. This cycle was repeated five times. The peptide solution was then divided into 50-μg aliquots and dried under vacuum in a ThermoSavant SpeedVac (UVS400A Universal Vacuum System). Aβ films were stored at $-20^{\circ}C$ until use.

Sample preparation

The 50- μg aliquots of lyophilized Aβ peptide were hydrated at room temperature in either 50 mM phosphate buffer pH 7.4 and 100 mM NaCl ("–Ca^{2+} condition") or 75 mM MOPS pH 7.4 and 2 mM $CaCl_2$ ("+Ca^{2+} condition"). The "$-Ca^{2+}$ condition" refers to the condition where no calcium was added to the buffer. However, contaminating calcium concentration was 21 ± 1.3 μM, as was determined with inductively coupled plasma optical emission spectroscopy (ICP-OES). The final concentration of the peptide for all samples was 100 μM unless otherwise stated. Samples were sonicated for 2 min in a water bath and incubated at $37^{\circ}C$ without agitation.

Thioflavin T (ThT) fluorescence measurements

The thioflavin T (Sigma-Aldrich) fluorescence assay [45] was used to follow the aggregation profile of Aβ peptides for 96 h in an LS55 fluorimeter (Perkin Elmer Instruments). Aliquots of 10 μl (~4 μg) of the incubated peptide solution were added to 1 ml of 50 mM glycine-NaOH buffer pH 8.5 and 5 μM ThT. The sample was maintained at $25^{\circ}C$ in a circulating water bath. Excitation and emission wavelengths were 450 nm and 482 nm, respectively. The emission spectra were collected for 500 s. The intensity of each spectrum was then averaged over approximately 400 s, following subtraction of the averaged (100 s) background fluorescence.

Western blot analysis

Peptide samples were diluted in a PAGE sample buffer and separated on a 12% bis-Tris gel at $4^{\circ}C$ for 2 h at 100 V. There

was no SDS in the acrylamide gel, but the sample buffer contained 4% SDS. Unboiled samples were loaded on the gel. The separated bands of protein were transferred onto a nitrocellulose membrane, which was then blocked for 1 h in 5% nonfat dry milk in Tris-buffered saline (TBS)/Tween-20 buffer. The membrane was incubated with a mixture of two mouse monoclonal Aβ antibodies, 6E10 (1:3000) and 4G8 (1:2000) (Sigma-Aldrich). Detection was carried out by enhanced chemiluminescence using horseradish peroxidase-conjugated goat anti-mouse antibody (1:2000) (Boehringer Mannheim). Images were recorded and analyzed using the ImageQuant 400 gel imager and ImageQuant TL software (GE Healthcare).

Fourier transform infrared (FTIR) spectroscopy

Infrared spectra were recorded on an Equinox 55 infrared spectrophotometer (Bruker Optics). The internal reflection element was a diamond crystal (2×2 mm) with an aperture angle of 45°, yielding a single internal reflection. The spectrometer was purged continuously with dried air. Spectra were obtained from 4000 cm^{-1} to 800 cm^{-1} at a resolution of 2 cm^{-1}. In order to achieve a good signal-to-noise ratio, 128 scans were acquired. All measurements were conducted at 24°C. Samples were prepared by spreading 2 µl of peptide solution on a diamond crystal surface and removing the excess fluid under nitrogen flow. The film was washed three times with milliQ water, which was then removed under nitrogen flow.

Spectral analysis

Data were processed using "Kinetics", a program developed in our laboratory and running under MatLab. Briefly, spectra were subjected to water-vapor subtraction using a reference water vapor spectrum, and to a smoothing procedure to 4 cm^{-1}. Spectra were deconvoluted using the Lorentzian deconvolution function and the Gaussian apodization function. A linear baseline was subtracted from all spectra at 1708, 1602, and 1482 cm^{-1}.

Atomic force microscopy (AFM)

AFM contact mode images were obtained at room temperature with a Nanoscope IV Multimode AFM (Veeco). Fresh mica surfaces (36 mm^2) were glued onto steel sample discs (Veeco) with Epotek 377 (Gentec Benelux). Atomically smooth surfaces were generated by cleaving layers with adhesive tape. Peptide solution (100 µl; 0.1 mg/ml) was adsorbed onto bare mica surfaces for 1 h. The mounted samples were immediately transferred into the AFM liquid cell, while avoiding dewetting. They were then imaged with oxide-sharpened microfabricated Si_3N_4 cantilevers (Microlevers, Veeco) with minimal applied force (<500 pN). The spring constants of the cantilevers measured by the thermal noise method (Picoforce, Veeco) were 0.011 N/m. Images (5 µm × 5 µm) were obtained from several areas on each sample.

Results

Preferential formation of oligomeric, not fibrillar, species by Aβ(1–40) in the presence of Ca^{2+}

Samples of Aβ(1–40) and Aβ(1–40)E22G were prepared and incubated for 96 h in either the presence or the absence of 2 mM Ca^{2+}. At time points corresponding to $t = 0, 2, 4, 6, 24, 72$, and 96 h, samples were analyzed by electrophoresis in SDS-free polyacrylamide gel (0.1% SDS was present in the migration buffer) and imaged by Western blotting (Fig. 1). Over time, the aggregation pattern of Aβ(1–40) showed striking differences in the presence and in the absence of added Ca^{2+} (Fig. 1A, C). Whereas after 24 h the range of oligomeric species in the samples with and without added Ca^{2+} was almost indistinguishable, at 72 h we observed a wide range of species in the presence of Ca^{2+}, but not in its absence. At 72 h and 96 h, Aβ(1–40) in the presence of Ca^{2+} contained monomers and oligomers whose molecular weights ranged from those consistent with dimers (around 8 kDa) to hexamers (Fig. 1C, two last lanes). Additional streaks in the same lanes suggested the presence of oligomers of even higher molecular weight, though they were not clearly identified. In the same samples, protofibrils and apparently some fibrils were also detectable at the top portion of the gel. It was difficult to differentiate between these aggregates because of the low resolution in this part of the gel and their low electrophoretic mobility. Fibrils, because of their extremely high molecular weight, do not penetrate into the separating part of the polyacrylamide gel; thus, when present, they appear as smears in the stacking portion of the gel. In the absence of added Ca^{2+}, Aβ(1–40) molecules had aggregated to such an extent that we were able to detect only bands with low electrophoretic mobility corresponding mainly to high-molecular-weight oligomers, protofibrils and fibrils, located in or near the stacking part of the polyacrylamide gel (Fig.1A, two last lanes).

In contrast to Aβ(1–40), samples of Aβ(1–40)E22G that were incubated under the same conditions as the Aβ(1–40) samples showed no differences in their aggregation profiles in the presence and absence of added Ca^{2+} (Fig. 1B, D). Moreover, already at $t = 0$ h we observed oligomers ranging from monomers to tetramers that were not present in Aβ(1–40) samples at the same time point. From $t = 24$ h, we observed an increase in the population of oligomers of low molecular weight as well as the appearance of high-molecular-weight oligomers in Aβ(1–40)E22G samples, in both conditions. By $t = 72$ h and $t = 96$ h a wide range of oligomers, including protofibrils, could be seen. These findings clearly indicated that Ca^{2+} had no influence on the ability of Aβ(1–40)E22G to aggregate as expected, with the generation mainly of oligomers and protofibrils.

A comparison of the results obtained for the two peptides thus clearly showed that in the presence of Ca^{2+} Aβ(1–40), like Aβ(1–40)E22G, aggregated to produce oligomers and protofibrils, whereas in the "–Ca^{2+}" condition fibrils were readily formed. The profile of oligomeric and protofibrillar species formed by Aβ(1–40) in the presence of Ca^{2+}, as detected by Western analysis, was essentially the same as that of Aβ(1–40)E22G in either condition.

Ca^{2+} inhibits formation of thioflavin T-positive Aβ(1–40) species but does not affect Aβ(1–40)E22G

The increase in ThT fluorescence over time was used to follow fibrillogenesis of amyloid peptides Aβ(1–40) and Aβ(1–40)E22G in solution in the presence and absence of added Ca^{2+}. We found that Ca^{2+} inhibited the formation of ThT-positive species of Aβ(1–40), but had no effect on Aβ(1–40)E22G (Fig. 2).

We performed a time-course study during 96 h of incubation with or without Ca^{2+} for both peptides. In the case of Aβ(1–40), ThT fluorescence intensity did not change in either the presence or the absence of added Ca^{2+} and remained low for the first 6 h, demonstrating that after 6 h of incubation the predominant species are oligomers. This result is in agreement with the reported finding that ThT fluorescence clearly discriminates between oligomers and fibrils of Aβ [46]. After 24 h of incubation, ThT fluorescence intensity was found to be increased significantly (about three fold) in the absence of added Ca^{2+} but only slightly in its presence. After 72 and 96 h of incubation the ThT fluorescence intensity in the absence of added Ca^{2+} increased dramatically, reaching values close to 500 arbitrary units. Control samples with known fibrillar content yielded similar fluorescence values (data not shown), leading us to

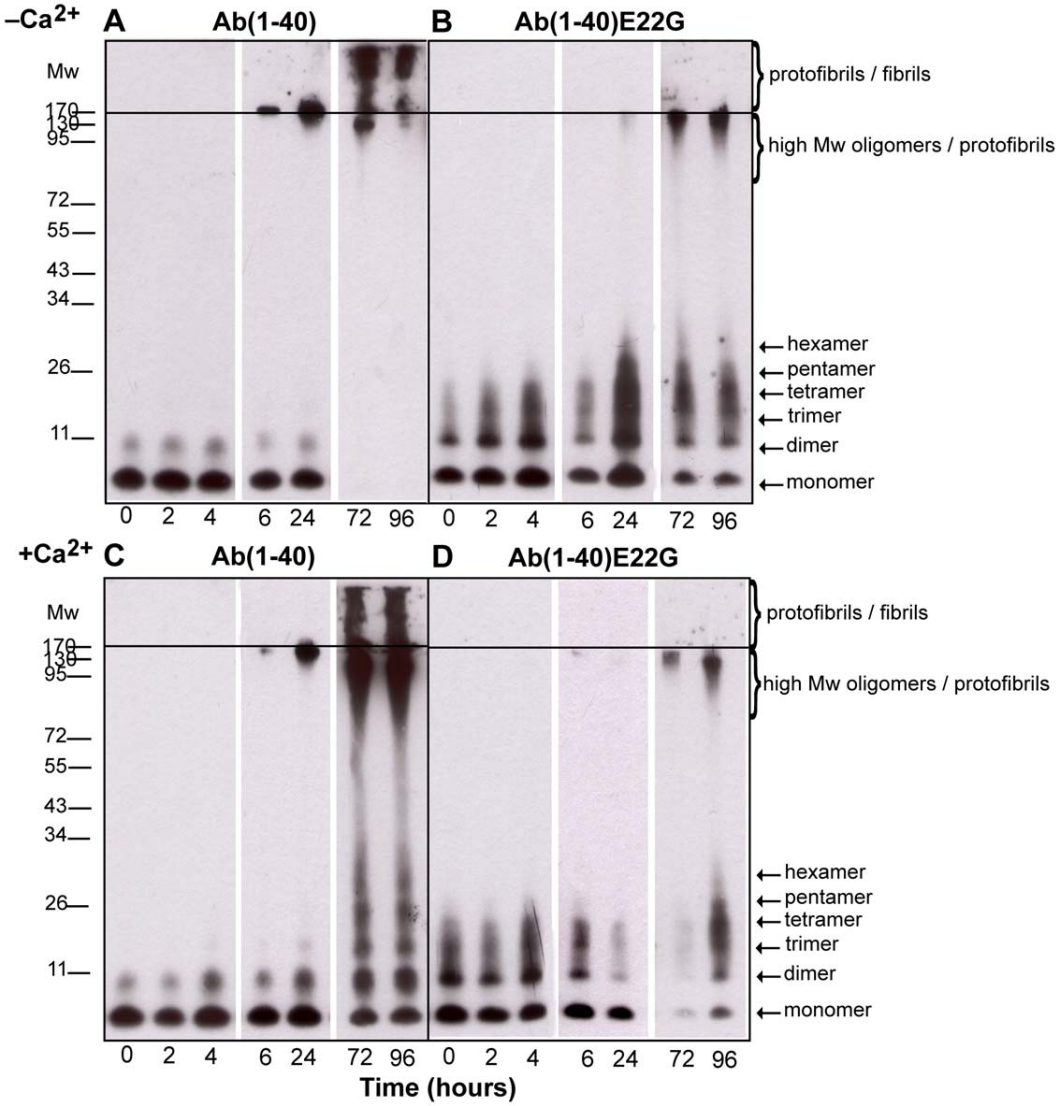

Figure 1. Aggregation profiles of Aβ(1–40) and Aβ(1–40)E22G by Western blot analysis. Aggregation profiles of Aβ(1–40) and Aβ(1–40)E22G during 96 h of incubation in the presence or absence of added Ca^{2+} were followed using Western blot analysis. Samples were separated using gel electrophoresis on a 12% bis-Tris gel. For each condition, samples were taken at $t = 0$, 2, 4, 6, 24, 72, and 96 h. Following the loading of 1 μg of protein sample into each lane, the membrane was probed with a mixture of monoclonal antibodies 6E10 and 4G8 that recognize residues 1–17 and 17–24, respectively. Panels A and B are representative Western blots of Aβ(1–40) and Aβ(1–40)E22G in phosphate buffer ("–Ca^{2+} condition"), respectively. Panels C and D are representative Western blots of Aβ(1–40) and Aβ(1–40)E22G in 2 mM Ca^{2+} ("+Ca^{2+} condition"), respectively. At least four separate experiments were carried out to confirm these results. All images were taken from a single 96-h experimental procedure.
doi:10.1371/journal.pone.0018250.g001

conclude that fibrils were the main species in our sample. This conclusion is supported by a number of studies in which the characteristic fluorescence exhibited by ThT was attributed to the binding of ThT molecules within a cavity that was present in some proteins and amyloid fibrils, but not in others [47,48]. After 96 h of incubation of Aβ(1–40) in the presence of Ca^{2+}, fluorescence intensity values remained low and were attributed to the existence of only a small population of ThT-positive species.

By contrast Aβ(1–40)E22G, both with and without Ca^{2+}, exhibited stable and relatively low ThT fluorescence intensity over the course of 96 h (Fig. 2), implying either that the aggregation process is significantly slower than for Aβ(1–40) or that Aβ(1–40)E22G has a relatively high propensity to form oligomers rather than fibrils. A high tendency of Aβ(1–40)E22G to form oligomers and protofibrils has already been demonstrated in several studies [49,19,20]. Moreover, it was suggested that this characteristic behavior may be responsible for the marked toxicity of Aβ(1–40)E22G [21]. Individuals carrying the Arctic mutation are known to be prone to development of AD early in life [19], possibly because of the formation of oligomers and protofibrils, considered to be more toxic aggregates of Aβ peptide than fibrils.

Oligomers formed by Aβ(1–40) in the presence of Ca^{2+} and oligomers formed by Aβ(1–40)E22G demonstrate similar secondary structures

Secondary structures of Aβ aggregates are known to possess high β-sheet content. Using ATR−FTIR spectroscopy, our group

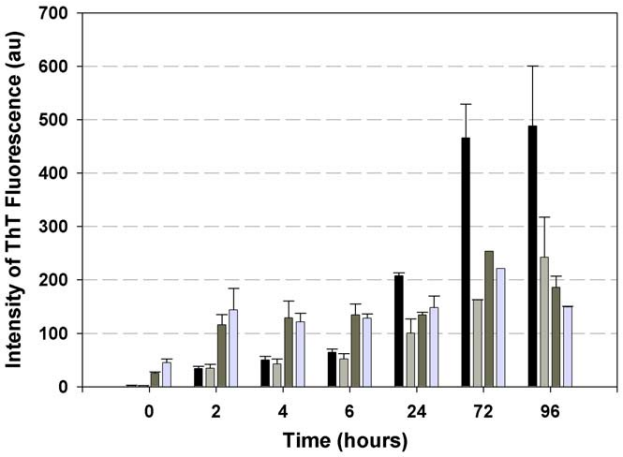

Figure 2. Oligomers and fibrils formation differentiated by ThT fluorescence. ThT fluorescence intensity was monitored to follow fibrillogenesis of Aβ(1–40) and Aβ(1–40)E22G in the presence and in the absence of 2 mM Ca^{2+}. Black bars, Aβ(1–40) in phosphate buffer ("–Ca^{2+} condition"); light grey bars, Aβ(1–40) in 2 mM $CaCl_2$; dark grey bars, Aβ(1–40)E22G in phosphate buffer; light blue bars, Aβ(1–40)E22G in $CaCl_2$. Shown are averages of values obtained in four independent experiments; error bars indicating the standard error of the average.
doi:10.1371/journal.pone.0018250.g002

recently showed that a characteristic signature of soluble oligomers of Aβ is an anti-parallel β-sheet conformation, whereas parallel β-sheet conformation is indicative of the presence of Aβ fibrils [50,51]. Working with Aβ(1–42) and Aβ(1– 40), they demonstrated that in anti-parallel β-sheet structures the amide I region displays two typical components: the major component has an average spectral wavenumber at ~1630 cm^{-1} while the minor component, about five fold weaker than the major one, is characterized by an average wavenumber at ~1695 cm^{-1}. For parallel β-sheet structures the amide I region displays only the major component of ~1630 cm^{-1}. The intensity ratio of 1695/1630 was suggested to be proportional to the percentage of anti-parallel β-strands arranged in a β-sheet [52].

Using ATR−FTIR, we studied the aggregation patterns of Aβ(1–40) and Aβ(1–40)E22G and followed the evolution of 1630-cm^{-1} and 1695-cm^{-1} peaks to assess the presence of oligomers or fibrils as a function of incubation time, based on discrimination of a β-sheet conformation. Figure 3 summarizes the results observed for each of these amyloid peptides in the presence and in the absence of added Ca^{2+}. For all conditions evaluated, during the first 48 h we observed two characteristic features: one peak at ~1695 cm^{-1} and another at ~1630 cm^{-1} (Fig. 3, panels A–D). The presence of a peak at ~1695 cm^{-1} in the infrared spectrum, in addition to a peak at ~1630 cm^{-1}, is characteristic of an anti-parallel β-sheet conformation, indicative of species structurally different from fibrils [51,50]. However, for Aβ(1–40) in the absence of added Ca^{2+} we observed a significant decrease in the ~1695 cm^{-1} peak at t = 48 h (Fig. 3A) and a shift towards lower wavenumbers and narrowing of the ~1630 cm^{-1} peak. This shift (from 1633 cm^{-1} to 1629 cm^{-1}) and narrowing were also detectable to some extent at earlier time points. This specific feature indicated formation of stable and/or long β-strands and strong hydrogen bonds, as would be expected for a stable fibrillar structure [53]. Given that the ratio of 1695/1630 is proportional to the percentage of anti-parallel arrangement of β-strands [52], we used this ratio to estimate the degree of structural change in our samples. For Aβ(1–40) in the "–Ca^{2+} condition" the 1695/1630 ratio decreased dramatically from 0.32 at $t = 0$ h to 0.08 at $t = 96$ h, meaning that there was four times less anti-parallel β-sheet structure after 96 h of incubation in the absence of added Ca^{2+}. This pattern of decrease in the amount of anti-parallel β-strands in a β-sheet points to the formation of fibrillar assemblies from oligomers initially present in the sample. This result complements the outcome of the PAGE analysis and the ThT fluorescence experiments, where after the first 24 h we detected mainly oligomers whose binding affinity for ThT was low, whereas at $t = 96$ h the species observed by PAGE were mainly of high molecular weight (including fibrils), which were highly ThT positive. This result for Aβ(1–40) in phosphate buffer portrayed a dynamic process of fibrillization of the Aβ(1–40) peptide in vitro, starting with monomers and dimers, which over time were converted into fibrils. It was interesting to note that at $t = 72$ h and $t = 96$ h, no monomers, dimers, or other low-molecular-weight oligomers were visible on Western blots, indicating abundant conversion to fibrils.

The behavior of Aβ(1–40) samples in the presence of Ca^{2+} differed from their behavior in the absence of added Ca^{2+}. Throughout the duration of the experiment with Aβ(1–40) in the presence of Ca^{2+} we always observed the two characteristic peaks at ~1695 cm^{-1} and ~1630 cm^{-1} (Fig. 2, panel C). Despite the slight decrease observed over time in the intensity of the ~1695 cm^{-1} peak, no significant narrowing of the peak width at ~1630 cm^{-1} was detected.

An interesting observation was that this spectral behavior of Aβ(1–40) in the presence of Ca^{2+} had the same features as that of Aβ(1–40)E22G in either the presence or the absence of Ca^{2+}. Under both conditions, the peaks exhibited by Aβ(1–40)E22G at ~1695 cm^{-1} and at ~1630 cm^{-1} throughout the 96-h time period were characteristic of an anti-parallel β-sheet conformation (Fig. 3, panels C, B, D), and the ratio between the peaks changed only slightly, mainly after the first 2 h. In addition, no narrowing of the peak at ~1630 cm^{-1} was detected. This finding, obtained by ATR−FTIR, showed good correlation with the results we obtained by PAGE analysis and in our ThT fluorescence experiments, all of which pointed—as expected, and in line with the published data [20,21]—to the formation of a wide range of oligomers and possibly also protofibrils by Aβ(1–40)E22G. The similarity in aggregation patterns of Aβ(1–40) in the "+Ca^{2+} condition" and of Aβ(1–40)E22G under both conditions, as observed here by three independent techniques, raises a fundamental question concerning a possible change in the mechanism of Aβ(1–40) aggregation when Ca^{2+} is present. It seems that calcium ions promote the preferential formation of oligomers and protofibrils, diverting the otherwise favored fibrillogenesis pathway.

Formation of Aβ(1–40) species morphologically similar to the species formed by Aβ(1–40)E22G in the presence of Ca^{2+}

Next we examined whether the oligomers formed by Aβ(1–40) in the presence of Ca^{2+} and the oligomers formed by Aβ(1–40)E22G in the presence and in the absence of added Ca^{2+} share morphological similarities. Using contact mode AFM, we followed oligomerization and fibrillogenesis of Aβ(1–40) and of Aβ(1–40)E22G, in all cases in the presence and absence of added Ca^{2+}, at three time points: $t = 0$, 6, and 72 h (Fig. 4). These times were chosen because most of the differences detected by Western blot analysis, ThT fluorescence, and ATR−FTIR spectroscopy were observed after 0, 6, and 72 h of incubation.

At $t = 0$ h, samples of Aβ(1–40) and of Aβ(1–40)E22G, in all cases both in the presence and in the absence of added Ca^{2+},

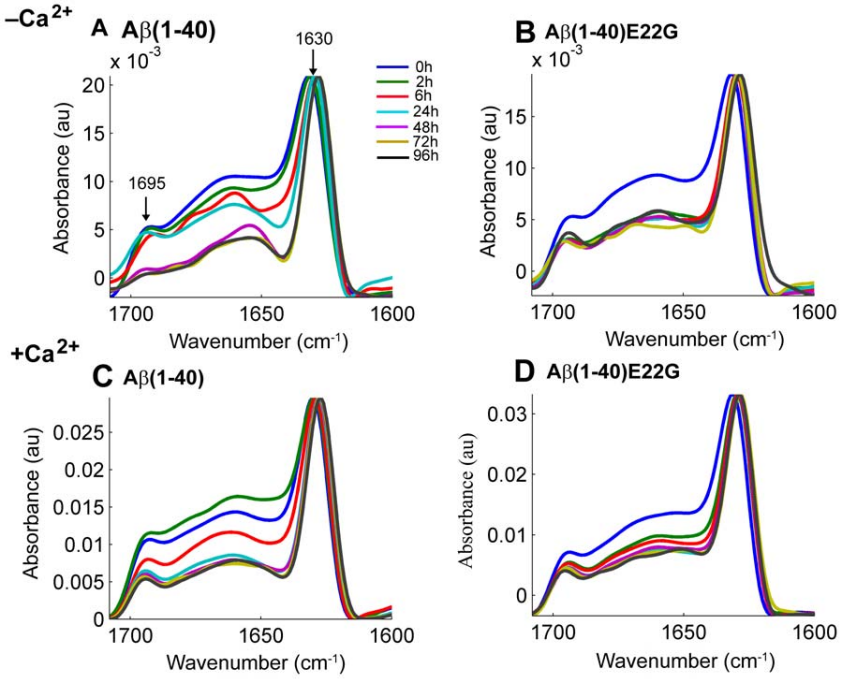

Figure 3. ATR-FTIR spectra of Aβ(1–40) and Aβ(1–40)E22G. FTIR spectra of Aβ(1–40) and Aβ(1–40)E22G were taken in the presence and in the absence of added Ca^{2+}, showing the amide I region of the spectra (1600–1700 cm^{-1}). Aliquots of 2 μl were taken from each sample at $t = 0$, 2, 6, 24, 48, 72, and 96 h (shown in blue, green, red, cyan, purple, mustard, and dark blue, respectively). The data shown here were collected in one continuous experiment and are representative of three independent trials.
doi:10.1371/journal.pone.0018250.g003

contained homogeneously distributed globular particles (Fig. 4, panels A, D, G, J), in agreement with previously reported data [54]. The height of the spherical aggregates was 2.8±0.3 nm ($n = 51$). Although some linear aggregates were detected in Aβ(1–40) samples in the absence of added Ca^{2+} (Fig. 4A), most of the population consisted of globular particles. Since no contribution was seen from the linear aggregates when these samples were tested with other techniques, it seems reasonable to assume that only an insignificant percentage of the peptide was present in the linear aggregate form (perhaps structurally different from fibrils) at the initial stages of incubation. Notably, this population was observed only in the Aβ(1–40) samples lacking Ca^{2+}, even though all the samples received identical treatment.

A second batch of samples was imaged at $t = 6$ h. As expected, no differences in aggregate morphology were noticed between the Aβ(1–40) samples in the presence of Ca^{2+} and the Aβ(1–40)E22G samples in the presence or absence of added Ca^{2+} (Fig. 4E, H, K). All of the particles appeared to be globular, though somewhat larger than at $t = 0$ h (height 3.3±0.5 nm, $n = 20$). Evolution of the species was observed only with Aβ(1–40) in the absence of added Ca^{2+}. In this case there was clear evidence of fibrillization, resulting in a large amount of string-like aggregates and a long, fibril-like species (Fig.4B). Although comparable in length (950±460 nm, $n = 20$) to previously reported fibril lengths [54], they were too thin to be categorized as fibrils. The string-like structures had become more abundant, and the fraction of spherical particles that remained was small (Fig. 4B).

The most striking differences were those observed between samples imaged at $t = 72$ h. The Aβ(1–40) samples without Ca^{2+} exhibited well-organized fibrils (Fig. 4C) whose dimensions (height 8.4±0.5 nm, $n = 13$; width 124±15 nm, $n = 12$; length 1±0.6 μm, $n = 67$) mostly correlated with those previously published for Aβ(1–40) [53]. When Aβ(1–40) was incubated in the presence of Ca^{2+} the resulting aggregates were not fibrillar, but rather spherical (height, 2.6±0.4 nm; $n = 24$) and (mostly) curvilinear (Fig. 4F) (height 3.0±0.5 nm; $n = 28$; length 250±73 nm; $n = 40$), which previous authors have referred to as oligomers and protofibrils, respectively [49]. Like the results described above and therefore in line with our expectations, Aβ(1–40) in the presence of Ca^{2+} and Aβ(1–40)E22G both in the presence and in the absence of added Ca^{2+} all formed the same oligomeric species: initially spherical particles, evolving to curvilinear structures after 72 h. These values are consistent with the data from Mastrangelo et al. [55], where the authors reported z-heights of 2–3 nm on average, for early (<1 h) oligomers and ~2 nm for monomers of Aβ(1–42) obtained by high resolution AFM under hydrated conditions. Detailed analysis of their results revealed that for low molecular weight oligomers as well as protofibrils the z-height ranged between 2 to 4 nm. Only for some of the high molecular weight oligomers Mastrangelo et al. reported values of z-height 4–6 nm. It is likely that Aβ(1–40) and Aβ(1–42) do not form the same type of high molecular weight oligomers and the growth of Aβ(1–40) oligomers might be restricted to the lateral dimension, without causing height changes from monomers to oligomers.

In the presence of Ca^{2+}, the aggregation pathway of Aβ(1–40) was clearly shifted towards formation of oligomers, and not of fibrils as occurred in the absence of added Ca^{2+}. Evidently, therefore, the presence of calcium ions has a significant impact on the aggregation process of Aβ(1–40).

Discussion

The pathogenesis of Alzheimer's disease is complex, and involves marked molecular, cellular, and physiological changes.

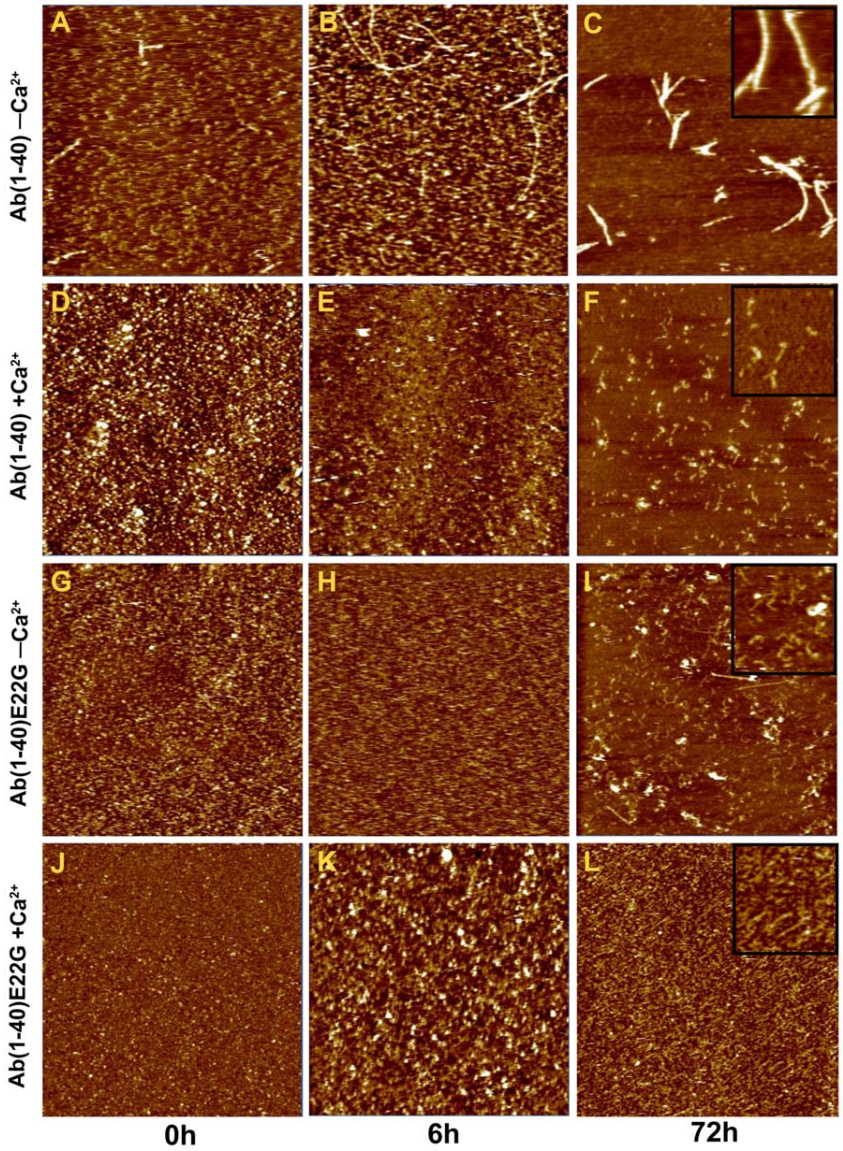

Figure 4. Morphological comparison of Aβ(1–40) and Aβ(1–40)E22G. Contact mode AFM images (5 μm × 5 μm, Z scale 15 nm) of Aβ(1–40) and Aβ(1–40)E22G peptides on mica, recorded either in phosphate buffer or in MOPS buffer with Ca^{2+}. Samples of Aβ(1–40) and Aβ(1–40)E22G in the presence and absence of added Ca^{2+} (marked as "+Ca^{2+}" or "−Ca^{2+}", respectively) at $t = 0$, 6, or 72 h. Closer views (1 μm × 1 μm, Z scale 15 nm) of oligomers, protofibrils and fibrils are shown as insets in the panel of $t = 72$ h (C, F, I, L). Images A, D, G, J were taken at $t = 0$; images B, E, H, K were taken at $t = 6$ h. Peptide concentration was the same in all samples.
doi:10.1371/journal.pone.0018250.g004

The Ca^{2+} hypothesis, which introduced the concept of regulation by Ca^{2+} of neuronal death both in age-related and in pathogenic processes, attempts to explain how disruptions in Ca^{2+} homeostasis that continue over a prolonged period are a proximate cause of neurodegeneration in Alzheimer's disease. Numerous studies have linked Aβ to Ca^{2+} through demonstrating Ca^{2+} up-regulation by amyloid aggregates and relating Ca^{2+} dysregulation to AD-causing mutations. Accumulation of Aβ aggregates has been shown to initiate a complex pathological cascade, leading ultimately to memory alterations, cognitive impairments, and neuronal death [56]. Questions remain, however, concerning the role of early preclinical processes that predate the pathology and may enable or accelerate the aggregation of Aβ, thereby contributing to development of the disease. In particular, the possible contributory effect of normal physiological changes that take place in old age is still unknown.

In this work we tried to determine whether calcium can facilitate the formation of oligomers that might in turn be held responsible for neuronal toxicity. Using four different techniques, we showed that Aβ(1–40) forms oligomers and protofibrils in the presence of 2 mM Ca^{2+} similar to those produced by Aβ(1–40)E22G both in the presence and in the absence of added Ca^{2+} (21 μM of calcium ion were present in "−Ca^{2+} condition" buffer due to their traces in MilliQ water and in HPLC-grade buffer). We found that in the "−Ca^{2+} condition" Aβ(1–40) readily formed fibrils, which were detectable by PAGE and by ThT fluorescence analysis as well as by FTIR, and differences in secondary structures were observed between oligomers and fibrils. Moreover,

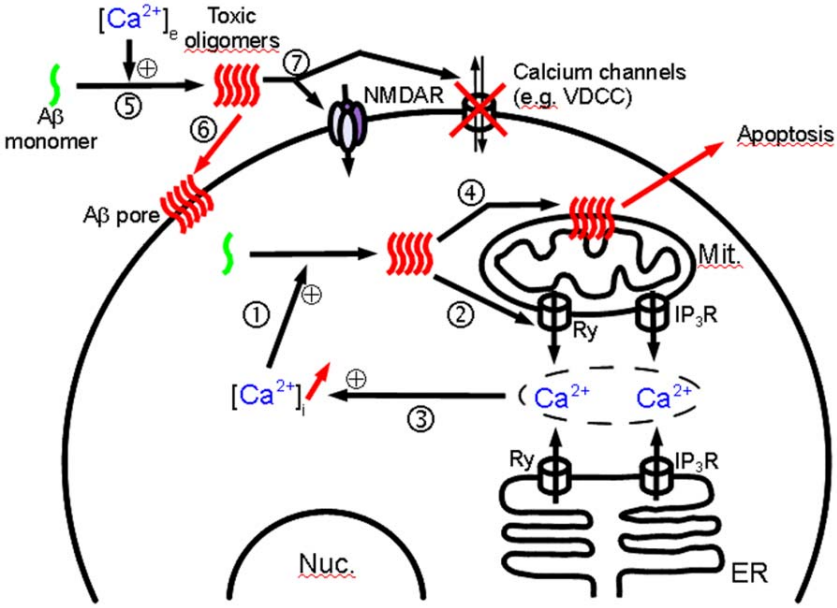

Figure 5. Potential interplay between Aβ oligomers, Ca^{2+}, and a target cell in the initial stages of Alzheimer's disease. (1) Age-related increase in $[Ca^{2+}]_i$ promotes oligomerization of intracellular Aβ. (2) Disruption of Ca^{2+} homeostasis by oligomers, by either binding to or modulating the activity of a number of receptors such as ryanodine (Ry) and inositol triphosphate (IP_3R) [25]. (3) Increase in $[Ca^{2+}]_i$. These three steps might form an inimical cycle leading to increases in both cytosolic calcium and Aβ oligomer concentrations. (4) Aβ oligomers disrupt intracellular membranes, leading to apoptosis [34,41,64]. (5) Extracellular calcium concentration ($[Ca^{2+}]_e$) promotes oligomerization of extracellular Aβ. (6) Oligomers form nonspecific pores in the plasma membrane, disturbing cellular integrity and leading to apoptosis [65]. (7) Aβ oligomers can interact and impair calcium channels at the membrane surface, opening calcium importers and blocking calcium exporters such as the voltage-dependent calcium channel [66]. Aβ oligomers can affect surface expression of N-methyl-D-aspartate receptors (NMDARs) [67], may increase [68] or decrease the conductance [69], and facilitate long-term synaptic depression by disrupting neuronal glutamate uptake [70].
doi:10.1371/journal.pone.0018250.g005

AFM imaging clearly revealed morphological similarities between oligomers of Aβ(1–40) and of Aβ(1–40)E22G, all of which were spherical or curvilinear in shape. Aβ(1–40)E22G has been shown to form oligomers and protofibrils in vivo and to cause early and severe signs of AD in mice [57]. It remains an open question whether the morphological similarity of oligomers of Aβ(1–40) formed in the presence of Ca^{2+} to oligomers of Aβ(1–40)E22G formed also in the absence of added Ca^{2+} implies that they have similar toxic effects.

Previous studies of the role of Ca^{2+} in Aβ aggregation have revealed acceleration of Aβ(1–42) fibril formation in the presence of Ca^{2+} [58,59], but without acceleration in the kinetics of Aβ(1–40) fibrillization [59]. In the present study, however, we focused on the role of Ca^{2+} in the formation of oligomers, rather than in fibril formation. Our experiments demonstrated that 2 mM Ca^{2+} catalyze the formation of oligomers of Aβ(1–40), whereas in the absence of added Ca^{2+} mostly fibrils were formed. To the best of our knowledge, this is the first time that Ca^{2+} has been shown to induce Aβ(1–40) to form oligomers. We conducted our present experiments with 2 mM added $CaCl_2$ and 100 μM Aβ. Ca^{2+} concentrations in the neuronal cytosol vary from hundreds of nanomolars to micromolars, which is consistent with the concentration of calcium traces in the "$-Ca^{2+}$ buffer". Higher cytosolic calcium concentration may occur for prolonged periods during slow after-polarization current of ER after Ca^{2+} release from intracellular stores during LTP induction [60]. The cytosolic Ca^{2+} load is an important factor in regulating the size of mitochondrial Ca^{2}+ stores [60], and during neuronal activity, which includes increases in cytosolic Ca^{2+}, mitochondria can take up significant loads of Ca^{2+} [61]. In addition, 2 mM Ca^{2+} is close to the concentration in the extracellular space, where formation of oligomers may be initiated and from where they might subsequently exert their toxic effect on the plasma membrane [62,63]. Comparison of experiments carried out at 20 μm and 2 mM calcium suggests that extracellular calcium promotes oligomerization of Aβ(1–40). From additional information obtained by measuring residual calcium in the "$-Ca^{2+}$" buffer it is tempting to conclude that the intracellular concentration of calcium does not promote oligomerization. It remains however, that the intracellular Aβ peptides and calcium concentrations are difficult to evaluate and the existence of an intracellular effect can not be rejected at this stage. Based on the previously published data (as outlined in the Introduction) as well as our present findings, we schematically summarize the potential effects of both extra- and intracellular calcium ions on Aβ and cells (Fig. 5).

To conclude, our results show that the formation of Aβ(1–40) oligomers is induced in the presence of 2 mM Ca^{2+}, whereas in the presence of as little as 20 μM Ca^{2+} Aβ(1–40) undergoes fibrillogenesis. The mechanism of Ca^{2+}-induced Aβ(1–40) aggregation is currently under investigation. Nevertheless, the above finding might constitute the missing link that connects early dysregulation in Ca^{2+} signaling to later onset of pathological and/or cognitive symptoms characteristic of AD. In their recent review focusing on intracellular Aβ production and its assembly states, LaFerla et al. [63] suggested that the buildup of intracellular Aβ might be an early event in the pathogenesis of AD as well as of Down syndrome. Taking that notion further, we contemplate that the early event in AD pathology might be the aggregation of intracellular Aβ in response to an increase in $[Ca^{2+}]_i$ as a result of natural aging processes. These early aggregates could in turn exert

their toxic effect to alter Ca^{2+} signaling, which may account for the progressive decline in memory and the increase in neuronal cell apoptosis that occurs during AD. This may constitute a possible reason why in old age, when calcium imbalance is pronounced, the probability of developing AD is increased. This may also offer an alternative approach to prevention and treatment strategies for this disease, targeting mechanistic causes rather than late-stage symptoms.

Acknowledgments

V.R. and Y.F.D. are Senior Research Associates at the National Foundation for Scientific Research (FNRS, Belgium).

Author Contributions

Conceived and designed the experiments: AI BB JMR VR. Performed the experiments: AI VD. Analyzed the data: AI VD YFD VR. Contributed reagents/materials/analysis tools: YFD BB JMR VR. Wrote the paper: AI VD JMR VR.

References

1. Hardy JA, Higgins GA (1992) Alzheimers-Disease - the Amyloid Cascade Hypothesis. Science 256: 184–185.
2. Cummings BJ, Cotman CW (1995) Image-Analysis of Beta-Amyloid Load in Alzheimers-Disease and Relation to Dementia Severity. Lancet 346: 1524–1528.
3. Näslund J, Haroutunian V, Mohs R, Davis KL, Davies P, et al. (2000) Correlation between elevated levels of amyloid beta-peptide in the brain and cognitive decline. Jama-J Am Med Assoc 283: 1571–1577.
4. Irizarry MC, Soriano F, McNamara M, Page KJ, Schenk D, et al. (1997) A beta deposition is associated with neuropil changes, but not with overt neuronal loss in the human amyloid precursor protein V717F (PDAPP) transgenic mouse. J Neurosci 17: 7053–7059.
5. Chui DH, Tanahashi H, Ozawa K, Ikeda S, Checler F, et al. (1999) Transgenic mice with Alzheimer presenilin 1 mutations show accelerated neurodegeneration without amyloid plaque formation. Nat Med 5: 560–564.
6. Klein WL, Krafft GA, Finch CE (2001) Targeting small A beta oligomers: the solution to an Alzheimer's disease conundrum? Trends Neurosci 24: 219–224.
7. Hardy J, Selkoe DJ (2002) Medicine - The amyloid hypothesis of Alzheimer's disease: Progress and problems on the road to therapeutics. Science 297: 353–356.
8. Lue LF, Kuo YM, Roher AE, Brachova L, Shen Y, et al. (1999) Soluble Amyloid {beta} Peptide Concentration as a Predictor of Synaptic Change in Alzheimer's Disease. Am J Pathol 155: 853–862.
9. Rowan MJ, Klyubin I, Wang Q, Hu NW, Anwyl R (2007) Synaptic memory mechanisms: Alzheimer's disease amyloid beta-peptide-induced dysfunction. Biochem Soc T 35: 1219–1223.
10. Mclean CA, Cherny RA, Fraser FW, Fuller SJ, Smith MJ, et al. (1999) Soluble pool of A beta amyloid as a determinant of severity of neurodegeneration in Alzheimer's disease. Ann Neurol 46: 860–866.
11. Bliss TVP, Lomo T (1973) Long-lasting potentiation of synaptic transmission in the dentate area of the anaesthetized rabbit following stimulation of the perforant path. Journal Physiol 232: 331–356.
12. Lambert MP, Barlow AK, Chromy BA, Edwards C, Freed R, et al. (1998) Diffusible, nonfibrillar ligands derived from A beta(1-42) are potent central nervous system neurotoxins. Proc Natl Acad Sci USA 95: 6448–6453.
13. Walsh DM, Klyubin I, Fadeeva JV, Cullen WK, Anwyl R, et al. (2002) Naturally secreted oligomers of amyloid beta protein potently inhibit hippocampal long-term potentiation in vivo. Nature 416: 535–539.
14. Wang HW, Pasternak JF, Kuo H, Ristic H, Lambert MP, et al. (2002) Soluble oligomers of beta amyloid (1-42) inhibit long-term potentiation but not long-term depression in rat dentate gyrus. Brain Res 924: 133–140.
15. Selkoe DJ (1991) The Molecular Pathology of Alzheimers-Disease. Neuron 6: 487–498.
16. Selkoe DJ (2001) Alzheimer's disease: Genes, proteins, and therapy. Physiol Rev 81: 741–766.
17. Bossy-Wetzel E, Schwarzenbacher R, Lipton SA (2004) Molecular pathways to neurodegeneration. Nat Rev Neurosci 10: S2–S9.
18. Stine WB, Dahlgren KN, Krafft GA, Ladu MJ (2003) In vitro characterization of conditions for amyloid-beta peptide oligomerization and fibrillogenesis. J Biol Chem 278: 11612–11622.
19. Nilsberth C, Westlind-Danielsson A, Eckman CB, Condron MM, Axelman K, et al. (2001) The 'Arctic' APP mutation (E693G) causes Alzheimer's disease by enhanced A[beta] protofibril formation. Nat Neurosci 4: 887–893.
20. Päiviö A, Jarvet J, Gräslund A, Lannfelt L, Westlind-Danielsson A (2004) Unique Physicochemical Profile of [beta]-Amyloid Peptide Variant A[beta]1-40E22G Protofibrils: Conceivable Neuropathogen in Arctic Mutant Carriers. JMB 339: 145–159.
21. Whalen BM, Selkoe DJ, Hartley DM (2005) Small non-fibrillar assemblies of amyloid [beta]-protein bearing the Arctic mutation induce rapid neuritic degeneration. Neurobiol Dis 20: 254–266.
22. Kamino K, Orr HT, Payami H, Wijsman EM, Alonso ME, et al. (1992) Linkage and Mutational Analysis of Familial Alzheimer-Disease Kindreds for the App Gene Region. Am J Hum Genet 51: 998–1014.
23. Mattson MP (2004) Pathways towards and away from Alzheimer's disease (vol 430, pg 631, 2004). Nature 431: 107–107.
24. Smith IF, Green KN, LaFerla FM (2005) Calcium dysregulation in Alzheimer's disease: Recent advances gained from genetically modified animals. Cell Calcium 38: 427–437.
25. Stutzmann GE (2005) Calcium dyspegulation, IP3 signaling, and Alzheimer's disease. Neuroscientist 11: 110–115.
26. Khachaturian ZS (1994) Calcium Hypothesis of Alzheimer's Disease and Brain Aging. Ann NY Acad Sci 747: 1–11.
27. Xiong J, Verkhratsky A, Toescu EC (2002) Changes in Mitochondrial Status Associated with Altered Ca2+ Homeostasis in Aged Cerebellar Granule Neurons in Brain Slices. J Neurosci 22: 10761–10771.
28. Bezprozvanny I, Mattson MP (2008) Neuronal calcium mishandling and the pathogenesis of Alzheimer's disease. Trends in Neurosci 31: 454–463.
29. Bojarski L, Herms J, Kuznicki J (2008) Calcium dysregulation in Alzheimer's disease. Neurochem Int 52: 621–633.
30. Green KN, LaFerla FM (2008) Linking calcium to A beta and Alzheimer's disease. Neuron 59: 190–194.
31. Etcheberrigaray R, Hirashima N, Nee L, Prince J, Govoni S, et al. (1998) Calcium responses in fibroblasts from asymptomatic members of Alzheimer's disease families. Neurobiol Dis 5: 37–45.
32. Ito E, Oka K, Etcheberrigaray R, Nelson TJ, Mcphie DL, et al. (1994) Internal Ca^{2+} Mobilization Is Altered in Fibroblasts from Patients with Alzheimer-Disease. Proc Natl Acad Sci USA 91: 534–538.
33. Mattson MP, Cheng B, Davis D, Bryant K, Lieberburg I, et al. (1992) Beta-Amyloid Peptides Destabilize Calcium Homeostasis and Render Human Cortical-Neurons Vulnerable to Excitotoxicity. J Neurosci 12: 376–389.
34. Kawahara M, Kuroda Y, Arispe N, Rojas E (2000) Alzheimer's β-Amyloid, Human Islet Amylin, and Prion Protein Fragment Evoke Intracellular Free Calcium Elevations by a Common Mechanism in a Hypothalamic GnRH Neuronal Cell Line. JBC 275: 14077–14083.
35. Mattson M, Engle M, Rychlik B (1991) Effects of elevated intracellular calcium levels on the cytoskeleton and tau in cultured human cortical neurons. Mol Chem Neuropathol 15: 117–142.
36. Mattson MP (1994) Calcium and Neuronal Injury in Alzheimer's Disease. Ann NY Acad Sci 747: 50–76.
37. Ferreiro E, Oliveira CR, Pereira C (2004) Involvement of endoplasmic reticulum Ca2+ release through ryanodine and inositol 1,4,5-triphosphate receptors in the neurotoxic effects induced by the amyloid-beta peptide. J Neurosci Res 76: 872–880.
38. Paula-Lima AC, Adasme T, SanMartín C, Sebollela A, Hetz C, et al. (2011) Amyloid β-Peptide Oligomers Stimulate RyR-Mediated Ca^{2+} Release Inducing Mitochondrial Fragmentation in Hippocampal Neurons and Prevent RyR-Mediated Dendritic Spine Remodeling Produced by BDNF. Antioxid Redox Signal 14.
39. Stutzmann GE (2007) The pathogenesis of alzheimers disease - Is it a lifelong "Calciumopathy"? Neuroscientist 13: 546–559.
40. De Felice FG, Velasco PT, Lambert MP, Viola K, Fernandez SJ, et al. (2007) A+¦ Oligomers Induce Neuronal Oxidative Stress through an N-Methyl-D-aspartate Receptor-dependent Mechanism That Is Blocked by the Alzheimer Drug Memantine. J Biol Chem 282: 11590–11601.
41. Arispe N, Pollard HB, Rojas E (1993) Giant multilevel cation channels formed by Alzheimer disease amyloid beta-protein [A beta P-(1-40)] in bilayer membranes. Proc Natl Acad Sci USA 90: 10573–10577.
42. Kagan BL, Azimov R, Azimova R (2004) Amyloid peptide channels. J Membrane Biol 202: 1–10.
43. Querfurth HW, Selkoe DJ (1994) Calcium Ionophore Increases Amyloid-Beta Peptide Production by Cultured-Cells. Biochemistry 33: 4550–4561.
44. Pierrot N, Santos SF, Feyt C, Morel M, Brion JP, et al. (2006) Calcium-mediated transient phosphorylation of tau and amyloid precursor protein followed by intraneuronal amyloid-beta accumulation. J Biol Chem 281: 39907–39914.
45. Naiki H, Higuchi K, Hosokawa M, Takeda T (1989) Fluorometric-Determination of Amyloid Fibrils Invitro Using the Fluorescent Dye, Thioflavine-T. Anal Biochem 177: 244–249.
46. Benseny-Cases N, Cócera M, Cladera J (2007) Conversion of non-fibrillar [beta]-sheet oligomers into amyloid fibrils in Alzheimer's disease amyloid peptide aggregation. Biochem Bioph Res Co 361: 916–921.
47. Groenning M, Olsen L, van de Weert M, Flink JM, Frokjaer S, et al. (2007) Study on the binding of Thioflavin T to beta-sheet-rich and non-beta-sheet cavities. J Struct Biol 158: 358–369.
48. Krebs MRH, Bromley EHC, Donald AM (2005) The binding of thioflavin-T to amyloid fibrils: localisation and implications. J Struct Biol 149: 30–37.

49. Lashuel HA, Hartley DM, Petre BM, Wall JS, Simon MN, et al. (2003) Mixtures of Wild-type and a Pathogenic (E22G) Form of A[beta]40 in Vitro Accumulate Protofibrils, Including Amyloid Pores. J Mol Biol 332: 795–808.
50. Cerf E, Sarroukh R, Tamamizu-Kato S, Breydo L, Derclaye S, et al. (2009) Antiparallel beta-sheet: a signature structure of the oligomeric amyloid beta-peptide. Biochem J 421: 415–423.
51. Chirgadze YN, Nevskaya NA (1976) Infrared-Spectra and Resonance Interaction of Amide-One Vibration of Anti-Parallel-Chain Pleated Sheet. Biopolymers 15: 607–625.
52. Goormaghtigh E, Cabiaux V, Ruysschaert JM (1994) Determination of soluble and membrane protein structure by Fourier transform infrared spectroscopy. I. Assignments and model compounds. Subcell Biochem 23: 329–362.
53. Dahlgren KN, Manelli AM, Stine WB, Jr., Baker LK, Krafft GA, et al. (2002) Oligomeric and Fibrillar Species of Amyloid-beta Peptides Differentially Affect Neuronal Viability. J Biol Chem 277: 32046–32053.
54. Haass C, Selkoe DJ (2007) Soluble protein oligomers in neurodegeneration: lessons from the Alzheimer's amyloid beta-peptide. Nat Rev Mol Cell Bio 8: 101–112.
55. Mastrangelo IA, Ahmed M, Sato T, Liu W, Wang CP, et al. (2006) High-resolution atomic force microscopy of soluble A beta 42 oligomers. Journal of Molecular Biology 358: 106–119.
56. Lord A, Kalimo H, Eckman C, Zhang XQ, Lannfelt L, et al. (2006) The Arctic Alzheimer mutation facilitates early intraneuronal A beta aggregation and senile plaque formation in transgenic mice. Neurobiol Aging 27: 67–77.
57. Isaacs AM, Senn DB, Yuan ML, Shine JP, Yankner BA (2006) Acceleration of amyloid beta-peptide aggregation by physiological concentrations of calcium. J Biol Chem 281: 27916–27923.
58. Ahmad A, Muzaffar M, Ingram VM (2009) Ca2+, within the physiological concentrations, selectively accelerates A[beta]42 fibril formation and not A[beta]40 in vitro. BBA - Proteins Proteom 1794: 1537–1548.
59. Kuroda Y, Kawahara M (1994) Aggregation of Amyloid Beta-Protein and Its Neurotoxicity - Enhancement by Aluminum and Other Metals. Tohoku J Exp Med 174: 263–268.
60. Budd SL, Nicholls DG (1999) Mitochondria in the life and death of neurons. Essays Biochem 33: 43–52.
61. LaFerla FM (2002) Calcium dyshomeostasis and intracellular signalling in Alzheimer's disease. Nat Rev Neurosci 3: 862–872.
62. Toescu EC (2007) Altered Calcium Homeostasis in Old Neurons.
63. LaFerla FM, Green KN, Oddo S (2007) Intracellular amyloid-beta in Alzheimer's disease. Nat Rev Neurosci 8: 499–509.
64. Arispe N, Rojas E, Pollard HB (1993) Alzheimer disease amyloid beta protein forms calcium channels in bilayer membranes: blockade by tromethamine and aluminum. Proc Natl Acad Sci USA 90: 567–571.
65. Bucciantini M, Calloni G, Chiti F, Formigli L, Nosi D, et al. (2004) Prefibrillar Amyloid Protein Aggregates Share Common Features of Cytotoxicity. J Biol Chem 279: 31374–31382.
66. Rovira C, Arbez N, Mariani J (2002) A[beta](25-35) and A[beta](1-40) act on different calcium channels in CA1 hippocampal neurons. Biochem Bioph Res Co 296: 1317–1321.
67. Dewachter I, Filipkowski RK, Priller C, Ris L, Neyton J, et al. (2009) Deregulation of NMDA-receptor function and down-stream signaling in APP[V717I] transgenic mice. Neurobiol Aging 30: 241–256.
68. Molnár Z, Soós K, Lengyel I, Penke B, Szegedi V, et al. (2004) Enhancement of NMDA responses by [beta]-amyloid peptides in the hippocampus in vivo. Neuroreport 15: 1649–1652.
69. Shankar GM, Bloodgood BL, Townsend M, Walsh DM, Selkoe DJ, et al. (2007) Natural Oligomers of the Alzheimer Amyloid-{beta} Protein Induce Reversible Synapse Loss by Modulating an NMDA-Type Glutamate Receptor-Dependent Signaling Pathway. J Neurosci 27: 2866–2875.
70. Li SM, Hong SY, Shepardson NE, Walsh DM, Shankar GM, et al. (2009) Soluble Oligomers of Amyloid beta Protein Facilitate Hippocampal Long-Term Depression by Disrupting Neuronal Glutamate Uptake. Neuron 62: 788–801.

COLOPHON

This thesis was typeset with LyX, a document processor released under a Free Software/Open Source license and available in several languages http://www.lyx.org/.

The typographic style was written for LaTeX by André Miede in homage to Bringhurst's "The Elements of Typographic Style". The LyX port of the original package, "classicthesis", was written by Nick Mariette and it is available at http://soundsorange.net/resources/classic-thesis-for-lyx/.

Final Version as of February 27, 2013 at 18:04.

DECLARATION

I hereby declare that this thesis is my own work and effort and that it has not been submitted anywhere for any award. Where other sources of information have been used, they have been acknowledged.

Strasbourg, France, May 2012

Anna Itkin